STUDIES ON LYOTROPIC CHROMONIC LIQUID CRYSTALS IN NEMATIC AND BIPHASIC REGIONS

A Dissertation
Presented to
The Academic Faculty

by

Xuxia Yao

In Partial Fulfillment
of the Requirements for the Degree
Doctor of Philosophy in the
School of Materials Science and Engineering

Georgia Institute of Technology
December, 2011

STUDIES ON LYOTROPIC CHROMONIC LIQUID CRYSTALS IN NEMATIC AND BIPHASIC REGIONS

Approved by:

Dr. Mohan Srinivasarao, Advisor
School of Materials Science and Engineering
Georgia Institute of Technology

Dr. Laren Tolbert
School of Chemistry and Biochemistry
Georgia Institute of Technology

Dr. Anselm Griffin
School of Materials Science and Engineering
Georgia Institute of Technology

Dr. Alberto Fernandez-Nieves
School of Physics
Georgia Institute of Technology

Dr. Jung Ok Park
School of Materials Science and Engineering
Georgia Institute of Technology

Date Approved: Aug. 26, 2011

To my parents.

ACKNOWLEDGEMENTS

I want to give my sincere thanks to my advisor, Prof. Mohan Srinivasarao. Without his guidance and support, I couldn't have finished my thesis work. I benefited greatly from his wealth of knowledge and excellent taste of science. I also appreciate the freedom and the time he gave me for doing research projects. He encouraged me to attend many academic conferences to communicate with people in my research field. I am also deeply grateful to Dr. Jung Ok Park for her encouragement, advice and her time on correcting my research proposal, papers and thesis.

I also wish to give my special thanks to Prof. Alejandro Rey at McGill University. It was wonderful to have him involved in my defect studies. Every discussion we had was very fruitful. I really appreciated his guidance, time and the effort he spent on the theoretical part of Chapter Five. I am deeply indebted to him.

I would like to thank my committee members, Prof. Anselm Griffin, Prof. Laren Tolbert and Prof. Alberto Fernandez-Nieves for their advice, valuable criticisms and time spent on reading and correcting my thesis.

Many thanks to my collaborators Dr. Mahmoud A Mahmoud and Qizhen Liang for the great experiments we did together. I also appreciated the generosity of Prof. Mostafa El-Sayed and Prof. C. P. Wong for letting me use equipment in their labs.

I have to give many thanks to group alumni Matija Crne and Vivek Sharma for their help when I first joined this group and afterwards. I also thank my current group members, Minsu Lee, Min-Sang Park, Beom-Jin Yoon and Karthik Nayani for their help.

I also wish to express my gratitude to Prof. Wallace Carr, Prof. Donggang Yao, Prof. Toan Nguyen and Prof. Elsa Reichmanis, Dr. Yaodong Liu, Dr. Wei Zhang, Dr. Ruihua Li, Dr. Jun Jia, Dr. Christina Gardner, Dr. Liwei Zhang, Jing Chen, Yao Li, Dr. Xuejia Yan, Dr. Bo Xu, Sarang Deodhar, Dr. Hongjin Jiang, Dr. Chunqing Peng, Dr. Jiongxin Lu, Dr. Kishor Gupta, Dr. Venkata Gundabala, Dr. Rahul Jain, Dr. Yunan Fang, Dr. Xuan Zhang, Wenwei Xu, Avishek Aiyar, as well as school staffs, Angie Beggs, Leslie Bayor, Hope Payne and Linda Roberson for their encouragement and help.

I appreciated the useful discussions with people from other schools: Prof. Satyendra Kumar, Prof. Suk-Wah Tam-Chang, Dr. Chenhui Zhu, and others.

I would like to thank the National Science Foundation for their financial support and the Georgia Tech Center for Organic Photonics and Electronics for awarding me the 2011 COPE Fellowship as well as the College of Engineering, Office of International Education and Student Government Association for supporting some of my conference travels.

Finally, I wish to thank my parents for their love and support.

TABLE OF CONTENTS

LIST OF TABLES

LIST OF FIGURES

LIST OF SYMBOLS

T	temperature
$\boldsymbol{n}$	director of liquid crystals
θ_m	angle between the mesogen molecule axis and the local director
T_C	clearing temperature
$T_{N\text{-}I}$	nematic-isotropic transition temperature
$T_{N\text{-}B}$	nematic-biphasic transition temperature
S	scalar order parameter
F	free energy density
F_0	free energy density for a completely uniformly aligned nematic director configuration
F_d	increase of F due to deformations
K_{11}, K_{22} and K_{33}	splay, twist and bend elastic constants, respectively
K	average elastic constant
$n_{//}$	refractive index parallel to the optical axis
$n_{\perp}$	refractive index perpendicular to the optical axis
λ	vacuum wavelength
d	sample thickness
n_o	refractive index which ordinary ray experiences
n_e	refractive index which extraordinary ray experiences
Δn	birefringence
ϕ	angle between the optic axis and the direction of light propagation
δ	phase difference
φ	azimuthal angle, i.e. the angle between the analyzer and the projection of the optic axis onto the sample plane
I_0	incident light intensity
I	transmitted light intensity

P	polarizer
A	analyzer
s	strength of disclinations
Ω'	rotation angle of director
N	nematic phase
N*	chiral nematic phase
(hexagonal) M	hexagonal columnar phase
H_1	hexagonal middle soap phase
β	slippage angle in J-type dye aggregates
k_B	Boltzmann constant
n_0	refractive index in the isotropic phase
W	capillary width
C	capillary thickness
∂	capillary wall thickness
$A_{//}$	absorption parallel to the director
$A\perp$	absorption perpendicular to the director
R_{di}	dichroic ratio
Å	angstrom
$\boldsymbol{\mu}$	induced dipole moment
$\boldsymbol{p}$	molecular polarizability
$\boldsymbol{E}$	electric field of the incident light
E_0	amplitude of the oscillation of incident light
v_0	frequency of the oscillation of incident light
q_k	distortion co-ordinates
$I_{//}$	Raman intensity with polarization parallel to the incident polarization
$I_{\perp}$	Raman intensity with polarization perpendicular to the incident polarization

θ	angle between the axis of a uniaxial molecule and the incident polarization direction
$p_x^{'}$, $p_y^{'}$, $p_z^{'}$	three components of the Raman tensor
n_x, n_y, n_z	laboratory frame
α, β, γ	Euler angles reflecting the orientational degrees of freedom
P_{lmn}	Legendre polynomial
$<P_{200}>$	second rank order parameter
$<P_{400}>$	fourth rank order parameter
$E_{//}$	electric field of the scattered light when the analyzed direction is parallel to the incident polarization
$E_{\perp}$	electric field of the scattered light when the analyzed direction is perpendicular to the incident polarization
$R(\theta)$	depolarization ratio
r	differential polarizability ratio
θ_0	flow alignment angle
α_i	Leslie viscosities coefficients
A_{ij}	symmetric part of the second-rank tensor of the velocity gradient
$\boldsymbol{D}$	symmetric strain rate tensor
$\boldsymbol{W}$	skew symmetric spin tensor
$\boldsymbol{h}$	molecular field
γ_1	rotational viscosity
γ_2	irrotational torque coefficient
c	number of molecules in unit volume
$\overline{D_r}$	rotational diffusion coefficient
a	molecular aspect ratio
d_{in}	intra-molecular spacing
D_a	aggregation diameter

$\xi_{//}$	longitudinal correlation length of the aggregate/column
ξ_0	asymptotic value of $\xi_{//}$
E	aggregation energy
$<N>$	average number of monomers in one aggregate
λ	tumbling parameter
U	dimensionless nematic potential
$\xi,\ \ell_{in}$	internal length scale of defects
$\boldsymbol{Q}$	symmetric traceless tensor order parameter
$\boldsymbol{\Lambda}$	unixial order parameter
$\boldsymbol{P}$	biaxial order parameter
$\boldsymbol{l, m, n}$	orthonormal directors
r_c	disclination core radius
σ_c	core energy per unit volume
$r_{cylindrical},\ \varphi_{cylindrical}$	cylindrical polar coordinates
ψ	orientation distortion angle
γ_ℓ	disclination line tension
R	system size or half width of the capillary
R_{loop}	radius of loop
ω_{bp}	branch point speed
$\boldsymbol{\beta_{bp}}$	viscosity associated with the translation of the branch point
C	constant
$\boldsymbol{t}$	unit tangent to each disclination line
$\boldsymbol{T}_\ell$	excess line stress tensor
$\boldsymbol{T}_\mathrm{b}$	bulk stress tensor

χ_{core}	disclination core energy
$\boldsymbol{\Delta}$	rate of entropy production due to the steady motion of the branch point
L	a characteristic length scale
$\boldsymbol{x}$	position vector
t	time
$\mathbf{N}$	unit normal
θ_n	normal angle
λ_L	Lagrange multiplier
γ_o	line tension of a straight disclination line
κ	curvature of the disclination line
$\boldsymbol{M}$	disclination line moment
$\boldsymbol{T}$	disclination line stress tensor
$\hat{A}_\ell$	Helmholtz free energy per unit length of disclination line
k_c	bending modulus of disclination line
$\boldsymbol{b}$	disclination line curvature tensor
w	normal velocity
$\alpha', \beta',$	disclination line shape fitting parameters
τ	disclination line relaxation time constant
H_∞	equilibrium position of the 1/2 disclination line
D_ℓ	disclination line diffusivity
ℓ_{ex}	external length scale of disclination line
D_o	effective orientation diffusivity for director reorientations
R_{sheet}	sheet resistance
V_{sheet}	voltage applied on the sheet
I_{sheet}	current flowing on the sheet

W_{sheet}	width of sheet the electrode covers
$L_{electrode}$	distance between two electrodes
R_t	radius of the circular arc of a tactoid
Θ	central angle corresponding to half circular arc of a tactoid
$r_{circular}$	Radius of circular capillary
$R_{curvature}$	curvature of the interface of isotropic and nematic DSCG chromonics inside a circular capillary

LIST OF ABBREVIATIONS

POM	polarized optical microscope
E7	a liquid crystal mixture consisting of several cyanobiphenyls with aliphatic tails
PDMS	polydimethylsiloxane
LCLC	lyotropic chromonic liquid crystal
DSCG	sodium cromoglycate
SSY	sunset yellow FCF
TEM	transmission electron microscopy
CMC	critical micelle concentration
CCA	critical concentration for aggregation
NMR	nuclear magnetic resonance
PEG	polyethylene glycol
nm	nanometer
μm	micrometer
mm	millimeter
cm	centimeter
kV	kilovolt
mA	milli ampere
L/D	aspect ratio of chromonics aggregates/columns
LA	long axis of the capillary
IR	Infrared spectroscopy
CARS	coherent anti-Stokes Raman
RR	resonance Raman
SERS	surface-enhanced Raman spectroscopy
PRS	polarized Raman spectroscopy

EM	electromagnetic enhancement
CM	chemical enhancement
ODF	orientational distribution function
CCD	charge coupled detector
PRLD	polar radial line defect
PPLD	planar polar line defect
ERRD	escape radial ring defect
ER	escape radial texture
7CB	4-heptyl-4'-cyanobiphenyl
8CB	4-octyl-4'-cyanobiphenyl
PTCDA	perylene-3,4,9,10-tetracarboxylic dianhydride
PDI	perylene-3,4,9,10-tetracarboxylic acid diimide derivative
DEDA	*N, N*-diethylethylenediamine
CF_3COOD	trifluoroacetic acid-d
AFM	atomic force microscopy
AuNP	gold nanoparticle
SCLC	space-charge-limited conductivity
pN	pica Newton
V_2O_5	vanadium pentoxide
WO_3	tungstic acid
TMV	tobacco mosaic virus
PBT	poly (1, 4-phenylene-2, 6-benzobisthiazole)
PDLCLC	polymer dispersed lyotropic chromonic liquid crystal
PVP	polyvinylpyrrolidone
PVA	polyvinyl alcohol
BSA	bovine serum albumin

SUMMARY

Lyotropic chromonic liquid crystals are reversibly self-assembling supramolecular systems, consisting of plank-like or disc-like molecules, such as many dyes, drugs and nucleic acids, etc. The π-π interaction between flat core areas of molecules mainly drives the formation of the supramolecular structures, which are usually rod-like or in columnar shape. However, the size of those aggregates/columns is polydisperse and the aspect ratio is quite low that it does not follow the predictions of the hard rod theory developed by Onsager for a system of rod-like molecules in solution to form an ordered phase. In an effort to understand this lyotropic phase better, studies on the phase behavior, defects formed in these systems and characterization of the order were performed.

We mainly studied three chromonic liquid crystal materials: Sunset Yellow FCF (SSY, a food dye), a cationic perylene diimide derivative (PDI, a conducting dye) and cromolyn sodium (DSCG, a drug). All of their behaviors were both temperature and concentration dependent and exhibited a wide nematic-isotropic coexistence region in comparison to thermotropic liquid crystals. Both the chromonic nematic N phase and biphasic phases were studied in this thesis.

Although lyotropic systems are notoriously difficult to align, we achieved homogeneously planar alignment (a planar aligned monodomain) of SSY nematics in a flat capillary, which was meaningful for both application and fundamental investigation purposes. By performing the polarized Raman measurement on this planar aligned monodomain, we obtained the second-rank ($<P_{200}>$) and fourth-rank ($<P_{400}>$) order parameters for SSY chromonics. Temperature and concentration dependence studies show that their values increase as concentration increases and decrease as temperature increases in the nematic region. By using order parameters at equilibrium we measured

and aspect ratios of SSY chromonic columns we calculated based on x-ray studies in the literature, we predicted the flow behavior of SSY chromonics in the nematic phase to be not flow-aligning in the limit of slow flows according to a molecular theory. We also studied the statics and dynamics of defects of SSY chromonics in the flat capillary with ribbon geometry during the formation of the planar-aligned monodomain, while defects of thermotropic liquid crystals under the confinement of a cylindrical capillary with homeotropic alignment have been widely studied in the literature. The monodomain originated from small uniform areas, which is the result of the splitting of the high strength disclination line into a pair of low strength lines at a branching point. The low strength lines emanating from the branch point evolve towards the edges of the capillary. The kinematics of the branch point moving at a constant speed was studied. Both theory and experiments were integrated to investigate the shape of disclination lines during the branching and relaxation and a comprehensive viscoelastic property set of SSY chromonics was obtained.

PDI was synthesized according to a reported method. We found the application of PDI thin films prepared by a dip-coating method in sensing H_2O and $H_2O \cdot HCl$ vapors. Both monolayer PDI thin films and oriented PDI thin films were prepared. The Raman scattering of the monolayer of a PDI film on the mica, characterized by AFM, was successfully enhanced by gold nanoparticles. Oriented PDI dried films were prepared by the rubbing method. Both absorbance measurement and electronic measurement show good anisotropy and PDI columns were aligned along the rubbing direction in the oriented dried film. The sheet resistance perpendicular to PDI columns is about 10 times that along the PDI columns. The order and orientation of the solid film most likely were inherited from those of the nematic PDI solution under rubbing. The good conductivity along the columns presumably arises from the overlap between the π systems. The power law dependence of the current on the distance between electrodes was also explored and compared with another similar law of other materials.

In the biphasic region, the tactoid growth and fluctuation were studied for SSY chromonics; elastic properties of DSCG chromonics based on the tactoid shape were derived. Interesting patterns of biphasic DSCG chromonics were also observed under capillary confinement with different geometries. Polymer dispersed lyotropic chromonic liquid crystals were also fabricated using three water soluble macromolecules PVP, PVA and BSA. Both planar alignment of spherical bipolar (SSY/PVP and SSY/BSA) and ellipsoidal bipolar droplets (SSY/PVA and DSCG/BSA), and homeotropic alignment of radial droplets (DSCG/PVP and DSCG/PVA) were created.

CHAPTER 1

INTRODUCTION

1.1 Introduction to liquid crystals

Many organic materials exhibit more than one transition in passing from solid to liquid. Partial molecular ordering, translational or rotational, or both, between that of a solid and that of an isotropic liquid, lies in these intermediate phases, known as "mesophases". There are two basically different types of mesophases: disordered crystal mesophases, known as "plastic crystals", and ordered fluid mesophases, commonly called "liquid crystals" [1, p. 2, 2, p. 7]. For the disordered crystal mesophases, the three-dimensional crystal lattice is retained and the molecules are translationally well-ordered but rotationally disordered, as the rotation barriers are small compared to lattice energy; for the liquid crystals, the molecules, with no lattice, show considerable rotational order (and in some cases partial translational order, too). Polymorphous smectic materials are the only substances that could exhibit both these mesophases. Due to the liquid-like (fluidity) and solid-like (molecular order) nature, liquid crystals posses many interesting properties as well as wide applications.

1.1.1 Liquid crystalline phases

There are two general categories of liquid crystalline materials: thermotropic and lyotropic [1, p. 3, 2, p. 21], as shown in Figure 1. Lyotropic phases form in the presence of (isotropic) solvent and are influenced by both temperature (T) and concentration, while the thermotropic phases form from single or multi components and are influenced only by temperature. Materials exhibiting both thermotropic and lyotropic phases are named "amphotropic" [3, p. 2]. Thermotropic liquid crystals, according to the various shapes of the molecules, are further classified as calamitic (rod-like), discotic (disk-like) and sanidic (lath-like) liquid crystals. The amphiphilic phases (soaps, surfactants, detergents,

etc.) are the conventional lyotropic liquid crystal phases. A number of biological important substances (lipids, lypopolysaccharides, proteins, etc.) also exhibit liquid crystalline phases. The first scientific documentation of a lyotropic liquid crystal is about myelin (consisting of lipid and proteins) in water by Virchow [4, p. 2]. Chromonic liquid crystals are a relatively new kind of lyotropic phases and will be the topic of this thesis.

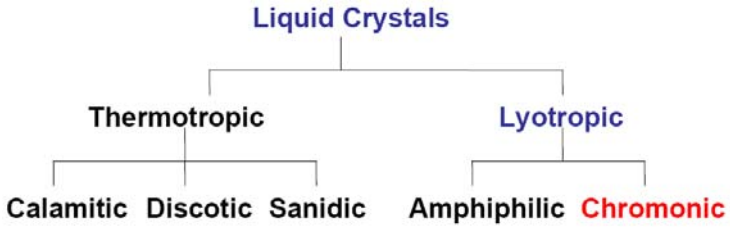

Figure 1.1. Two basic groups of liquid crystals with further classification.

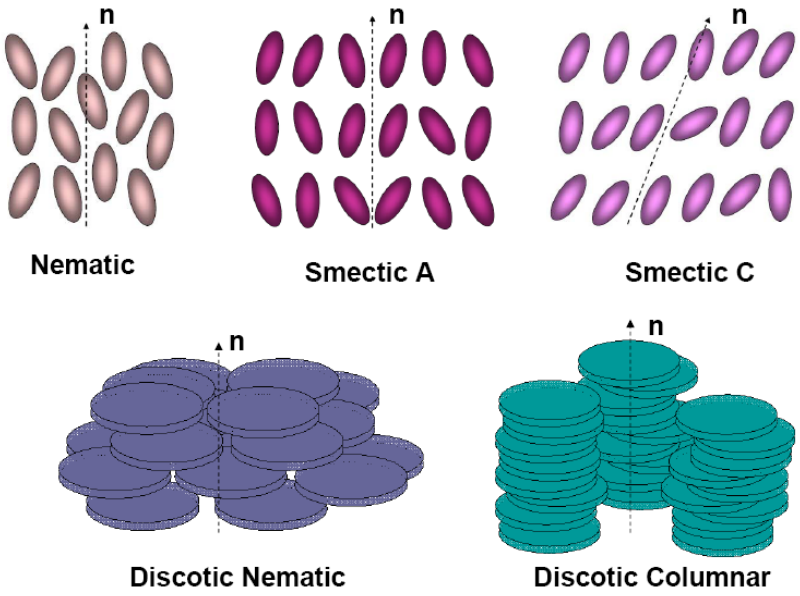

Figure 1.2. Typical phases of liquid crystals. The arrows point in the direction of the local director ***n***.

1.1.2 More concepts about liquid crystals

The local director ***n***, a dimensionless unit vector, is the preferred direction in a liquid crystal sample, as shown in Figure 1.3.a, which is a "snapshot" of the thermally fluctuating molecules [1, p. 5, 2, p. 10]. Nematics are turbid; they scatter light strongly, because of the spontaneous fluctuations of the director alignment [5, p. 101]. Assuming that all the molecules undergo the same type of random motion, the orientation one molecule has at one time is the same as another molecule has at another time. Performing an average of any given molecule's orientation in many instances should be equivalent to performing an average of many molecules' orientation at any given time [2, p. 10].

The order parameter indicates the degree of order in a liquid crystal. Orientational order is fully described by a tensor order parameter [5, p. 23]. For a nematic liquid crystal, a scalar order parameter, *S*, is usually used to describe the order. *S* is defined based on the average of the second Legendre polynomial [5, p. 24]:

$$S = \left\langle P_2\left(\cos\theta_m\right)\right\rangle = \left\langle \frac{3\cos^2\theta_m - 1}{2} \right\rangle \tag{1.1}$$

where θ_m is the angle between the mesogen molecule axis and the local director and the brackets denote both a temporal and spatial average. For a perfectly aligned sample with no fluctuation, S=1; for completely disordered phase, S=0; for a typical liquid crystal sample, S is on the order of 0.3 to 0.8, and generally decreases as the temperature increases, as shown in Figure 1.3.b. S can be determined experimentally by birefringence [6, 7], Raman scattering [8, 9], diamagnetism [10, 11] and NMR [12, 13] etc. Other higher-order Legendre polynomials would provide more ordering information, but they are more complicated to measure. We will present the measurement of both the second and fourth Legendre polynomials based on the polarized Raman scattering in this thesis.

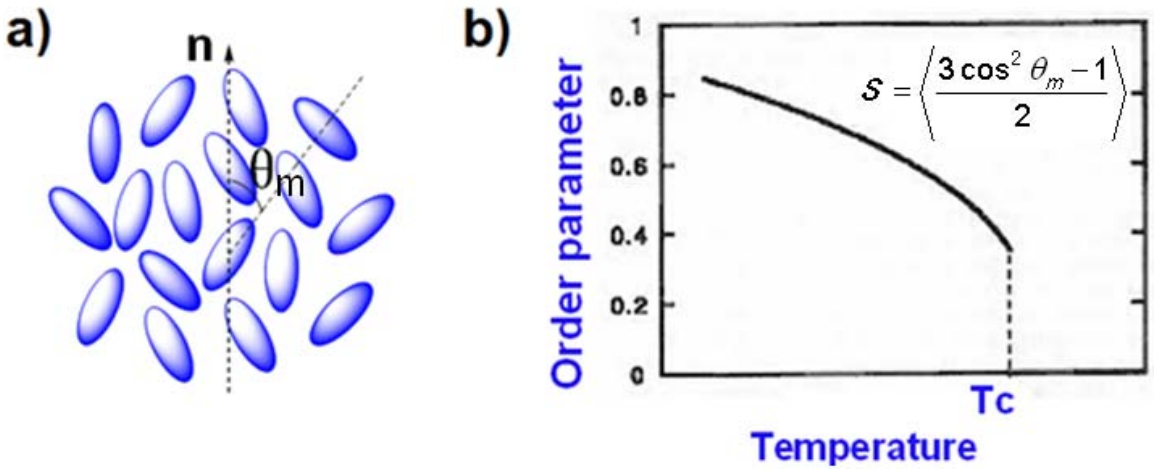

Figure 1.3. Schematic for definitions of director and order parameter in liquid crystals. The left figure (a) shows the "snapshot" of the phase. ***n*** is the local director, which is the 'preferred direction' in a liquid crystal sample. θ_m is the angle between the mesogen molecule axis and the local director. The right figure (b) shows a typical relation of order parameter S with the change of temperature. T_C is the clearing temperature, i.e. the liquid crystalline phase-isotropic phase transition temperature [2, p. 10].

Liquid crystals could be deformed by external forces, such as boundary forces or other mechanical, electric or magnetic fields. The free energy density F increases as compared to a completely uniformly aligned nematic director configuration with free energy density F_0. There are three basic deformations in the nematic phase: splay, twist and bend as shown in Figure 1.4. The increase of F due to deformations, F_d, is described by the continuum theory [14]:

$$F_d = \frac{1}{2}K_{11}\left(\nabla \bullet n\right)^2 + \frac{1}{2}K_{22}\left(n \bullet \nabla \times n\right)^2 + \frac{1}{2}K_{33}\left(n \times \nabla \times n\right)^2 \qquad (1.2)$$

where K_{11}, K_{22} and K_{33} are the elastic constants corresponding to splay, twist and bend deformation, respectively.

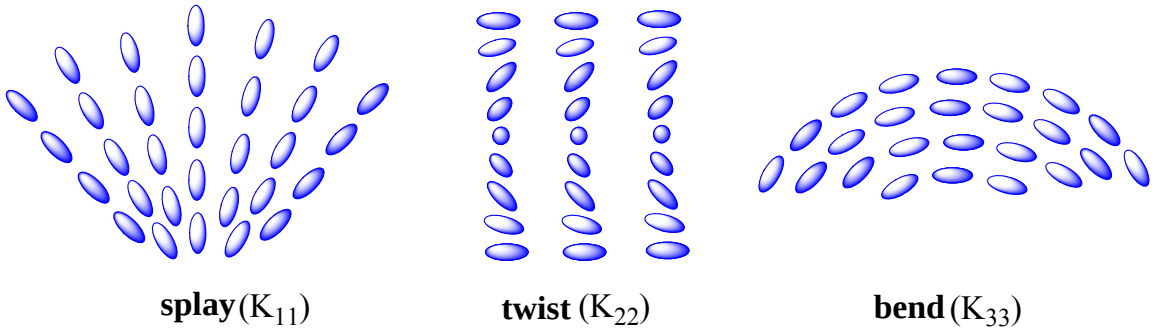

Figure 1.4. Splay, twist and bend deformations of nematic phases.

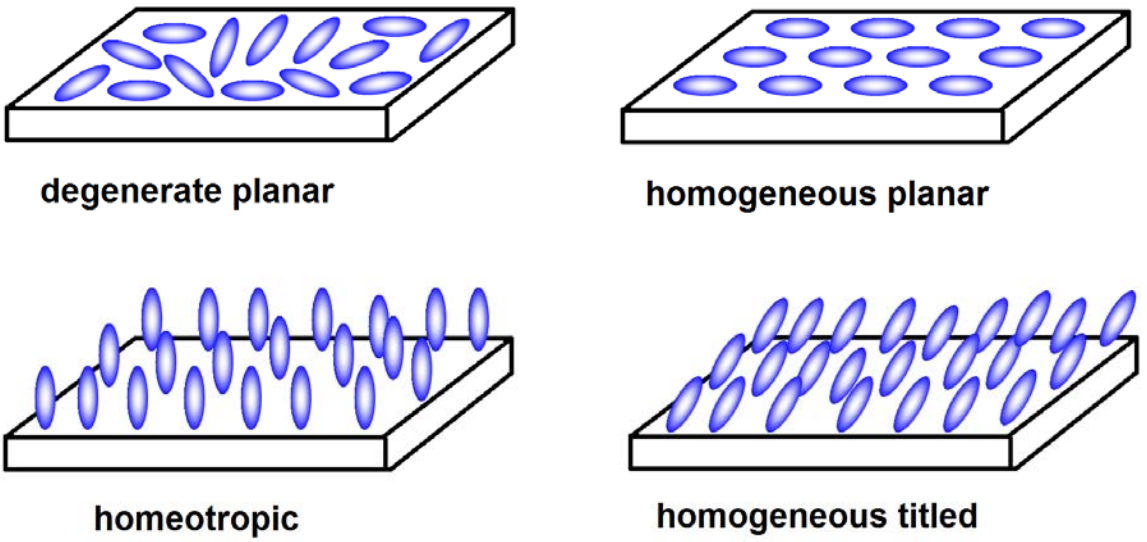

Figure 1.5. General types of molecular alignment of liquid crystals.

Liquid crystals can also be aligned by various treatments of the confining substrates [3, p. 22, 5, p. 71]. For example, unidirectional rubbing on the glass slides or on the polyimide coated surface creates micro-grooves that promote alignment. General types of molecular alignment on the substrates are schematically depicted in Figure 1.5. The long molecular axis pointing along an arbitrary direction in the substrate plane, pointing along a preferred direction in the substrate plane, pointing perpendicular to the substrate plane,

or pointing oblique to the substrate plane with a fixed direction, are corresponding to degenerate planar alignment, homogeneous planar alignment, homeotropic alignment and homogeneous titled alignment, respectively.

Splay can be observed by placing a uniform planar nematic in a wedge cell. Bend can correspondingly be realized for homeotropic anchoring in a wedge cell. Twist distortions are obtained by twisting parallel substrates with uniform planar alignment [3, p. 28].

1.1.3 Liquid crystal optics and polarized optical microscopy

Most uniaxial liquid crystals are optically positive, that is, the refractive index parallel to the optical axis $n_{//}$ is larger than that perpendicular to the optical axis $n_{\perp}$ ($n_{//}$ - $n_{\perp}$>0), although there are others, e.g. chromonic liquid crystals, that are optically negative ($n_{//}$ - $n_{\perp}$<0). Light passing through liquid crystals usually decomposes into two rays: ordinary and extraordinary, whose polarizations are perpendicular to each other. They experience different velocities and refractive indices and result in a phase difference δ [15, p. 6 and 142, 16, p. 336]

$$\delta = \frac{2\pi}{\lambda}(n_e - n_o)d \tag{1.3}$$

where λ is the vacuum wavelength, d is the sample thickness, n_o is the refractive index which ordinary ray experiences, n_e is the refractive index which extraordinary ray experiences. n_o and n_e have the following relations with principal refractive indices $n_{\perp}$ and $n_{//}$ [15, p. 74]:

$$n_o = n_{\perp} \tag{1.4}$$

$$n_e = \frac{n_{//} n_{\perp}}{\sqrt{n_{//}^2 \cos^2 \phi + n_{\perp}^2 \sin^2 \phi}} \tag{1.5}$$

where ϕ is the angle between the optic axis and the direction of light propagation, as shown in Figure 1.6.

When a liquid crystal sample is placed between crossed analyzer and polarizer, the transmitted intensity of monochromatic light is given by [3, p. 37]

$$I = I_0 \sin^2(2\varphi) \sin^2(\delta/2) \tag{1.6}$$

where I_0 is the incident light intensity, δ is the phase difference and φ is the azimuthal angle, i.e. the angle between the analyzer and the projection of the optic axis onto the sample plane as shown in Figure 1.6. Figure 1.7 shows the polarized optical microscope (POM) configuration. Rotation of the birefringent/anisotropic sample will induce an intensity change due to the change of azimuthal angle φ if $\sin(\delta/2)$ is not zero.

POM images of liquid crystal textures provide information about the alignment and director configuration of liquid crystals [3, p. 167-212]. Figure 1.8 shows an example. E7 is a typical thermotropic liquid crystal and exhibits nematic phase at room temperature. The POM images reveal that polydimethylsiloxane (PDMS) induces homeotropic alignment of E7 at the interface and thus the radial drop configuration. The textures don't change under rotation on the sample plane, as the drop configuration is symmetric about any axis through the center point, including z axis. The birefringence rings exist due to interference of the transmitted light of each wavelength (λ) associated with the light path (d) and the director orientation (ϕ) inside the E7 drop.

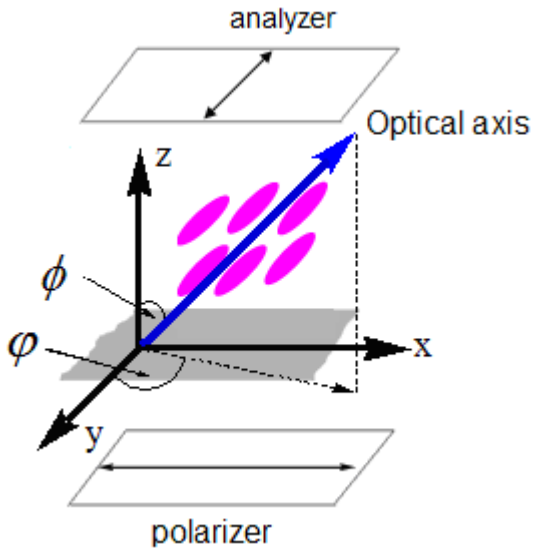

Figure 1.6. Schematic figure of a uniformly oriented, uniaxial liquid crystal for the definition of different angles.

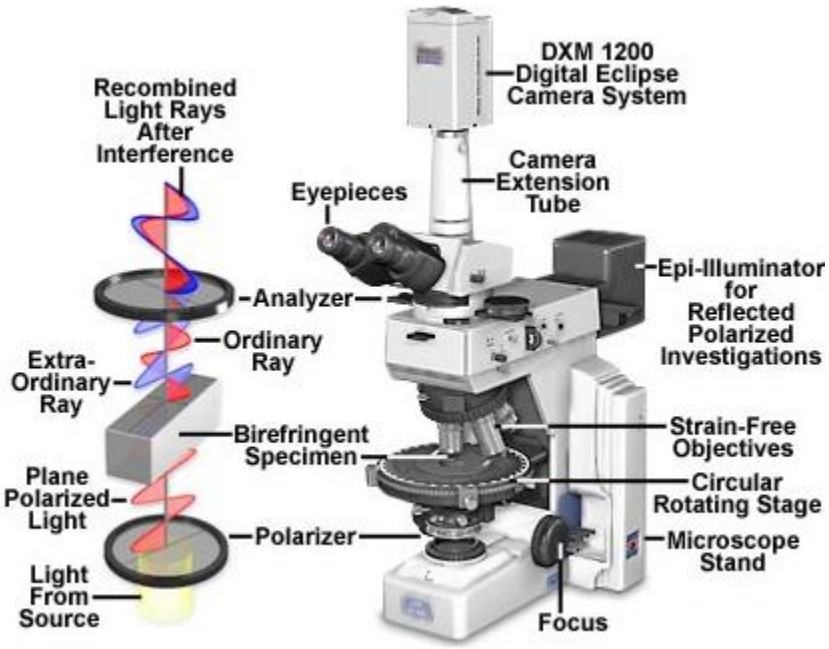

Figure 1.7. Configure for polarized optical microscope (POM). Copied from Nikon website [17].

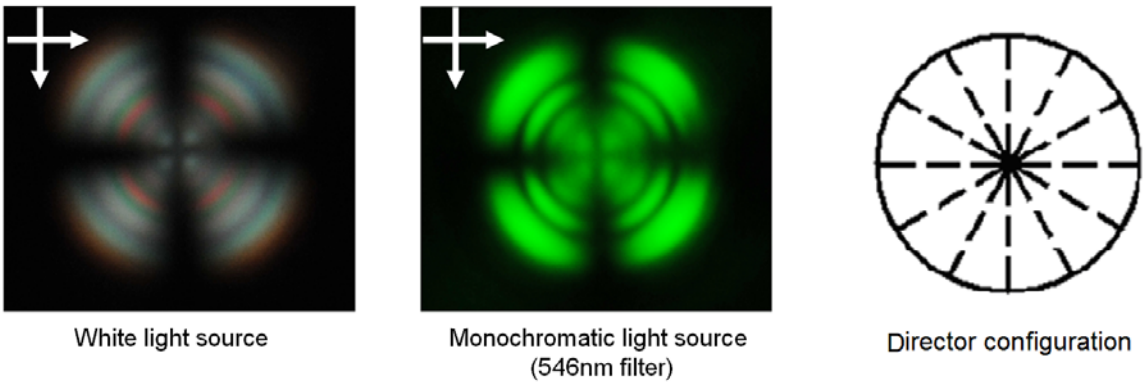

Figure 1.8. POM images and radial director configuration of polydimethylsiloxane (PDMS, viscosity: 1000cs) dispersed E7 nematic liquid crystal drop under crossed polarizer and analyzer at room temperature. The dark area surrounding the drop consists of PDMS.

1.1.4 Liquid crystal defects

Defects are standard objects in liquid crystals [18-21]. There are basically two categories of origin of liquid crystal defects [18, p. 419]: first, equilibrium topological defects, existing as a feature of the equilibrium of state of the system, such as point defects in the freely suspended nematic droplets or defects generated by mechanical impurities, air bubbles, etc.; second, defects caused by far-from-equilibrium processes, such as thermal or pressure quenching from isotropic phase to liquid crystalline phase or by flow in the regimes of high Ericksen numbers.

Liquid crystal defects can be classified in different ways: singular and non-singular defects; point, line and wall defects; wedge disclination (axis of rotation is along the disclination line), twist disclination (axis of rotation is perpendicular to the disclination line) and loops [18-21]. Singular points form either in the bulk or at the surfaces. Point defects in the bulk are called “hedgehogs”; point defects at the surface are called “boojums” [18, p. 400]. Dislocation of rotation, usually called disclinations, is line defects along which the symmetry of rotation is broken. Disclinations and point defects

are common in uniaxial nematics. Figure 1.9 gives examples of wedge disclinations. The strength of disclinations, *s*, is defined as follows [18, p. 390]: let there be a closed circuit surrounding a wedge line, give this circuit an arbitrary direction and starting form a point of origin on this circuit, trace the direction of nematic director that circuit meets. If the rotation direction of the director along the circuit is the same as the circuit, *s* will be positive number and equal to $\Omega'/2\pi$, where Ω' is the angle the director turned. All the strengths are a multiple of $\pm 1/2$. Disclinations may coalesce with each other: disappear ($s_1+s_2=0$) or form a new singularity ($s_1+s_2=s'$).

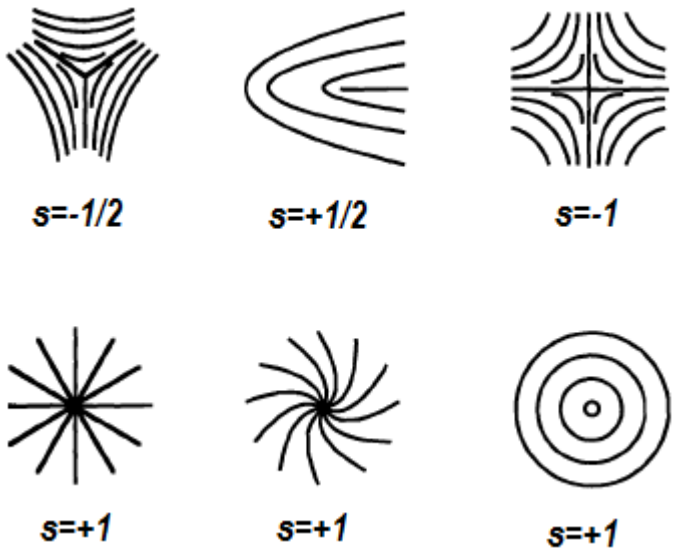

Figure 1.9. Wedge disclinations [18]. The lines show the molecular orientation in the neighborhood of a disclination.

Characteristic defect structures together with textures also reveal the phase type observed [3, p. 167-212]. Figure 1.10 shows some POM texture images of typical Schlieren texture of a nematic phase, cholesteric polygonal (fingerprint) texture and fan-shaped texture of a Smectic A phase. Liquid crystal defects also serve as good models to study cosmological defects because they are analogous, and liquid crystal defects may help to explain some of the largest-scale structures seen in the Universe today [22]. Other

advantages are the variety of liquid crystal defects created at low temperature and the easy observation with optical microscopy [22]. For research in this thesis, we studied the statics and dynamics of chromonic liquid crystal defects to generate the viscoelastic properties.

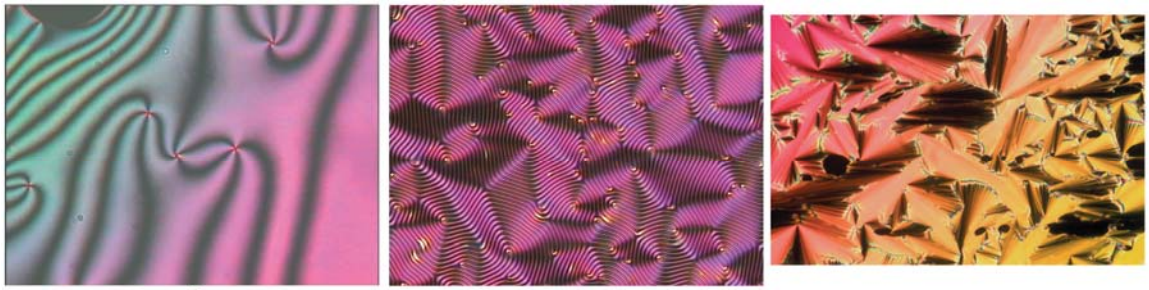

Figure 1.10. POM textures of liquid crystals. **a**, Schlieren texture of a nematic phase under planar anchoring conditions. Note that the curved brushes converge into singular point defects and that brushes connect different defects, which have the same strength but opposite sign. **b**, Cholesteric polygonal (fingerprint) texture of a sample with a relatively long pitch, such that the helical N* superstructure can be resolved by polarizing microscopy. **c**, Typical fan-shaped texture of a Smectic A phase. The director basically lies in the plane of the substrate and the smectic layers are curved across the fans. From reference [3, p. 170, 174 and 188].

1.2 Introduction to lyotropic chromonic liquid crystals

1.2.1 Molecular structure and chromonic liquid crystalline properties

Lyotropic chromonic liquid crystals (LCLCs) were first reported by Sandquist in 1915 and have gained increasing attention in the last three decades as an interesting but not well-studied and still poorly-understood class of lyotropic liquid crystals [23-27]. LCLCs consist of many dyes, drugs, nucleic acids, antibiotics, carcinogens and anti-cancer agents [23-31], therefore the practical importance of LCLCs is evident. The generic name “chromonic” originated from an antiasthmatic drug “sodium cromoglycate (DSCG)” (Figure 1.11a), which is so far the most extensively studied [28, 29]. The name

chromonic liquid crystals, was considered (by the discoverer at least) as a good name because of the fortuitous combination of connotations of both color (with reference to dyestuff) and chromosome (with reference to nucleic acids).

The main structural feature of LCLC molecules is the disk-like or plank-like rigid aromatic core with hydrophilic ionic or hydrogen-bonding solubilizing groups around it. In a solvent (usually water), these molecules reversibly stack into polydisperse rod-like aggregates, though layered structures have also been reported [23]. The aggregation process so far has been believed to be mainly by π-π interaction of the aromatic cores, while the hydrophilic ionic or hydrogen bonding groups at the periphery of the molecules contribute to the solubility. Figure 1.11 shows the representative LCLC molecules [28-36]. The nature, number and position of solubilizing groups are all very important. For structures like copper-tetracarboxyphthocyanine (Figure 1.11.b), a minimum of four solubilizing groups is necessary for mesophase induction, which is also true for other chromonic porphyrin metal complexes [33]. Certain substitution position for solubilizing groups is not always appropriate for the formation of mesophases [33, 34]. Although the -COOH substitution in the same position as that in Figure 1.11.b can induce mesophases for both Cu(II) and Co(II) complexes, the other substitution position neighboring to the core only works for Cu(II), not Co(II) [25].

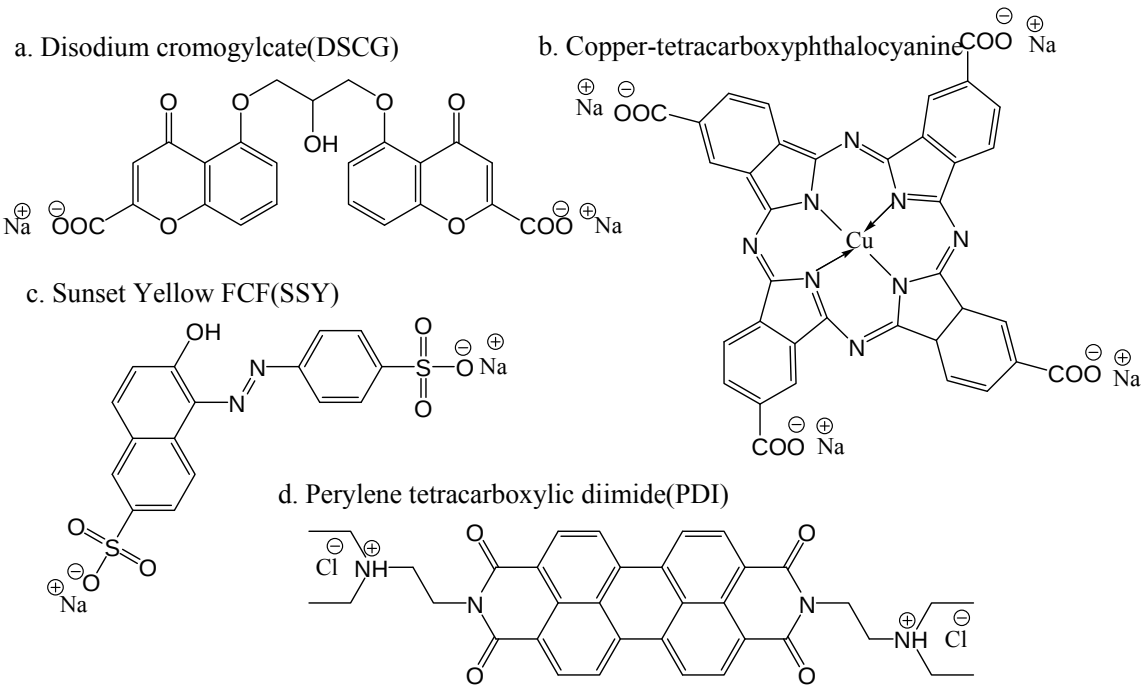

Figure 1.11. A selection of chromonic molecules: **a**. sodium cromoglycate [28, 29]; **b**. copper tetracarboxyphthalocyanine [33, 34]; **c**. sunset yellow FCF [30-32]; **d**. a perylene diimide derivative [35, 36].

Chromonic mesophases are considered to be the lyotropic counterparts of thermotropic discotic mesophases, although not all the counterparts of the discotic mesophases have been found so far. There are only two principal well characterized chromonic mesophases, namely the N and M phases [25]. The designation N and M came from early polarized light microscopy studies of DSCG, as the N phase of DSCG forms a Schlieren texture similar to that of thermotropic nematics and the M phase of DSCG forms an optical texture similar to that of the hexagonal H_1 (middle) soap phase [28, 29]. The basic structural unit of both N and M phases is the untilted stack of molecules, as illustrated in Figure 1.12. The M phase is a fairly concentrated phase with a hexagonal ordering of molecular stacks. The N phase is a more dilute phase with a nematic like arrangement of probably the same stacks while losing hexagonal ordering; the columns are more or less parallel to each other. For example, in Figure 1.13, as the concentration increases (from about 6wt % to 38wt %), the mesophase of the DSCG-water system goes

from N to M, according to Cox et al [28]. Molecular columns shown in Figure 1.12 are in a highly stylized way, but they are not necessarily such simple one-molecule-wide stacks. Even as the most studied LCLC molecule, the real structure of DSCG aggregates is still a matter of debate [37-39]. The details of the molecular aggregation in these two phases are also still the subject of discussion [23, 26].

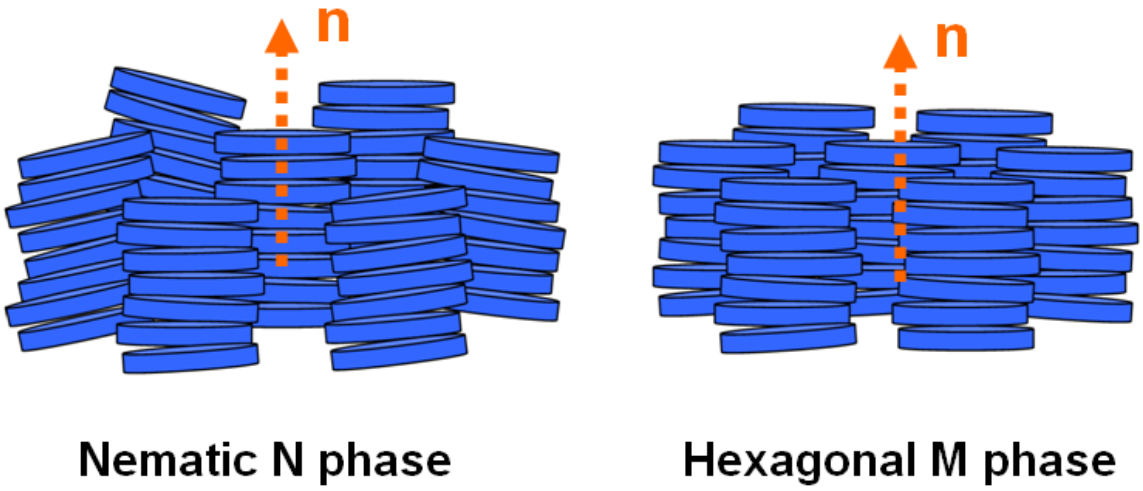

Figure 1.12. Schematic representations of two principle chromonic mesophases, nematic N phase and hexagonal M phase. The arrows are pointing the direction of the local director ***n***.

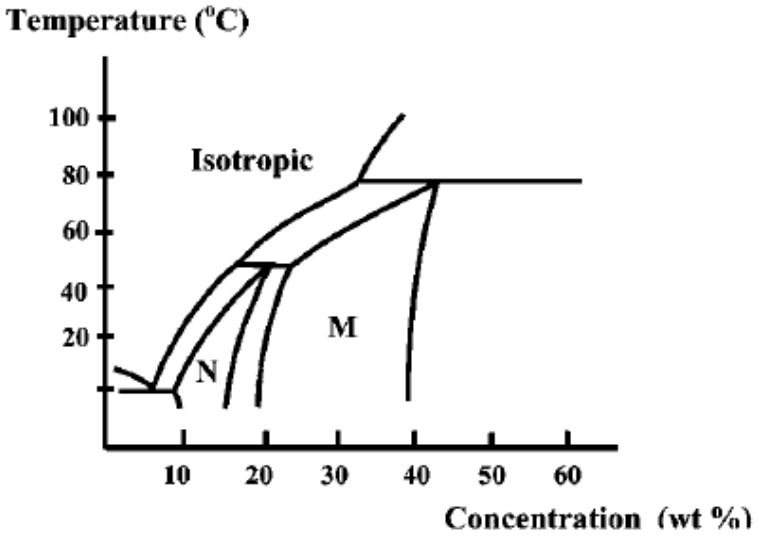

Figure 1.13. A phase diagram of the cromolyn sodium (DSCG) in water [20].

Other chromonic structures also have been proposed, such as molecular aggregates into J-types, brickwork patterns, or hollow tubes, as shown in Figure 1.14 [40, 41]. Compared with those of single monomeric state, the geometric arrangement of the chromonic molecules within the aggregate modifies their spectroscopic properties. Depending on the slippage angle ʒ in J-type, the absorption spectra can be shifted toward longer or shorter wavelengths. For J(Jelly)-type aggregates, with large tilts ("staircases", low ʒ), a red (bathochromic) shift towards longer wavelength is observed; H-type aggregates, with less tilted stacks ("ladders", high ʒ) give a blue (hypsochromic) shift towards shorter wavelength [41-42].

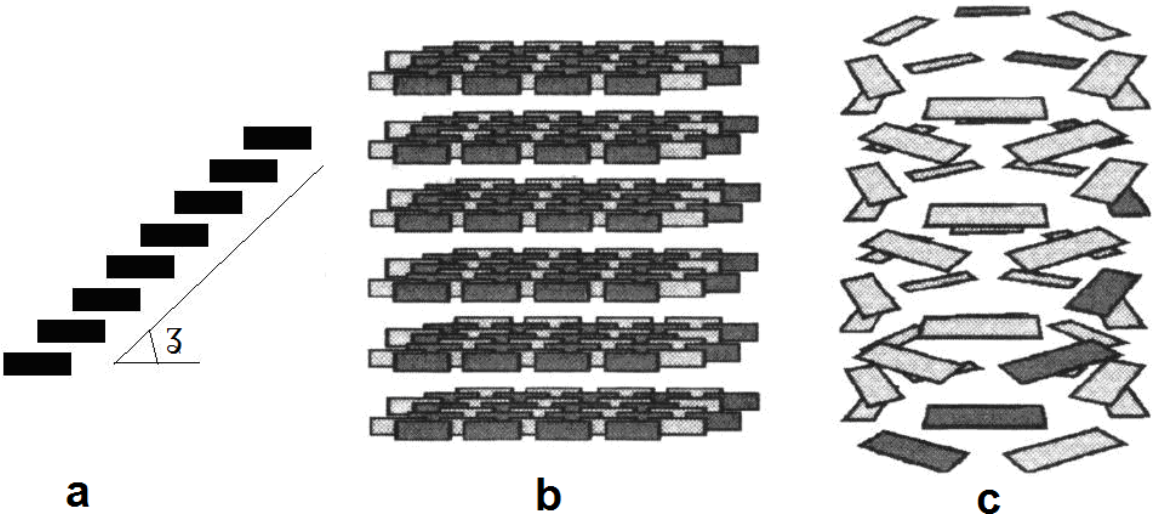

Figure 1.14. Schematic representations of other chromonic mesophases: **a**. J-aggregate of the cyanine dyes; **b**. brickwork structure of the cyanine dye layer; **c**. hollow tube structure of the CI Acid Red 266 aggregates [40, 41].

Studies show the addition of some salts shifts the isotropic-nematic phase boundary upward or downward by more than 10 ºC, perhaps because the rod-like aggregates transform a higher order aggregation into bundles in the presence of salts according to the cryo-TEM images [43]. The aggregation behavior, aggregation structures, salt effects and

the other possible phases are still not quite understood and are the subjects of current research.

It has also been reported that small variations from DSCG molecular structures can completely abolish the formation of the LC phase [39]. Some dyes with similar structure also show very different phase diagrams [44]. The relationship between the molecular structure and the phase behavior is quite obscure.

As the formation of LCLC phases has been a main topic in recent decades, the properties of LCLCs have rarely been studied. Only the viscoelastic properties of DSCG [45] and aqueous perylenetetracarboxylic acid dye solutions [46], and rheological and dielectric properties of SSY [47] have been reported. More investigation on LCLC properties needs to be done.

1.2.2 Comparison with other lyotropic liquid crystal systems

Chromonic molecular structures are quite different from those of other kinds of lyotropic system, like amphiphilic and polymeric mesophases. Their properties are compared in Table 1.1. As for chromonic systems, there is no critical micelle concentration (CMC). Chromonic molecules stack together into columns to avoid the unfavorable contact of the hydrophobic part of the molecules with the aqueous or hydrophilic solvent. This kind of stacking or aggregation takes place even in very dilute solution. As the concentration increases, the column length increases and the fraction of the total molecular surface exposed to the solvent decreases without reaching minimum free energy state. There is wide-spread experimental evidence that there is no optimum column length or aggregation number [30, 42]. Such aggregation behavior is termed “isodesmic”. The addition or removal of one molecule to a stack is always associated with the same change of free energy, irrespective of the length of the existing column. Figure 1.15 compares the free energy change of non-isodesmic and isodesmic behavior for amphiphilies and chromonic molecules, respectively. Usually the aggregation is only

a weak association where both ΔH and ΔS are negative, so it is enthalpically rather than entropically driven. The free energy is of the order of the thermal energy, k_BT, about 2.5kJ per mole [23, p. 988].

Table 1.1. Properties of different chemical classes of lyotropic mesophases [48, 49].

	Amphiphilic mesophases	Chromonic mesophases	Polymeric mesophases
Molecular structure	Molecules with distinct hydrophilic and hydrophobic parts (usually flexible alkyl chains)	Planar polyaromatic molecules bearing hydrophilic substituents	Linear rigid polymers
typical compounds	Soaps, Detergents	Drugs, dyes	Biological or synthetic polymers
Surface properties	Highly surface active	No special surface activity	Can be surface active
Type of molecular aggregation	Micellar aggregates form only above a critical concentration, due to the hydrophobic effect. Micelles can be spherical, cylindrical, disc-shaped or extended double lamellae	No critical concentration for aggregation; gradual aggregation process at low concentrations. Molecules usually stack and form untilted columns	None
Thermal behavior	Exhibit a Krafft temperature	No Krafft temperature	No Krafft temperature
Mesophase type	Cubic; hexagonal(H_1); lamaellar and/or inverse phase; micellar nematic phases	Nematic (N) and hexagonal (M) phases well established (layer structures also suggested)	Nematic and many phases
X-ray diffraction patterns	Characteristic diffuse reflections at 4.5Å, arising from the aggregation of fluid alkyl chains	Characteristic strong, sharp reflection at 3.4Å, arising from the stacking of aromatic molecules	Hexagonal packing for larger, rod-like polymers [4, p.17]

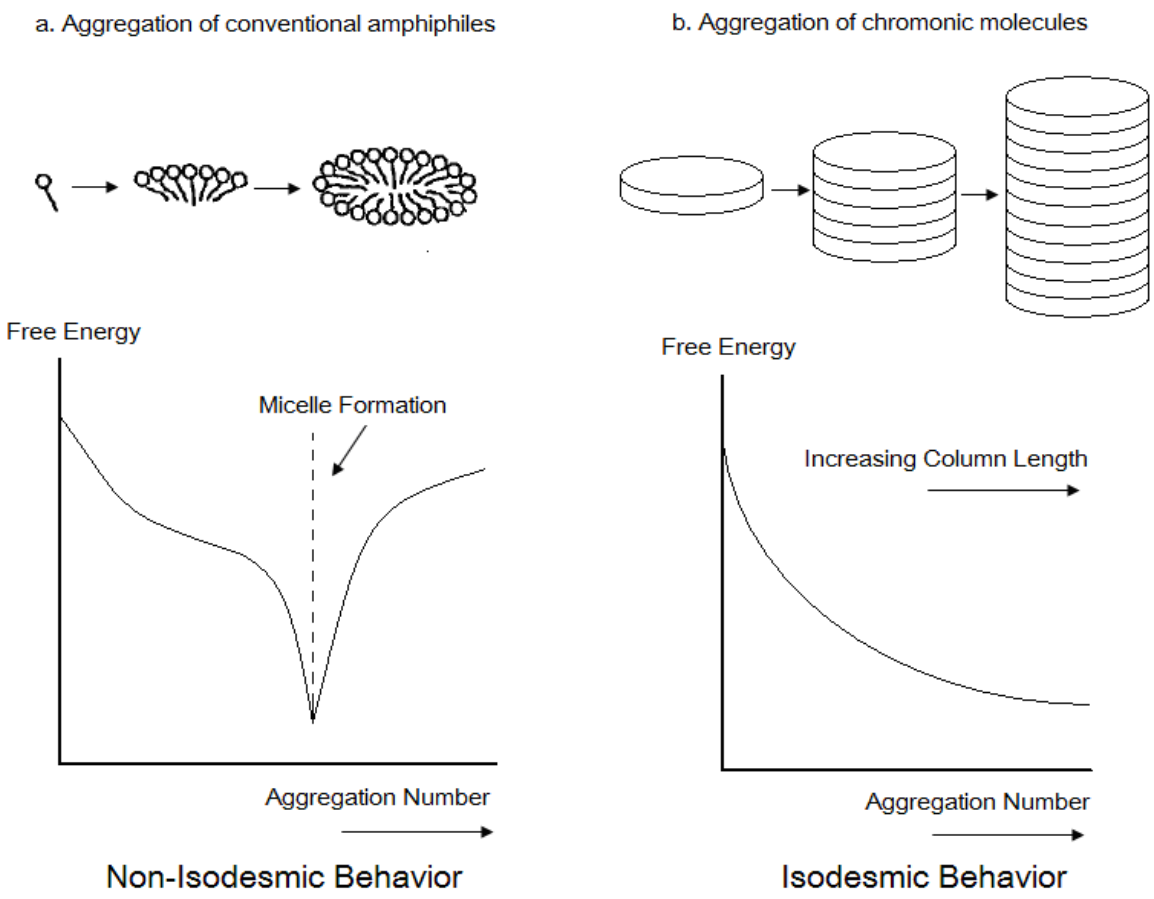

Figure 1.15. The contrast between the aggregation behavior of amphiphiles (a) and chromonic molecules (b) [23].

Generally, simple isodesmic behavior is characteristic of chromonic systems. However, some studies have shown there is a critical concentration for aggregation (CCA) for certain chromonic dyes like Benzopurpurine 4B and Congo Red; below CCA, only single molecules are present in the solution [26].

Another distinction between conventional amphiphilic and chromonic system concerns the behavior at low temperature limit of the mesophases. Amphiphilic mesophases consist of the aqueous micro-phase region and a hydrophobic aliphatic micro-phase region. When the temperature is lowered, the motion of the alkyl chains in the hydrophobic region usually freezes out and a gel phase forms, which makes

molecular packing into micelles impossible. The term “Krafft temperature” characterizes this lower temperature limit for conventional amphiphilic mesophases. For chromonic systems, there is no alkyl chain or no long alkyl chain in the molecule, so no Krafft temperature appears. Instead, as water is usually the solvent in chromonic system, the lower temperature is limited by ice formation and is always a few degrees below 0°C. Adding antifreeze to the system also can help achieve the monotropic chromonic mesophase at sub-zero temperatures [42, 48].

1.2.3 Potential applications

Good alignment of LCLCs is the most basic requirement both for fundamental research and for applications. Unfortunately, lyotropics, including LCLCs, are notoriously difficult to align. Most thermotropic liquid crystals can be aligned easily using a rubbed polyimide alignment layer, while the same process can provide LCLCs with little alignment or patched alignment in small micro-areas. In addition to the polymer coated surface, other alignment methods are also reported for LCLCs, such as applying direct mechanical rubbing force (coating) [50-52], strong magnetic fields [44] and photoalignment [54], and doping block co-polymers [55]. Applications of LCLCs have been recently explored as: thin film polarizers [56-63], optical compensators in twisted nematic displays [64, 65], biosensors [66-68], precursors of aligned graphene [69] and templates for mesoporous nanofibers [70]. It is also necessary to point out that a certain method may only work for one LCLC system. It is desired to better understand the properties of LCLC materials and the alignment mechanism for chromonic systems, to explore reliable alignment techniques, and to develop more applications.

1.3 Thesis outline

Research in this thesis aims to understand lyotropic chromonic liquid crystals more on their phase behavior, defects, viscoelastic and flow properties and explore more potential applications of LCLC systems.

Chapter One gives introduction to liquid crystalline phases and related concepts like director $\boldsymbol{n}$, order parameters, elastic deformation, molecular alignment, liquid crystal optics and defects. Lyotropic chromonic liquid crystals are also introduced and compared with other lyotropic mesophases.

Chapter Two introduces a LCLC material, Sunset Yellow FCF (SSY), and describes the preparation of SSY nematic chromonics with homogeneous planar alignment as well as the methods of characterization of alignment. It also describes the rubbing method to align the SSY LCLC and studies on the anisotropy of the obtained dried film.

Chapter Three introduces Raman spectroscopy and describes its application in determination of the tautomeric structure of SSY molecules in different phases as well as measurement of the second and fourth rank order parameters based on polarized Raman spectroscopy.

In Chapter Four, the order parameters were used for prediction of the flow behavior of SSY chromonics, as liquid crystals are the subject of interest from the viewpoint of rheology. Especially, chromonic liquid crystals consisting of supramolecular columns differ from conventional liquid crystals.

Chapter Five describes the static and dynamics of defects of SSY chromonics in a flat capillary with ribbon shape geometry during the formation of monodomain, based on which a comprehensive set of viscoelastic properties was obtained.

In Chapter Six, the synthesis and characterization of a cationic perylene diimide derivative (PDI), are summarized. Its chromonic liquid crystalline behavior was studied and the application of PDI thin films as H_2O vapor and H_2O/HCl vapor sensor was explored. Studies were also performed on the gold-nanoparticle enhanced Raman scattering of the PDI thin film as well as the electronic properties of the oriented PDI film made by rubbing method.

Chapter Seven is about the orientation, fluctuation, growth and deformation under confinement of LCLC tactoids as well as the fabrication and director configuration of polymer dispersed LCLC droplets.

1.4 References

[1] Priestley, E. B., Wojtowicz, P. J., Sheng, P., Editors. Introduction to Liquid Crystals. **1975**, Plenum: New York, 356 pp.

[2] Collings, P. J. Liquid Crystals: Nature's Delicate Phase of Matter (2nd Edition). **2002**, Princeton University Press: Princeton, 222 pp.

[3] Dierking, I. Texture of Liquid Cryatals. **2003**, Wiley-VCH: Weinheim, 218 pp.

[4] Petrov, A. G. The Lyotropic State of Matter: molecular physics and living matter physics. **1999**, Gorden and Breach Science: Amsterdam, 549 pp.

[5] De Gennes, P. G. The Physics of Liquid Crystals. **1979**, Oxford University Press: Oxford, 347 pp.

[6] Kuczynski, W., Zywucki, B., and Malecki, J. Determination of orientational order parameter in various liquid-crystalline phases. Molecular Crystals and Liquid Crystals Science and Technology, Section A: Molecular Crystals and Liquid Crystals **2002**, 381, 1-19.

[7] Fakruddin, K., Kumar, R. Jeevan, Datta Prasad, P. V., and Pisipati, V. G. K. M. Orientational order parameter - 1 A birefringence study. Molecular Crystals and Liquid Crystals **2009**, 511, 1603-1615.

[8] Miyano, K. Raman depolarization ratios and order parameters of a nematic liquid crystal. Journal of Chemical Physics **1978**, 69(11), 4807-4813.

[9] Sidir, M., and Farhi, R. On the determination of orientational order parameters in liquid crystals from Raman scattering: CB9 revisited. Liquid Crystals **1995**, 19(5), 573-9

[10] Picken, S. J. Measurements and values for selected order parameters. EMIS Datareviews Series **2000**, 25(Physical Properties of Liquid Crystals: Nematics), 89-102.

[11] Poggi, Y., Atten, P., and Aleonard, R. Application of the Landau approximation to the nematic phase of liquid crystals. Physical Review A: Atomic, Molecular, and Optical Physics **1976**, 14(1), 466-8.

[12] Hagemeyer, A., Tarroni, R., and Zannoni, C. Determination of orientational order parameters in liquid crystals from temperature-dependent ^{13}C NMR experiments. Journal of the Chemical Society, Faraday Transactions **1994**, 90(22), 3433-42.

[13] Abe, A., and Yamazaki, T. Orientational order of α-helical poly(γ-benzyl glutamate) in the lyotropic liquid-crystalline state: comparison of theory with experiments. Macromolecules **1989**, 22(5), 2145-9.

[14] Frank, F. C. Liquid crystals: theory of liquid crystals. Discussions of the Faraday Society **1958**, No. 25, 19-28.

[15] Bloss, F. D. An Introduction to the Methods of Optical Crystallography. **1961**, Holt, Rinehart, and Winston: New York, 294 pp.

[16] Hecht, E. Optics (4th Edition). **2001**, Addison Wesley: San Francisco, 698 pp.

[17] http://www.microscopyu.com/articles/polarized/polarizedintro.html.

[18] Kleman, M. Points, Lines and Walls: In Liquid Crystals, Magnetic Systems and Various Ordered Media. **1983**, Wiley: New York, 322 pp.

[19] Kleman, M., Lavrentovich, O. D., and Nastishin, Y. A. Dislocations and Disclinations in Mesomorphic Phases. In Dislocations in Solids edited by Nabarro, F. R. N. and Hirth, J. P. Vol. 12. Ch. 66. **2004**, Elsevier: Amsterdam, 590 pp.

[20] Kleman, M., and Lavrentovich, O. D. Soft Matter Physics: An Introduction. **2003**, Springer-Verlag: New York, 637 pp.

[21] Bunkov, Y. M., and Godfrin, H. (Ed.) Topological Defects and the Non-Equilibrium Dynamics of Symmetry Breaking Phase Transitions. In: NATO Sci. Ser., Ser. C. **2000**, Kluwer academic: Dordrecht, 394 pp.

[22] Chuang, I., Durrer, R., Turok, N., and Yurke, B. Cosmology in the laboratory: defect dynamics in liquid crystals. Science **1991**, 251, 1336-42.

[23] Lydon, J. Chromonics. In: Demus D, Goodby J, Gray GW, Speiss H-W, Vill V, editors. Handbook of Liquid Crystals, Wiley VCH: Weinheim, **1998**, 2B, 981-1007, 536 pp.

[24] Lydon, J. Chromonic liquid crystal phases. Current Opinion in Colloid & Interface Science **1998**, 3(5), 458-466.

[25] Lydon, J. Chromonic mesophases. Current Opinion in Colloid & Interface Science **2004**, 8(6), 480-490.

[26] Lydon, J. Chromonic review. Journal of Materials Chemistry **2010**, 20(45), 10071-10099.

[27] Vasilevskaya, A. S., Generalova, E. V., and Sonin, A. S. Chromonic mesophases. Russian Chemical Reviews **1989**, 57, 1575-1596 (Translated from Uspekhi Khimii **1989**, 58(9), 1575-96).

[28] Cox, J. S., Woodard, G. D., and McCrone, W. C. Solid-state chemistry of cromolyn sodium (disodium cromoglycate). Journal of pharmaceutical sciences **1971**, 60(10), 1458-65.

[29] Hartshorne, N. H., and Woodard, G. D. Mesomorphism in the system disodium chromoglycate-water. Molecular Crystals and Liquid Crystals **1973**, 23(3/4), 343-68.

[30] Horowitz, V. R., Janowitz, L. A., Modic, A. L., Heiney, P. A., and Collings, P. J. Aggregation behavior and chromonic liquid crystal properties of an anionic monoazo dye. Physical Review E: Statistical, Nonlinear, and Soft Matter Physics **2005**, 72(4-1), 041710/1-041710/10.

[31] Park, H.-S., Kang, S.-W., Tortora, L., Nastishin, Y., Finotello, D., Kumar, S., and Lavrentovich, O. D. Self-assembly of lyotropic chromonic liquid crystal Sunset Yellow and effects of ionic additives. Journal of Physical Chemistry B **2008**, 112(51), 16307-16319.

[32] Edwards, D. J., Jones, J. W., Lozman, O., Ormerod, A. P., Sintyureva, M., and Tiddy, G. J. T. Chromonic liquid crystal formation by Edicol Sunset Yellow. Journal of Physical Chemistry B **2008**, 112(46), 14628-14636.

[33] Donnio, Bertrand. Lyotropic metallomesogens. Current Opinion in Colloid & Interface Science **2002**, 7(5, 6), 371-394.

[34] Sierra, T. Low molecular weight lyotropic metallomesogens. Metallomesogens **1996**, 29-42.

[35] Tam-Chang, S.-W., Huang, L., Gyan, A., Seo, W., Mahinay, D., and Iverson, I. K. Designing chromonic mesogens for the fabrication of anisotropic optical materials. Proceedings of SPIE **2008**, 6911(Emerging Liquid Crystal Technologies III), 691107/1-691107/12.

[36] Tam-Chang, S.-W., and Huang, L. Chromonic liquid crystals: properties and applications as functional materials. Chemical Communications **2008**, 17, 1957-1967.

[37] Lydon, J. E. New models for the mesophases of disodium cromoglycate (INTAL). Molecular Crystals and Liquid Crystals **1980**, 64(1), 19-24.

[38] Hui, Y. W., and Labes, M. M. Structure and order parameter of a nematic lyotropic liquid crystal studied by FTIR spectroscopy. Journal of Physical Chemistry **1986**, 90(17), 4064-4067.

[39] Wu, L., Lal, J., Simon, K. A., Burton, E. A., and Luk, Y.-Y. Nonamphiphilic assembly in water: polymorphic nature, thread structure, and thermodynamic incompatibility. Journal of the American Chemical Society **2009**, 131(21), 7430-7443.

[40] Harrison, W. J., Mateer, D. L., and Tiddy, Gordon J. T. Liquid-crystalline J-aggregates formed by aqueous ionic cyanine dyes. Journal of Physical Chemistry **1996**, 100(6), 2310-21.

[41] Tiddy, G. J. T., Mateer, D. L., Ormerod, A. P., Harrison, W. J., and Edwards, D. J. Highly ordered aggregates in dilute dye-water systems. Langmuir **1995**, 11(2), 390-393.

[42] Maiti, P. K., Lansac, Y., Glaser, M. A., and Clark, N. A. Isodesmic self – assembly in lyotropic chromonic systems. Liquid Crystals **2002**, 29(5), 619-626.

[43] Kostko A. F, Cipriano B. H, Pinchuk O. A, Ziserman L., Anisimov M. A, Danino D., and Raghavan S. R. Salt effects on the phase behavior, structure, and rheology of chromonic liquid crystals. Journal of Physical Chemistry B **2005**, 109(41), 19126-19133.

[44] Ormerod, A. P. The formation of chromonic liquid crystals by water-soluble azo-dyes. Ph.D. Thesis, University of Salford, **1994**, 267 pp.

[45] Nastishin, Y., Neupane, K., Baldwin, A. R., Lavrentovich, O. D., and Sprunt, S. Elasticity and viscosity of a lyotropic chromonic nematic studied with dynamic light scattering. arXiv.org, e-Print Archive, Condensed Matter **2008**, 1-4, arXiv: 0807.2669v1.

[46] Remizov, S., Krivoshchepov, A., Nazarov, V., and Grodsky, A. Rheology of the lyotropic liquid crystalline material for thin film polarizers. Molecular Crystals and Liquid Crystals Science and Technology, Section C: Molecular Materials **2001**, 14(2), 179-190.

[47] Prasad S K., Nair G. G, Hegde G., and Jayalakshmi V. Evidence of wormlike micellar behavior in chromonic liquid crystals: rheological , X-ray, and dielectric studies. Journal of Physical Chemistry B **2007**, 111(33), 9741-9746.

[48] Attwood, T. K., Lydon, J. E., Hall, C., and Tiddy, G. J. T. The distinction between chromonic and amphiphilic lyotropic mesophases. Liquid Crystals **1990**, 7(5), 657-668.

[49] Tanford. C. The hydrophobic effect: formation of micelles and biological membranes. **1980**, New York: Wiley, 233pp.

[50] Crowley, T. L., Bottrill, C., Mateer, D., Harrison, W. J., and Tiddy, G. J. T. Lyotropic chromonic liquid crystals. Neutron scattering studies of shear-induced orientation and reorientation. Colloids and Surfaces A: Physicochemical and Engineering Aspects **1997**, 129,130, 95-115.

[51] Iverson, I. K., and Tam-Chang, S.-W. Cascade of molecular order by sequential self - organization, induced orientation, and order transfer processes. Journal of the American Chemical Society **1999**, 121(24), 5801-5802.

[52] Iverson, I. K., Casey, S. M., Seo, W., Tam-Chang, S.-W., and Pindzola, B. A. Controlling Molecular Orientation in Solid Films via Self - Organization in the Liquid-Crystalline Phase. Langmuir **2002**, 18(9), 3510-3516.

[53] Luoma, R. J. X - ray scattering and magnetic birefringence studies of aqueous solutions of chromonic molecular aggregates. Ph.D. thesis, Brandeis Univ., **1995**, 104 pp.

[54] Matsunaga, D., Tamaki, T., Ichimura, K. Azo-pendant polyamides which have the potential to photoalign chromonic lyotropic liquid crystals. Journal of Materials Chemistry **2003**, 13(7), 1558-1564.

[55] Lavretovich, O. D., Schneider, T., Golovin, A. B., and Lee, J.-C. A design and fabrication of an aligned lyotropic chromonic liquid crystal films with improved optical properties and alignment uniformity. U.S. Pat. Appl. Publ. **2006**, US 2006040069.

[56] Tam-Chang, S.-W., Seo, W., Rove, K., and Casey, S. M. Molecularly designed chromonic liquid crystals for the fabrication of broad spectrum polarizing materials. Chemistry of Materials **2004**, 16(10), 1832-1834.

[57] Boiko, O. P., Vasyuta, R. M., Nazarenko, V. G., Pergamenshchik, V. M., Nastishin, Yu. A., and Lavrentovich, O. D. Polarizing properties of functional optical films

based on lyotropic chromonic liquid crystals. Molecular Crystals and Liquid Crystals **2007**, 467, 181-194.

[58] Park, S., Kim, S.-E., Kim, D.-Y., Kang, S.-W., Shin, S., Kuo, S.-W., Hwang, S.-H., Lee, S. H., Lee, M.-H., and Jeong, K.-U. Polymer-stabilized chromonic liquid-crystalline polarizer. Advanced Functional Materials **2011**, 21(11), 2129-2139.

[59] Kim, B., Chang, E., and Shin, S. Preparation of optically anisotropic film by sunset yellow chromonic liquid crystal. Kongop Hwahak **2011**, 22(1), 81-86.

[60] Bae, Y.-J., Yang, H.-J., Shin, S.-H., Jeong, K.-U., and Lee, M.-H. A novel thin film polarizer from photocurable non-aqueous lyotropic chromonic liquid crystal solutions. Journal of Materials Chemistry **2011**, 21(7), 2074-2077.

[61] Lee, M. H., Jung, G. U., and Shin, S. H. Method for manufacturing micro-patterned polarizer by using monomer based lyotropic chromonic liquid crystal. Repub. Korean Kongkae Taeho Kongbo **2010**, KR 2010128986.

[62] Shin, S. H., Lee, M. H., Jung, G. U., Jang, Y. J., Lee, S. J., and Park, M. S. Method for manufacturing polarizer film using naphthalene derivative lyotropic chromonic liquid crystal composition. Repub. Korean Kongkae Taeho Kongbo **2010**, KR 2010128987.

[63] Shin, S. H., Lee, M. H., Jung, G. U., Jang, Y. J., Lee, S. J., Park, M. S., Su J., and Park, M. S. Naphthalene derivative lyotropic chromonic liquid crystal composition for multilayer polarizer film. Repub. Korean Kongkae Taeho Kongbo **2010**, KR 2010129001.

[64] Lavrentovich, M., Sergan, T., and Kelly, J. Planar and twisted lyotropic chromonic liquid crystal cells as optical compensators for twisted nematic displays. Liquid Crystals **2003**, 30(7), 851-859.

[65] Lavrentovich, M., Sergan, T., and Kelly, J. Lyotropic chromonic liquid crystals for optical applications - An optical retardation plate for twisted nematic cells. Molecular Crystals and Liquid Crystals **2004**, 409, 21-28.

[66] Shiyanovskii, S. V., Schneider, T., Smalyukh, I. I., Ishikawa, T., Niehaus, G. D., Doane, K. J., Woolverton, C. J., and Lavrentovich, O. D. Real-time microbe detection based on director distortions around growing immune complexes in

lyotropic chromonic liquid crystals. Physical Review E: Statistical, Nonlinear, and Soft Matter Physics **2005**, 71(2-1), 020702/1-020702/4.

[67] Helfinstine, S. L., Lavrentovich, O. D., and Woolverton, C. J. Lyotropic liquid crystal as a real-time detector of microbial immune complexes. Letters in Applied Microbiology **2007**, 44(3), 342.

[68] Tortora, L., Park, H.-S., Antion, K., Finotello, D., and Lavrentovich, O. D. Lyotropic chromonic liquid crystals as materials for optical and biosensing applications. Proceedings of SPIE-The International Society for Optical Engineering **2007**, 6487(Emerging Liquid Crystal Technologies II), 64870I/1-64870I/15.

[69] Guo, F., Mukhopadhyay, A., Sheldon, B. W., and Hurt, R. H. Vertically aligned graphne layer arrays from chromonic liquid crystal precursors. Advanced Materials **2011**, 23(4), 508-513.

[70] Rodriguez-Abreu, C., Torres, C. A., and Tiddy, G. J. T. Chromonic liquid crystalline phases of pinacyanol acetate: characterization and use as templates for the preparation of mesoporous silica nanofibers. Langmuir **2011**, 27, 3067-3073.

CHAPTER 2

ALIGNED SUNSET YELLOW CHROMONIC LIQUID CRYSTAL SOLUTIONS AND DRIED FILMS

2.1 Introduction to Sunset Yellow FCF chromonics

Sunset Yellow FCF (SSY) is commonly used as a food dye, and also known as FD&C Yellow Number 6 or C. I. Food Yellow 3. It is a sodium salt of 6-hydroxy-5-[(4-sulfophenyl)azo]-2-naphthalenesulfonic acid. Because SSY is a food dye, it is available in a purer form than many other textile dyes.

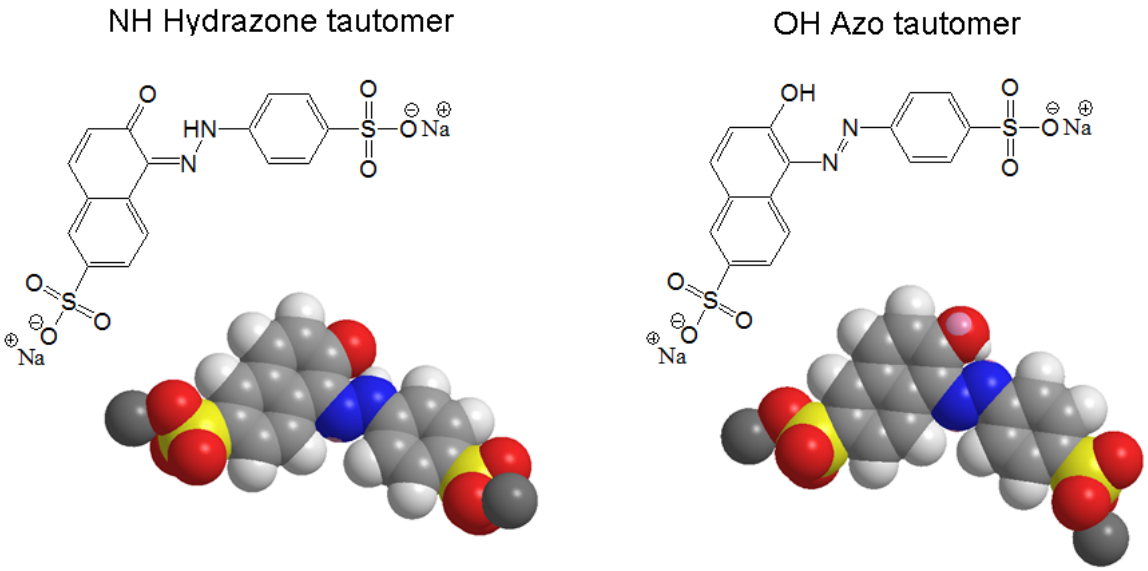

Figure 2.1. Tautomeric structures of Sunset Yellow FCF: NH hydrazone tautomer and OH azo tautomer (software used: ChemDraw).

SSY is becoming the second most studied LCLC after DSCG [1]. High-angle x-ray studies of SSY by Ormerod [2] indicated that the middle phase possesses hexagonal symmetry, and a dimer type repeat exists along the stacks, which were shown to a uni-molecular cross-section. Luoma [3] studied the growth of stacks of SSY by x-ray

scattering and magnetic birefringence. He found, for the 0.21 volume fraction sample at the phase transition, the average stack size is about 7 monomers (L/D is about 1.5), which is very low and it does not follow the predictions of the hard rod theory developed by Onsager for a system of rodlike molecules in solution to form an ordered phase. X-ray studies also gave the order parameters from 0.72 near isotropic-nematic phase transition to 0.90 near a possible nematic-columnar transition [3]. In 2005, Horowitz et al [4] performed optical absorption measurements and revealed that the aggregation takes place at all concentrations, with aggregation number increasing with concentration. For 0.04M isotropic sample, the average stack size is about 4 monomers; for 1.1 M isotropic sample, the average stack size is about 19.7 monomers (aspect ratio L/D is about 6). A theory based on the law of mass action and an isodesmic aggregation process agrees very well with absorption data and yields the "bond" energy between monomers to be 7.25 k_BT. Birefringence for SSY LCLC is negative, from -0.06 and -0.15 for nematic samples with various temperatures and concentrations [4]. With birefringence (Δn) as well as the absorption measurement, order parameters (S) were determined to be between 0.6 and 0.75 by using the relation $S = \frac{n_{//}A_{//} - n_{\perp}A_{\perp}}{n_{//}A_{//} + 2n_{\perp}A_{\perp}}$, where $n_{//} \approx n_0 + \frac{2}{3}\Delta n$, $n_{\perp} \approx n_0 - \frac{1}{3}\Delta n$, n_0 is the refractive index in the isotropic phase, "//" and "⊥" mean the direction parallel and perpendicular to the director, respectively. They also found alignment of SSY LCLCs was never perfect when just common rubbed glass and rubbed polyimide coated glass were used [4]. In 2007, Prasad et al [5] reported rheological, x-ray and dielectric investigations of SSY LCLC with and without addition of salt. The salt-concentration dependence of the steady-state viscosity at low shear rates has a non-monotonic variation and is qualitatively similar to the behavior seen in wormlike micellar systems, a surprising result since chromonic systems are expected to be non-micellar in character [5]. In 2008, Park et al [6] also explored the salt effects. There are two general

trends: (a) stabilization of the N phase by adding mono and divalent salts; and (b) suppression of N phase by increasing the pH. Their x-ray measurement shows the correlation length associated with the stacking is too short to explain the orientational order by the Onsager model and they proposed more complicated aggregate structures containing "stacking faults" such as junctions with a shift of neighboring molecules, and three-fold junctions, etc., based on the dynamic light scattering measurement which shows the aggregates are larger than the correlation length. Edwards et al [7] used ^{1}H and ^{13}C NMR spectra (particularly ^{13}C) and demonstrated that the hydrazone tautomer prevails in all the phases. The order parameters are between 0.54 and 0.65 in the nematic phase based on naphthalene ring by ^{1}H NMR spectroscopy. They also proposed the head-to-tail single molecular packing in the aggregate according to the x-ray diffraction pattern [7]. Joshi et al [8] reported the aggregation process is non-isodesmic according to the temperature and concentration dependence of the scission energy based on x-ray measurement. The scission energy, determined from the Arrhenius thermal evolution of the longitudinal correlation length, is found to be 4.3±0.3 k_BT and 3.5±0.2 k_BT, in the nematic and columnar phases, respectively [8]. Chami and Wilson's atomic simulation study [9] indicated a preference for head-to-tail stacking and antiparallel dipole order of SSY molecules. Stacks are dynamic entities in which rotational transitions (flips) can occur between antiparallel and parallel configurations. A value for the free energy of binding of a molecule to a stack of 7 k_BT was obtained for stacks of three and eight SSY molecules, with a slightly larger value (additional 2 kJ/mol) obtained for the dimer binding energy, indicating that aggregation is approximately isodesmic [9]. Renshaw and Day [10] employed diffusion nuclear magnetic resonance methods to investigate the hydrodynamic properties of sunset yellow aggregates in isotropic solution. The results show that the aggregates are comprised of tens to hundreds of monomer units at the concentrations investigated and the average number of molecules per aggregate is approximately 5 larger than previously reported [10]. Jones et al [11] have employed

changes in the ^{1}H NMR chemical shifts to monitor the aggregate formation in solution. SSY concentrations, low levels of salinity appear to alter aggregate shape and size, resulting in a disaggregation/aggregation effect occurring over four orders of magnitude of added electrolyte. The isodesmic theory of aggregation is too simple to accurately describe the aggregation process from the monomer to the pre-nematic phase concentrations. NMR quadrupole splittings indicate that there is no specific Na^{+} ion binding to the stacks. At the very highest concentrations of Edicol and sodium chloride the aggregates and mesophases are destabilized [11]. Park et al [12] studied the condensation of SSY in aqueous solutions crowded with polyethylene glycol (PEG) and doped with salt NaCl. PEG causes the isotropic SSY solutions to condense into a liquid crystalline region, causes separation of nematic (N) phase into the coexisting N and I domains or into the coexisting columnar hexagonal (C) phase and I phase. They qualitatively explained this behavior by the depletion (excluded volume) effects and suggest that the salt-induced screening of electric charges at the surface of chromonic aggregates leads to two different effects: (a) increase of the scission energy and the contour length of aggregates and (b) decrease of the persistence length of SSY aggregates [12].

In this Chapter, we focus on the preparation and characterization of aligned SSY chromonic liquid crystal solution and dried film for further fundamental investigation and application.

2.2 Preparation of aligned SSY chromonic liquid crystal solutions

Sunset Yellow FCF with 90% dye content was purchased from Sigma-Aldrich. It was purified by twice-precipitating the dye from a 10% deionized water (resistivity ≥18 megohm) solution by addition of 90% ethanol, which was followed by 48-hour drying in a vacuum oven at room temperature. Figure 2.2 shows the phase diagram of SSY in

water. Phase transitions were judged by observing the change of textures under POM with crossed polarizer and analyzer, while the SSY/water filled glass cells were heated with rate 0.4ºC/min controlled by a Linkam THM 600 hot stage with accuracy of 0.1°C. Phase transition temperatures of higher concentration SSY solutions are close to the boiling point of water and difficult to measure. Figure 2.3 shows the textures of SSY/water systems in different phases made with different concentrations at room temperature: isotropic (0.7M), biphasic (0.9M), nematic N (1.0M-1.5M) and hexagonal M phase which was obtained by leaving the glass cell open to allow slow water evaporation and condensation from the nematic N phase.

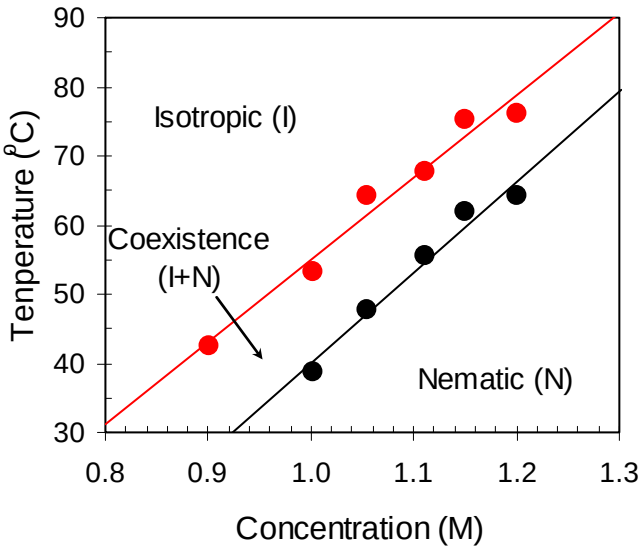

Figure 2.2. Phase diagram of Sunset Yellow FCF in water with heating rate 0.4°C/min. Sample temperature was controlled by a Linkam THM 600 hot stage with accuracy of 0.1°C.

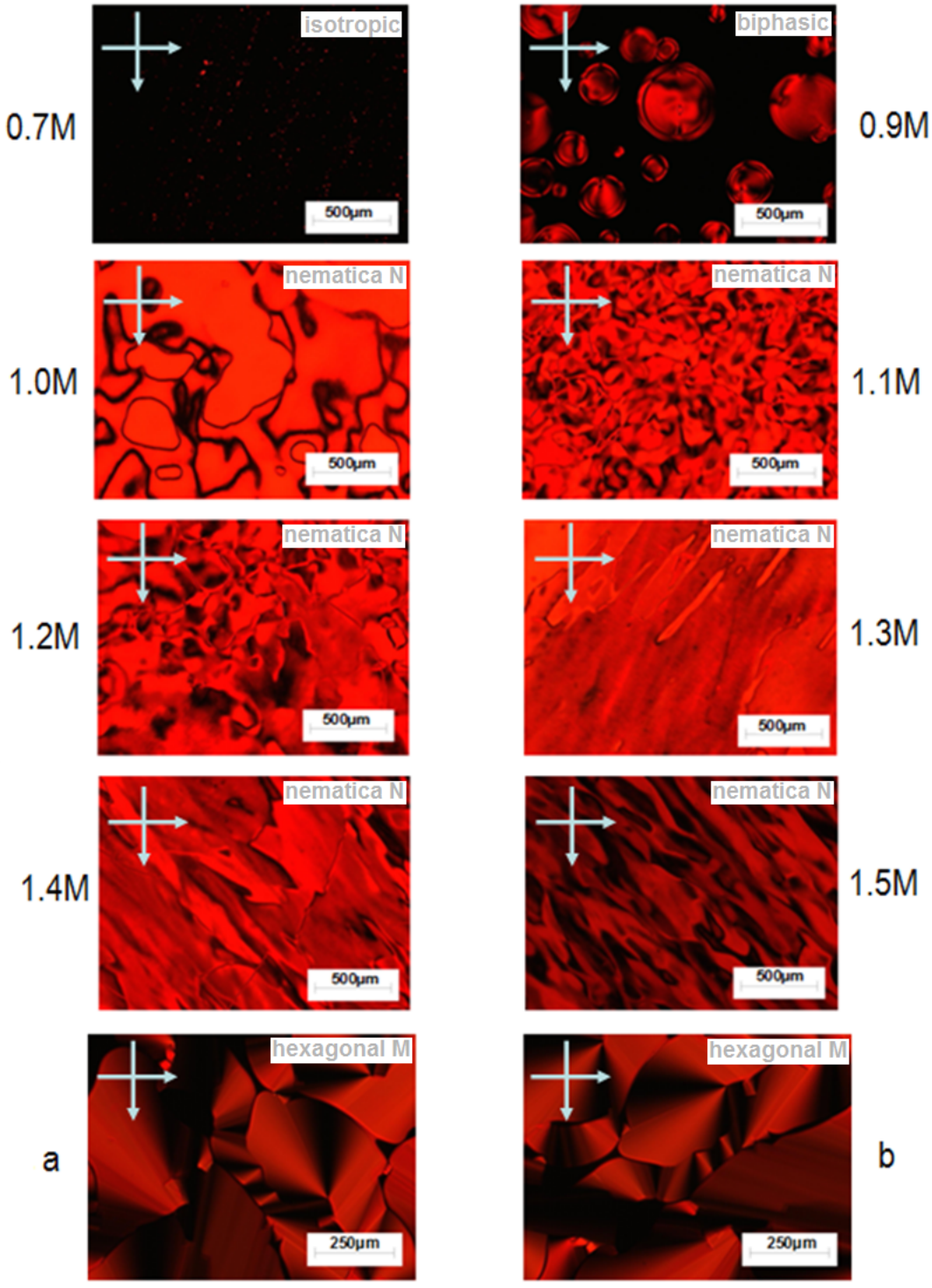

Figure 2.3. POM images of SSY aqueous solutions with different concentrations in uncoated glass cells with thickness 10µm under crossed polarizer and analyzer at room temperature. Sample (a) was more concentrated than 1.5M and made by slow water evaporation from the open cell. Image (b) was taken after 90º rotation of the sample from a.

Flat capillaries (three sizes, 200μm/20μm/5cm; 500μm/50μm/5cm; 1000μm/ 50μm/5cm, as shown in Figure 2.4.) were purchased from Vitrocom and used as received without further surface treatment except cleaning. SSY solutions with different concentrations were prepared by dissolving purified SSY in deionized water and heated up to isotropic phase. Silicone oil was used to seal the reservoir of SSY solutions to prevent water evaporation at high temperature. Figure 2.5 shows the detailed steps for sample preparation: step 1, heat the nematic N phase SSY solution into isotropic phase; steps 2 and 3, insert the flat capillary into solution; step 4, seal the two ends of the capillary. As silicone oil filled into the capillary before the SSY solution, it also cleaned the capillary by carrying away the dust which might contaminate the SSY solution; meantime, silicone oil also prevented water evaporation in the capillary. The other end of the filled capillary was dipped into silicone grease and both ends were sealed by Permaoxy fast cure epoxy.

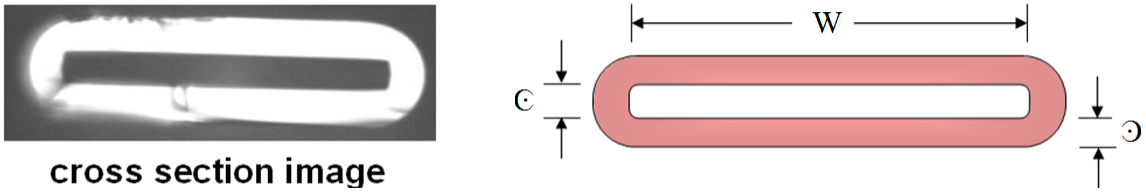

Figure 2.4. Cross-sectional view of the flat capillary made of borosilicate glass. The left image is the real image provided by Vitrocom®, with a schematic shown on the right. Three sizes of capillaries were used: 1. *W*=200μm, *t* =20μm, *d* =20μm; 2. *W*=500μm, *t* =50μm, *d* =50μm; 3. *W*=1000μm, *t*=50μm, *d*=50μm, where *W* is width, *t* is thickness, *d* is wall thickness. The length of all capillaries is 5cm.

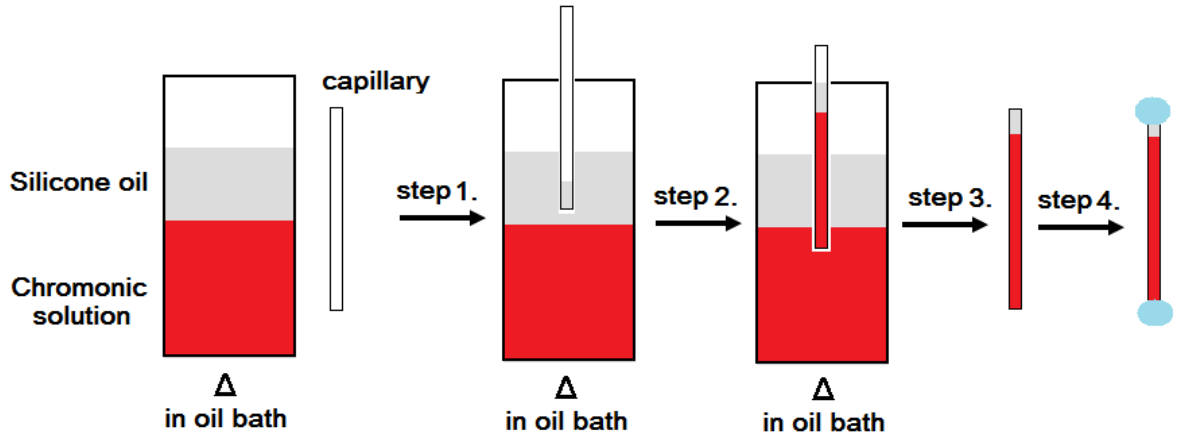

Figure 2.5. Preparation of aligned SSY chromonic liquid crystal solution sample in a flat capillary.

2.3 Characterization of domain alignment

By rotating the prepared capillary sample under POM with crossed polarizer and analyzer, the texture appearance has a periodicity of 90°. The transmitted intensity is uniform everywhere in the capillary except the edge areas, and maximizes when the capillary is 45° to the polarizer or analyzer and minimizes when the capillary is 0° or 90° to polarizer or analyzer, as shown in Figure 2.6 c and d. For uniaxial materials, the transmitted light intensity under crossed polarizer and analyzer is given by equation (1.6) in Chapter One: $I = I_0 \sin^2(2\varphi)\sin^2(\delta/2)$. Figure 2.7 shows the definition of angles for LCLCs system and the optical axis is the long axis of aggregates/columns. For a homogeneous planar uniaxial sample, δ is a constant, so the transmitted light intensity only changes with $\sin^2(2\varphi)$ which has a maximum for φ=45° and a minimum for φ=0° and φ=90°. So it is quite possible that aggregates/columns in the flat capillary are homogeneous planar aligned.

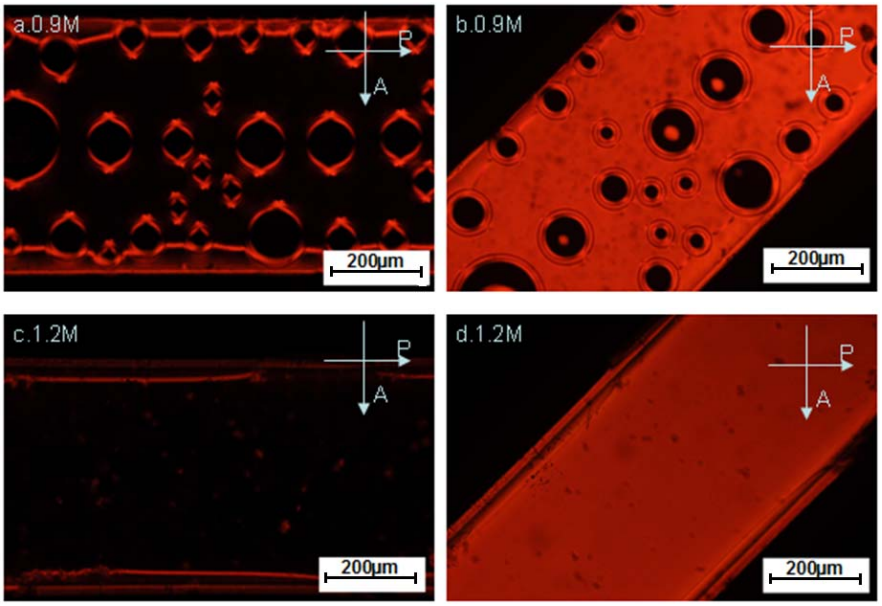

Figure 2.6. POM images of SSY aqueous solutions filled in flat capillaries under the crossed polarizers. Scale bars are 200μm. a. 0.9M, long axis of the capillary is parallel to the polarizer; b. 0.9M, long axis is 45° to the polarizer; c. 1.2M, long axis is parallel to the polarizer; d. 1.2M, long axis is 45° to the polarizer. "P" means polarizer and "A" means analyzer.

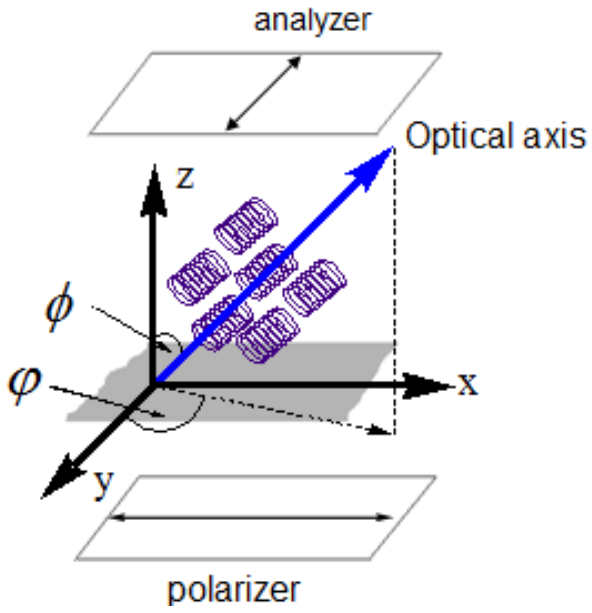

Figure 2.7. Schematic figure of a uniformly oriented LCLC for angle definitions.

To ascertain the alignment direction of the monodomain, we used tactoids, which are nematic droplets in the isotropic phase (positive tactoids) or isotropic bipolar droplets in the nematic phase (negative tactoids) as the nuclei of the new phase [13-15]. We tried to use tactoids as "compasses" of the surrounding director field. When the sample was heated to biphasic region or made in biphasic region with relatively low concentration at room temperature, negative tactoids appeared and all oriented perpendicular to the long axis of the flat capillary (LA) without any external electric or magnetic force. Therefore, the director field surrounding the tactoids must be perpendicular to the LA, according to which, it is reasonable to assume the director of original nematic monodomain is perpendicular to the LA.

To confirm this assumption, we used x-ray diffractometry as well as polarized Raman spectroscopy described in the next chapter. The x-ray measurement was done using wavelength 1.54Å and transmission geometry. The capillary was mounted vertically with the flat area facing to the source. The resultant diffraction pattern and azimuthal intensity profile, as shown in Figure 2.8 a' and b', verify that the direction of π-π stacking is perpendicular to LA, and it follows that the stacking columns as well as director are perpendicular to LA. Joshi et al [8] used external magnetic field to align SSY chromonics in a rotating cylindrical capillary, and π-π stacking is along the long axis of the capillary, according to the x-ray result.

Impéror-Clerc et al [16, 17] achieved highly oriented flow-aligned samples of lyotropic liquid-crystalline hexagonal phases of block copolymers and surfactants with orientation along the flat capillary. We succeeded in aligning SSY chromonics in nematic N phase, but failed to align SSY chromonics in hexagonal M phase by this simple capillary technique. For the above alignment in the nematic N phase, the directors of the aggregates/columns in the monodomain were all perpendicular to the flow direction.

In summary, planar aligned monodomain of SSY chromonics formed in a flat capillary. The alignment of the monodomain has been characterized by polarized optical

microscopy and x-ray diffractometry. The director was perpendicular to long axis of the capillary or flow direction.

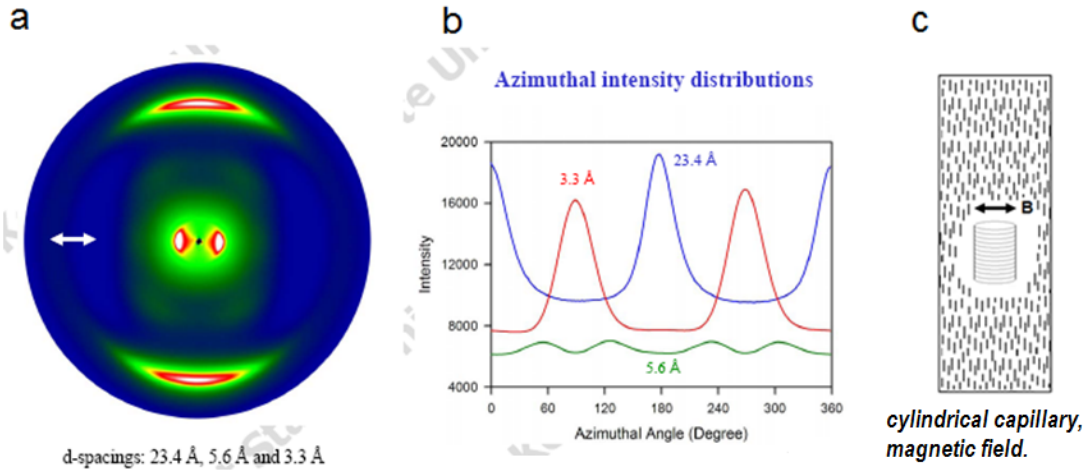

Physical Review E. (2009), 80(4-1), 041703/1-041703/8.

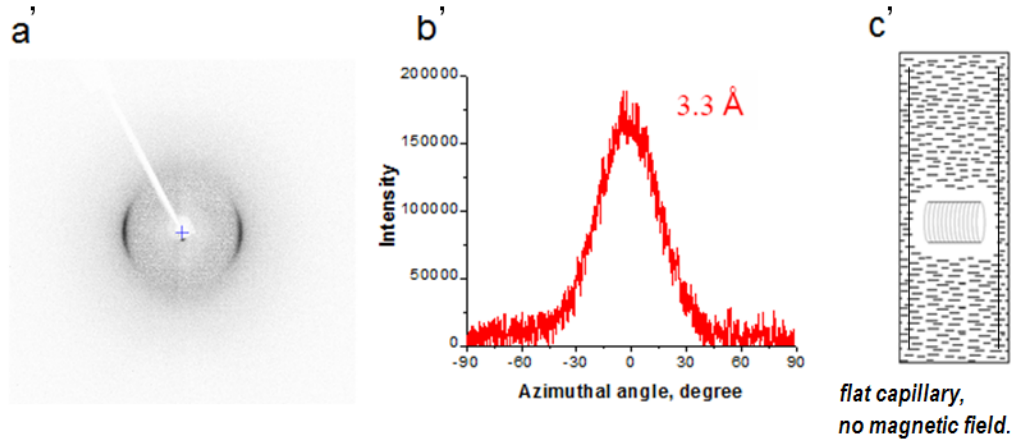

Figure 2.8. X-ray diffraction of SSY chromonics samples. Structures a, b and c are from reference [8]. a'. Wide-angle x-ray diffraction pattern for monodomain in the flat capillary; b'. Azimuthal intensity plot for d-spacing 3.3Å. 0° represents the meridional direction; c'. The capillary was mounted vertically with the flat area facing to the source. Wide-angle X-ray scattering was done on the Rigaku MicroMax 002 X-ray generator operated at 45 kV and 0.66 mA and equipped with Raxis VI++ detector using wavelength 1.54Å and transmission geometry. The diffraction patterns were recorded using a high-resolution image-plate detector MAR345 placed at a distance of 100 mm from the sample. The orientation from wide angle x-ray diffraction was determined using the software MDI Jade 6.1. AreaMax software was used for background subtraction and integration.

2.4 Oriented SSY dried films

Oriented SSY thin films were made by mechanically rubbing the 1.0M SSY aqueous solution in the chromonic nematic N phase on the glass slide substrate using a wirewound wet-film applicator rod with wires of 0.003 inches. Figure 2.9 shows more information about the rod. The film had been dried in air at room temperature for three weeks when measurements were taken.

For uniaxial materials, the transmitted light intensity changes with $\sin^2(2\varphi)$ which has a maximum for φ=45° and a minimum for φ=0° and φ=90°. As shown in Figure 2.10, the texture of the dried SSY film has a periodicity of 90° when rotated under crossed polarizers; the transmitted intensity maximizes as the shearing direction is 45° to the polarizer or analyzer, which shows the dried film inherits or preserves some order of the chromonic liquid crystal phase which has been aligned by rubbing.

The absorption measurement in Figure 2.11 shows that the oriented film exhibits stronger absorption of light when the polarization axis of the incident beam is perpendicular to the rubbing direction than when the polarization axis of the incident beam is parallel to the rubbing direction. This indicates that SSY aggregates/columns on the glass substrate are oriented with their long axes parallel to the rubbing direction, as the absorption dipole moment of SSY is aligned normal to the aggregates hence perpendicular to the incident polarization. The dichroic ratio R_{di}, given by $A_{//}/A_{\perp}$, here equal to $A_{90°}/A_{0°}$, is not very high in Figure 2.12, which is probably due to limitation of effectiveness of this rubbing method. Other causes such as, the capillary flow induced reorientation of SSY molecules during the drying process, may be also possible. Hopefully, using more concentrated SSY solution will shorten the drying time and improve the orientation along the rubbing direction.

To summarize, mechanical rubbing can induce alignment of the SSY LCLCs in nematic N phase and the solid film can inherit the order from the nematic N phase, which tells us it is possible to make polarizer film from LCLCs just by this rubbing method.

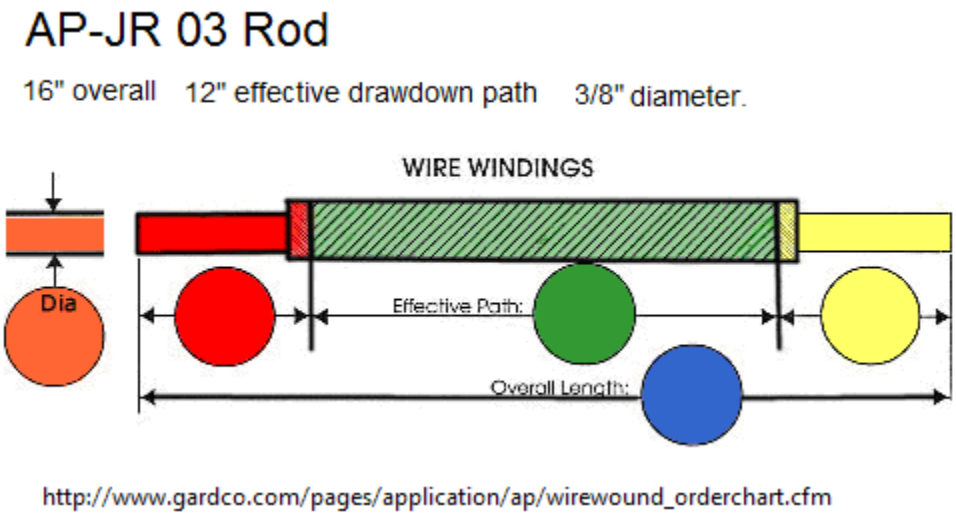

Figure 2.9. Scheme of a wirewound wet-film applicator rod used for rubbing. This JR 03 rod was purchased from Paul N. Gardner Company, Inc. Wire size is 0.003 inches. Overall length is 16 inches. Effective drawdown path is 12 inches. Diameter of the rod is 3/8 inches. http://www.gardco.com/pages/application/ap/wirewound_orderchart.cfm.

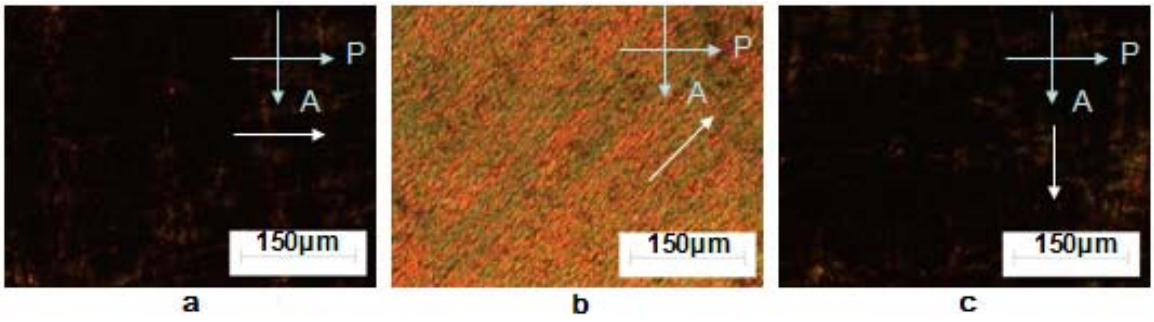

Figure 2.10. The oriented SSY film under crossed polarizers (blue arrows). Rubbing direction (white arrow) is 0°, 45° and 90° to the analyzer in the image a, b and c, respectively.

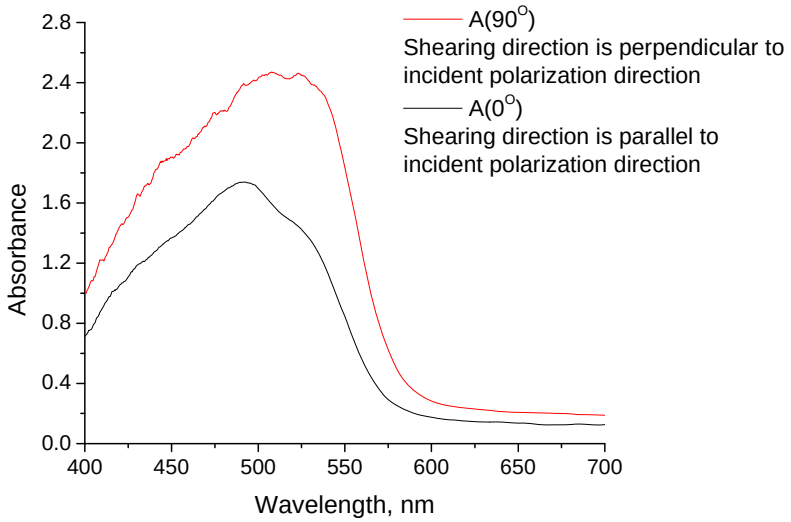

Figure 2.11. Anisotropic absorption of the oriented SSY film, only with polarizer and no analyzer in the optical path.

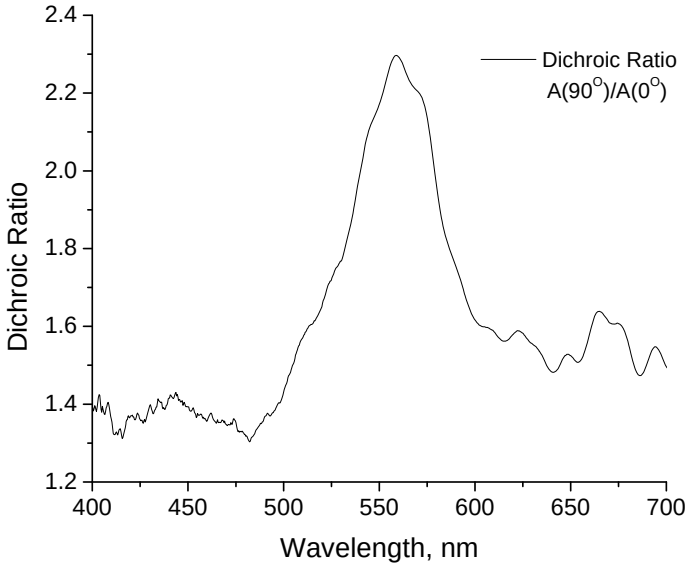

Figure 2.12. Dichroic ratio for the oriented SSY film.

2.5 Conclusions

In this chapter, both aligned SSY chromonic liquid crystal solution and anisotropic dried film were achieved. The homogeneous planar aligned monodomain was prepared in a flat capillary where silicone oil was used in the process to prevent water evaporation and carry away dust. The alignment of aggregates/columns in the monodomain, perpendicular to the long axis of capillary, was characterized by polarized optical microscopy and x-ray diffractometry. This aligned monodomain of SSY chromonics can be used for other fundamental investigations, such as the measurement of order parameters using polarized Raman spectroscopy and studies on the Brownian motion of particles in the anisotropic medium. Similar to aligned DSCG chromonics in polyimide coated and rubbed cells for biosensor device [18-20], this aligned monodomain of SSY chromonics in the flat capillary also can be used directly in biosensor applications. It is also an easier and cheaper method just by using the commercial available capillary compared to coating and rubbing polyimide. Mechanical rubbing gives alignment to SSY film and could be a method for making a chromonic polarizer.

2.6 References

[1] Lydon, J. Chromonic review. Journal of Materials Chemistry **2010**, 20(45), 10071-10099.

[2] Ormerod, A. P. The Formation of Chromonic Liquid Crystals by Water-Soluble Azo-Dyes. Ph.D. Thesis, University of Salford, **1994**, 267 pp.

[3] Luoma, R. J. X-Ray Scattering and Magnetic Birefringence Studies of Aqueous Solutions of Chromonic Molecular Aggregates. Ph.D. Thesis, Brandeis University, **1995**, 104 pp.

[4] Horowitz, V. R., Janowitz, L. A., Modic, A. L., Heiney, P. A., and Collings, P. J. Aggregation behavior and chromonic liquid crystal properties of an anionic

monoazo dye. Physical Review E: Statistical, Nonlinear, and Soft Matter Physics **2005**, 72, 041710/1-041710/10.

[5] Prasad, S. K., Nair, G. G., Hegde, G., and Jayalakshmi, V. Evidence of wormlike micellar behavior in chromonic liquid crystals: Rheological, x-ray, and dielectric studies. Journal of Physical Chemistry B **2007**, 111, 9741-9746.

[6] Park, H.-S., Kang, S.-W., Tortora, L., Nastishin, Y., Finotello, D., Kumar, S., and Lavrentovich, O. D. Self-assembly of lyotropic chromonic liquid crystal Sunset Yellow and effects of ionic additives. Journal of Physical Chemistry B **2008**, 112, 16307-16319.

[7] Edwards, D. J., Jones, J. W., Lozman, O., Ormerod, A. P., Sinty-ureva, M., and Tiddy, G. J. T. Chromonic liquid crystal formation by Edicol Sunset Yellow. Journal of Physical Chemistry B **2008**, 112, 14628-14636.

[8] Joshi, L., Kang, S.-W., Agra-Kooijman, D. M., and Kumar, S. Concentration, temperature, and pH dependence of sunset-yellow aggregates in aqueous solutions: An x-ray investigation. Physical Review E: Statistical, Nonlinear, and Soft Matter Physics **2009**, 80, 041703/1-041703/8.

[9] Chami, F., and Wilson, M. R. Molecular order in a chromonic liquid crystal: A molecular simulation study of the anionic azo dye Sunset Yellow. Journal of the American Chemical Society **2010**, 132, 7794-7802.

[10] Renshaw, M. P., and Day, I. J. NMR characterization of the aggregation state of the azo dye Sunset Yellow in the isotropic phase. Journal of Physical Chemistry B **2010**, 114(31), 10032-10038.

[11] Jones, J. W., Lue, L., Ormerod, A. P., and Tiddy, G. J. T. The influence of sodium chloride on the self-association and chromonic mesophase formation of Edicol Sunset Yellow. Liquid Crystals **2010**, 37, 711-722.

[12] Park, H.-S., Kang, S.-W., Tortora, L., Kumar, S., and Lavrentovich, O. D. Condensation of self-assembled lyotropic chromonic liquid crystal Sunset Yellow in aqueous solutions crowded with polyethylene glycol and doped with salt. Langmuir **2011**, 27, 4164-4175.

[13] Verhoeff, A. A., Bakelaar, I. A., Otten, R. H. J., van der Schoot, P., and Lekkerkerker, H. N. W. Tactoids of plate-like particles: size, shape, and director field. Langmuir **2011**, 27(1), 116-125.

[14] Nastishin, Y. A., Liu, H., Schneider, T., Nazarenko, V., Vasyuta, R., Shiyanovskii, S. V., and Lavrentovich, O. D. Optical characterization of the nematic lyotropic chromonic liquid crystals: Light absorption, birefringence, and scalar order parameter. Physical Review E: Statistical, Nonlinear, and Soft Matter Physics **2005**, 72(4-1), 041711/1-041711/14.

[15] Tortora, L., and Lavrentovich, O. D. Chiral symmetry breaking by spatial confinement in tactoidal droplets of lyotropic chromonic liquid crystals. Proceedings of the National Academy of Sciences of the United States of America **2011**, 108(13), 5163-5168, S5163/1-S5163/3.

[16] Imperor-Clerc, M., and Davidson, P. An x-ray scattering study of flow-aligned samples of a lyotropic liquid-crystalline hexagonal phase. European Physical Journal B: Condensed Matter Physics **1999**, 9(1), 93-104.

[17] Imperor-Clerc, M., Hamley, I. W., and Davidson, P. Fast and easy flow-alignment technique of lyotropic liquid-crystalline hexagonal phases of block copolymers and surfactants. Macromolecules **2001**, 34(10), 3503-3506.

[18] Shiyanovskii, S. V., Schneider, T., Smalyukh, I. I., Ishikawa, T., Niehaus, G. D., Doane, K. J., Woolverton, C. J., and Lavrentovich, O. D. Real-time microbe detection based on director distortions around growing immune complexes in lyotropic chromonic liquid crystals. Physical Review E: Statistical, Nonlinear, and Soft Matter Physics **2005**, 71(2-1), 020702/1-020702/4.

[19] Helfinstine, S. L., Lavrentovich, O. D., and Woolverton, C. J. Lyotropic liquid crystal as a real-time detector of microbial immune complexes. Letters in Applied Microbiology **2007**, 44(3), 342.

[20] Tortora, L., Park, H.-S., Antion, K., Finotello, D., and Lavrentovich, O. D. Lyotropic chromonic liquid crystals as materials for optical and biosensing applications. Proceedings of SPIE-The International Society for Optical Engineering **2007**, 6487(Emerging Liquid Crystal Technologies II), 64870I/1-64870I/15.

CHAPTER 3

THE TAUTOMERIC STRUCTURE AND ORDER PARAMETERS BY RAMAN SPECTROSCOPY

3.1 Introduction to Raman spectroscopy

3.1.1 Raman scattering

When incident light interacts with a molecule, the electric field of the light induces a changing dipole moment in the molecule because of its polarizability. Due to the oscillation of the electric field of the incident light, this induced dipole moment, $\boldsymbol{\mu}$, is also oscillating, described by the molecular polarizability, $\boldsymbol{p}$, and the electric field of the incident light, $\boldsymbol{E}$:

$$\mu = pE \tag{3.1}$$

$$E = E_0 \cos\left(2\pi\nu_o t\right) \tag{3.2}$$

where E_0 and ν_0 are the amplitude and the frequency of the oscillation of incident light, respectively, and t is the time. The oscillating dipole moment can absorb or emit energy by transition between different energy levels. Infrared spectroscopy (IR) monitors the energy transfer from photon of incident light to molecules, which is the energy absorption process [1, 2]. For the subsequent emission process of the excited molecules returning to the lower energy level, the energy transition is usually energetically elastic, where the energy of the incident photons equals the energy of the scattered photons, and is called "Rayleigh scattering", named after the British physicist Lord Rayleigh [1]. A very small fraction of light is scattered at energies different than that of the incident photons. The scattering associated with this inelastic energy transition is called "Raman scattering",

named after the Indian physicist Sir C. V. Raman, who first observed the Raman effect in 1928 [3]: "Experiments on the scattering of visible light when an intense beam is passed through a pure dust-free liquid or vapor show that the scattered light of the original wave length is accompanied by a small quantity of scattered light of lower frequency……". Sir C.V. Raman was awarded the Nobel Prize in Physics in 1930. There are two situations arising with Raman scattering: (1). scattered photons have a lower energy (Stokes scattering – phonon emitted); (2). scattered photons have a higher energy (anti-Stokes scattering – phonon absorbed), as shown in the Figure 3.1 [4]. The Stokes scattering intensity observed is usually higher than the corresponding anti-Stokes scattering intensity, which can be understood by a quantum mechanical description [5, 6].

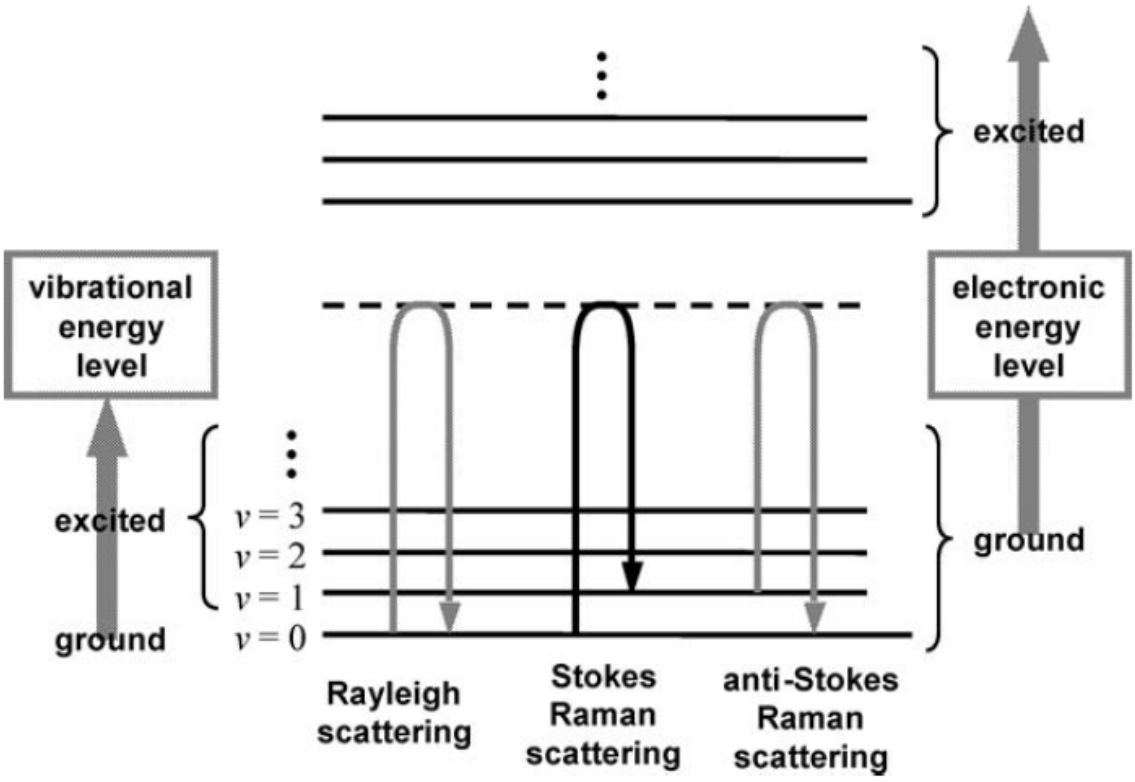

Figure 3.1. A schematic diagram for energy transitions during Rayleigh scattering, Stokes Raman scattering and anti-Stokes Raman scattering [4].

The intensity of the Raman scattered light is proportional to the square of the polarizability derivative with respect to the distortion co-ordinates, q_k [4-6]:

$$I \propto \left[\left(\frac{\partial p}{\partial q_k} \right)_{q_k=0} \right]^2 \tag{3.3}$$

In order to be Raman active ($I \neq 0$), the polarizability of the vibrational mode should not be at a maximum or minimum when atoms are at their equilibrium position ($q_k = 0$). Vibration of some bonds, such as C-C stretching, has small polarizability, but large differential polarizability $\left(\frac{\partial p}{\partial q_k} \right)_{q_k=0}$ values, so it is Raman active. Raman spectra are less influenced by water than IR spectra, as the differential polarizability $\left(\frac{\partial p}{\partial q_k} \right)_{q_k=0}$ of water molecule is small although their polarizability is large. The Raman intensity is related linearly to the number of chemical bonds in the samples; IR intensity is related exponentially in accordance with Lambert-Beer's Law.

The differential polarizability is a tensor quantity, and can be presented by three components in the form of a second-rank tensor [4-6]:

$$\left(\frac{\partial p}{\partial q_k} \right)_{q_k=0} = \begin{bmatrix} p'_x & 0 & 0 \\ 0 & p'_y & 0 \\ 0 & 0 & p'_z \end{bmatrix} \tag{3.4}$$

Thus, by measuring the angular dependence of the Raman intensity of certain vibrational mode, information on the degree of order of the sample can be obtained.

A Raman system typically consists of four major components [5-7]: (1). excitation source (laser); (2). sample illumination system and light collection optics; (3).

wavelength selector (filter or spectrophotometer); 4. detector (photodiode array, charge-coupled device or photomultiplier tubes). Spontaneous Raman scattering is weak. Only about 0.001% of the incident photons produce inelastic Raman scattering. In order to reduce Rayleigh scattering and obtain high-quality Raman spectra, instruments such as laser stop apertures, notch filters, tunable filters, double and triple spectrometric systems are used. Efforts have constantly been made on improving the Raman spectroscopy technique in many ways. For example, stimulated Raman [8], coherent anti-Stokes Raman (CARS) [9], resonance Raman (RR) [10], and surface-enhanced Raman spectroscopy (SERS) [11] have been developed.

Raman spectroscopy has been widely applied in the research on different materials such as polymers [4], liquid crystals [12-14], ceramics and metals [15-17], coal [18] and carbon nanotubes [19, 20] as well as graphene [20, 21]. Water being a weak Raman scatterer lends Raman to analysis and study of molecules in aqueous solution including the study of lyotropic liquid crystals and biomolecules. In this thesis, we study lyotropic chromonic liquid crystals by polarized Raman spectroscopy (PRS) in this Chapter and surface-enhanced Raman spectroscopy (SERS) in Chapter Six. Introduction to SERS and PRS will be given as follows.

3.1.2 Surface-enhanced Raman spectroscopy

Surface-enhanced Raman spectroscopy (SERS) as an advancement of Raman scattering overcomes some of the limitations of normal Raman scattering. Raman scattering is an inherently weak process. Fluorescence often accompanies Raman scattering and can sometimes overwhelm the bands in the spectrum and contaminate the spectrum rendering the data useless. However, Raman signals from molecules adsorbed on certain metal surfaces can be 3-6 orders of magnitude stronger than that from the same molecules in bulk volume [22]. This surface enhancement effect was first reported by

Fleischmann et al. in 1974, although the name "SERS" was not indicated [23]. The mechanisms of SERS are still under debate and not completely understood. Two mechanisms have been proposed so far: "electromagnetic enhancement (EM)", proposed by Jeanmarie and Van [24], and "chemical enhancement (CM)", proposed by Albrecht and Creighton [25], both in 1977. EM relates to the presence of surface plasmons on the substrate; CM involves charge transfer between the chemisorbed species and the metal surface [24, 25].

Excitation of the localized surface plasmon resonance of a metallic nanostructured surface or nanoparticle is the key of SERS [26-36]. Usually, enhancement is the largest for rough surfaces of 10-100 nm [26-28]. There are basically three kinds of SERS substrates: (1) metallic nanoparticle in suspension; (2) metallic nanoparticle immobilized on solid substrates; (3) nanostructures fabricated directly on solid substrates using nanolithography and template synthesis of nanostructures. Figure 3.2 gives some examples of SERS-active nanostructures [26]. Both the frequency and magnitude of the enhancement are strongly dependent on the shape, size and arrangement of the metallic nanofeatures. For single molecule and single particle system, the enhancement could be up to 10^{14}-10^{15}[31-34]. It is also recognized that systems of interacting particles produce the largest enhancements and a great deal of effort has been directed towards the study of the electrodynamics of coupled systems [22, 35, 36].

The types of metal on the surface are also important. The important parameter is both the imaginary and real part of the dielectric constant of the metal. Silver, gold and copper are mostly used, because the SERS phenomenon occurs most efficiently on their surfaces with the visible-wavelength excitation [22, 26, 28].

Studies of the thin film of a perylene diimide derivative by SERS will be shown in the Chapter Six.

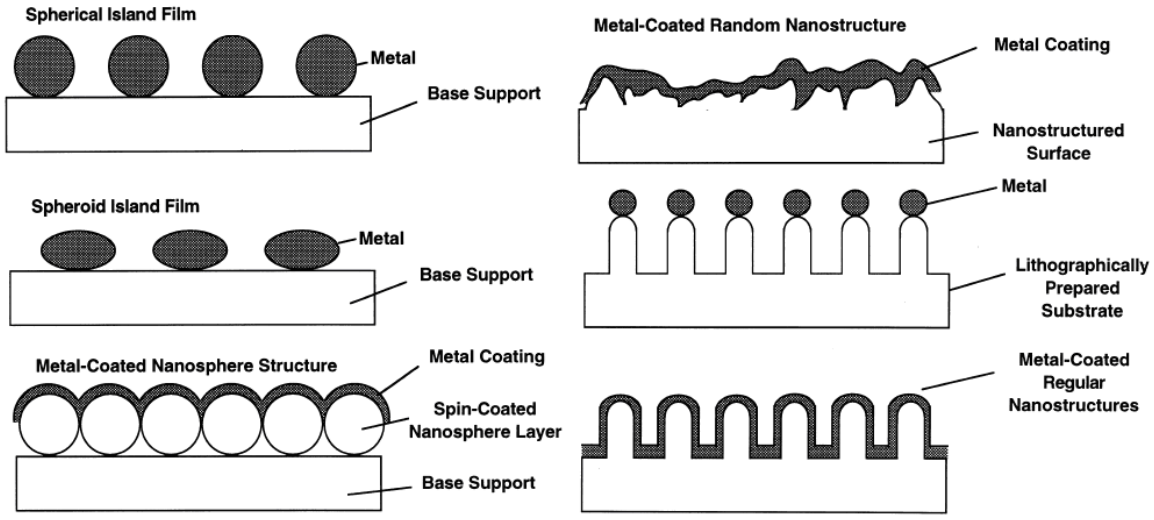

Figure 3.2. Various types of SERS-active nanostructures [26].

3.1.3 Polarized Raman spectroscopy

Polarized Raman spectroscopy (PRS) has been used to study and quantify the orientation [37-55] of polymer films [38-40], polymer fibers [41-43], crystals [44], carbon nanotubes [45-47], graphene [48], aligned liquid crystals [49-52], and biological systems [53-55] etc. In PRS, we measure scattered intensity with polarization parallel to the incident polarization ($I_{//}$) and that perpendicular to the incident polarization ($I_{\perp}$). Figure 3.3 illustrates the back-scattering geometry of PRS. By rotating the sample, $I_{//}$ and $I_{\perp}$ can be collected at various angles. The ratio of $I_{\perp}$ and $I_{//}$, called depolarization ratio, whose mathematical form incorporating order parameters, can be used to determine the values of order parameters of the aligned samples [4, 37, 50-52]. We will take a uniaxial liquid crystal as an example to derive the mathematical form of depolarization ratio [4, 50-52].

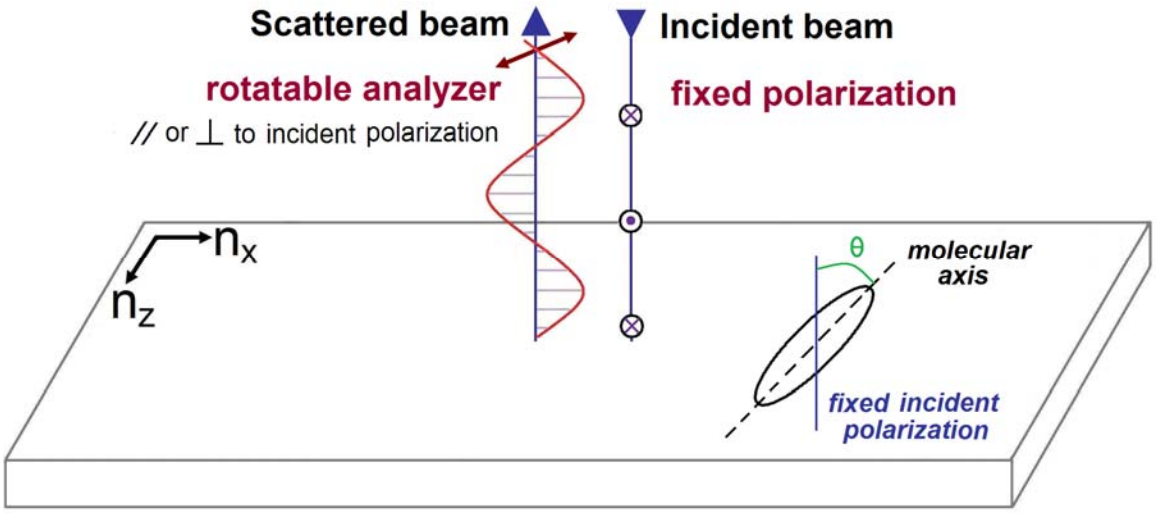

Figure 3.3. Polarized Raman scattering of back-scattering geometry. The n_x, n_z are the laboratory frame. Specimen is within the plane of n_x and n_z. θ is an angle between the axis of a uniaxial molecule and the incident polarization direction. By rotating the specimen, the angle θ can be varied.

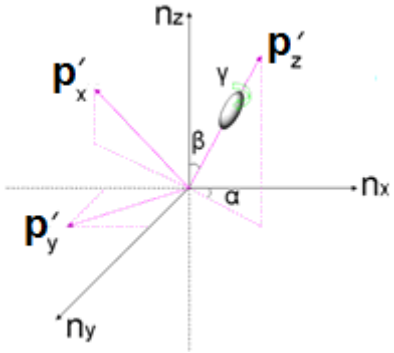

Figure 3.4. Rotation of a uniaxial molecule related to the laboratory frame. The p_x', p_y', and p_z' are three components of the Raman tensor. The n_x, n_y, n_z are the laboratory frame. The α, β and γ are Euler angles reflecting the orientational degrees of freedom.

Figure 3.4 shows the rotation of a uniaxial molecule in the nematic phase in the reference frame n_x, n_y and n_z. The p_x', p_y' and p_z' are three components of the Raman

tensor. The angles α, β and γ, called Euler angles, reflect the rotational degrees of freedom and are governed by an orientational distribution function (ODF) $f(\alpha,\beta,\gamma)$ containing order parameters of the system. The observed intensity is a function of the electrical field and ODF integrated over all possible orientations [56]:

$$I_{ji}(\theta) = I_0 \int_{\alpha}\int_{\beta}\int_{\gamma} f(\alpha,\beta,\gamma)(E_{ji}(\alpha,\beta,\gamma))^2 \, d\alpha d\beta d\gamma \tag{3.5}$$

The orientational distribution function (ODF) describes how the molecules are distributed among the possible directions about the director; hence it gives the probability of finding a molecule at some angle from the director [57, p. 72, 58, p. 57]. It can be approximated by expressing the exact ODF as a Fourier transform in terms of the Wigner rotation matrices, $D^L_{mn}(\alpha,\beta,\gamma)$ [59]:

$$f(\alpha,\beta,\gamma) = \sum_{L=0}^{\infty} \sum_{m=-L}^{+L} \sum_{n=-L}^{+L} \frac{2L+1}{8\pi^2} < D^{L^*}_{mn} > D^L_{mn}(\alpha,\beta,\gamma) \tag{3.6}$$

where *L*, *m*, and *n* represent the symmetry conditions under the rotations about α, β and γ, respectively. $< D^{L^*}_{mn} >$ is the statistical average of the Wigner function and * denotes the complex conjugate. The Wigner function can be expressed by small Wigner function, d^L_{mn} and is a function of β only:

$$D^L_{mn}(\alpha,\beta,\gamma) = e^{-im\alpha} d^L_{mn}(\beta) e^{-in\gamma} \tag{3.7}$$

For the homogeneous planar-aligned uniaxial sample, both assumption and simplification can be made as follows [50, 59]:

1. We are unable to distinguish between any 180° rotation due to the symmetry of the system, hence *L*, *m*, *n* must take even values.
2. In general the measured Raman bands are uniaxially symmetric ($p'_z > p'_x (= p'_y)$), so all the order parameters associated with rotation about γ are zero and only terms with n=0 are non-zero.

3. Provided that the sample has mirror symmetry in the xz, yz and xy planes, the imaginary components are eliminated.
4. Conventionally all the biaxial terms are set to zero for uniaxial systems, therefore only the order parameters $<P_{200}>$ and $<P_{400}>$ remain in the ODF.

Thus, the ODF can be simplified as a function of β, $<P_{200}>$ and $<P_{400}>$ [58, p. 58]:

$$f(\beta)=\frac{1}{8\pi^2}[1+\frac{5}{2}<P_{200}>(3\cos^2(\beta)-1)+\frac{9}{8}<P_{400}>(3-30\cos^2(\beta)+35\cos^4(\beta))] \tag{3.8}$$

Based on above assumption, the electric field equations for a homogeneous planar-aligned molecule also can be simplified as follows [50]:

$$E_{//zx}=p_z'[\cos(\beta)\cos(\theta)-\sin(\beta)\sin(\theta)]^2+p_x'[\sin(\beta)\cos(\theta)+\cos(\beta)\sin(\theta)]^2 \tag{3.9}$$

$$\begin{aligned}E_{\perp zx}&=p_z'[\cos(\beta)\cos(\theta)-\sin(\beta)\sin(\theta)][\cos(\beta)\sin(\theta)+\sin(\beta)\cos(\theta)]\\&+p_x'[\sin(\beta)\cos(\theta)+\cos(\beta)\sin(\theta)][\sin(\beta)\sin(\theta)-\cos(\beta)\cos(\theta)]\end{aligned} \tag{3.10}$$

where $E_{//}$ is used when the analyzed direction is parallel to the incident polarization; $E_{\perp}$ is used when the analyzed direction is perpendicular to the incident polarization. The angle θ is the angle between the long axis of the molecule and incident polarization direction.

As a result, we can obtain the simplified mathematical formula of the depolarization ratio *R(θ)* for all incident linear polarizations for a homogeneous planar-aligned uniaxial liquid crystal in the back-scattering geometry:

$$\begin{aligned}R(\theta)&=\frac{I_{\perp}(\theta)}{I_{//}(\theta)}=\frac{I_0\int_{\alpha,\beta,\gamma}f(\beta)(E_{\perp zx}(\beta,\theta))^2d\beta}{I_0\int_{\alpha,\beta,\gamma}f(\beta)(E_{//zx}(\beta,\theta))^2d\beta}\\&=\frac{(-1+r)^2(-56-40<P_{200}>-9<P_{400}>}{-56(3+4r+8r^2)+40<P_{200}>(-1+r)(3+4r)(1+3\cos(2\theta))}\\&\quad\frac{+105<P_{400}>\cos(4\theta))}{-3<P_{400}>(-1+r)^2(9+20\cos(2\theta)+35\cos(4\theta))}\end{aligned} \tag{3.11}$$

where $r=p_x'/p_z'$, is the differential polarizability ratio.

As described earlier, experimental values of depolarization ratio $R(\theta)$ can be obtained by PRS and after fitting them with the equation (3.11), $\langle P_{200} \rangle$, $\langle P_{400} \rangle$ and r can be generated.

3.2 Determination of the tautomeric structure by Raman scattering

SSY solutions with different concentrations were filled into the flat capillaries by capillary action in the isotropic phase, as described in the Chapter Two. A Kaiser 5000 Raman microscope, equipped with a 785 nm diode laser operating at 192 mW and with a 10x microscope objective, was used to measure Raman scattering as shown in Figure 3.5. Incident polarization was fixed, while the analyzer and sample stage were rotatable. Sample temperature was controlled by using a Linkam THM 600 hot stage with accuracy of 0.1°C. One advantage of using Raman spectroscopy is that scattering only from SSY will be collected, as water is not Raman active.

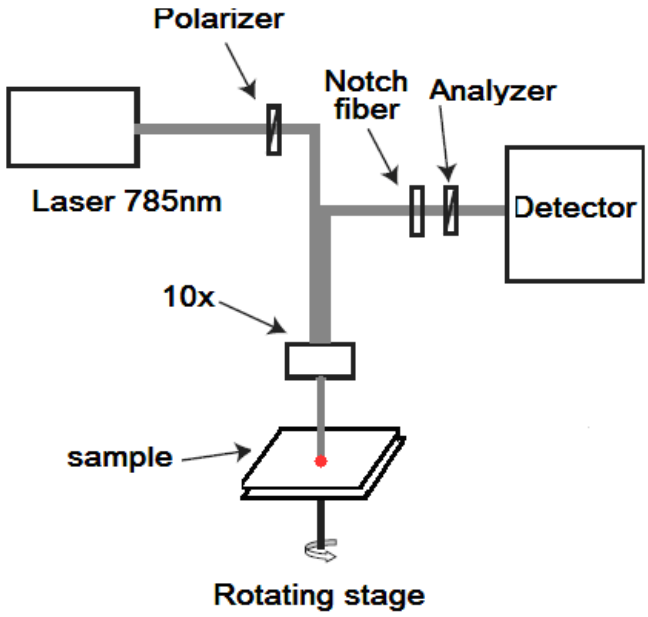

Figure 3.5. Back-scattering geometry of a Kaiser 5000 Raman microscope. It is equipped with a 785nm diode laser operating at 192mW with a 10x microscope objective. Spectra were collected by the HoloGRAMNS software coupled to a charge coupled detector (CCD). Expose time was set to 10 seconds and accumulations were set to 8 for Raman bands to exceed the strong background signals which mainly come from the dye itself. Incident polarization was fixed, while the analyzer and sample stage were rotatable.

Sunset Yellow is an azo dye with two possible tautomeric forms: the OH azo form and the NH hydrazone form (see Figure 3.6 for their tautomer structures). It was always mentioned as an OH azo form, and only recently it has been shown that the NH hydrzone structure prevails in both dilute solution and chromonic mesophases using NMR spectroscopy [60], which was later confirmed by the atomistic computer modeling [61].

We characterized the structure of the tautomer by identifying the existence of the peak assigned to N=N stretching mode in a Raman spectrum, which indicates the existence of azo group, thus differentiating whether the azo group is predominant or the hydrazone form is predominant. It is a simple but rigorous method to elucidate the

chemical structure, because the vibrational energy is unique to the type of chemical bond in a molecule [1]. The symmetric N=N vibration is usually forbidden or weak in the infrared, but expected to be strongly allowed in Raman with a very intense band [62, p. 197]. The effect of conjugation results in frequency lowering of the N=N mode. Usually, Raman spectra of azo compounds which contain N=N show a strong peak assigned to N=N stretching mode at around 1580-1300 cm^{-1} and the trans-azobenzene have an intense N=N stretching band at 1463-1380 cm^{-1} [62, p. 198]. But the assignment of the N=N stretch mode is more difficult for azo naphthols and azo naphthylamine than for azo benzene, as the N=N band is overlaid by not only aromatic ring vibration bands but also the C=N- stretching bands arising from the tautomerism effect [62, p. 199-201]. A characteristic strong band seen at 1390-1370 cm^{-1} is for most disubstituted naphthalenes including azo naphthols [62, p. 294].

A measured Raman spectrum for SSY in aqueous solution in the nematic N phase is presented in Figure 3.6. No significant changes with peak position and their relative intensities were observed compared to those in isotropic and chromonic M phases as shown in Figure 3.7. Quite strong peaks were observed between 1300 and 1580 cm^{-1} in Figures 3.6 and 3.7. One may assign one of the peaks between 1463-1380 cm^{-1} to N=N stretching band since the Raman peak assigned to N=N stretching in azo compound have been reported to position at around this frequency range as mentioned above.

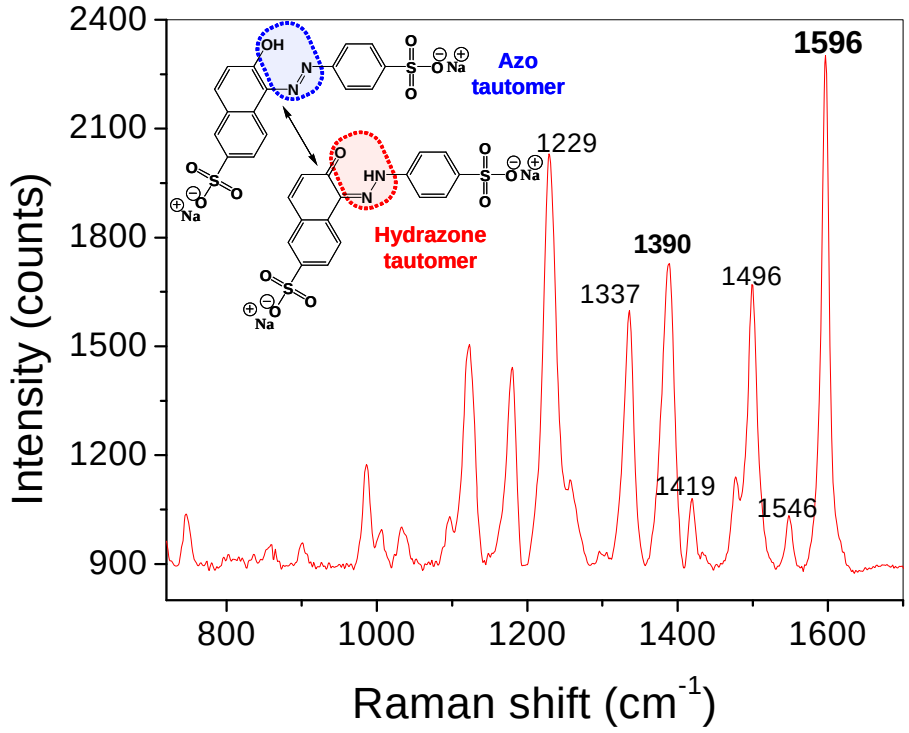

Figure 3.6. Raman spectrum of SSY in water (1.0M concentration at room temperature, under parallel polarization).

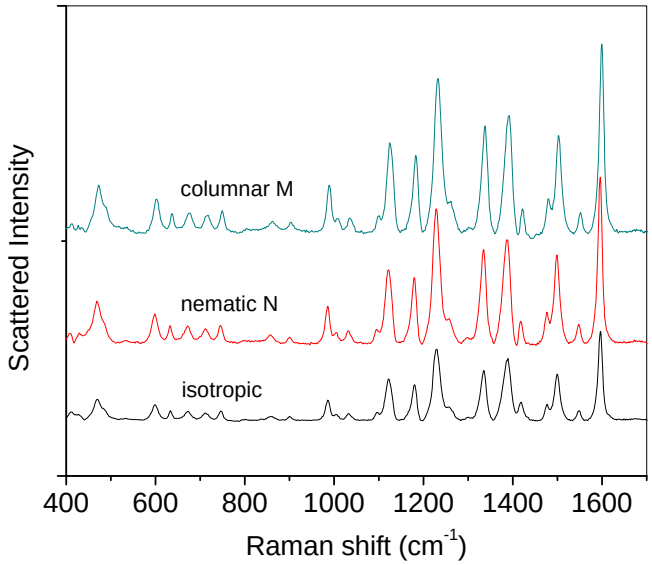

Figure 3.7. Raman spectra of SSY solutions in different phases (isotropic phase with 0.7M concentration, nematic N phase with 1.1M concentration, columar M phase with 1.7M concentration at room temperature, under parallel polarization). Making a solution with high concentrations (also very viscous) should avoid water evaporation carelly.

It is always quite complicated and not definite to assign vibration bands based on experimentally obtained spectrum, unless a quantum calculation for vibration energy is carried out in parallel. Nevertheless, we ruled out the possibility of these peaks being attributed to N=N stretching mode, based on the results in previous literatures: 1) It should be noted that the symmetric N=N stretching mode in the trans-azobenzene, usually, induces even more change in the polarizability than phenyl ring stretching does [62, 63]. Accordingly, the Raman peak from the symmetric N=N stretching is stronger than that from phenyl C-C stretching (the peak at 1596 cm^{-1} in Figure 3.6). However, all peaks between 1463 and 1380 cm^{-1} are weaker than the peak at 1596cm^{-1}. Moreover, the peak at 1390 cm^{-1} with medium strength is most possibly from naphthalene stretching. 2) The Orange II dye has very similar structure and tautomerism as SSY, while only one less sulfonyl group is attached to the naphthalene ring. It exists as hydrazone ($\geq$ 95%) in aqueous solution [64]. Its Raman spectrum is almost the same as that of SSY [64], which also confirms that the NH hydrazone structure of SSY is dominant in all phases. 3) UV-visible absorption spectrum of SSY dilute solution, which shows strong absorption around 480 nm [65] provides additional evidence that the NH hydrazone tautomer is dominant. Abbott et al [64] also reported that the OH group in azo structure has strong absorption between 400 nm and 440 nm, while the NH hydrazone form has strong absorption between 475 and 510 nm, which agrees well with our spectra.

To summarize, there is no strong scattering from N=N stretching vibration in Raman spectra, while UV-vis spectra shows strong NH hydrazone group, hence we conclude that the SSY molecules exist predominantly as the hydrazone tautomer in water.

3.3 Order parameters by polarized Raman scattering

We quantified the degree of orientation of the aggregate columns of SSY in nematic N phase by obtaining the expansion coefficients of orientational distribution function (ODF) from the measurement of polarized Raman scattering. In order to minimize defect structures which can distort accurate information on the orientation, the preparation of a monodomain sample is essential. Homogeneous planar alignment of SSY aqueous solution in the nematic N phase was achieved in the flat capillary, as described in Chapter Two. Using aligned samples, we measured two components of the polarized Raman intensities, $I_{//}$ and $I_{\perp}$, respectively. The back-scattering geometry of the polarized Raman spectroscopy on SSY planar aligned domain is shown in Figure 3.8. The orientational order parameters were obtained from the measurement of $I_{//}$ and $I_{\perp}$ by rotating the sample stage relative to the fixed direction of polarization of the incident beam, as shown in Figure 3.9.

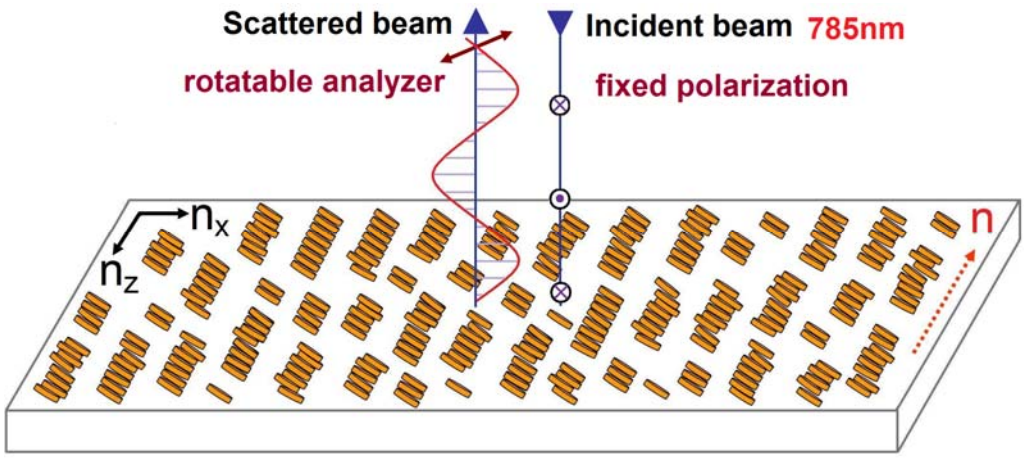

Figure 3.8. Back-scattering geometry of polarized Raman spectroscopy on SSY planar aligned domain.

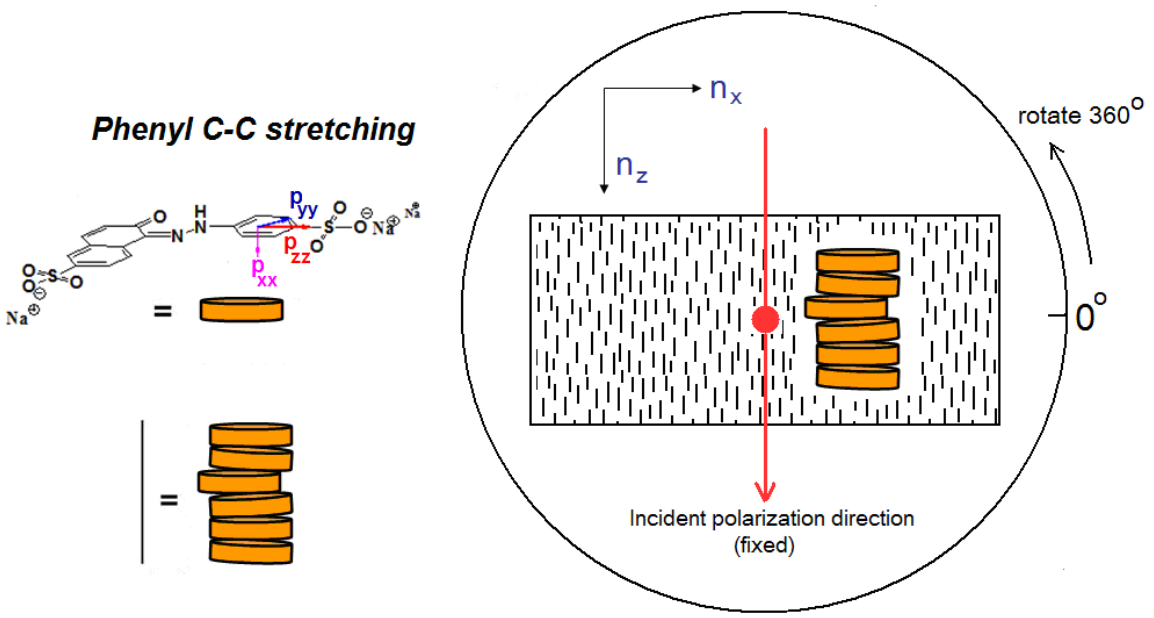

Figure 3.9. Top view of the directions of incident polarization, stacking columns and the Raman tensor of the C-C stretching mode of the phenyl ring when the flat capillary is rotated. The n_x, n_z are the reference frame. The red spot is the position for the laser.

Figure 3.10 gives an example of the evolution of the spectrum of $I_{//}(\theta)$ by rotating the sample stage. Figure 3.11 shows angular dependence of polarized Raman intensity values, both $I_{//}(\theta)$ and $I\perp(\theta)$, measured using macroscopically aligned SSY in nematic N phase (1.0 M at 24.5°C). We analyzed the intensity of the peak at 1596 cm^{-1}, which is assigned to phenyl C-C stretching, for the calculation of orientational order parameters of stacking columns since the symmetry of this vibration is thought to occur on the plane of molecular plates stacking into columns. Therefore, the column is considered to be perpendicular to the direction of the vibrational symmetry of phenyl ring. It is verified by the dependence of $I_{//}(\theta)$ and $I\perp(\theta)$. In Figure 3.11, $I_{//}(\theta)$ shows twofold rotational symmetry and has the highest value at $\theta = 90^\circ$ and 270° and its minimum is at $\theta = 0^\circ$ and 180°. This observation is in agreement with the determination of $\theta = 0^\circ$ when the director is parallel to the polarization direction of incident light and the director is collinear with the axis of column. As a result, when $\theta = 90^\circ$ and 270°, the symmetry axis of phenyl C-C

stretching is parallel to polarization direction of incident light, thus we can obtain the most intense peak at 1596 cm^{-1}. Therefore, SSY LCLC in a flat capillary has planar alignment with the director of aggregates or columns perpendicular to the long axis of the capillary, which is the flow direction.

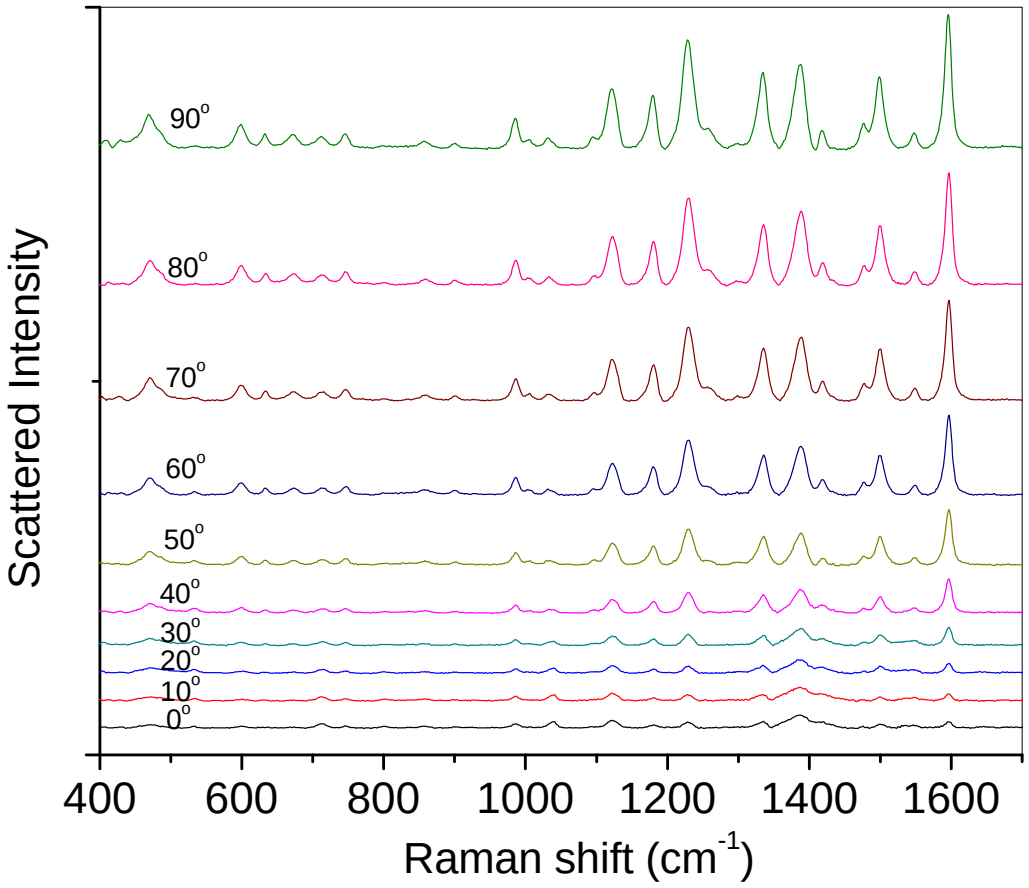

Figure 3.10. Evolution of the spectrum by rotating the sample stage. The sample is 1.1 M SSY at 28.8ºC.

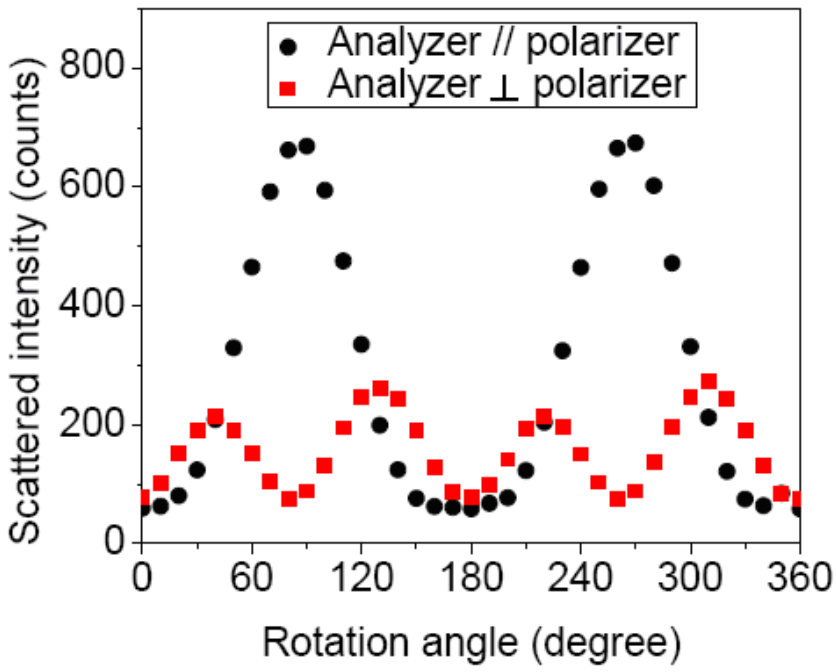

Figure 3.11. The intensity profile of phenyl C-C stretching at 1596 cm^{-1} in 1.0 M SSY aqueous solution at 24.5°C, taken at 10° intervals over an entire 360°.

Unlike rod-like or bent-core liquid crystals [49-52], chromonic liquid crystals have supramolecular stacking columns and it is their orientation distribution that needs to be explored. By measuring the polarized Raman scattering of the aligned SSY chromonic monodomain, both $\langle P_{200} \rangle$ and $\langle P_{400} \rangle$ can be determined, due to the fourth rank tensor nature of the scattering interaction. The depolarization ratio data in Figure 3.12 was obtained by the relation of $R(\theta) = I_{\perp}(\theta)/I_{//}(\theta)$. By fitting the experimentally obtained $R(\theta)$ to the theoretical equation (3.11) of $R(\theta, \langle P_{200} \rangle, \langle P_{400} \rangle, r)$ (derivation shown in the Introduction), where r is the differential polarizability, p_x'/p_z', three parameters $\langle P_{200} \rangle$, $\langle P_{400} \rangle$, and r can be calculated. The value of $\langle P_{200} \rangle$, $\langle P_{400} \rangle$, and r calculated from the fitting of $R(\theta)$ in Figure 3.12 is 0.41, 0.22, and -0.12, respectively. It should be noted that $\langle P_{200} \rangle$ and $\langle P_{400} \rangle$ values thus far represent the orientation distribution of the principal

axis of phenyl C-C stretching. Assuming there is no correlation between the orientational fluctuations of the column (relative to the director) and the orientational fluctuations of the molecules within the column relative to the aggregate axis, a simple relation between the order parameters of individual bonds and the whole chain (stacking column) [4], $P_{lmn,,chain} = P_{lmn}/[P_{lmn}(\cos \Omega)]$, can be used to get the order parameters of the stacking columns. Here, Ω is the angle between the principal axis of a Raman tensor and molecular chain (stacking column) axis, P_{lmn} is the Legendre polynomial with $P_{200}(x)=(3x^2-1)/2$ and $P_{400}(x)=(35x^4-30x^2+3)/8$ [4]. Therefore, Ω is the angle between the principal axis of the Raman tensor of phenyl C-C stretching mode and the long axis of the stacking columns. The phenyl C-C stretching mode is strongly polarized within the molecular plane and perpendicular to the columnar axis (director). Accordingly, Ω is 90°, $P_{200}(\cos \Omega)$ is -1/2, and $P_{400}(\cos \Omega)$ is 3/8. Therefore, for the stacking columns in the 1.0 M SSY chromonics at 24.5°C, $\langle P_{200} \rangle$ is 0.82, $\langle P_{400} \rangle$ is 0.43.

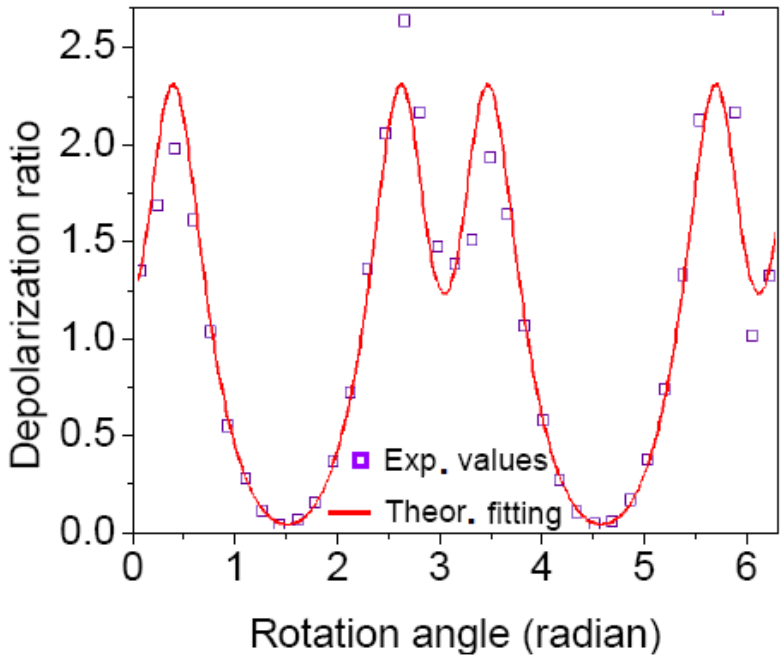

Figure 3.12. The depolarization ratio profile of phenyl C-C stretching at 1596 cm^{-1} in 1.0 M SSY aqueous solution at 24.5°C, taken at 10° intervals over an entire 360°. Fitting was done in Matlab with the angle expressed in radian.

Order parameters, both $<P_{200}>$ and $<P_{400}>$, depend on concentration and temperature. Table 3.1 presents order parameters of the stacking columns of the SSY chromonics with various concentrations at 28.8°C and 36.8°C. It shows $<P_{200}>$ and $<P_{400}>$ increase as concentration increases and decrease as temperature increases.

Table 3.1. Concentration and temperature dependence of order parameters of SSY chromonics (columns).

	Temp.	1.0 M	1.05 M	1.1 M
$<P_{200}>$	28.8°C	0.79 ± 0.02	0.82 ± 0.02	0.85 ± 0.03
$<P_{200}>$	36.8°C	0.78± 0.02	0.80 ± 0.02	0.84 ± 0.03
$<P_{400}>$	28.8°C	0.50 ± 0.08	0.58 ± 0.11	0.62 ± 0.02
$<P_{400}>$	36.8°C	0.49 ± 0.09	0.52 ± 0.13	0.59 ± 0.02

Figure 3.13 shows the temperature dependence of order parameters for 1.1 M SSY chromonic before reaching nematic-to-biphasic transition temperature T_{NB}. $<P_{200}>$ falls into the range of 0.75 and 0.90 in chromonic nematic N phase, which is higher than 0.6~0.75 by absorption measurement [65] and 0.54~0.65 by NMR measurement [60] in the same phase, but closer to 0.72~0.9 by the x-ray measurement [66] and to 0.7~0.8 predicted by Taylor and Herzfeld's hard-particle model for reversibly self-assembling rodlike polydiperse system for volume faction between 0.24 to 0.28 (between 1.0M to 1.2M) at phase transition [67, 68].

The measured $<P_{200}>$ (or S) values were fitted by an empirical formula based on the mean field theory where the temperature dependence of order parameter is described over the entire nematic N temperature range by the simple relation $S = S_0(1 - T/T_{NB})^{\eta}$ [69, 70].

For 1.1M SSY chromonics, S_0 is about 0.87, η is about 0.044. Compared to lots of thermotropic nematic liquid crystals with η between 0.1 and 0.2 [69, 70], η for SSY chromonics is small, that is, S has less temperature dependence. It should be pointed out that chromonics experience a wider nematic-isotropic coexistent region before reaching isotropic phase than thermotropics, so the order parameters can be predicted to continue to decrease in this coexistent region.

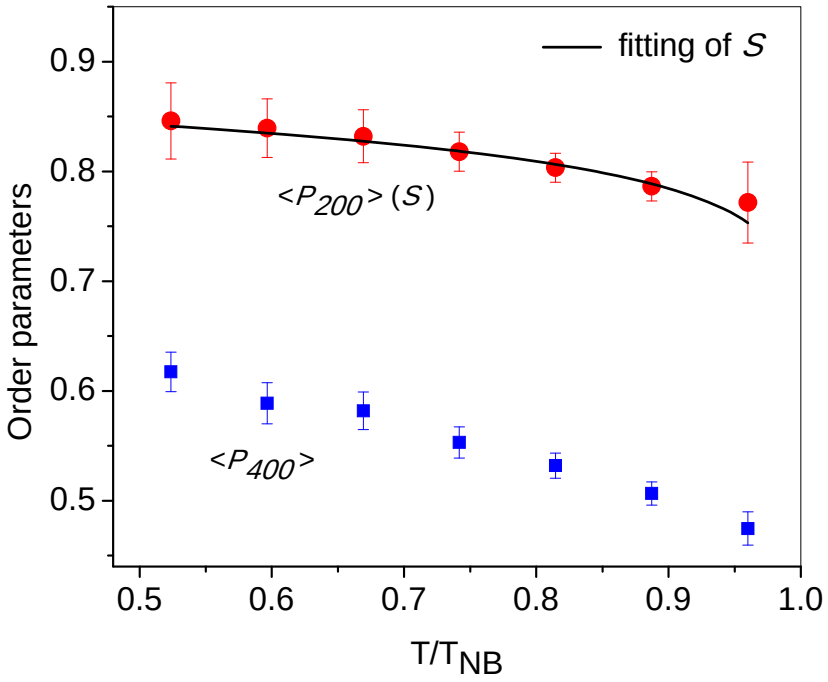

Figure 3.13. Temperature dependence of order parameters of 1.1 M SSY chromonics. Red points with error bars indicate the values of $<P_{200}>(=S)$ and black line is the fitting of them with equation $S=S_0(1-T/T_{NB})^{\eta}$. T_{NB} here is the nematic-biphasic transition temperature. T_{NB} is about 52.8°C for 1.1M SSY chromonics. Blue squares with error bar indicate the values of $<P_{400}>$.

3.4 Conclusions

In conclusion, the tautomeric structure of SSY in water was found to be predominantly hydrazone in isotropic, nematic and columnar phases. A homogeneously planar aligned SSY LCLC sample was obtained in a flat capillary. An unusual phenomenon that columns were aligned perpendicular to the flow direction was observed, which is due to the special combination of the size and geometry of the flat capillary, elastic properties of the SSY LCLC and interaction between capillary inner surface and SSY LCLC. Polarized Raman spectroscopy provides a means to determine the second and fourth rank order parameters, of which both temperature and concentration dependence in the nematic N phase have been studied. $<P_{200}>$ values are higher than those of conventional thermotropic liquid crystals, probably due to the existence of the wide biphasic region and thus being far away from the isotropic phase. $<P_{200}>$ values are higher than those determined by absorption measurement and NMR measurement, but closer to those determined by x-ray measurement and the prediction from the model by Taylor and Herzfeld's for the reversibly self-assembling rodlike polydiperse system [67, 68].

3.5 References

[1] Steele, D. Theory of Vibrational Spectroscopy. **1971**, Saunders: Philadelphia, 226 pp.

[2] Alpert, N. L., Keiser, W. E., and Szymanski, H. A. IR: Theory and Practice of Infrared Spectroscopy. **1970**, Plenum Press: New York, 380 pp.

[3] Raman, C. V., and Krishnan, K. S. A new type of secondary radiation. Nature **1928**, 121, 501-502.

[4] Tanaka, M., and Young, R. J. Review: Polarized Raman spectroscopy for the study of molecular orientation distributions in polymers. Journal of Materials Science **2006**, 41(3), 963-991.

[5] Laserna, J. J. (ed.) Modern Techniques in Raman Spectroscopy. **1996**, John Wiley & Sons: Chichester, 446 pp.

[6] Banwell C. N., and Mccash, E. M. Fundamentals of Molecular Spectroscopy. **1994**, McGraw-Hill: London, 416 pp.

[7] Raman Spectroscopy Basics from Princetion Instruments: http://content.piacton.com/Uploads/Princeton/Documents/Library/UpdatedLibrary/Raman_Spectroscopy_Basics.pdf

[8] Bloembergen, N. Stimulated Raman effect. American Journal of Physics **1967**, 35(11), 989-1023.

[9] Spiro, T. G., and Czernuszewicz, R. S. Resonance Raman spectroscopy. Physical Methods in Bioinorganic Chemistry **2000**, 59-119.

[10] Day, J. P. R., Domke, K. F., Rago, G., Kano, H., Hamaguchi, H.-O, Vartiainen, E. M., and Bonn, M. Quantitative coherent anti-Stokes Raman scattering (CARS) microscopy. Journal of Physical Chemistry B **2011**, 115(24), 7713-7725.

[11] Moskovits, M. Surface-enhanced Raman spectroscopy: A brief retrospective. Journal of Raman Spectroscopy **2005**, 36(6/7), 485-496.

[12] Bulkin, B. J. Infrared and Raman spectroscopy of liquid crystals. Applied Spectroscopy **1976**, 30(3), 261-269.

[13] Hayashi, N. Raman applications in liquid crystals. In: Raman Spectroscopy for Soft Matter Applications **2009**, 145-179, 301 pp.

[14] Fontana, M. P. Raman and IR fluctuation spectroscopy of liquid crystals. NATO ASI Series, Series C: Mathematical and Physical Sciences **1994**, 431(Molecular Dynamics of Liquid Crystals), 403-430.

[15] Osada, M., and Kakihana, M. Recent advances in Raman spectroscopy and their applications to ceramics. Seramikkusu **2006**, 41(12), 1026-1031.

[16] Helsen, J. A. Raman spectroscopy in metals and ceramics. Sonderbaende der Praktischen Metallographie **1996**, 27, 43-45.

[17] Ren, B., Liu, G.-K., Lian, X.-B., Yang, Z.-L., and Tian, Z.-Q. Raman spectroscopy on transition metals. Analytical and Bioanalytical Chemistry **2007**, 388(1), 29-45.

[18] Potgieter-Vermaak, S., Maledi, N., Wagner, N., van Heerden, J. H. P., van Grieken, R., and Potgieter, J. H. Raman spectroscopy for the analysis of coal: a review. Journal of Raman Spectroscopy **2011**, 42(2), 123-129.

[19] Jorio, A., Saito, R., Dresselhaus, G., and Dresselhaus, M. S. Determination of nanotubes properties by Raman spectroscopy. Philosophical Transactions of the Royal Society of London, Series A: Mathematical, Physical and Engineering Sciences **2004**, 362(1824), 2311-2336.

[20] Dresselhaus, M. S., Jorio, A., and Saito, R. Characterizing graphene, graphite, and carbon nanotubes by Raman spectroscopy. Annual Review of Condensed Matter Physics **2010**, 1, 89-108.

[21] Ferrari, A. C., Meyer, J. C., Scardaci, V., Casiraghi, C., Lazzeri, M., Mauri, F., Piscanec, S., Jiang, D., Novoselov, K. S., Roth, S., and Geim, A. K. Raman Spectrum of Graphene and Graphene Layers. Physical Review Letters **2006**, 97(18), 187401/1-187401/4.

[22] Campion, A., Kambhampati, P. Surface-enhanced Raman scattering. Chemical Society Reviews **1998**, 27(4), 241-250.

[23] Fleischmann, M., Hendra, P. J. and McQuillan, A. J., Raman spectra of pyridine adsorbed at a silver electrode. Chemical Physics Letter, **1974**, 26, 163–166.

[24] Jeanmaire, D. L., Van D., and Richard, P. Surface Raman spectroelectrochemistry. Part I. Heterocyclic, aromatic, and aliphatic amines adsorbed on the anodized silver electrode. Journal of Electroanalytical Chemistry and Interfacial Electrochemistry **1977**, 84(1), 1-20.

[25] Albrecht, M. G., and Creighton, J. A. Anomalously intense Raman spectra of pyridine at a silver electrode. Journal of the American Chemical Society **1977**, 99(15), 5215-5217.

[26] Vo-Dinh, T. Surface-enhanced Raman spectroscopy using metallic nanostructures. Trends in Analytical Chemistry **1998**, 17(8+9), 557-582.

[27] Stiles, P. L., Dieringer, J. A., Shah, N. C., and van Duyne, R. P. Surface-enhanced Raman spectroscopy. Annual Review of Analytical Chemistry **2008**, 1, 601-626.

[28] Fan, M. Andrade, G. F. S., and Brolo, A. G. A review on the fabrication of substrates for surface enhanced Raman spectroscopy and their applications in analytical chemistry. Analytica Chimica Acta **2011**, 693(1-2), 7-25.

[29] Lee, P. C., and Meisel, D. Adsorption and surface-enhanced Raman of dyes on silver and gold sols. Journal of Physical Chemistry **1982**, 86(17), 3391-3395.

[30] Cao, Y. C., Jin, R., and Mirkin, C. A. Nanoparticles with Raman spectroscopic fingerprints for DNA and RNA detection. Science **2002**, 297(5586), 1536-1540.

[31] Nie, S. M., and Emory, S. R. Probing single molecules and single nanoparticles by surface-enhanced Raman scattering. Science **1997**, 275(5303), 1102-1106.

[32] Qian, X.-M., and Nie, S. M. Single-molecule and single-nanoparticle SERS: from fundamental mechanisms to biomedical applications. Chemical Society Reviews **2008**, 37(5), 912-920.

[33] Doering, W. E., and Nie, S. M. Single-molecule and single-nanoparticle SERS: Examining the roles of surface active sites and chemical enhancement. Journal of Physical Chemistry B **2002**, 106(2), 311-317.

[34] Kneipp, K., Wang, Y., Kneipp, H., Perelman, L. T., Itzkan, I., Dasari, R. R., and Feld, M. S. Single molecule detection using surface-enhanced Raman scattering (SERS). Physical Review Letters **1997**, 78(9), 1667-1670.

[35] Taylor, R. W., Lee, T.-C., Scherman, O. A., Esteban, R., Aizpurua, J., Huang, F. M., Baumberg, J. J., and Mahajan, S. Precise subnanometer plasmonic junctions for SERS within gold nanoparticle assemblies using cucurbit[n]uril “glue”. ACS Nano **2011**, 5(5), 3878-3887.

[36] Kneipp, K., Kneipp, H., Corio, P., Brown, S. D. M., Shafer, K., Motz, J., Perelman, L. T., Hanlon, E. B., Marucci, A., and Dresselhaus, G., et al. Surface-enhanced and normal Stokes and anti-Stokes Raman spectroscopy of single-walled carbon nanotubes. Physical Review Letters **2000**, 84(15), 3470-3473.

[37] Lagugné-Labarthet, F. Polarized measurements in Raman microscopy. Annual Reports on the Progress of Chemistry, Section C: Physical Chemistry **2007**, 103, 326-350.

[38] Purvis, J., Bower, D. I., and Ward, I. M. Molecular orientation in poly (ethylene terephthalate) studied by polarized Raman scattering. Polymer **1973**, 14(8), 398-400.

[39] Tanaka, M., and Young, R. J. Molecular orientation distributions in uniaxially oriented poly(L-lactic acid) films determined by polarized Raman spectroscopy. Macromolecules **2006**, 39(9), 3312-3321.

[40] Park, M. S., Wong, Y. S., Park, J. O., Venkatraman, S. S., and Srinivasarao, M. A simple method for obtaining the information of orientation distribution using polarized Raman spectroscopy: Orientation study of structural units in poly(lactic acid). Macromolecules **2011**, 44(7), 2120-2131.

[41] Citra, M. J., Chase, D. B., Ikeda, R. M., and Gardner, K. H. Molecular orientation of high-density polyethylene fibers characterized by polarized Raman spectroscopy. Macromolecules **1995**, 28(11), 4007-4012.

[42] Frisk, S., Ikeda, R. M., Chase, D. B., and Rabolt, J. F. Determination of the molecular orientation of poly (propylene terephthalate) fibers using polarized Raman spectroscopy: a comparison of methods. Applied Spectroscopy **2004**, 58(3), 279-286.

[43] Thomas, G. J., Jr., Benevides, J. M., Overman, S. A., Ueda, T., Ushizawa, K., Saitoh, M., and Tsuboi, M. Polarized Raman spectra of oriented fibers of A DNA and B DNA: anisotropic and isotropic local Raman tensors of base and backbone vibrations. Biophysical Journal **1995**, 68(3), 1073-88.

[44] Amer, M. S., Maguire, J., Cai, L., Biggers, R., Busbee, J., and LeClair, S. R. Local grain orientation and strain in polycrystalline YBa2Cu3O7-δ superconductor thin films measured by Raman spectroscopy. Journal of Applied Physics **2001**, 89(12), 8030-8034.

[45] Duesberg, G. S., Loa, I., Burghard, M., Syassen, K., and Roth, S. Polarized Raman spectroscopy on isolated single-wall carbon nanotubes. Physical Review Letters **2000**, 85(25), 5436-5439.

[46] Gommans, H. H., Alldredge, J. W., Tashiro, H., Park, J., Magnuson, J., and Rinzler, A. G. Fibers of aligned single-walled carbon nanotubes: Polarized Raman spectroscopy. Journal of Applied Physics **2000**, 88(5), 2509-2514.

[47] Venkateswaran, U. D., Rao, A. M., Richter, E., Menon, M., Rinzler, A., Smalley, R. E., and Eklund, P. C. Probing the single-wall carbon nanotube bundle: Raman scattering under high pressure. Physical Review B: Condensed Matter and Materials Physics **1999**, 59(16), 10928-10934.

[48] Liang, Q., Yao, X., Wang, W., Liu, Y., and Wong, C. P. A three-dimensional vertically aligned functionalized multilayer graphene architecture: An approach for graphene-based thermal interfacial materials. ACS Nano **2011**, 5(3), 2392–2401.

[49] Jen, S., Clark, N. A., Pershan, P. S., and Priestley, E. B. Polarized Raman scattering studies of orientational order in uniaxial liquid crystalline phases. Journal of Chemical Physics **1977**, 66(10), 4635-4661.

[50] Southern, C. D., and Gleeson, H. F. Using the full Raman depolarization in the determination of the order parameters in liquid crystal systems. European Physical Journal E: Soft Matter **2007**, 24(2), 119-127.

[51] Gleeson, H. F., Southern, C. D., Brimicombe, P. D., Goodby, J. W., and Gortz, V. Optical measurements of orientational order in uniaxial and biaxial nematic liquid crystals. Liquid Crystals **2010**, 37(6-7), 949-959.

[52] Park, M. S., Yoon, B.-J., Park, J. O., Prasad, V., Kumar, S., and Srinivasarao, M. Raman scattering study of phase biaxiality in a thermotropic bent-core nematic liquid crystal. Physical Review Letters **2010**, 105, 027801.

[53] Pezolet, M., Pigeon, M., Menard, D., and Caille, J. P. Raman spectroscopy of cytoplasmic muscle fiber proteins: Orientational order. Biophysical Journal **1988**, 53(3), 319-325.

[54] Tsuboi, M., Overman, S. A., and Thomas, G. J. Jr. Orientation of tryptophan-26 in coat protein subunits of the filamentous virus Ff by polarized Raman microspectroscopy. Biochemistry **1996**, 35(32), 10403-10410.

[55] Thomas, G. J. Jr. Raman spectroscopy of protein and nucleic acid assemblies. Annual Review of Biophysics and Biomolecular Structure **1999**, 28, 1-27.

[56] Jones, W. J., Thomas, D. K., Thomas, D. W., and Williams, G. Raman scattering studies of homogeneous and twisted-nematic liquid crystal cells and the determination of $<P_2>$ and $<P_4>$ order parameters. Journal of Molecular Structure **2002**, 614(1-3), 75-85.

[57] Priestley, E. B., Wojtowicz, P. J., and Sheng, P. (ed.) Introduction to Liquid Crystals. **1975**, Plenum Press: New York and London, pp 356.

[58] Dunmur, D. A., Fukuda, A., and Luckhurst, G. R. Physical Properties of Liquid Crystals: Nematics. **2001**, Inspec: London, 671 pp.

[59] van Gurp, M. The use of rotation matrixes in the mathematical description of molecular orientations in polymers. Colloid and Polymer Science **1995**, 273(7), 607-625.

[60] Edwards, D. J., Jones, J. W., Lozman, O., Ormerod, A. P., Sinty-ureva, M., and Tiddy, G. J. T. Chromonic liquid crystal formation by Edicol Sunset Yellow. Journal of Physical Chemistry B **2008**, 112, 14628-14636.

[61] Chami, F., and Wilson, M. R. Molecular order in a chromonic liquid crystal: A molecular simulation study of the anionic azo dye Sunset Yellow. Journal of the American Chemical Society **2010**, 132, 7794-7802.

[62] Lin-Vien, D., Colthup, N. B., Fateley, W. G., and Grasselli, J. G. The Handbook of Infrared and Raman Characteristic Frequencied of Organic Molecules. **1991**, Academic: San Diego, 503 pp.

[63] Trotter, P. J. Azo dye tautomeric structures determined by laser-Raman spectroscopy. Applied Spectroscopy **1977**, 31(1), 30-35.

[64] Abbott, L. C., Batchelor, S. N., Oakes, J., Gilbert, B. C., Whitwood, A. C., Lindsay Smith, J. R., and Moore, J. N. Experimental and computational studies of structure and bonding in parent and reduced forms of the azo dye orange II. Journal of Physical Chemistry A **2005**, 109(12), 2894-2905.

[65] Horowitz, V. R., Janowitz, L. A., Modic, A. L., Heiney, P. A., and Collings, P. J. Aggregation behavior and chromonic liquid crystal properties of an anionic monoazo dye. Physical Review E: Statistical, Nonlinear, and Soft Matter Physics **2005**, 72, 041710/1-041710/10.

[66] Luoma, R. J. X-Ray Scattering and Magnetic Birefringence Studies of Aqueous Solutions of Chromonic Molecular Aggregates. Ph.D. Thesis, Brandeis University, **1995**, 104 pp.

[67] Taylor, M. P., and Herzfeld, J. A model for nematic and columnar ordering in a self-assembling system. Langmuir **1990**, 6(5), 911-915.

[68] Taylor, M. P., and Herzfeld, J. Shape anisotropy and ordered phases in reversibly assembling lyotropic systems. Physical Review A **1991**, 43(4), 1892.

[69] Maier, W., and Saupe, A. A simple molecular theory of the nematic crystalline-liquid state. Zeitschrift fuer Naturforschung **1958**, 13a, 564-566.

[70] Haller, I. Thermodynamic and static properties of liquid crystals. Progress in Solid State Chemistry **1975**, 10, Pt.2, 103-118.

CHAPTER 4

PREDICTION OF THE FLOW BEHAVIOR OF SUNSET YELLOW CHROMONICS

4.1 Introduction to the flow behavior of uniaxial nematic liquid crystals

Isotropic liquids exhibit flow induced birefringence due to the orientation of the constituent molecules. The long axes of molecules align preferentially at an angle between the direction of flow and the velocity gradient [1]. The angle θ_0 between the preferred molecular axis and direction of flow, called the flow-alignment angle. In this chapter, we will explore the flow behavior of uniaxial nematic chromonic liquid crystals.

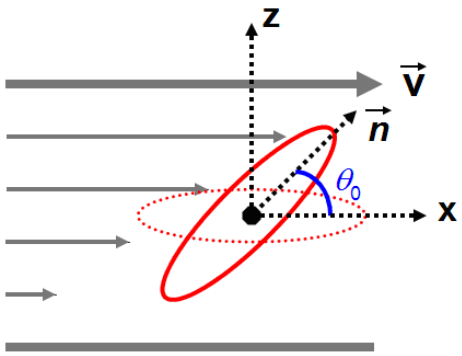

Figure 4.1. Schematics of rod-like molecules under steady shear, in which x is the flow direction, z is the velocity gradient direction, ***n*** is director vector, θ_0 is the flow alignment angle.

The Ericksen-Leslie theory for uniaxial nematic liquid crystals introduces six viscosity coefficients α_i (called the Leslie coefficients) for the viscous stress tensor, which determines the continuous hydrodynamics, as shown in equation below [2-7]:

$$\overline{\sigma_{ij}} = \alpha_1 n_i n_j n_k n_l A_{kl} + \alpha_2 n_i N_j + \alpha_3 n_j N_i + \alpha_4 A_{ij} + \alpha_5 n_i n_k A_{kj} + \alpha_6 n_j n_k A_{ki} \qquad (4.1)$$

where $\boldsymbol{n}$ is the director, A_{ij} is symmetric part of the second-rank tensor of the velocity gradient, $\boldsymbol{N} = \dot{\boldsymbol{n}} - \boldsymbol{W} \cdot \boldsymbol{n}$ is the corotational time derivative of the director. However, only two of these Leslie coefficients appear in the director equation for shear flow [2-7]:

$$\boldsymbol{0} = (\boldsymbol{1} - \boldsymbol{nn}) \cdot [\boldsymbol{h} + (a_2 - a_3)\boldsymbol{N} - (a_2 + a_3)\boldsymbol{D} \cdot \boldsymbol{n}] \tag{4.2}$$

where $\boldsymbol{D}$ is the symmetric strain rate tensor, $\boldsymbol{W}$ is the skew symmetric spin tensor, and $\boldsymbol{h}$ is the molecular field. The difference of α_3 and α_2 is the rotational viscosity, γ_1, while sum of them is the irrotational torque coefficient, γ_2, denoted by:

$$\gamma_1 = \alpha_3 - \alpha_2 \tag{4.3}$$

$$\gamma_2 = \alpha_2 + \alpha_3 \tag{4.4}$$

The flow-alignment angle θ_0 is a function of the tumbling parameter, λ [2-7]:

$$\theta_0 = 0.5 \cos^{-1}(1/\lambda) \tag{4.5}$$

where,

$$\lambda = -\frac{\gamma_2}{\gamma_1} = \frac{\alpha_2 + \alpha_3}{\alpha_2 - \alpha_3} \tag{4.6}$$

There are three possibilities [8]:

1). $0 \geq \alpha_3 \geq \alpha_2$, $\lambda > 1$, flow aligned;

2). $\alpha_3 \geq 0 \geq \alpha_2$, $-1 < \lambda < 1$, tumbling;

3). $\alpha_3 \geq \alpha_2 \geq 0$, $\lambda < -1$, flow aligned.

For case 2), $-1 < \lambda < 1$, there is no steady-state solution for the flow-alignment angle to exist, and the hydrodynamic torque acts to continuously rotate the director in a direction opposite to the flow alignment direction, thus leading to tumbling where the director continuously rotates in the in the plane that contains the velocity and the velocity gradient. In fluid dynamics, vorticity is the curl of the fluid velocity and is a vector quantity, whose direction is along the axis of the fluid's rotation [9 (p. 383)].

As the tumbling parameter λ has a large effect on the flow behavior on nematic liquid crystals in a shearing flow, it would be useful to predict the value of λ from molecular theory. Molecular theories by Kuzuu and Doi [10, 11] predict tumbling behavior of rod-like polymer nematic liquid crystals at lower shear rates, which was first confirmed by experimental studies of Srinivasarao and Berry, Burghardt and Fuller, and others [12-14]. Kuzuu and Doi also derived the Ericksen-Leslie equation from Doi's equation, and determined the Leslie coefficients written in terms of three parameters: order parameters $<P_{200}>$ and $<P_{400}>$ and tumbling parameter λ [7, 10]:

$$
\begin{aligned}
\alpha_1 &= -2\bar{\eta}L^2(a) < P_{400} > \\
\alpha_2 &= -\bar{\eta}L(a)(1+\frac{1}{\lambda}) < P_{200} > \\
\alpha_3 &= -\bar{\eta}L(a)(1-\frac{1}{\lambda}) < P_{200} > \\
\alpha_4 &= \bar{\eta}L^2(a)\frac{2}{35}(7-5 < P_{200} > -2 < P_{400} >) \\
\alpha_5 &= \bar{\eta}L(a)[\frac{1}{7}L(a)(3 < P_{200} > +4 < P_{400} >) + < P_{200} >] \\
\alpha_6 &= \bar{\eta}L(a)[\frac{1}{7}L(a)(3 < P_{200} > +4 < P_{400} >) - < P_{200} >]
\end{aligned}
\tag{4.7}
$$

where $\bar{\eta} = \frac{ck_BT}{2\overline{D_r}}$, $L(a) = \frac{a^2-1}{a^2+1}$, where c is number of molecule in unit volume, k_B is Boltzmann constant, $\overline{D_r}$ is a rotational diffusion coefficient which depends on the concentration, molecular weight and temperature, and a is the molecular aspect ratio [7, 10].

A similar molecular theory has been applied to thermotropic small-molecule liquid crystals composed of ellipsoidal particles. Specifically, Archer and Larson [15] and Kroenger and Sellers [8, 16] have derived an approximate analytical expression for λ in

terms of the molecular aspect ratio a, and order parameters $<P_{200}>$ and $<P_{400}>$ in the limit of slow flows [15]:

$$\lambda = -\frac{\gamma_2}{\gamma_1} = \frac{\alpha_2 + \alpha_3}{\alpha_2 - \alpha_3} = L(a)\frac{(5 < P_{200} > +16 < P_{400} > +14)}{35 < P_{200} >} \quad (4.8)$$

Thus, the flow behavior of nematics is not universal; it depends on the shape of the liquid crystal molecules and their orientation distribution with respect to the director. For small-molecule nematics away from critical points, the orientation distribution of molecules about the director is assumed to be mostly unperturbed by flow, except at extremely high shear rates (though it could be applied to polymeric nematics in the limit of very slow flows), $<P_{200}>$ and $<P_{400}>$ will be close to their equilibrium values [14-16]. It is therefore possible to use values of $<P_{200}>$ and $<P_{400}>$ measured in the absence of flow to calculate the λ and predict the flow behavior.

4.2 Calculation of the aspect ratio of SSY aggregates

In order to predict the flow behavior of SSY chromonics, molecular aspect ratio a, and order parameters need to be determined. All these parameters are both temperature and concentration dependent. Order parameters $<P_{200}>$ and $<P_{400}>$ of 1.1M SSY chromonics as a function of temperature have been measured from polarized Raman studies as described in the previous chapter. The calculation of molecular aspect ratio a as a function of temperature is shown below.

Kumar et al [17] reported the x-ray investigation on SSY chromonics. The intra-molecular spacing, d_{in}, is about 0.332nm; the aggregation diameter, D_a, is about 1.34nm. Both are independent of temperature and concentration. The linearity of $\ln \xi_{//}$ vs. $1/T$ reveals an Arrhenius behavior, as shown in Figure 4.2.a, described by the fits to the equation

$$\xi_{//} = \xi_0 \exp(\frac{E}{2k_B T}) \tag{4.9}$$

$\xi_{//}$ is the longitudinal correlation length of the aggregate/column and is measured by x-ray, E is the "scission" energy, determined from the Arrhenius thermal evolution of $\xi_{//}$, and ξ_0 represents the asymptotic value of $\xi_{//}$ and is assumed to be 0.486nm in the nematic N phase [17]. Figure 4.2.b and Figure 4.2.c show the concentration dependence of $\xi_{//}$ and E at room temperature, according to which, values of $\xi_{//}$ and E for 1.1M (33.2 wt%) at room temperature are estimated to be 3.8nm and 4.2 k_BT, respectively. By using these two values and the equation (4.9), ξ_0 is calculated to be 0.465nm, close to 0.486nm in reference [17]. The temperature dependence of $\xi_{//}$ can be derived by using ξ_0=0.486nm and E=4.2 k_BT:

$$\ln \xi_{//} = -0.72 + 625.8\frac{1}{T} \tag{4.10}$$

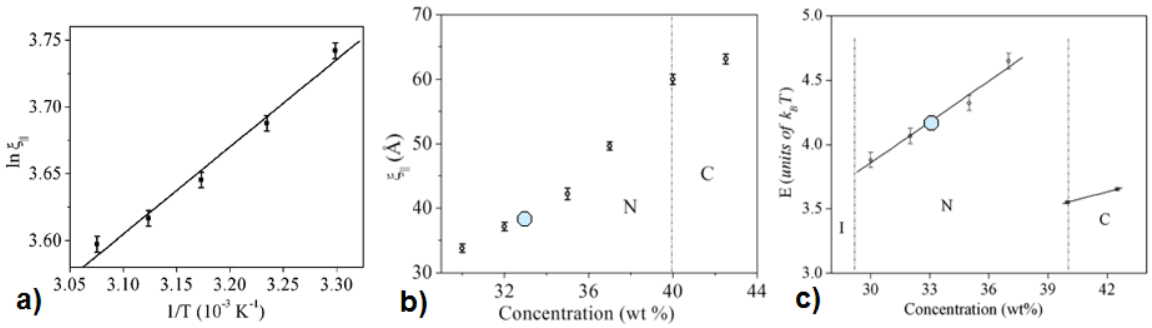

Figure 4.2. a). Longitudinal correlation length of the aggregate/column as a function of inverse temperature, for 35wt% (1.19M) SSY water solution; b). Longitudinal correlation length of the aggregate/column as a function of concentration; c). Scission energy as a function of concentration. Three figures were taken from the reference [17]. Green points: 33.2wt%(1.1M), $\xi_{//}$≈38Å (3.8nm), at room temperature; E≈4.2 k_BT, by using ξ_0=4.86 Å (0.486nm).

Collings et al [18] reported aggregate size distribution and volume fraction for two concentrations, 0.4M and 1.1M, according to their simple theory using parameters appropriate to SSY at room temperature. The average number of SSY monomers in one aggregate, $<N>$, is about 19.7 for 1.1M at room temperature. They also calculated the "bond" energy between molecules in an aggregate, E, is about 7.25 k_BT based on the law of mass action and an isodesmic aggregation process. $\xi_{//}$ for 1.1M at room temperature can be calculated to be 6.5nm by the relation $\xi_{//} = <N> d_{in}$. By using the $\xi_{//}$ and E values and the equation (4.9), ξ_0 is calculated to be 0.173nm. The temperature dependence of $\xi_{//}$ can be derived by using ξ_0=0.173nm and E=7.25 k_BT:

$$\ln \xi_{//} = -1.75 + 1080.25 \frac{1}{T} \tag{4.11}$$

By using the equation (4.10) for E=4.2 k_BT and the equation (4.11) for E=7.25 k_BT as well as the relation $<N> = \xi_{//}/d_{\text{in}}$ and $<a> = \xi_{//}/D_a$, temperature dependence of $\ln \xi_{//}$, $<N>$ and $<a>$ for 1.1M SSY chromonics are all obtained, as shown in Figure 4.3. As temperature increases, $<N>$ and $<a>$ decrease, that is, the aggregate/column shortens. When it is close to nematic-biphasic transition, the aspect ratio is extraordinarily low.

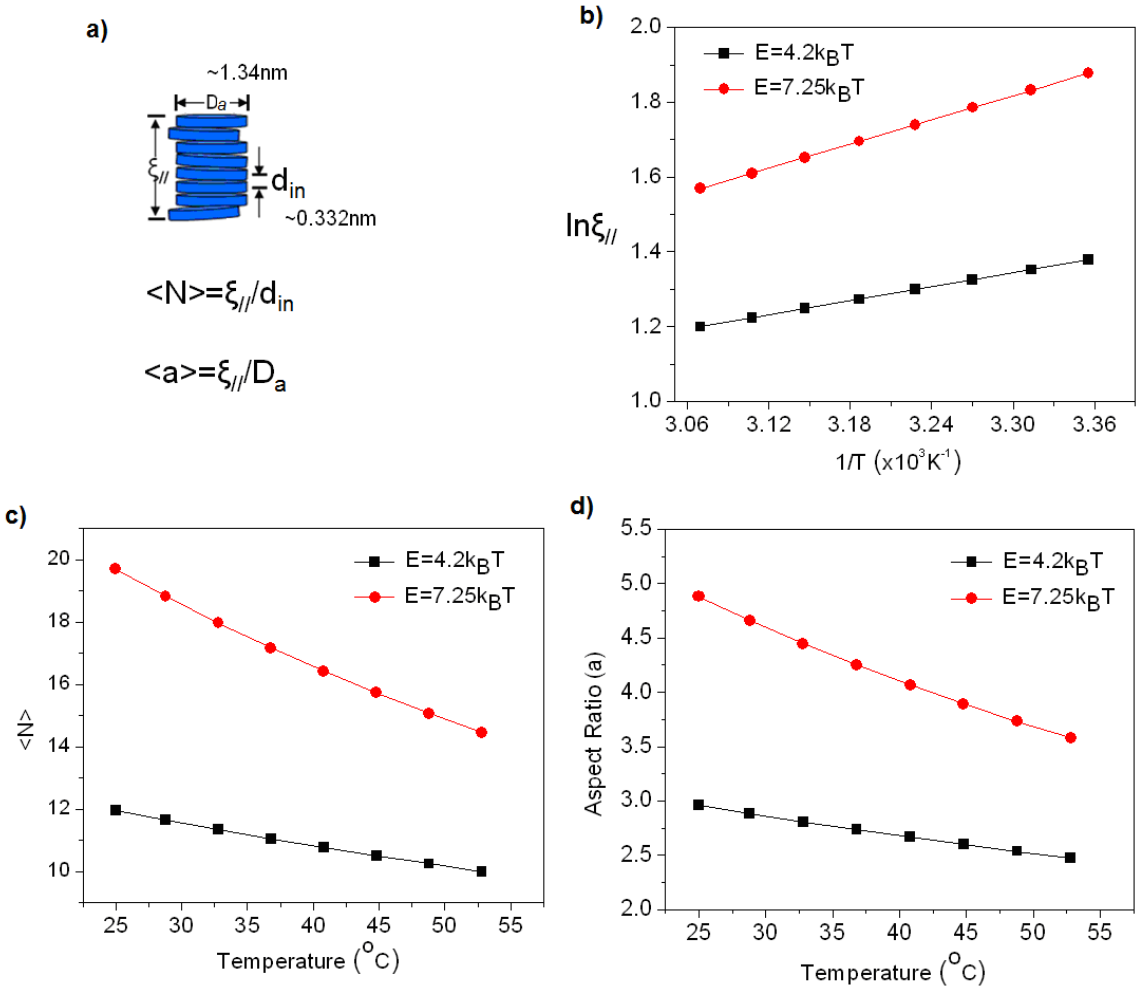

Figure 4.3. a).Schematics of an aggregate/column. b), c) and d). Temperature dependence of longitudinal correlation length $\xi_{//}$, average number of molecules <*N*> in one aggregate/column and average aspect ratio <*a*> for 1.1M SSY chromonics, using different aggregation energies obtained by Kumar et al [17] and Collings et al [18].

4.3 Prediction of the flow behavior of 1.1M SSY chromonics

Considering the aspect ratio of SSY chromonics is small and aggregates/columns are not large, we assume that the orientation distribution of chromonic aggregates/columns about the director is largely unperturbed by flow under slow shear. Thus, we will determine λ of SSY chromonics according to equation (4.18) by using $\langle P_{200} \rangle$ and $\langle P_{400} \rangle$ measured from polarized Raman measurements in the absence of flow, which was presented in the previous chapter.

By combining the calculated aspect ratios and measured order parameters, tumbling parameter λ at various temperatures is obtained for 1.1M SSY chromonics in the nematic N phase, as shown in Figure 4.4. λ decreases as temperature increases, and is always less than 1. Thus, it is tumbling, instead of flow aligning, for 1.1M SSY chromonics in the nematic N phase.

Theoretically, λ increases as temperature increases according to the prediction of the molecular theory of Archer and Larson [15] for both an infinite aspect ratio (solid line) and for an aspect ratio of a=4 (dashed line) shown in Figure 4.5.a. Experimentally, most of the measured values for λ increases as temperature increase as shown in Figure 4.5.a and b, although for E7, λ decreases as temperature increases and then maintains a constant value close to the transition temperature [19]. For all these systems, molecular aspect ratio doesn't change with temperature and only order parameters contribute to the change of λ. However, for chromonics, aspect ratio changes with temperature as well as concentration. Figure 4.6 shows the change of $L(a)$ and $\frac{(5<P_{200}>+16<P_{400}>+14)}{35<P_{200}>}$ with temperature for the 1.1M SSY chromonics. $L(a)$ decreases as temperature increases, which plays an important role in continuous decrease of λ. The values of $\frac{(5<P_{200}>+16<P_{400}>+14)}{35<P_{200}>}$ are less than 1, so λ here can't be larger than 1 because of the limitation $L(a) \leq 1$. It should be noted that both $<P_{200}>$ and $<P_{400}>$ are influenced by the fact that aggregate/column length or aspect ratio changes with temperature.

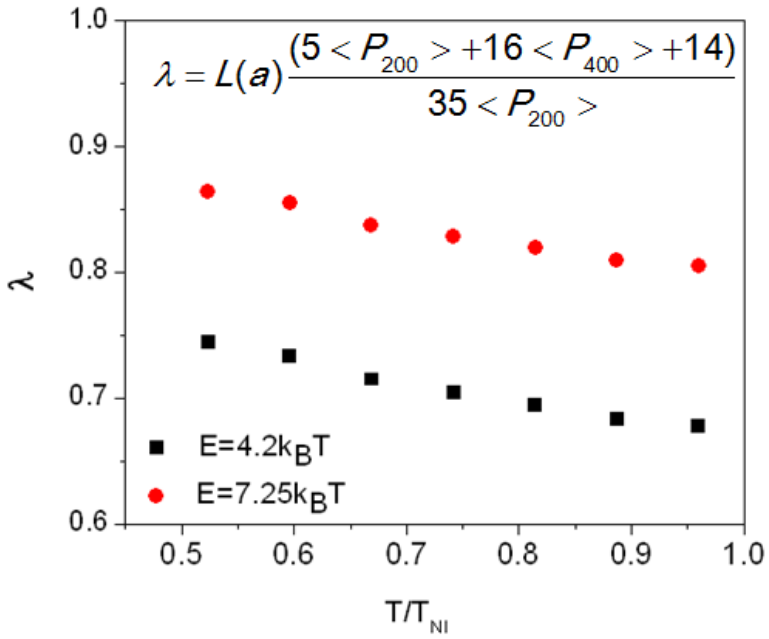

Figure 4.4. Tumbling parameter λ versus T/T_{NB} for 1.1M SSY chromonics. T_{NB} is 52.8ºC.

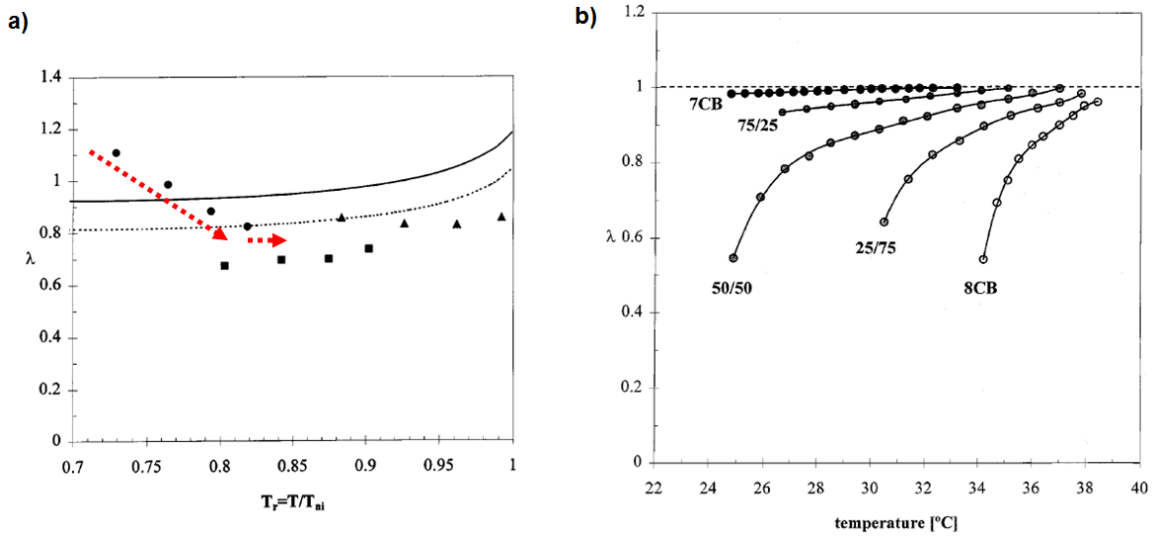

Figure 4.5. Tumbling parameter λ at different temperatures for various systems. Both figures are copied from reference [19]. a). Measured λ versus T_r for the commercial mixtures E7 (●), ZLI-3449-100 (■), and ZLI-3308 (▲). Also, the prediction of the molecular theory of Archer and Larson (1995) is shown for both an infinite aspect ratio (solid line) and for an aspect ratio of a=4 (dashed line). b). Results for 7CB/8CB mixtures as obtained by the rheological method [19].

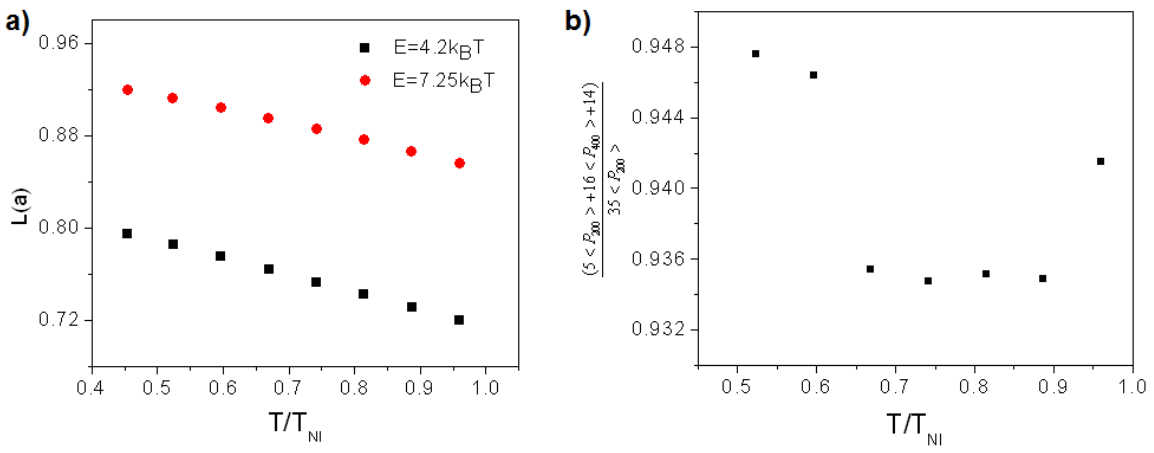

Figure 4.6. a). Temperature dependence of $L(a)$ contributing to tumbling parameter λ. b). Temperature dependence of $\frac{(5 < P_{200} > +16 < P_{400} > +14)}{35 < P_{200} >}$, contributing to tumbling parameter λ.

4.4 Prediction of the flow behavior of 1.25M SSY chromonics

Collings et al [17] also calculated the scalar order parameter S (=$<P_{200}>$) based on birefringence and absorption measurement for 1.25M SSY chromonics, as shown in Figure 4.7. We tried to calculate $<P_{400}>$ values based on the following functional relation of $<P_{200}>$ and $<P_{400}>$ for ellipsoidal particles [20]:

$$\left\langle P_{400}\right\rangle = \left\langle P_{200}\right\rangle \left(1-\left(1-\left\langle P_{200}\right\rangle\right)^{\wp}\right) \tag{4.12}$$

where $\wp$=0.6 for ellipsoidal particles according to references [20]. Figure 4.7 also shows the calculated values of $<P_{400}>$ for 1.25M SSY chromonics.

Aggregation energy E would be 7.25 k_BT according to Collings et al and would be 4.6 k_BT when the concentration is 1.25M (~36.4 wt %) according to Kumar's group in Figure 4.2.c [16]. Similarly to the case of 1.1M SSY chromonics, the temperature dependence of $\xi_{//}$ can be derived by using the ξ_0=4.86 Å and E: for E=7.25 k_BT, equation (4.11) can be used again; for E=4.6 k_BT, the equation is as follows:

$$\ln \xi_{//} = -0.721 + 685.4 \frac{1}{T} \tag{4.13}$$

Therefore, aspect ratio a and tumbling parameters λ also can be obtained. Figure 4.8 shows the calculated tumbling parameters λ. For both cases, λ is less than 1 and it would be tumbling. For E=7.25 k_BT, λ has the increasing trend as temperature increases, close to the prediction of the molecular theory of Archer and Larson [15]. However, for E=7.25 k_BT, we used the same equation (4.11) for different concentrations to calculate the temperature dependence of $\xi_{//}$ as well as the aspect ratio due to the lack of data. Therefore, λ values may be not meaningful.

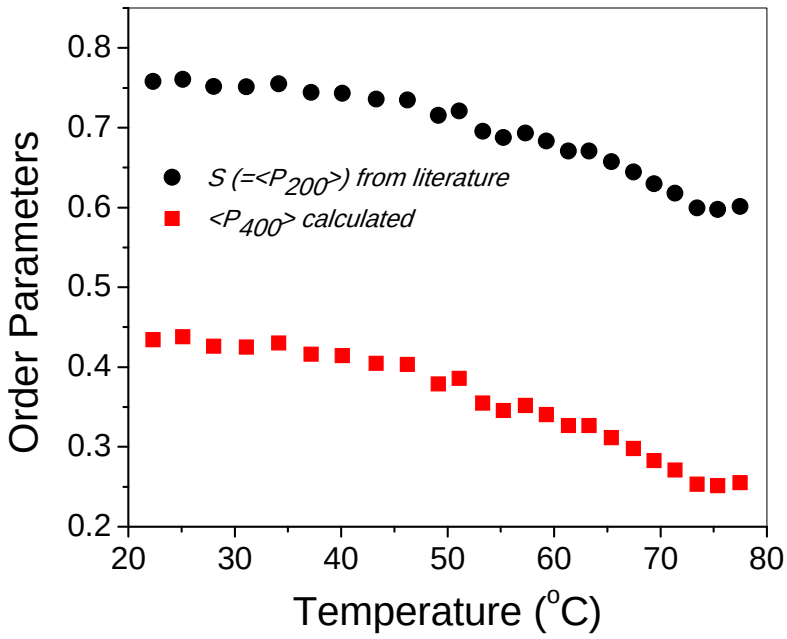

Figure 4.7. Orientational order parameters as a function of temperature for 1.25M SSY chromonics. Values of S (=$<P_{200}>$) were replotted according to reference [18]. Values of $<P_{400}>$ were calculated by us.

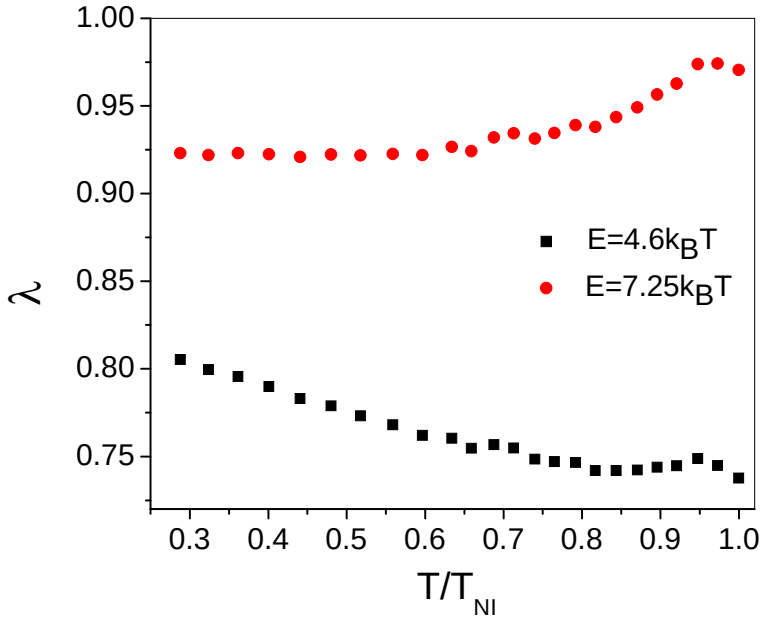

Figure 4.8. Tumbling parameter λ versus T/T_{NB} for 1.25M SSY chromonics. T_{NB} is 77.5ºC.

4.5 Conclusions

In this chapter, flow behavior of SSY chromonics in the nematic phase was predicted based on a molecular theory that the tumbling parameter λ is a function of the molecular aspect ratio and order parameters $\langle P_{200} \rangle$ and $\langle P_{400} \rangle$ at show shear rate. Aspect ratios of SSY aggregates/columns were calculated based on x-ray data in the literature. Values of $\langle P_{200} \rangle$ and $\langle P_{400} \rangle$ for 1.1M SSY were from the polarized Raman measurement in the previous chapter. Values of $\langle P_{200} \rangle$ for 1.25M SSY were used from the literature and values of $\langle P_{400} \rangle$ were calculated from $\langle P_{200} \rangle$ by using a relationship for ellipsoidal particles. As a result, the tumbling parameter λ is less than 1 and SSY chromonics are not flow-aligning, for both cases of 1.1M and 1.25M in the nematic phases. However, we assume that the orientation distribution of chromonic aggregates/columns about the director is largely unperturbed by flow under slow shear as the aggregates/columns are not large. In reality, it might be more complicated, since disassociation of molecules in

aggregates/columns may happen in the presence of certain shearing forces, thus more small aggregates/columns exist and the viscosity of the system may change. The distribution of size and the number of columns will be dynamic and will also depend on the shearing force. For future work, shear-flow experiments should be performed to validate the predictions made based on the measured values of $\langle P_{200} \rangle$ and $\langle P_{400} \rangle$.

4.6 References

[1] Frenkel J. Kinetic Theory of Liquids. **1955**, Dover: New York, 485 pp.

[2] Ericksen, J. L. Conservation laws for liquid crystals. Transactions of the Society of Rheology **1961**, 5, 23-34.

[3] Leslie, F. M. Some constitutive equations for anisotropic fluids. Quarterly Journal of Mechanics and Applied Mathematics **1966**, 19, 357-370.

[4] Leslie, F. M. Some thermal effects in cholesteric liquid crystals. Proceedings of the Royal Society of London, Series A: Mathematical, Physical and Engineering Sciences **1968**, 307(1490), 359-372.

[5] Leslie, F. M. Theory of flow phenomena in liquid crystals. Advances in Liquid Crystals **1979**, 4, 1-81.

[6] Leslie, F. M. Viscometry of nematic liquid crystals. Molecular Crystals and Liquid Crystals **1981**, 63(1-4), 111-127.

[7] Larson, R. G. The Structure and Rheology of Complex Fluids. **1999**, Oxford University Press: New York. p. 443-475, 688 pp.

[8] Kröger, M. and Sellers, S. On the signs of the Leslie viscosities α_2 and α_3 for nematics and discotic nematics. Molecular Crystals and Liquid Crystals **1997**, 293, 17-27.

[9] Tropea, C., Yarin, A. L., and Foss, J. F. (ed.) Springer Handbook of Experimental Fluid Mechanics **2007**, Springer-Verlag: Berlin, Heidelberg, 1557 pp.

[10] Kuzuu, N., and Doi, M. Constitutive equation for nematic liquid crystals under weak velocity gradient derived from a molecular kinetic equation. Journal of the Physical Society of Japan **1983**, 52(10), 3486-3494.

[11] Kuzuu, N., and Doi, M. Constitutive equation for nematic liquid crystals under weak velocity gradient derived from a molecular kinetic equation. II. Leslie coefficients for rodlike polymers. Journal of the Physical Society of Japan **1984**, 53(3), 1031-1038.

[12] Srinivasarao, M., and Berry, G. C. Rheooptical studies on aligned nematic solutions of a rodlike polymer. Journal of Rheology **1991**, 35(03), 379-397.

[13] Magda, J. J., Baek, S. G., DeVries, K. L., and Larson, R. G. Shear flows of liquid crystal polymers: measurements of the second normal stress difference and the Doi molecular theory. Macromolecules **1991**, 24(15), 4460-4468.

[14] Burghardt, W. R., and Fuller, G. G. Role of director tumbling in the rheology of polymer liquid crystal solutions. Macromolecules **1991**, 24(9), 2546-2555.

[15] Archer, L. A., and Larson, R. G. A molecular theory of flow alignment and tumbling in sheared nematic liquid crystals. Journal of Chemical Physics **1995**, 103(8), 3108-3111.

[16] Kroeger, M., and Sellers, H. S. Viscosity coefficients for anisotropic, nematic fluids based on structural theories of suspensions. Journal of Chemical Physics **1995**, 103(2), 807-817.

[17] Joshi, L., Kang, S.-W., Agra-Kooijman, D. M., and Kumar, S. Concentration, temperature, and pH dependence of sunset-yellow aggregates in aqueous solutions: An x-ray investigation. Physical Review E: Statistical, Nonlinear, and Soft Matter Physics **2009**, 80(4-1), 041703/1-041703/8.

[18] Horowitz, V. R., Janowitz, L. A., Modic, A. L., Heiney, P. A., and Collings, Peter J. Aggregation behavior and chromonic liquid crystal properties of an anionic monoazo dye. Physical Review E: Statistical, Nonlinear, and Soft Matter Physics **2005**, 72(4-1), 041710/1-041710/10.

[19] Ternet, D. J., Larson, R. G., and Leal, L. G. Flow-aligning and tumbling in small-molecule liquid crystals. Pure components and mixtures. Rheologica Acta **1999**, 38(3), 183-197.

[20] Fhrentraut H., and Hess, S. Viscosity coefficients of partially aligned nematic and nematic discotic liquid crystals. Physical Review E: Statistical, Nonlinear, and Soft Matter Physics **1995**, 51(3) 2203.

CHAPTER 5

DEFECT DYNAMICS OF SUNSET YELLOW CHROMONICS

5.1 Introduction

Nematic liquid crystals under confinement usually display singular and nonsingular defects as a consequence of frustration emanating from fixed orientation at curved bounding surfaces. Typical examples are carbon fibers spun from carbonaceous discotic nematic mesophases with circular and ribbon spinneret cross sections [1-5] and nematic liquid crystals in capillaries [6-8]. The usual situation [9] under capillary confinement is summarized in the generic texture phase diagram shown in Figure 5.1, given in terms of a dimensionless nematic potential U as a function of dimensionless capillary radius R/ξ, where ξ scales with a defect core radius. For thermotropes the nematic potential is a dimensionless temperature $U=3T_c/T$ where T_c is the clearing temperature, while for lyotropes the potential is a dimensionless concentration, $U=3C/C_c$. The texture phase diagram under capillary confinement contains four textures: (i) polar radial line defects (PRLD), (ii) planar polar line defects (PPLD), (iii) escape radial ring defects (ERRD), and (iv) escape radial (ER) textures. The figure shows the stability range of each texture. The PRLD is stable in nanocapillaries or close to the nematic-isotropic (N-I) transition and has a +1 singular line defect at the axis. The PPLD has two +1/2 line defects along the axis separated by a distance 0.665 times the capillary diameter. The metastable ERRD consists of a lattice of hedgehog and hyperbolic ring defects and is unstable to either loop annihilation or loop break. The ER is an escaped texture with a non-singular +1 defect core.

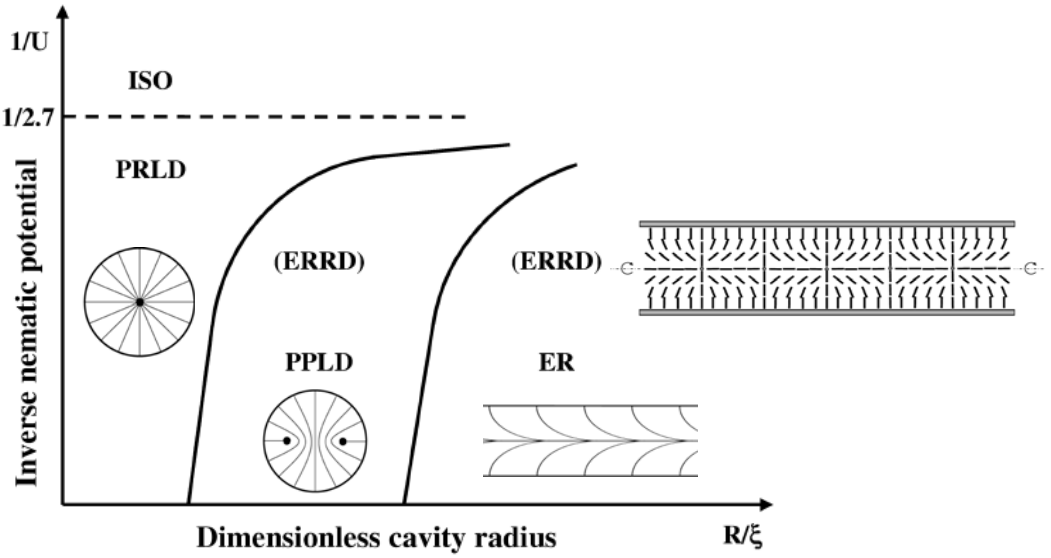

Figure 5.1. Texture phase diagram in terms of inverse nematic potential U ($U=3T/T_c$, dimensionless temperature) as a function of dimensionless capillary radius R/ξ for uniaxial nematics under capillary confinement, indicating the geometric and thermal conditions. The horizontal dashed line is the nematic-isotropic transition temperature T_c. The internal length scale ξ is proportional to the size of a defect core. ISO denotes the isotropic temperature, PRLD is the planar radial line defect texture with a s=+1 defect at the center, PPLD is the planar polar line defect texture with two s=+1/2 defects, ER is the escaped radial texture where the director tilts out of the cross sectional plane, and ERRD is the escaped radial ring defect texture, consisting of a periodic lattice of alternating +1 and -1 point defects separated by a distance close to the capillary radius. From reference [9].

Capillary texturing provides a wealth of important information on interfacial effects, phase transitions, elasticity, and defect physics, as follows:

1. The smaller radius at which the PRLD texture persists provides indications on anchoring energies,

2. The chimney parallel along the N-I transition exists due to competition between bulk and defect core energies and its width provides information on both,

3. The PRLD/PPLD boundary describes the defect instability: $s = +1 \rightarrow 2s = +1/2$ driven by bulk elasticity reduction, and hence its location on the texture diagram provides information on bulk elasticity,

4. The ERRD is a metastable state that coarsens by loop splitting or loop/loop interactions and its kinetics provides information on viscoelasticity of the liquid crystals through defect speeds and annihilation times,

5. Escape textures arise to minimize splay in this configuration. Hence the boundary between PPLD/ER provides elastic anisotropy information.

Changing the geometry from cylindrical to a ribbon capillary has been analyzed but a complete understanding is lacking and a texture phase diagram has not been presented. Figure 5.2 shows predictions of geometry-driven texture transformation for the radial and planar polar textures computed for a thermotropic carbonaceous mesophase. The pure splay of the radial texture develops a splay-bend configuration in the ribbon, and the bipolar develops an aligned layer [3-5].

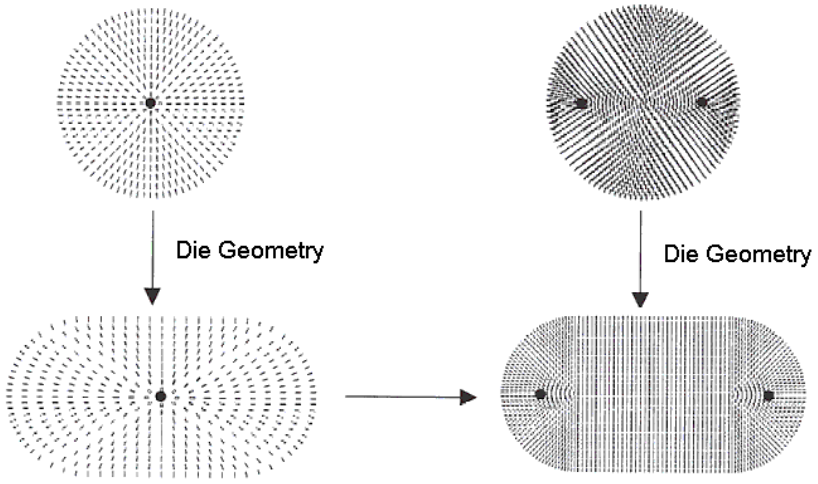

Figure 5.2. Geometric effects on texturing under capillary confinement. Circular symmetry breaking distorts the director field patters and relocates the defect positions. This figure is from reference [5].

In this chapter, we will present a study of defect of SSY chromonics in a flat capillary with ribbon geometry and planar alignment, focusing on static and dynamics associated with point (3). By integrating theory and experiments, important viscoelastic material constants of chromonics will be accessed. In order to study the defect theoretically, we will give more relevant theoretical introduction to defects in this part below.

The molecular order and orientation of uniaxial nematic liquid crystals are described by a symmetric traceless tensor order parameter $\boldsymbol{Q}$:

$$\boldsymbol{Q} = \Lambda(\boldsymbol{nn} - \boldsymbol{I}/3) + \boldsymbol{P}(\boldsymbol{mm} - \boldsymbol{ll}) \tag{5.1}$$

where (Λ, $\boldsymbol{P}$) are the uniaxial and biaxial order parameters and ($\boldsymbol{n}$, $\boldsymbol{m}$, $\boldsymbol{l}$) are the orthonormal directors [10, p. 59, 11, 12]. For uniaxial phases at equilibrium $\boldsymbol{P}$=0 and the equilibrium uniaxial scalar order parameter $\Lambda = \Lambda_e$ is a function of temperature and/or concentration, in this state the orientation is captured by the uniaxial director $\boldsymbol{n}$. Given the low deformation moduli K of these materials, uniaxial nematic liquid crystals display singular and nonsingular orientational line defects, called disclination lines. Figure 5.3 shows a cross-sectional visualization of the tensor $\boldsymbol{Q}+\boldsymbol{I}/3$, on a plane normal to the disclination, around a wedge disclination of strength s=1/2, that shows typical splay-bend distortions of $\boldsymbol{n}$ when encircling the defect and changes in molecular order when moving to the defect center. In singular wedge line defects, relevant to study in this chapter, the equilibrium uniaxial nematic disclination core (the core radius r_c is of nm size) has a complex heterogeneous order characterized by a biaxial ring where $\Lambda \neq 0, \boldsymbol{P} \neq 0$, while at the disclination core center uniaxiality is regained and $\boldsymbol{P}$=3Λ. The defect-associated order parameter heterogeneities ($\nabla\Lambda \neq 0, \nabla\boldsymbol{P} \neq 0$) result in a core energy per unit volume $\sigma_c \approx s^2 K / r_c^2$ [10-12]. Outside the wedge disclination core ($r>r_c$) the distorted orientation $\boldsymbol{n}$ is planar (normal to the disclination line) [10, p. 129], in

cylindrical polar coordinates ($r_{cylindrical}$, $\varphi_{cylindrical}$), the director $\boldsymbol{n}$ angle is $\psi = s\varphi_{cylindrical} + C$, where s is the strength of the defect and C is a constant. The orientation distortion given $\psi = \psi(\varphi_{cylindrical})$ in a macroscopic domain R results in a dominant line tension contribution $\gamma_\ell = \pi s^2 K \ln(R / r_c)$, in addition to the smaller core contribution $\pi r_c^2 \sigma_c$. The orientation energy per unit length (line tension) associated with the line defect scales with s^2 and hence ±1/2 lines are energetically preferred [10, p. 128]. When the disclination line is curved additional distortions arise because the normal planes to the line are splayed and this splay contributes to the line energy in the form of a bending energy that is of the same order of magnitude as tension energy when the director curvature and the line curvature are of the same order. A simple example of tension/bending equi-contributions is a shrinking 1/2 disclination loop of radius $R_{loop}(t)$, where at sufficiently long times $R_{loop}(t)$ becomes comparable to the radius of curvature of the director. Based on these observations we conclude that the statics and dynamics of disclination lines are analogous to other elastic filaments since they possess both tension and bending resistance. Finally, nonsingular disclinations, where the director escapes into the third dimension and where the defect core is macroscopic, are also observed.

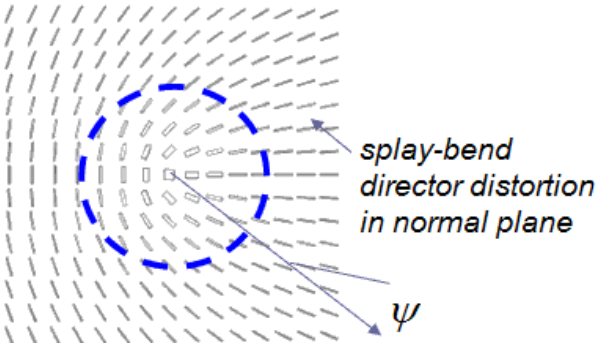

Figure 5.3. Tensor order parameter ($\boldsymbol{Q}$ + $\boldsymbol{I}$/3) visualization of a wedge disclination of strength s=1/2. The line is normal to the page. In the core region (dashed circle) the order parameters change. The director field is planar (2D) and normal to the plane and has a splay-bend distortion. The distortions result in a line tension that is proportional to defect strength square, s^2.

5.2 Experimental observation

The dimension of the flat capillary used is width (W) 200 μm, thickness 20 μm and length 5cm. After filling with 1.0M SSY chromonics in the isotropic phase, the two ends of the capillary were dipped into silicone grease immediately and sealed with Permaoxy fast cure epoxy. Immediately after preparation, the prepared sample was observed under a polarized optical microscope (POM) equipped with a Nikon D300 camera at room temperature.

Upon cooling from the isotropic phase, defects of SSY nematic chromonics were observed in the capillary under the crossed polarized optical microscope. Figure 5.4 A-J shows a temporal sequence of POM images that summarizes the texture transformation process. The orientation of the crossed polarizer and analyzer is shown in the lower right, the (x, y) coordinates on the upper left, W is the capillary width (200μm), and the times of the frames are indicated besides each figure. Initially (A) there were small uniform areas that grew (B-E) and coarsened, leading finally to a monodomain formed throughout the capillary. If the small uniform areas happened to be far away from each other, it was observed that they were linked by a long center disclination line (C-H). The uniform areas were the result of the splitting of the s=+1 disclination line into a pair of s =+1/2 lines at a branching point (F-H and left and right insets, also shown in Figure 5.5). The s =+1/2 lines emanating from the branch point evolve towards the edges of the capillary (see B-H). Each uniform area is a ribbon-shaped region (as shown with schematic diagram in the bottom left of Figure 5.4) defined by the two s=+1/2 lines that end at two branch points (right inset for F).

The growth speeds of the uniform area in x and y directions were not constant when it was still small as shown in Figure 5.6. However, when it was close to the wall of the capillary, the branch points started to move at a constant speed of about 0.11μm/s along the long axis of the capillary, and as a consequence the shrinking speed of the length of the +1 line was about 0.22μm/s, as shown in Figure 5.7 at region A. During this

monodomain growth process (branch point precollision stage, frames C-H in Figure 5.4), the disclination line close to the branch points maintained an exponential shape while further away was straight. Subsequently, the collision of two branch points was observed (H and left I frame in Figure 5.4), the s=+1 was entirely consumed and the s=+1/2 lines of neighboring domains merged. During postcollision (I in Figure 5.4), the merged curved disclination lines relaxed to the edge of the capillary and a monodomain with two s=+1/2 straight lines was formed (right I frame in Figure 5.4). Some parts of these two +1/2 lines were locked by irregularities on the wall, other parts escaped after one or two days (J in Figure 5.4). The monodomain was homogeneously planar aligned with the director perpendicular to the long axis of the capillary as characterized by polarized optical microscopy, polarized Raman spectroscopy and x-ray diffractometry described in previous chapters.

There were also point defects randomly distributed on the center disclination line. They stayed stable with no drifting or annihilation or redistribution, until the growing uniform domain reaches them and merges them. It is possible that some invisible dust or impurities were captured by the disclination line and lowered the energy of the system.

Studies of kinematics of branch point and dynamics of line shapes were conducted in collaboration with Prof. Alejandro Rey at McGill University. Prof. Alejandro Rey worked on the theory and the models including the kinematics of branch point (5.3), disclination theory (5.4.1.1 to 5.4.1.4) and traveling mode and relaxation mode (5.4.4).

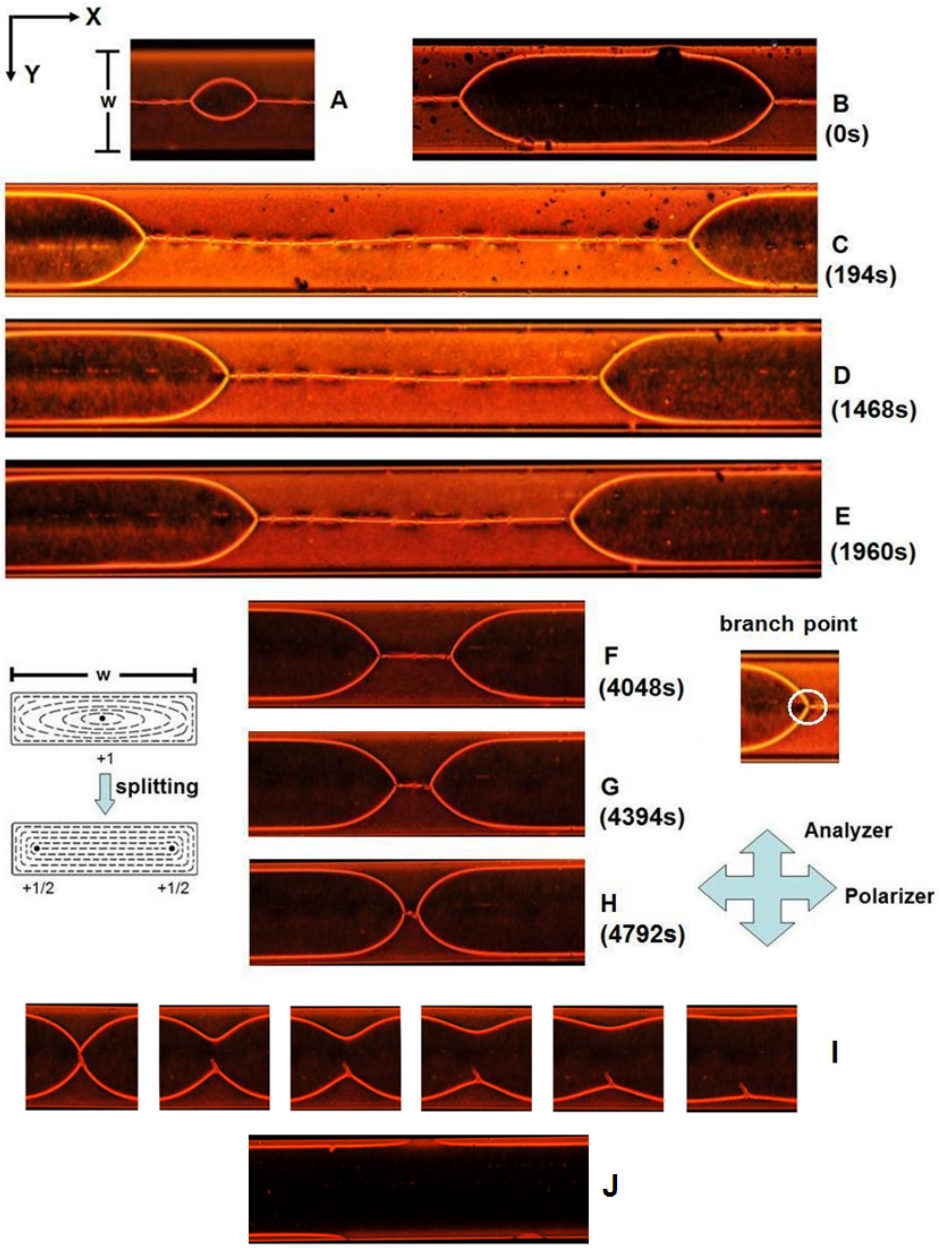

Figure 5.4. Texture transformation processes used to determine viscoelastic parametric data. All the POM images were taken under crossed polarizer and analyzer (see lower right inset) and the times are indicated below each frame label. A: growth from small uniform domain at non-constant speed, B: the uniform domain stops growing in y direction as it reaches the edge of the capillary, and it starts to grow at a constant speed along x direction (B is set as time t=0), C: The +1 line branches into two pairs of +1/2 lines, D- H: the +1 line shrinks as the branch points moves towards each other. The series images of I show the lines relaxed back to the edge after collision and pinch-off. The image J was taken after one day. Left-bottom schematics show the enlarged cross-section view of the change of director configures for the highly unstable +1 line splitting into two stable +1/2 lines. "W" is 200μm, the width of capillary.

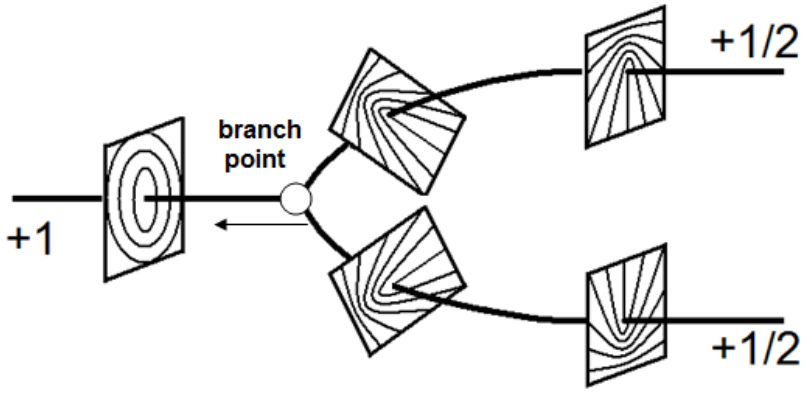

Figure 5.5. Disclination line with strength +1 splitting into two +1/2 lines.

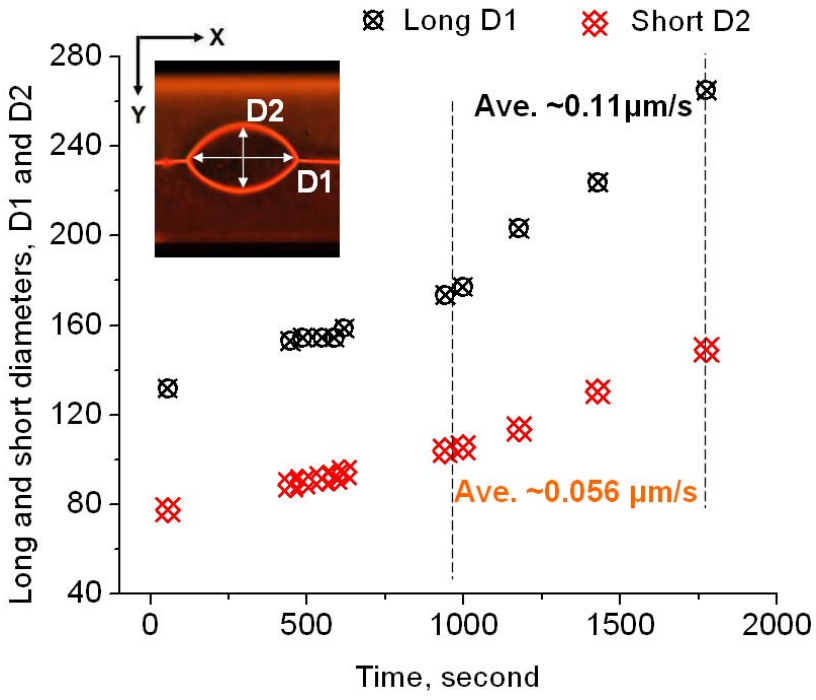

Figure 5.6. Growth dynamics of the small uniform domain.

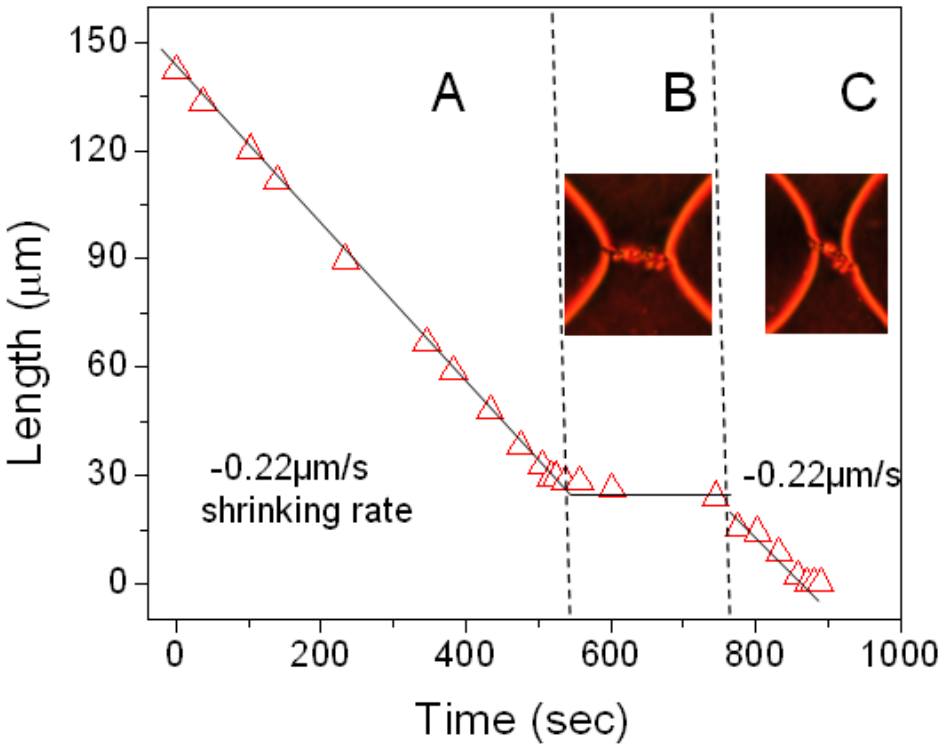

Figure 5.7. Shrinkage of the center disclination line. A: average shrinking rate was about -0.22μm/s, B: center disclination shrunken to two point defects, motion slowed down and a plateau appeared, C: after rearrangement, two point defects kept shrinking at the rate of about -0.22 μm/s. Red triangles indicate the measured data; black lines are the fitting lines.

5.3 Kinematics of the branch point

The kinematics of the branch point when three disclination lines meet is studied. The force balance on the branch point under confinement has two sources of contributions: a bulk stress contribution and a line stress contribution:

$$\underbrace{\beta_{bp}\omega_{bp}}_{\substack{branch\ point \\ viscosity \times speed}} = \underbrace{\left(\oiint_{A_s}(\boldsymbol{k}\bullet\boldsymbol{T}_b)dA_s\right)}_{bulk} + \underbrace{\left(\sum_{jun}\boldsymbol{t}\bullet\boldsymbol{T}_\ell\right)}_{line} \tag{5.2}$$

where ω_{bp} is the branch point speed, β_{bp} is the viscosity associated with the translation

of the branch point, $\iint_A (\boldsymbol{k}\bullet\boldsymbol{T}_b)dA$ is the bulk force and $\iint_{A_s} (\boldsymbol{k}\bullet\boldsymbol{T}_b)dA_s$ is a spherical area integral evaluated at the branch point , $\sum_{\text{jun}} \boldsymbol{t}\bullet\boldsymbol{T}_\ell$ is the sum of excess line forces evaluated at the branch point, $\boldsymbol{t}$ is the unit tangent to each disclination line, $\boldsymbol{T}_\ell$ is the excess line stress tensor, and $\boldsymbol{T}_\text{b}$ is bulk stress tensor. Assuming that the bulk stress is shear-free, $\boldsymbol{T}_\text{b} = \text{C}\boldsymbol{I}$, the speed of the branch point in the x-direction is

$$\boldsymbol{\beta}_{bp}\boldsymbol{\omega}_{bp} = \sum_{jun} \boldsymbol{T}_\ell : \boldsymbol{t}\boldsymbol{\delta}_x \tag{5.3}$$

where δ_x is a unit vector in the x-direction.

Using previous results the line stress tensor is given by:

$$\boldsymbol{T}_\ell = \underbrace{\pi \text{Ks}^2 \, ln\left(\frac{\text{R}}{\text{r}_\text{c}}\right)}_{\text{line tension}} \boldsymbol{tt} + \chi_{\text{core}}\boldsymbol{tt} \tag{5.4}$$

where K is the Frank elastic constant, s is the strength of the disclination line, R is the system size and χ_{core} is the core energy, usually estimated to be 5% of the line tension . This equation is derived using the following rate of entropy production due to the steady motion of the branch point:

$$\Delta = \int \gamma_1 \left(\frac{d\boldsymbol{Q}}{dt}\right)^2 dV = \int \gamma_1 \left(\boldsymbol{\omega}_{bp}\cdot\nabla\boldsymbol{Q}\right) : \left(\boldsymbol{\omega}_{bp}\cdot\nabla\boldsymbol{Q}\right)dV = \int \gamma_1 \omega_{bp}^2 \left(\boldsymbol{\delta}_x\cdot\nabla\boldsymbol{Q}\right) : \left(\boldsymbol{\delta}_x\cdot\nabla\boldsymbol{Q}\right)dV =$$
$$\gamma_1 \omega_{bp}^2 \int \left(\frac{\partial\boldsymbol{Q}}{\partial x}\right) : \left(\frac{\partial\boldsymbol{Q}}{\partial x}\right)dV \tag{5.5}$$

where γ_1 is the rotational viscosity and were we neglected back-flow effects, the second expression is in a frame that translates with the moving branch point, the integrand in the last expression is a geometric factor that can be written as a characteristic length scale:

$$L = \int \left(\frac{\partial\boldsymbol{Q}}{\partial x}\right) : \left(\frac{\partial\boldsymbol{Q}}{\partial x}\right)dV \tag{5.6}$$

The expression of Δ is also found by the rate of work of the forces acting on the point:

$$\Delta = \boldsymbol{\omega}_{bp} \cdot \left(\sum_{jun} \boldsymbol{T}_{\ell} : \boldsymbol{t}\boldsymbol{\delta}_{x} \right) = \beta_{bp} \boldsymbol{\omega}_{bp} \cdot \boldsymbol{\omega}_{bp} = \beta_{bp} \omega_{bp}^{2} \tag{5.7}$$

Setting these two expressions equal to each other, we get:

$$\beta_{bp} \omega_{bp}^{2} = \gamma_{1} \omega_{bp}^{2} L \tag{5.8}$$

Finally, the branch point translational viscosity is

$$\beta_{bp} = \gamma_{1} L \tag{5.9}$$

The physical situation we wish to describe consist of a +1 disclination line along the x-axis and two +1/2 disclination lines at angle φ_{bp} from the x-axis, as illustrated in Figure 5.8. Introducing equations (5.4) and (5.9) into equation (5.3) we find:

$$\omega_{bp} = \frac{1}{\gamma_{1} R} \left\{ \pi K \ln\left(\frac{R}{r_c}\right) \left(1 - 2\left(\frac{1}{2}\right)^{2} \cos\varphi_{bp} \right) + \left(\chi_{+1} - 2\chi_{+1/2} \cos\varphi_{bp} \right) \right\} \tag{5.10}$$

The above model was built by Prof. Alejandro Rey. Using values $K / \gamma_1 \approx 10^{-12} m^2 / s, R \approx 100 \mu m, r_c \approx 10 nm, \varphi_{bp} \approx 60^{o}$ and neglecting the core energies, we get a speed ω_{bp} of the order of 10^{-1}μm/sec, which matches very well with the experimental value 0.11μm/s. Later in this chapter, we will show that $K / \gamma_1 \approx 10^{-12} m^2 / s$ and $r_c \approx 10 nm$ are reasonable assumptions.

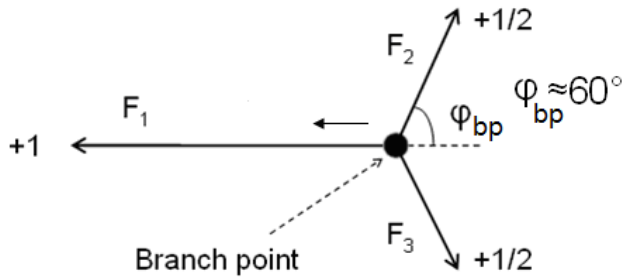

Figure 5.8. Schematic drawing of force balance on the branch point.

5.4 Disclination dynamics at precollision stage and postcollision stage

5.4.1 Theory

The theoretical work (sections from 5.4.1.1 to 5.4.1.4) was done by collaborator Prof. Alejandro Rey.

5.4.1.1 Disclination line geometry

The geometry of the disclination follows the method described in reference [13]. Figure 5.9 defines the geometry of a disclination evolving in a plane, while non-planar modes are left for future work. The disclination is described by a planar space curve, $\boldsymbol{x} = \boldsymbol{x}(g,t)$, where $\boldsymbol{x}$ is the position vector, g is arc length and t is time. The unit tangent $\boldsymbol{t}(g,t)$, and the unit normal $\boldsymbol{N}(g,t)$ to the filament are given by:

$$\boldsymbol{t}(g,t) = \frac{\partial \boldsymbol{x}(g,t)}{\partial g} \quad ; \quad \frac{\partial \boldsymbol{t}(g,t)}{\partial g} \equiv \frac{\partial^2 \boldsymbol{x}(g,t)}{\partial g^2} = \kappa \boldsymbol{N}(g,t) \tag{5.11a, b}$$

where $\kappa = \boldsymbol{N} \cdot \partial \boldsymbol{t} / \partial g$ is the curvature, quantifying the deviation from linearity. Since $\boldsymbol{t}$ is a unit vector, it can be expressed with the normal angle $\theta_n(g,t)$: $\boldsymbol{t}(g,t) = (\sin\theta_n(g,t) - \cos\theta_n(g,t))$. In the normal angle parameterization, the curvature κ is given by $\kappa = \partial\theta_n / \partial g \equiv \theta_{n,g}$.

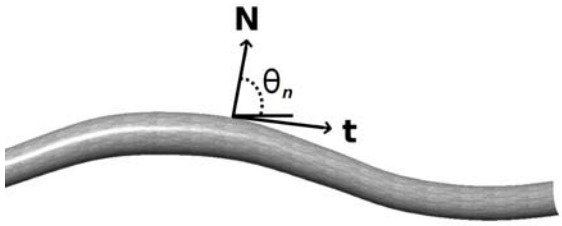

Figure 5.9. Schematic of the wedge disclination core geometry. The unit tangent is **t** and unit normal is **N**. The normal angle is θ_n. The relaxation of the line shape is driven by tension and bending energies.

5.4.1.2 Straight wedge singular disclinations

The Frank gradient elasticity density f for uniaxial nematic liquid crystals, using the one constant approximation is [10]:

$$F = \frac{K}{2}\left((\nabla \cdot \boldsymbol{n})^2 + (\nabla \times \boldsymbol{n})^2\right) \tag{5.12}$$

where $\boldsymbol{n}$ is the director field whose minimum satisfies the Euler Lagrange equation $K\nabla^2 \boldsymbol{n} = \lambda_L \boldsymbol{n}$, K is the Frank elastic constant, and λ_L is the Lagrange multiplier that takes into account the restriction $\boldsymbol{n} \cdot \boldsymbol{n} = 1$. As mentioned above, using a planar director parameterization $\boldsymbol{n} = (cos\psi, sin\psi, 0)$ and planar polar coordinates ($r_{cylindrical}$, $\varphi_{cylindrical}$), a wedge disclination solution, located at the coordinate origin, to the Euler Lagrange equation is $\psi = s\varphi_{cylindrical} + C$, where s is a multiple of $\pm 1/2$ and C a constant. The energy per unit length of a straight disclination line $\gamma_\ell(\kappa = 0) = \gamma_o$ obtained by integrating the free energy density F (equation (5.12)) is [10], κ is curvature:

$$\begin{aligned}\gamma_o &= \frac{1}{L}\int_{r_c}^{R}\int_{0}^{2\pi}\int_{0}^{L} \mathrm{F}\, r_{cylindrical} dr_{cylindrical} d\varphi_{cylindrical} ds_{cylindrical} + \pi\sigma_c r_c^2 \\ &= K\pi\left(s^2\, ln\left(\frac{R}{r_c}\right)\right) + \pi\sigma_c r_c^2 r_c^2 = K\pi\left(s^2\, ln\left(\frac{R}{r_c}\right)\right) + \pi\sigma_c r_c^2\end{aligned} \tag{5.13}$$

where r_c is the core radius and σ_c the core energy density, which can be estimated to be $\sigma_c \approx s^2 K / r_c^2$ and is typically assumed to be less than 10% of the total line tension [10].

5.4.1.3 Curved disclinations

According to the thermodynamics of line phases [14], the Helmholtz free energy per unit length $\hat{A}_\ell$ is given by the disclination tension γ_ℓ: $\hat{A}_\ell(\kappa) = \gamma_\ell(\kappa)$, where the dependence on curvature κ is noted. Next we use this equality ($\hat{A}_\ell(\kappa) = \gamma_\ell(\kappa)$) to

calculate: (i) the line tension for arbitrarily curved *s*= +1/2 lines , (ii) the corresponding line moment tensor $\boldsymbol{M}$, and (iii) the line stresses tensor $\boldsymbol{T}$ for curved disclinations.

(i) Line tension $\gamma_\ell\left(\kappa \neq 0\right)$. Consider a disclination of strength *s* =1/2 of curvature κ and assume that the planar director field in a local polar coordinate system ($r_{cylindrical}$, $\varphi_{cylindrical}$) is $\psi = \varphi_{cylindrical}/2$. The Frank elastic energy per unit volume *F* has the rectilinear contribution plus an additional term due to the curvature:

$$F = \frac{K}{2}\left\{\frac{\left(d\psi / d\varphi_{cylindrical}\right)^2}{r^2_{cylindrical}} + \frac{\kappa^2 \cos^2\psi}{\left(1-\kappa r_{cylindrical}\cos\varphi_{cylindrical}\right)^2}\right\} \tag{5.14}$$

The line tension $\gamma_\ell\left(\kappa\right) = \hat{A}_\ell\left(\kappa\right)$ then is:

$$\gamma_\ell = \frac{1}{L}\int_{r_c}^{R}\int_{0}^{2\pi}\int_{0}^{L} \mathrm{F}\, r_{cylindrical} dr_{cylindrical} d\varphi_{cylindrical} ds_{cylindrical} + \pi\sigma_c r_c^2$$
$$= \frac{1}{L}\iiint\left\{\frac{K}{2}\left\{\frac{\left(d\psi / d\varphi_{cylindrical}\right)^2}{r^2_{cylindrical}} + \frac{\kappa^2\cos^2\psi}{\left(1-\kappa r\cos\varphi_{cylindrical}\right)^2}\right\}\right\} r_{cylindrical} dr_{cylindrical} d\varphi_{cylindrical} ds_{cylindrical}$$
$$+\pi\sigma_c r_c^2 \tag{5.15}$$

Integration yields

$$\gamma_\ell = \frac{K\pi}{4}\left(\ln\left(\frac{R}{r_c}\right)\right) + \frac{K\pi}{2}\left(1 - \frac{1}{\sqrt{\left(1-\left(\kappa R\right)^2\right)}} + \ldots.\right) + \pi\sigma_c r_c^2 \tag{5.16}$$

To first second order in curvature (κ^2) the line tension γ_ℓ is given by the sum of straight γ_o, and bending $k_c\kappa^2/2$ contributions:

$$\gamma_\ell = \gamma_o + \frac{k_c}{2}\kappa^2, \quad \gamma_o = \frac{K\pi}{4}\ln\left(\frac{R}{r_c}\right) + \pi\sigma_c r_c^2, \quad k_c = \frac{KR^2\pi}{\sqrt{2}} \tag{5.17a,b,c}$$

where $k_c = KR^2\pi/\sqrt{2}$ is the bending modulus. Assuming that for a macroscopic domain $\ln(R/r_c) \approx 10$, equation (5.17) indicate that the bending effect becomes non-negligible at $\kappa \approx 10^{-2}\,\mu m^{-1}$.

(ii) The bending line moment tensor $\boldsymbol{M}$ is found from the differential of $\hat{A}_\ell$ [14, 15],

$$\boldsymbol{M} = -\left(\rho\frac{\partial \hat{A}_\ell}{\partial \nabla_\ell \boldsymbol{N}}\right) = \left(\rho\frac{\partial \hat{A}_\ell}{\partial \boldsymbol{b}}\right) \tag{5.18a,b}$$

where we introduce the line curvature tensor $\boldsymbol{b} \equiv -\nabla_\ell \boldsymbol{N} = \kappa \boldsymbol{I}_\ell$, where $\nabla_\ell(\bullet) = \boldsymbol{t}\partial(\bullet)/\partial g$ is the line gradient operator. Using the definition $\kappa = \boldsymbol{b} : \boldsymbol{I}_\ell$, the moment tensor $\boldsymbol{M}$ is shown to be a lineal 1x1 tensor: $\boldsymbol{M} = M\boldsymbol{I}_\ell$, where $M = \rho(\partial \hat{A}_\ell / \partial \kappa)$ is the scalar moment.

(iii) To find the 1x2 line elastic stress tensor $\boldsymbol{T}$, we perform a variation of the total Helmholtz free energy $\hat{A}_\ell$ due to tangential and normal displacements, $\delta\boldsymbol{R} = \boldsymbol{u}_{//} + \zeta\,\boldsymbol{k}$, and find [14, 15]:

$$\boldsymbol{T} = \left(\hat{A}_\ell - \boldsymbol{M} : \boldsymbol{b}\right)\boldsymbol{I}_\ell - \frac{\partial M}{\partial g}\boldsymbol{t}\boldsymbol{N} \tag{5.19}$$

where $\hat{A}_\ell \boldsymbol{I}_\ell$ is the thermodynamic tension stress analogous to 3D pressure. The line stress $\mathbf{T}$ has a mechanical contributions ($-\boldsymbol{M} : \boldsymbol{b}$), since there can be no bending without tension. The last term in equation (5.19) are the bending stresses that arise under curvature gradients ($\partial\kappa/\partial g \neq 0$). Using equations (5.17-5.19), the moment M, line moment tensor $\boldsymbol{M}$, and line elastic stress tensor $\boldsymbol{T}$ are:

$$M = k_c\kappa\,, \boldsymbol{M} = k_c\kappa\boldsymbol{I}_\ell\,, \quad \boldsymbol{T}_\ell = \left(\gamma_o - \frac{k_c}{2}\kappa^2\right)\boldsymbol{I}_\ell - k_c\frac{\partial\kappa}{\partial g}\boldsymbol{t}\boldsymbol{N} \tag{5.20a,b,c}$$

Neglecting the bending modulus $(k_c = 0)$ leads to disclination mechanics with no bending resistance, for which $M = 0, \boldsymbol{M} = 0, \boldsymbol{T} = \gamma_o \boldsymbol{I}_\ell$, and this fails to capture the shape evolution of disclinations.

5.4.1.4 Disclination shape equation

The force balance equation is given by the sum of line force $\nabla_\ell . \boldsymbol{T}$ and the surrounding medium force [16]:

$$\nabla_\ell \bullet \boldsymbol{T} + \oint_{\partial F} \left(\boldsymbol{N} \bullet \boldsymbol{T}_b \right) \mathrm{d}\ell = 0 \tag{5.21}$$

where $\boldsymbol{N} \cdot \boldsymbol{T}_b$ is the force acting on the disclination by the suspending phase, and the integral is over the disclination circumference ∂F. Assuming a local dissipative interaction caused by normal motion of the disclination, the normal component of equation (5.21) or dynamic shape equation found by replacing equation (5.20c) in equation (5.21) is:

$$\gamma_1 w = \gamma_o \kappa - k_c \left(\kappa_{gg} + \frac{\kappa^3}{2} \right) \tag{5.22}$$

where γ_1 is the rotational viscosity of the liquid crystal and w is normal material velocity of the disclination. Here the "diffusive" term $k_c \kappa_{gg} = k_c \partial^2 \kappa / \partial g^2$ and the nonlinearity $k_c \kappa^3 / 2$ arise due to the bending stresses in equation (5.20c). If we neglect k_c, the line shape dynamics is linear and local: $\gamma_1 w = \gamma_o \kappa$.

Next we analyze the linear regime of disclination dynamics given by the linearized version equation (5.22) obtained by neglecting $k_c \kappa^3 / 2$ and approximating the curvature κ. Assuming that in a (x, y) frame, the disclination's shape is described by a curve $y=H(x,t)$, and $H_x \equiv \partial H / \partial x$ is sufficiently small, then the normal velocity w and curvature κ are: $w = \partial H / \partial t, \kappa = H_{xx}$ and the disclination shape equation (5.22) becomes:

$$\frac{\partial H}{\partial t} = \rho \frac{\partial^2 H}{\partial x^2} - \delta' \frac{\partial^4 H}{\partial x^4} \tag{5.23}$$

where $\rho = \gamma_o / \gamma_1$, $\delta' = k_c / \gamma_1$. For an *s*=+ 1/2 disclination, the tension γ_o and bending k_c moduli are given in equations (5.17b and c).

As discussed above, the transformation of a +1 line texture to a pair of 1/2 line texture involves the motion and collision of pairs of disclination branch points. The transformation consists of three stages: (i) pre-collision, (ii) collision, and (iii) post collision. During precollision, the *s*=+ 1/2 disclinations translate with no shape change and in a co-moving coordinate frame the shape of an *s*=+1/2 branch satisfies $\gamma_o h_{xx} - k_c h_{xxxx}$, that is, the shape translates but does not change. Denoting the location of the two moving branch points $x_{b\pm}(t)$, the equation ($\gamma_o H_{xx} - k_c H_{xxxx}$) holds in the domain $-\infty < x < x_{b-}(t), x_{b+}(t) < x < \infty$. During postcollision, each *s*=+1/2 disclination $(-\infty < x < +\infty)$ relaxes to a straight line according to equation (5.23). Fitting the precollision and postcollision predictions to experimental shape H(x) data we can obtain the viscoelastic parameters $(\gamma_1, \gamma_o, k_c)$ as shown below.

5.4.2 Disclination line shape in the precollision stage

In this section we summarize the key line shape measurements corresponding to frames C-H in Figure 5.4. Figure 5.10 shows the relative positions of disclination lines inside the capillary. Figure 5.11 shows the shape (*y=y(x)*) of a superposed set of *s*=+1/2 lines emanating from the moving branch point taken at different times (*t*=0-4792s). The origin of these lines is the branch point (see inset next to frame F of Figure 5.4) and the superposition is achieved by a translation factor ω_{bp} x *t*, where ω_{bp} is the branch point speed and *t* is the time. The data of Figure 5.11 shows that in the precollision stage the *s*=+1/2 lines translate uniformly without shape change in the vicinity of the branch point (see also frames C-E in Figure 5.4). Due to small fluctuations the *s*=+1 line was not

perfectly straight, which resulted in the slight deviation of the branch point from the center axis of the capillary and in small perturbations of the line shape. It is found that an exponential function, $y=\alpha' exp(-x/\beta')$ can fit the line shape very well. Figure 5.12 shows the measured line shape at t=194s and the exponential fit. The parameter α' corresponds to the position of the branch point and as discussed below β' is related to the curvature of the line and material properties of the SSY chromonic LCs. The average fitting value of β' at different times is about 42μm.

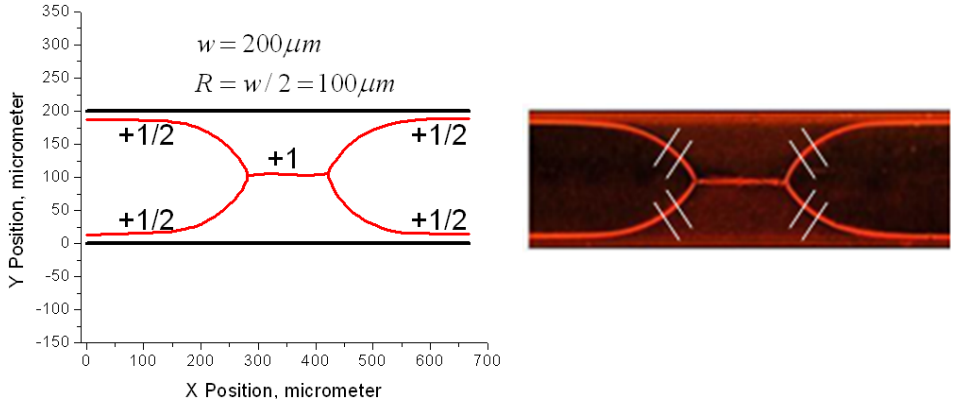

Figure 5.10. Relative positions of disclination lines inside the capillary. The +1/2 line at equilibrium is ~12.5μm away from the capillary wall. $H_\infty \approx 12.5\mu m$.

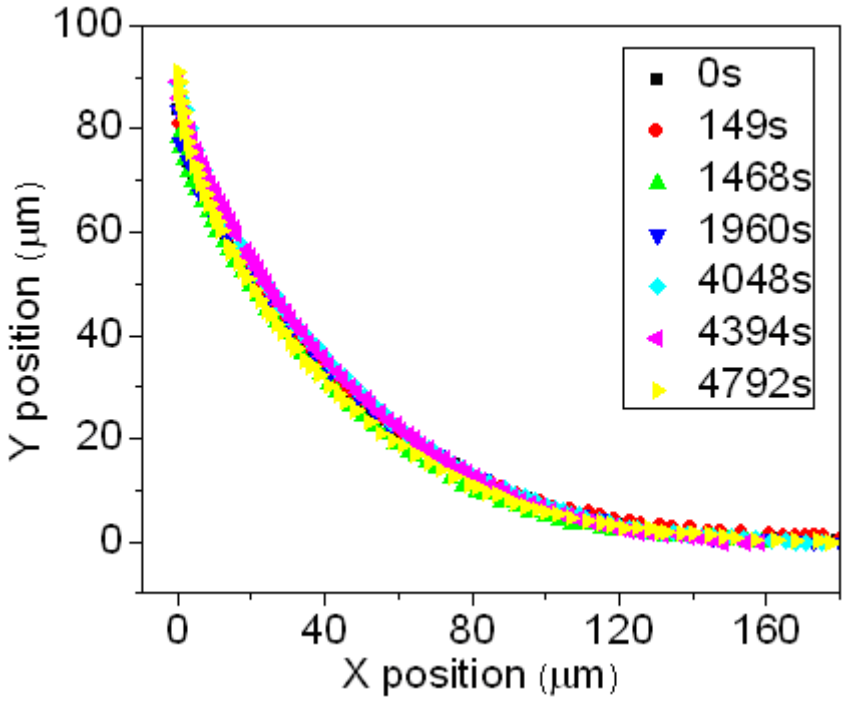

Figure 5.11. Sections of the s=+1/2 disclination lines, starting at branch point (x_{br}=0) and continuing towards the boundary of the capillary $\left(x \approx 160 \mu m\right)$.

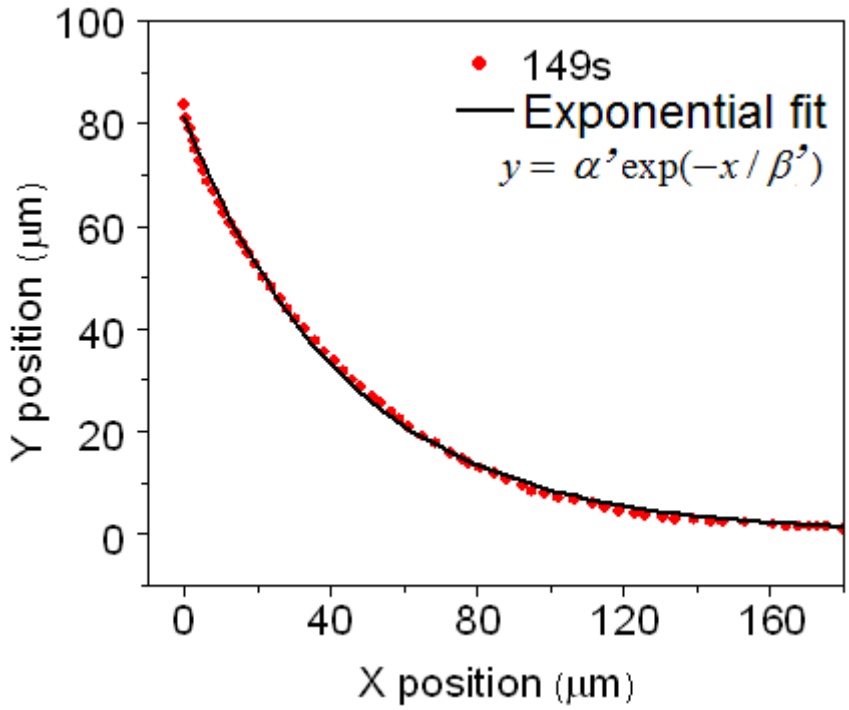

Figure 5.12. Exponential fit $y=\alpha' e^{-x/\beta'}$ of the line shape at time t=194s corresponding to the precollision regime, α' = 81.2±0.3μm, β' =44.5±0.3μm.

5.4.3 Disclination line shape relaxation in the postcollision stage

Figure 5.13 (upper #1- #4 frames) shows the relaxation of a single *s*=+1/2 after branch point collision. The lower frames show the measured shape (*y=y(x)*) and the best fit. The data shows that the relaxation is at constant shape. The disclination shape is well fitted by a sine wave with a half wave length of 200μm. The Fast Fourier Transform in Figure 5.14 confirms the sine-wave feature of the relaxation shape instead of triangular-wave shape. Figure 5.15 shows the relaxation of the amplitude H (see inset) as a function of time. The amplitude data is well fitted with $H = H_o e^{-t/\tau}$, where the time constant is $\tau = 71.4\,s$. It is noted that this phenomenon is similar to smectic A filament buckling in the early stage, which is described by exponential growth and spatial sine modulation [17, 18].

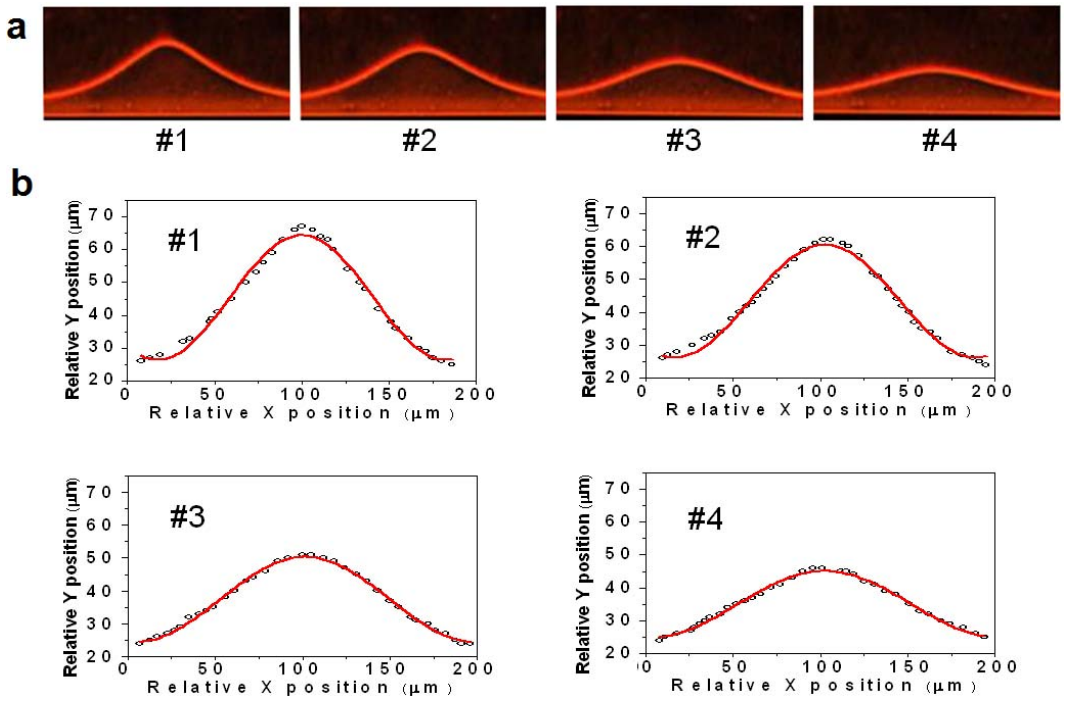

Figure 5.13. Evolution of the shape of the *s*=+1/2 lines after collision of branch points (top). a. Enlarged parts of POM images in Figure 5.4 I. b. The shapes are replotted (bottom) as circles at various times indicated by #1 to #4, and the red lines are fittings with a harmonic (sine) function $y = y_1 + y_2 \sin(\frac{\pi}{2R}x)$ with *R=W/2*=100μm.

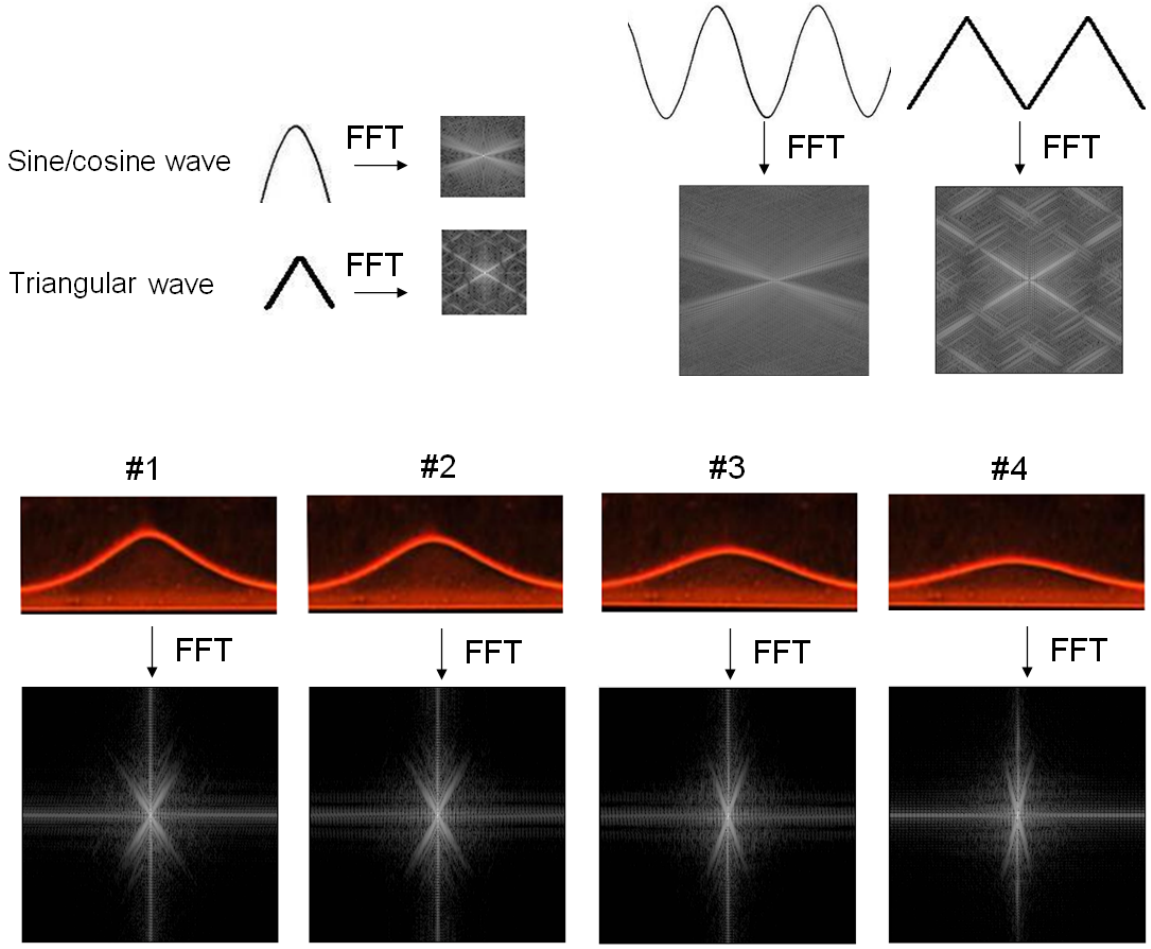

Figure 5.14. Fast Fourier Transform of typical sine/cosine shape waves and disclination waves during relaxation. According to the patterns, disclination lines have shapes closer to sine/cosine wave than triangular wave.

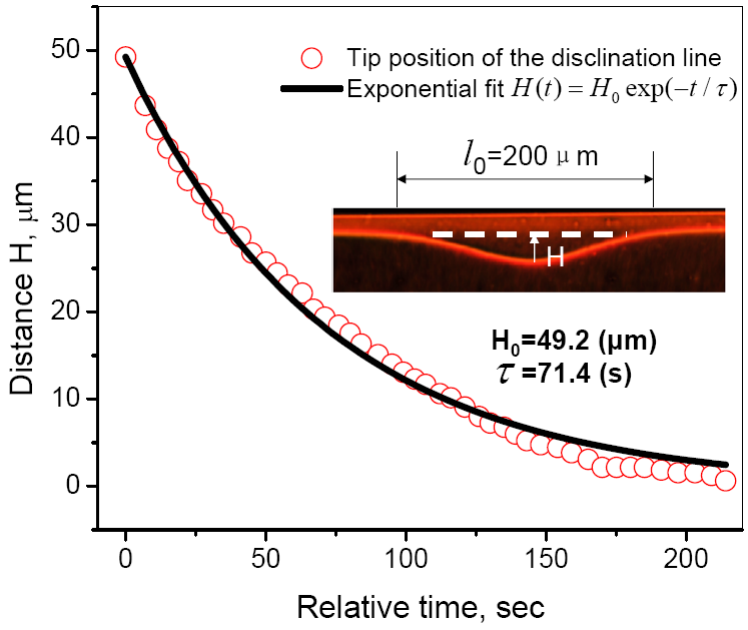

Figure 5.15. The disclination tip position *H(t)* of the *s*=+1/2 disclination line as a function of elapsed time, during the shape relaxation in the post collision regime. The full line is the exponential fit $H = H_0 e^{-t/\tau}$ and the time constant is $\tau = 71.4s$.

5.4.4 Disclination shape analysis of experimental results

Now we use equation (5.23) to predict the precollision invariant disclination shapes and the post collision relaxation process and to extract viscoelastic parameters from the experimental results summarized in Figures 5.11, 5.13 and 5.15.

(A) Precollision stage: travelling mode

From the experimental data (Figures 5.11 and 5.12) the disinclination shape around the branch point undergoes a uniform translation without shape changes. In a frame that translates with the constant disclination velocity, the linearized shape equation (5.23) is:

$$0=\gamma_o H_{xx} - k_c H_{xxxx} \tag{5.24}$$

The translating and constant shape solution is

$$H(x)=H_\infty+\left(R-H_\infty\right)e^{-x/\ell_{in}} \ , \quad \ell_{in}=1/\sqrt{\frac{\gamma_o}{k_c}} \tag{5.25}$$

where H_∞ is the equilibrium position of the 1/2 disclination and ℓ_{in} is the internal length scale of the disclination. For R=100 μm, $H_\infty \approx 12.5\mu m$, as shown in Figure 5.10. The curvature H_{xx} of the line is:

$$H_{xx} = \frac{(R - H_\infty)}{\ell_{in}^2} e^{-x/\ell_{in}} \tag{5.26}$$

The above model was built by Prof. Alejandro Rey. Fitting the experiments (Figures 5.11 and 5.12) and the model (equation (5.26)) we find the ratio of line tension γ_o and bending stiffness k_c with a value of $\gamma_0/k_c = 5.5 \times 10^8 m^{-2}$. Hence the internal length scale of the disclination is $\ell_{in} = 1/\sqrt{\gamma_0 / k_c} = 42\mu m$, which is of the same order of magnitude as the capillary half width of W/2=100μm. Since $W/2\ell_{in} \approx 2$, the importance of bending stiffness k_c in the shape selection during the precollision stage is established.

(B) Postcollision stage: relaxation mode

According to equation (5.23), after collision of two branch points, the relation of the 1/2 disclination line is given by

$$\frac{\partial H}{\partial t} = \alpha H_{xx} - \delta H_{xxxx} \tag{5.27}$$

The linearized solution of the relaxing shape around the collision point (x=0) is

$$H = H_\infty + (R - H_\infty) e^{-t/\tau} \cos qx, \quad \frac{1}{\tau} = D_\ell \left(q^2 + q^4 \bullet \ell_{in}^2\right), \quad D_\ell = \frac{\gamma_o}{\gamma_1} \tag{5.28}$$

where τ is the relaxation time, and D_ℓ is the line diffusivity. Assuming a decay vector $q = \pi/(2R)$, where R is the characteristic geometric scale (half width of the capillary W/2=100μm), the relaxation time τ is given the line diffusion term ℓ_{ex}^2 / D_ℓ times the length scale factor $1/\left(1 + \left(\ell_{in}/\ell_{ex}\right)^2\right)$:

$$\tau = \frac{\ell_{ex}^2}{D_\ell}\left(\frac{1}{1+\left(\frac{\ell_{in}}{\ell_{ex}}\right)^2}\right); \qquad \ell_{ex} = \frac{2R}{\pi} \tag{5.29}$$

where ℓ_{ex} is the external length scale. Hence measuring $\left(\tau, \ell_{ex}, \ell_{in}\right)$ gives the line diffusivity $D_\ell = \gamma_o / \gamma_1$ and the elastic bending/viscous rotation ratio: $\ell_{in}^2 D_\ell = k_c / \gamma_1$.

The above model was built by Prof. Alejandro Rey. From experimental fittings (Figure 5.15), we obtain a value for the relaxation time $\tau = 71.4\text{s}$. Using $\gamma_0 / k_c = 5.5\times10^8 m^{-2}, \tau = 71.4s$ and equation (5.29) we find the line diffusivity $\mathrm{D}_\ell = \gamma_0/\gamma_1 \approx 3.9\times10^{-11} m^2/s$ and the elastic bending/viscous rotation ratio: $k_c / \gamma_1 = \ell_{\mathrm{in}}^2 \mathrm{D}_\ell \approx 7.11\times10^{-20} m^4/s$. Using equation (5.17c) for the bending modulus $k_c = KR^2\pi/\sqrt{2}$, we also estimate the effective orientation diffusivity for director reorientations: $D_o = K/\gamma_1 \approx 3.2\times10^{-12} m^2/s$.

5.4.5 Consistency of viscoelastic parametric values

In this section we show that the experimentally fitted values: $K/\gamma_1 \approx 3.2\times10^{-12} m^2/s$, $\gamma_0/\gamma_1 \approx 3.9\times10^{-11} m^2/s$, and $k_c/\gamma_1 \approx 7.11\times10^{-20} m^4/s$ yield a orientation/line diffusivity ratio D_o / D_ℓ that is consistent with K/γ_0 values obtained from the line tension formula (equation (5.13)) [1]. The disclination core radius is $r_c \approx 10nm$, which is about two SSY columns long, if we assume an aspect ratio of 4. Thus the length is about 4 times the width 1.34nm (see Chapter Four) for the column of 1.0M SSY chromonics at room temperature. This is consistent with observation by molecular imaging of disclination cores of the lyotropic nematic phase of tobacco mosaic virus [19].

Using equation (5.13), $r_c \approx 10nm$, and the given geometry, we estimate the bulk /line elastic ratio K/γ_0 to be:

$$\frac{K}{\gamma_0} = \frac{1}{\pi s^2 \left[ln\left(\frac{R}{r_c}\right) + 1 \right]} \approx 0.1 \tag{5.30}$$

Using the experimentally fitted values $\gamma_0 / k_c \approx 5.5 \times 10^8 m^{-2}$, $k_c / \gamma_1 \approx 7.11 \times 10^{-20} m^4 / s$ and $K / \gamma_1 \approx 3.2 \times 10^{-12} m^2 / s$, we calculated the bulk/line elastic tension ratio (or diffusivity ratio) $D_o / D_\ell = K / \gamma_0 \approx 0.08$. The agreement between the theoretical value from statics (equation (5.30)) and those obtained from our dynamic experiments and modeling is quite satisfactory.

Assuming the Frank elastic constant $K \approx 10 pN$, which is a measured value for a well-studied chromonic LC-DSCG by dynamic light scattering [20], we find that the bare line tension is $\gamma_0 \approx 100 pN$, the bending modulus is $k_c \approx 2 \times 10^{-7} pN \cdot m^2$, and the rotational viscosity is $\gamma_1 \approx 3 Pa \cdot s$ for the SSY chromonic LC. Compared to the bulk elastic constant *K*, the disclination tension γ_0 in the SSY chromonic LC is larger by a factor of 10. Its rotational viscosity γ_1 is larger than that of typical thermotropic liquid crystals, for example γ_1 is 0.15 $Pa \cdot s$ at 20°C and 0.11 $Pa \cdot s$ at 25°C for MBBA [21]. It is consistent with the reported values of another chromonic liquid crystal, disulfoindanthrone/water system, for which the twist elastic constant K_{22}, agrees within an order of magnitude with those for thermotropic nematics but the rotational viscosity deviates by 2 orders of magnitude [22].

5.4.6 Conclusions

Theory and experiment were integrated to characterize texture transformations and defect processes under capillary confinement, and to use defect shapes to determine

viscoelastic material data for SSY chromonic liquid crystals. Using capillary confinement under strong anchoring, defect instabilities involving the transformation between high (s=+1) and low strength (s=+1/2) disclinations were monitored using optical microscopy. The essential feature of the instability is the two s=+1/2 lines that are curved in the bifurcation region. In the precollision stage, neighboring branch points approach each other, but the shapes of the s=+1/2 lines remain invariant. After the branch point collision, the four s=+1/2 lines merge and pinch off into a pair that eventually relaxes in two straight lines. The shape relaxation from curved to straight lines is exponential and the shape is invariant and sinusoidal. The measured defect shapes are analyzed using a high strength disclination shape equation that includes tension and bending stresses. The presence of bending stresses is shown to be essential in describing disclination branching and relaxation. When fitting the experiment to the precollision stage, the internal length scale $\ell_{in} = \sqrt{k_c / \gamma_0}$ was found to be of the order of the capillary half-width. When fitting the experimental to the postcollision relaxation stage, the director diffusivity $D_o = K / \gamma_1$, the line diffusivity $D_\ell = \gamma_0 / \gamma_1$ and the elastic bending/viscous rotation ratio: $k_c / \gamma_1 = \ell_{\text{in}}^2 \mathrm{D}_\ell$ were found. Consistency was established by comparing the diffusivity ratio D_o / D_ℓ with the elasticity ratio K / γ_0 found from the standard line tension formula. Finally, by adopting a Frank elasticity estimate, the rotational viscosity γ_1 was found to be an order of magnitude larger than for nematic thermotropes. In all, we have shown that modeling and experiments of defects under confinement yield a comprehensive viscoelastic property set of chromonics solely based on self-organization, anisotropy, and response to surfaces.

5.5 Point defects on the disclination line

Oswald et al observed point defects distributed on disclination lines in three systems [23-25]: (i): 8CB (4-octyl-4'-cyanobiphenyl) liquid crystal in the nematic phase was

partially filled between two glass plates with a uniform spacing between them and treated to induce homeotropic anchoring. Point defects of opposite signs can alternately nucleate on the disclination line that forms near the free surface of a confined 8CB nematic liquid crystal. Metastable configurations consisting of periodic repetitions of such defects existed. These configurations were characterized by a minimal interdefect spacing that is seen to depend on sample thickness and on an applied electric field. The time evolution of the defect distribution suggests that the defects attract at small distances and repel at large distances [23]. Figure 5.16 shows the related images from the reference for explanation. (ii). Formation of point defect distributions on a disclination line was controlled by directional melting from the Smectic A phase of 8CB to nematic phase in a temperature gradient [24]. (iii). Chiral additives in the nematic 8CB altered the dynamics of point defects moving on a disclination line. They exerted a constant force on defects, leading to the bimodal distribution of distances between them at long times. The evolution of the system of defects in the presence of chiral additives provides a very direct proof of the existence of repulsive forces between the defects at large distances. They also found that addition of a sufficient amount of chiral compound removed all point defects from the system [25].

During the formation of monodomain, point defects were also observed on the center disclination line, as shown in Figure 5.17 and 5.18. It is obvious that these point defects were best visualized with polarizer and analyzer. From that the brushes appear alternatively on the two sides of the center disclination line and also based on the feature of optical textures of the alternative points, it is likely that negative and positive point defects are neighboring to each other on the line. In the Figure 5.19, red points and blue stars are used to represent two consecutive point defects to schematically show the relative positions. During the shrinkage of the center disclination line and growth of the

uniform domains, point defects remain in the same position. They were stable until the moving uniform domains reached them and consumed them. In Figure 5.20, we also tried to plot the distribution of separation distances between two consecutive point defects for the case of A in the Figure 5.19. The average distance is about 46.7μm and the minimum distance is about 26μm. We can speculate that if the distance is less than 26μm, the neighboring positive and negative defect points would attract and annihilate each other, thus being unstable for very close defect points to exist.

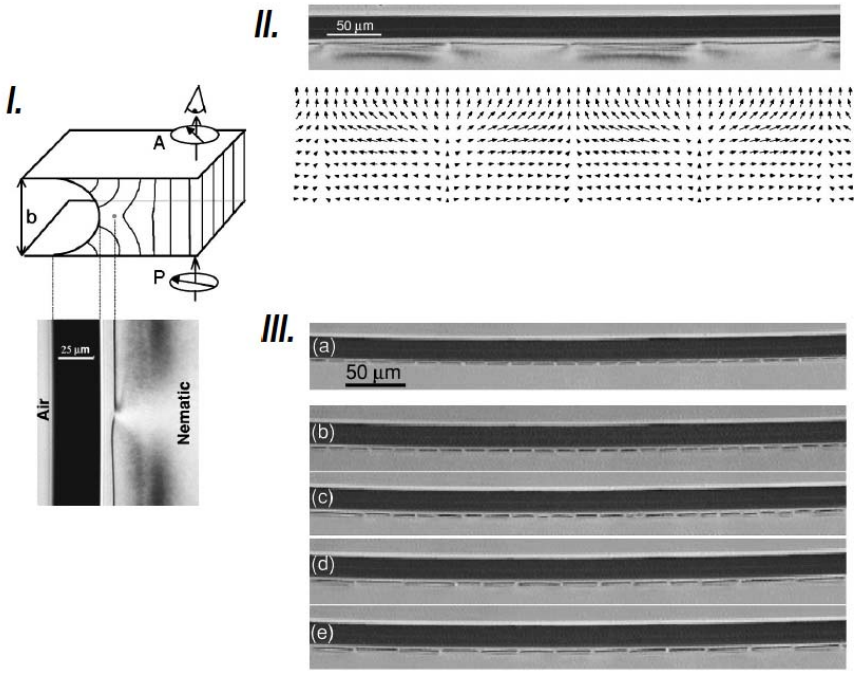

Figure 5.16. I. A disclination line forms in the vicinity of the free interface of the 8CB nematic liquid crystal confined between two plates with a uniform spacing b between them and treated to induce a homeotropic anchoring. Top view of an actual sample, where b=100μm, was observed with a polarizing microscope with the polarizer and the analyzer partially crossed. II. Top: top view image of the region near the N/air interface in a b=50 μm sample observed between partially crossed polarizers. Note that the optical properties of the nematic phase alternate between consecutive point defects. Bottom: XY projection of the director field of the nematic phase near the midplane (z=0) of the sample. III. Top view of a sample during the reorganization of the defect distribution after a quench of the electric field into an unstable configuration. (a). Initial equilibrium distribution at voltage equal to 2.26 V. (b). Suddenly quenched to voltage equal to 0.86 V. (c), (d) and (e) are 20 s 70 s and 240 s after the quench, respectively. All I, II and III are from reference [23].

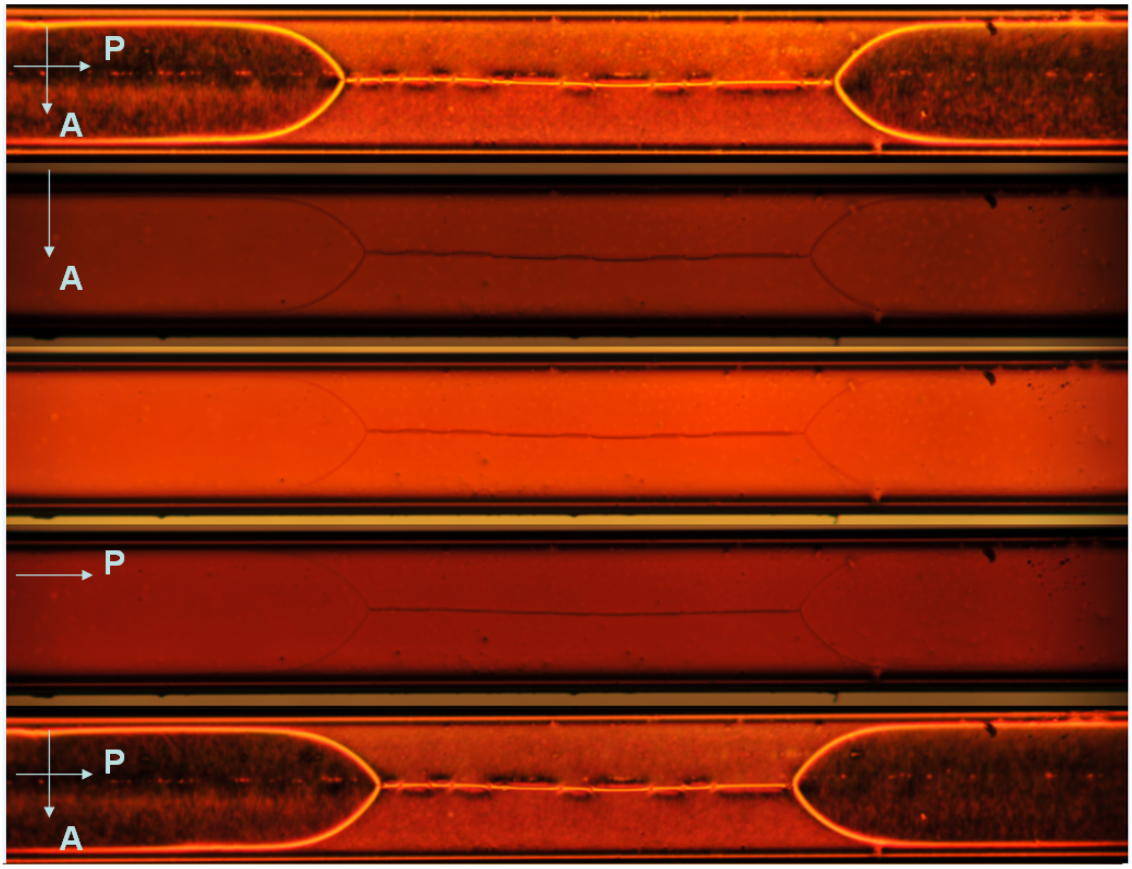

Figure 5.17. POM images of point defects on the center disclination line with or without polarizer or analyzer. Note that the center disclination line was shrinking and uniform domains were growing or expanding with time. Capillary width is 200μm. The time duration between the first and last POM images is 492s, during which the center disclination line shrunk 111μm totally; the moving speed of branch point is about 0.11μm/s.

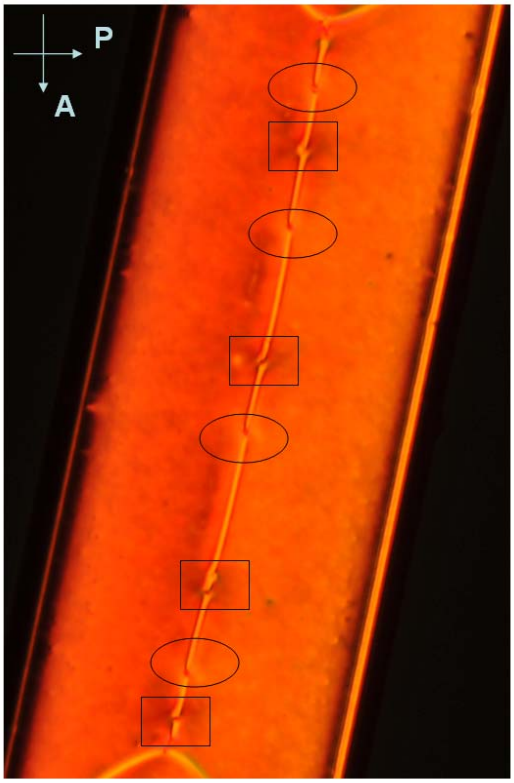

Figure 5.18. Enlarged POM image of point defects on the center disclination line.

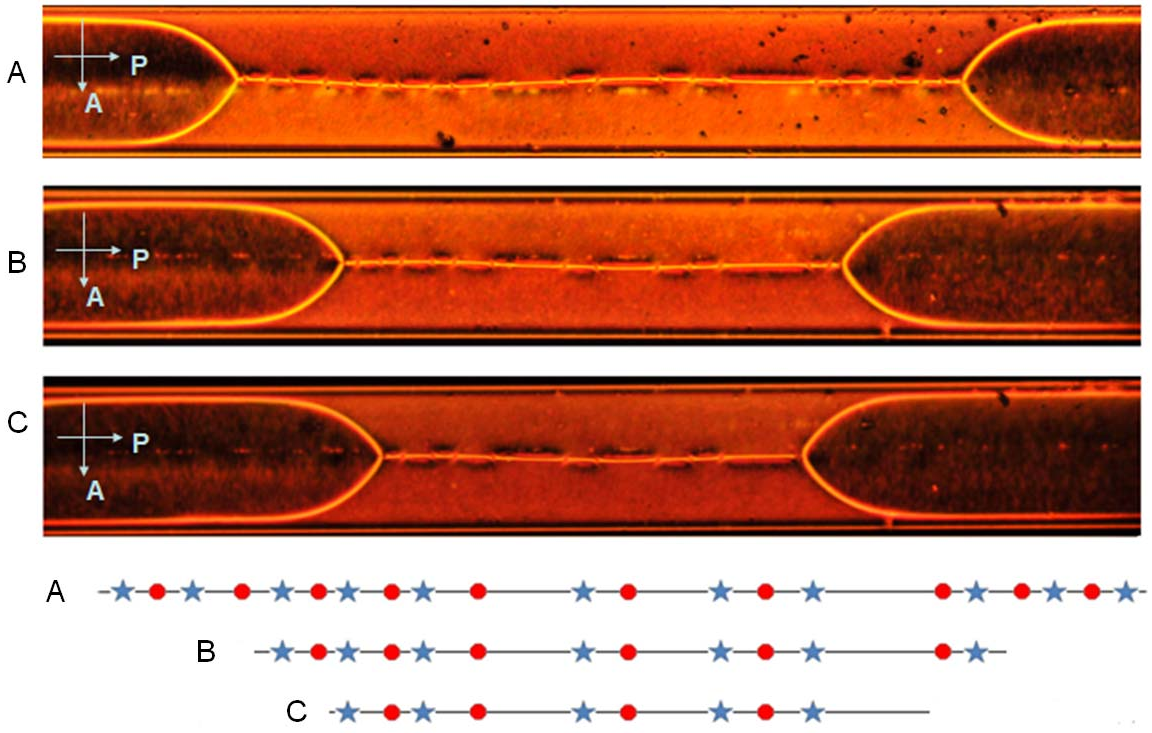

Figure 5.19. Point defects distribution on the center disclination line at different times. Red points and blue stars are used to represent two neighboring point defects for case A, B and C. Length of center disclination line in A is 972μm, in B 690 μm, in C 579 μm. The time duration between A and B is 1274s, during which the center disclination line shrunk 282μm totally; the time duration between B and C is 492s, during which the center disclination line shrunk 111μm totally. The moving speed of branch point is about 0.11μm/s.

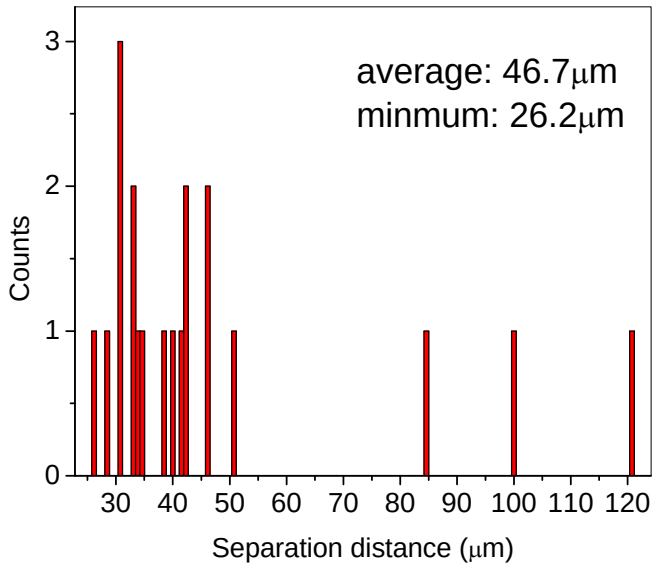

Figure 5.20. Histogram of distribution of separation distances between two neighboring point defects for the case of A in the Figure 5.19.

We can't rule out the possibility that some dust or impurities were captured by the center disclination line and lowered the energy of the system. Other unknown sources may also probably have contributed to perturb the director field in the vicinity of the center disclination line and to promote the nucleation of point defects. Further study on the formation of point defects on the lines is necessary.

5.6 Summary

In this chapter, we summarized statics and dynamics of defects of 1.0M SSY chromonics in a flat capillary (20μm/200μm/5cm) with ribbon geometry during the formation of monodomain. Small uniform areas grew and coarsened leading finally to a monodomain formed throughout the capillary. If the small uniform areas happened to be

far away from each other, it was observed that they were linked by a long center disclination line. The uniform areas were the result of the splitting of the *s*=+1 line into a pair of *s*=+1/2 lines at a branching point, which was moving along the long axis of the capillary at a constant speed 0.11μm/sec. By studying the kinematics of the branch point, we were able to theoretically estimate the speed to be on the order of 10^{-1} μm/sec, which matches very well with the experimental value. Before the collision of branch points, that is, in the precollision stage, the shapes of the *s*=+1/2 lines remained invariant. After the branch point collision, the four *s*=+1/2 lines merged and pinched off into a pair that eventually relaxed into two straight lines. Models were built for both the line shape in the precollision stage and the relaxation process in the postcollision stage. By integrating theory and experiments, a comprehensive viscoelastic property set of chromonics was obtained, as summarized in Table 5.1. The random distribution of point defects on the center disclination line was also observed. However, the formation mechanism needs further study.

Table 5.1. Summary of disclination line and bulk properties of 1.1 M SSY chromonics based on our study.

Properties of 1.1M SSY chromonics	Values
internal length scale of the disclination	$\ell_{in} = 1/\sqrt{\gamma_0 / k_c} = 42\mu m$
line tension/bending stiffness ratio	$\gamma_0 / k_c = 5.5x10^8 m^{-2}$
line diffusivity	$D_\ell = \gamma_0 / \gamma_1 \approx 3.9\times10^{-11} m^2 / s$
elastic bending/viscous rotation ratio	$k_c / \gamma_1 = \ell_{in}^2 D_\ell \approx 7.11\times10^{-20} m^4 / s$
effective orientation diffusivity for director reorientations	$D_o = K / \gamma_1 \approx 3.2\times10^{-12} m^2 / s$
bulk/line elastic tension ratio (or diffusivity ratio)	$D_o / D_\ell = K / \gamma_0 \approx 0.08$
the bare line tension	$\gamma_0 \approx 100 pN$, assuming $K \approx 10 pN$
the bending modulus	$k_c \approx 2\times10^{-7} pN \cdot m^2$, assuming $K \approx 10 pN$
rotational viscosity	$\gamma_1 \approx 3 Pa \cdot s$, assuming $K \approx 10 pN$

5.7 References

[1] Golmohammadi, M., and Rey, A. D. Structural modeling of carbonaceous mesophase amphotropic mixtures under uniaxial extensional flow. Journal of Chemical Physics **2010**, 133, 034903/1-034903/11.

[2] Grecov, D., and Rey, A. D. Computational rheology of carbonaceous mesophases. Carbon **2004**, 42, 1257.

[3] Yan, J., and Rey, A. D. Theory and simulation of texture formation in mesophase carbon fibers. Carbon **2002**, 40, 2647.

[4] Yan, J., and Rey, A. D. Texture formation in carbonaceous mesophase fibers. Physical Review E **2002**, 65, 031713.

[5] Yan, J., and Rey, A. D. Modeling elastic and viscous effects on the texture of ribbon-shaped carbonaceous mesophase fibers. Carbon **2003**, 41, 105-121.

[6] Crawford, G. P., Allender, D. W., and Doane, J. W. Surface elastic and molecular-anchoring properties of nematic liquid crystals confined to cylindrical cavities. Physical Review A: Atomic, Molecular, and Optical Physics **1992**, 45(12), 8693-708.

[7] Bradac, Z., Kralj, S., Svetec, M., and Zumer, S. Annihilation of nematic point defects: Postcollision scenarios. Physical Review E: Statistical, Nonlinear, and Soft Matter Physics **2003**, 67(5-1), 050702/1-050702/4.

[8] Svetec, M., Bradac, Z., Kralj, S., and Zumer, S. Hedgehog annihilation in a confined nematic liquid crystal. Molecular Crystals and Liquid Crystals **2004**, 413, 2179-2187.

[9] De Luca, G., and Rey, A. D. Point and ring defects in nematics under capillary confinement. Journal of Chemical Physics **2007**, 127(10), 104902/1-104902/11.

[10] de Gennes, P. G. The Physics of Liquid Crystals, **1974**, Clarendon, Oxford, 347 pp.

[11] Mulder, B. M. Solution of the excluded volume problem for biaxial particles. Liquid Crystals **1986**, 1, 539-551.

[12] Straley, J. P. Ordered phases of a liquid of biaxial particles. Physical Review A **1974**, 10, 1881-1887.

[13] Gurtin, M. E. Thermomechanics of Evolving Phase Boundaries in the Plane. **1993**, Clarendon: Oxford.

[14] Rey, A. D. Capillary models for liquid crystal fibers, membranes, films, and drops. Soft Matter **2007**, 3, 1349.

[15] Cheong, A. G., and Rey, A. D. Cahn-Hoffman capillarity vector thermodynamics for curved liquid crystal interfaces with applications to fiber instabilities. Journal of Chemical Physics **2002**, 117, 5062.

[16] Rey, A. D. Nematostatics of triple lines. Physical Review E: Statistical, Nonlinear, and Soft Matter Physics **2003**, 67(1-1), 011706/1-011706/14.

[17] Rey, A. D., and Abukhdeir, N. M. Mechanical model for filament buckling and growth by phase ordering. Langmuir **2008**, 24, 662

[18] Rey, A. D., and Abuklideir, N. M. Flow perturbation model for filament buckling. Journal of Non-Newtonian Fluid Mechanics **2008**, 153, 177.

[19] Zasadzinski, J. A. N., and Meyer, R. B. Molecular imaging of tobacco mosaic virus lyotropic nematic phases. Physical Review Letters **1986**, 56, 636.

[20] Nastishin, Yu., Neupane, K., Baldwin, A. R., Lavrentovich, O. D., and Sprunt, S. Elasticity and viscosity of a lyotropic chromonic nematic studied with dynamic light scattering. arXiv.org, e-Print Archive, Condensed Matter **2008**, 1-4, arXiv: 0807. 2669v1.

[21] Kneppe, H., Schneider, F., and Sharma, N. K. Rotational viscosity-gamma-1 of nematic liquid crystals. Journal of Chemical Physics **1982**, 77, 3203.

[22] Golovanov, A. V., Kaznacheev, A. V., and Sonin, A. S. Viscoelastic properties of a lyotropic chromonic nematic. Molecular Crystals and Liquid Crystals Science and Technology, Section C: Molecular Materials **1993**, 3(2), 147-155.

[23] Ignes-Mullol, J., Baudry, J., and Oswald, P. Formation and distribution of point defects on a disclination line near a free nematic interface. Physical Review E: Statistical, Nonlinear, and Soft Matter Physics **2001**, 63(3-1), 031701/1-031701/9.

[24] Ignes-Mullol, J., Scurtu, L., and Oswald, P. Controlled nucleation of point defects on a disclination line near a free surface during smectic-A-to-nematic directional melting. European Physical Journal E: Soft Matter **2003**, 10(3), 281-288.

[25] Zywocinski, A., Pawlak, K., Holyst, R., and Oswald, P. Chirality-biased point defects dynamics on a disclination line in a nematic liquid crystal. Journal of Physical Chemistry B **2005**, 109(19), 9712-9718.

CHAPTER 6

CONDUCTING CHROMONICS

6.1 Introduction

Perylene monoimides and diimides have been attracting considerable attention as the best air stable n-type organic semiconductors, highly efficient fluorophores and lightfast colorants, etc [1-10]. Perylene-3,4,9,10-tetracarboxylic dianhydride (PTCDA) is usually used as the parent compound for perylene derivatives. Figure 6.1 shows the structure and the van der Waals dimension of PTCDA [11]. Their behavior can even be tuned from n-type to p-type by controlling the substituents. "Bay-area" substituents affect both optical and electronic properties; imide substituents have little effect on molecular-level optical and electronic properties but can affect aggregation and solubility [12]. Figure 6.2 shows the substituent positions. Tam-Chang's group [13-29] and others [30-31] molecularly designed chromonic liquid crystals based perylene monoimides and diimides for fabrication of anisotropic optical materials, for examples, broad spectrum polarizing materials [16, 18-22] and highly anisotropic fluorescent films [25]. Most of those perylene based chromonic liquid crystals have not been thoroughly and widely studied due to the lack of commercial availability. They are of our great interest due to their combination of liquid crystalline and conducting behavior and water solubility. This Chapter summarizes our studies on a synthesized ionic diimide perylene compound which exhibits a liquid crystalline phase.

Dip-coating experiments were done in collaboration with Dr. Mahmoud A Mahmoud in Prof. Mostafa El-Sayed's lab. Gold nanoparticle coated substrates for SERS were also provided by Dr. Mahmoud A Mahmoud. Electronic measurements were done in collaboration with Dr. Qizhen Liang in Prof. C. P. Wong's lab.

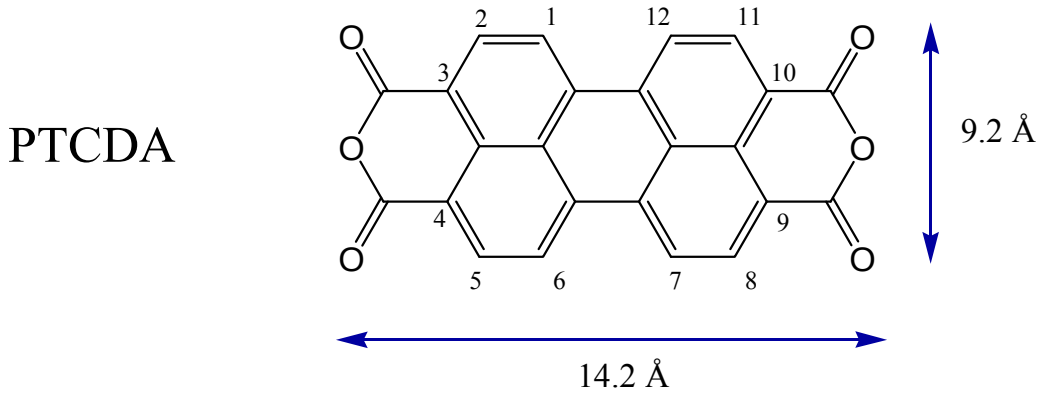

Figure 6.1. Molecular structure and van der Waals dimension of perylene-3,4,9,10-tetracarboxylic dianhydride (PTCDA) [11].

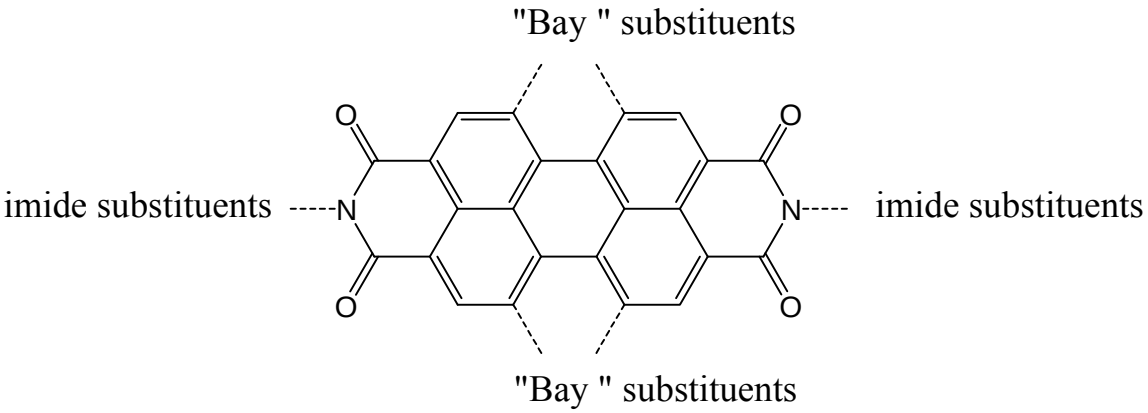

Figure 6.2. Substituent positions of perylene-3,4,9,10-tetracarboxylic acid diimide derivatives (PDIs).

6.2 Synthesis and characterization of an ionic perylene compound

Symmetrically *N, N'*-disubstituted perylene-3,4,9,10-tetracarboxylic acid diimide derivatives (PDIs) are accessible by the condensation of PTCDA with appropriate primary amines. An ionic compound, a derivative of perylene-3,4,9,10-tetracarboxylic diimides (PDI) in Figure 6.3 has been synthesized according to Tam-Chang's method [28, 29]. Perylene-3,4,9,10-tetracarboxylic dianhydride (PTCDA) and *N, N*-diethylethylenediamine (DEDA) were purchased from Sigma-Aldrich and used without further purification. PTCDA (5 grams) and DEDA (30ml) were mixed and refluxed for 26 hours and then cooled down. Methanol (50ml) was added to the reaction flask and boiled with the reaction mixture for 30 minutes. The reaction mixture was filtered and washed with additional methanol and diethyl ether. The solid b in Figure 6.3 was dried in a vacuum oven and yielded about 7 grams (yield 93%). Aqueous solutions of compound c were prepared in situ by dissolving compound b in dilute HCl containing two equivalents of HCl.

Characterization of bis-(*N*, *N*-diethylaminoethyl)perylene-3,4,9,10-tetracarboxylic diimide (compound b) was done by Fourier transform infrared spectroscopy (FTIR) and nuclear magnetic resonance (NMR) spectroscopy. The FTIR spectrum of b dispersed in a KBr matrix is compared with that of PTCDA before reaction, as illustrated in Figure 6.4. Absorption peaks for b are: 2968, 2808, 1701, 1653, 1592, 1575, 1439, 1405, 1355, 1342, 1245, 1169, 806, 797 and 746 cm^{-1}. Due to reaction, 1750-1810 range assigned to OC-O-CO of PTCDA shows no peak in the spectrum of b. Its structure was confirmed by this disappearance of the anhydride C=O vibration bands at 1743 and 1774 cm^{-1} and appearance of imide C=O stretching vibration bands at 1653 and 1701 cm^{-1}. Trifluoroacetic acid-d (CF_3COOD) was used as a solvent for b in ^1H NMR measurement, based on the chemical shifts and relative numbers of ^1H at different chemical environments, experimental ratios (H1+H2): H3: H4: H5: H6=8.47: 4.42: 4.05: 8.61:

12.54, are close to theoretical ones (H1+H2): H3: H4: H5: H6=8: 4: 4: 8: 12, as shown in Figure 6.5. Therefore, the ^{1}H NMR spectrum of b also confirms the structure of b.

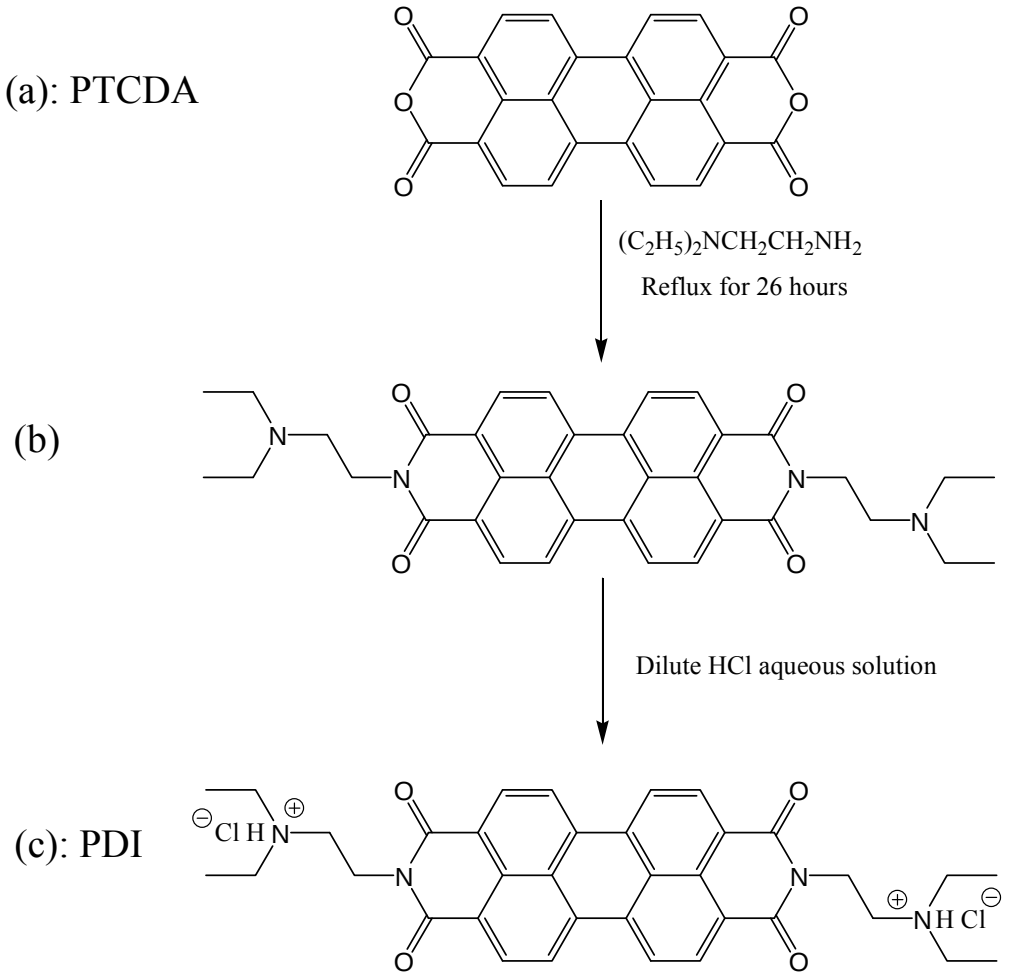

Figure 6.3. Methods of synthesis for anionic perylene tetracarboxylic diimides [28, 29].

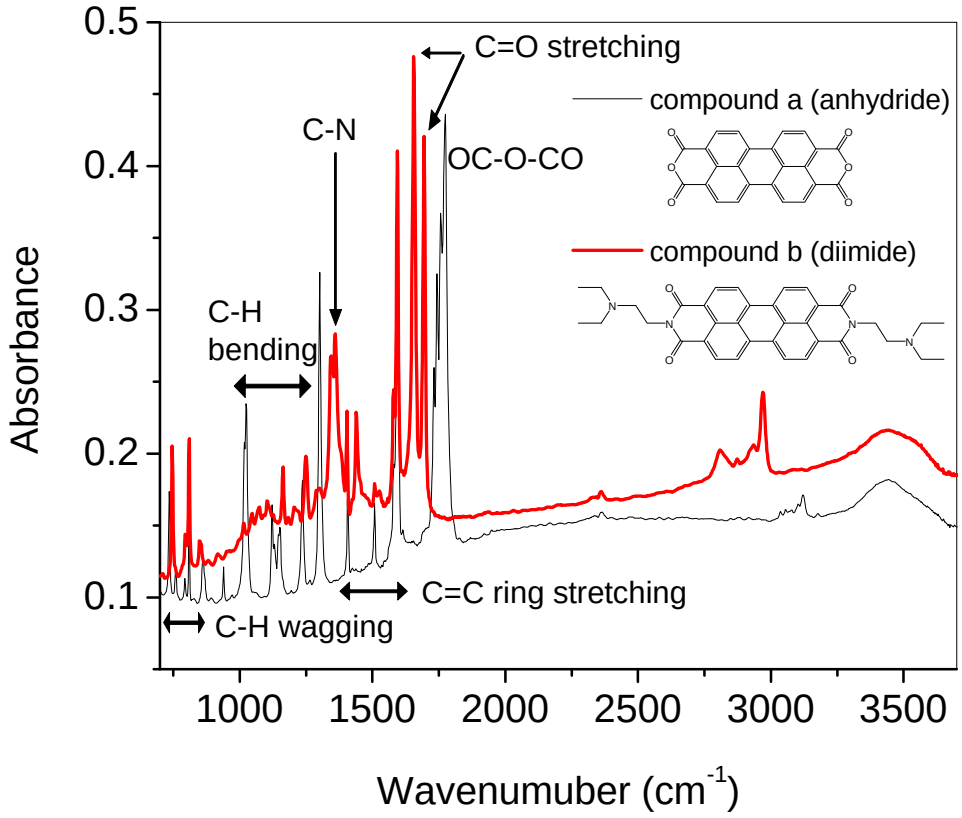

Figure 6.4. FTIR spectra of compound a and b.

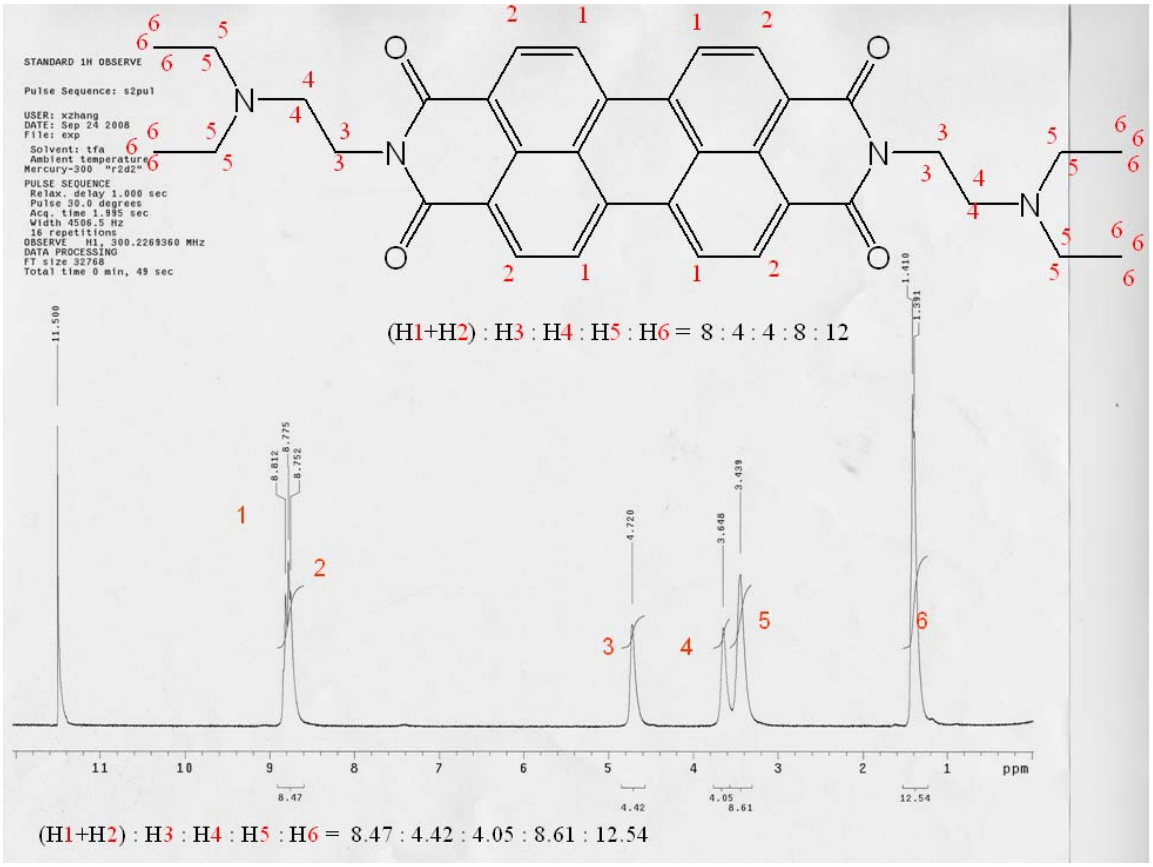

Figure 6.5. ^{1}H-NMR spectrum of compound b in trifluoroacetic acid-d (CF_3COOD) (at ambient temperature; H1 300MHz).

6.3 Chromonic liquid crystalline behavior

For compound c (PDI) aqueous solutions at dilute concentrations, absorbance increases as concentration increases; however, the absorption coefficient, calculated by the Beer-Lambert Law, actually decreases as the concentration increases, as shown in Figure 6.6, which is also an evidence of aggregation. According to a conference report on x-ray studies of PDI, models of PDI columns were proposed where there is only one PDI molecule in the cross section of columns and neighboring molecules have a titled angle between them, instead of stacking exactly on top of each other [32].

Figure 6.7 shows the phase diagram of compound c (PDI) in water. The phase transition was judged by observing the change of textures of cells filled with PDI aqueous solutions under POM with crossed polarizer and analyzer, while the sample cells were heated with rate 0.4ºC/min controlled by a Linkam THM 600 hot stage with accuracy of 0.1°C. The phase transition temperature of very high concentrations was close to the boiling point of water hence was not measurable reliably. For the SSY/water system, the biphasic region is about 10ºC for each concentration measured as shown in Chapter 2; while for PDI/ water system, the biphasic region is about 5ºC for each concentration as shown in Figure 6.7. Figure 6.8 shows the textures of PDI/water systems in different phases made with different concentrations at room temperature.

PDI chromonics, just like other lyotropic liquid crystals, are difficult to be aligned into a monodomain. Using rubbed polyimide coated glass cells (commonly for obtaining planar aligned thermotropic liquid crystals) and we were able to obtain planar alignment with area about 400μm x 300μm, as shown in Figure 6.9. The white line indicates the rubbing direction of polyimide. The periodic intensity change accompanying the rotation of sample under crossed polarizer and analyzer confirmed the planar alignment of PDI chromonics. The equation describing the transmitted light intensity under crossed polarizer and analyzer is given as equation (1.6) in Chapter One.

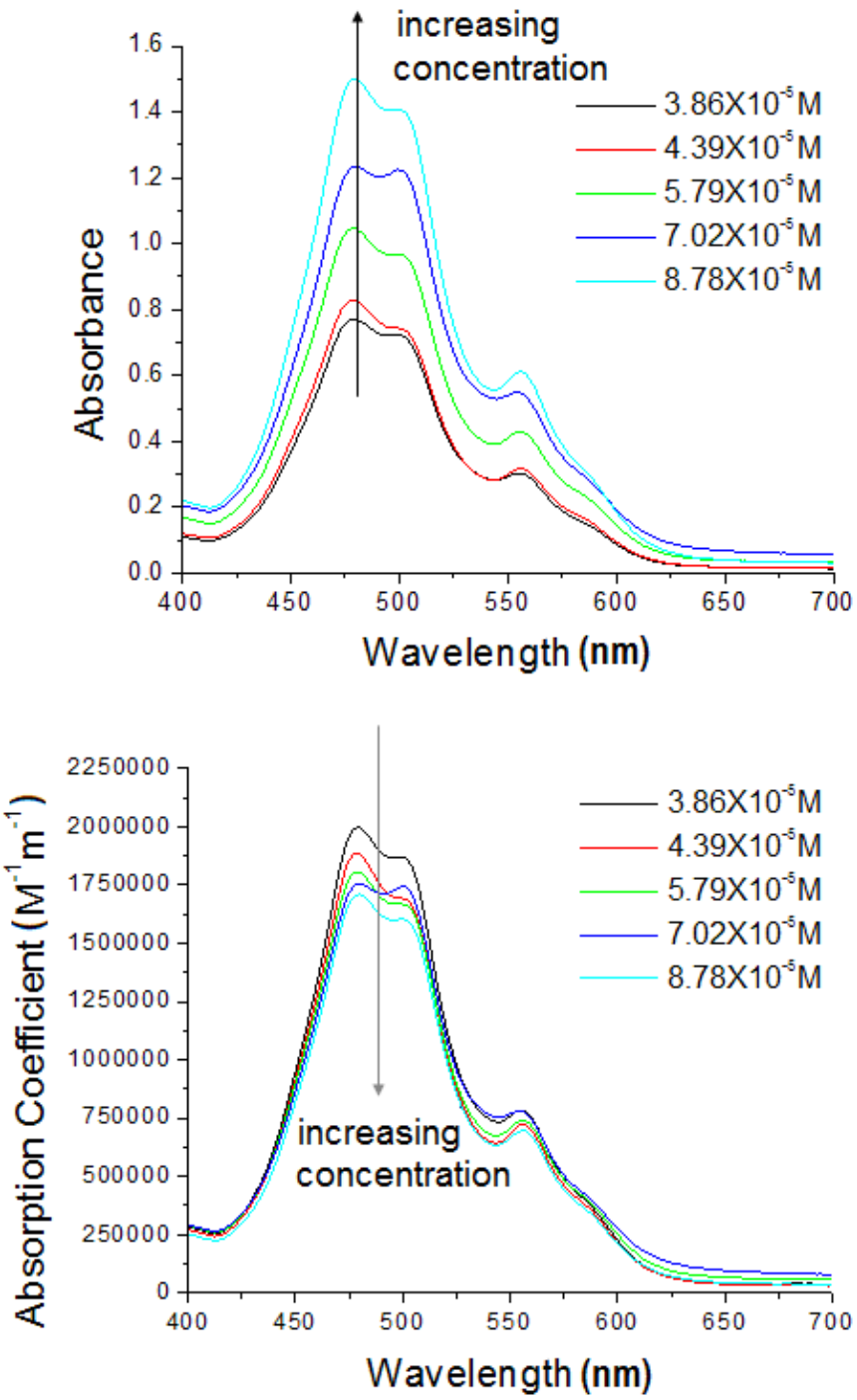

Figure 6.6. Absorption of PDI (c) dilute aqueous solutions in the visible range.

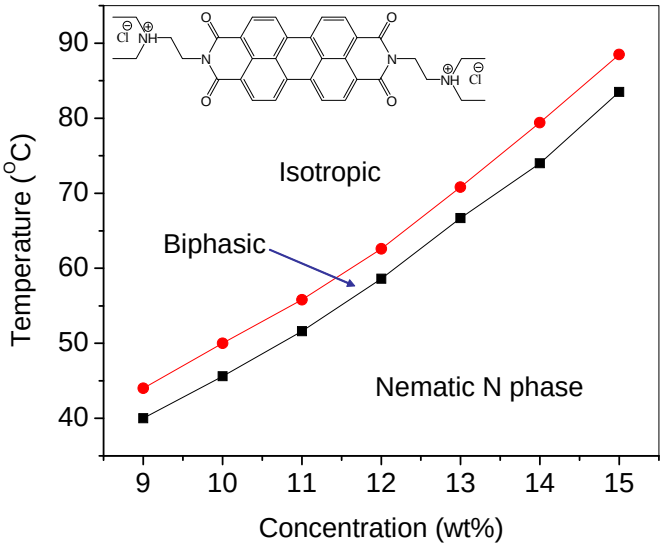

Figure 6.7. Phase diagram of PDI (c) in water with heating rate 0.4°C/min. Sample temperatures were controlled by a Linkam THM 600 hot stage with accuracy of 0.1°C.

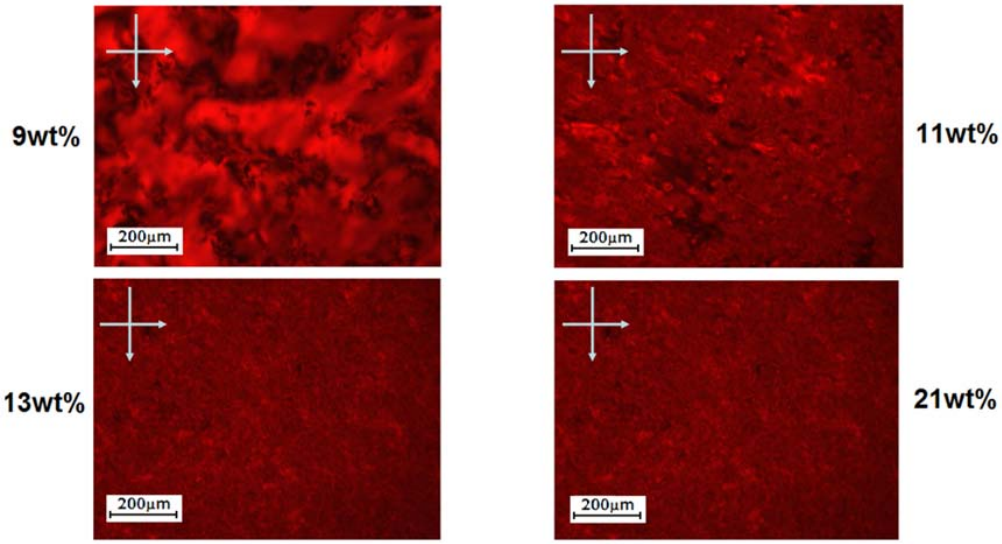

Figure 6.8. POM images of PDI (c) aqueous solutions with different concentrations in uncoated glass cells with thickness 10μm under crossed polarizer and analyzer at room temperature.

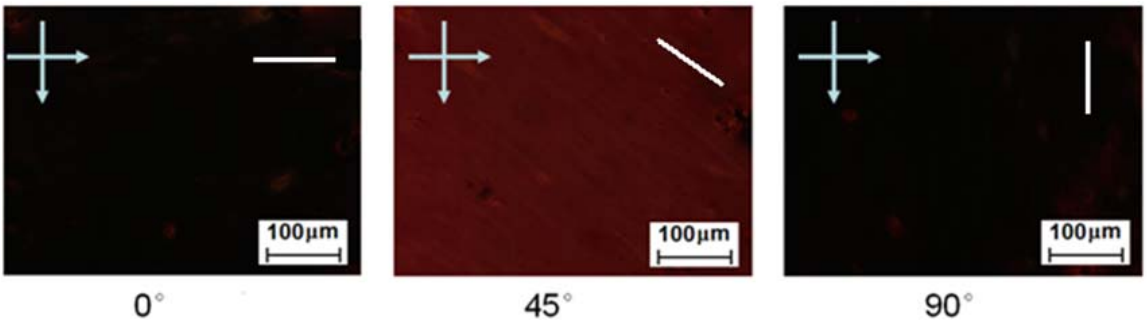

Figure 6.9. POM images of a planar aligned area of 9wt% PDI chromonics in a coated glass cell with thickness 10μm under crossed polarizer and analyzer (arrows) at room temperature. The glass cell was coated with polyimide and rubbed in the direction along the white line.

6.4 Thin films of perylene chromonics in sensor application

6.4.1 Preparation of thin films on glass substrates

Various coating methods are commonly used for concentrated liquid deposition processes in industry [33-36]. Previous research in our group has been worked on coating on cylindrical objects (forced coating of isotropic [37] and nematic [38] solutions on polymer fibers) and on butterfly wing scales [39]. For planar substrates, dip-coating and spin-coating are widely used to produce homogeneous coatings [40, 41]. We chose to use dip-coating method to coat PDI solutions on flat surfaces in this Chapter, as it produces no waste, and more importantly, it is a "mild" technique without using strong external forces and keeps the original aggregation structure of chromonics, while spin-coating doesn't have these advantages [42-44]. There are models to describe the formation of a homogeneous fluid layer by dip-coating. For example, the Landau-Levich model predicts that the thickness of a Newtonian and non-evaporating fluid on the surface of the

substrate depends on the density, the surface tension, and the viscosity of the fluid and is proportional to the withdrawal speed at a power of 2/3 [42]. Faustini et al [43] presented a simple experimental study of non-Newtonian fluids associated with time-dependent evaporation-induced concentration and viscosity gradients in the solution. They show that two regimes of film formation independently exist at extreme withdrawal speeds: the capillarity regime (governed by interdependent evaporation and capillarity rise at lower speeds) and the draining regime (governed by gravity-induced viscous drag at higher speeds), as illustrated in Figure 6.10 [43]. They combine into a third regime at intermediate speeds [43].

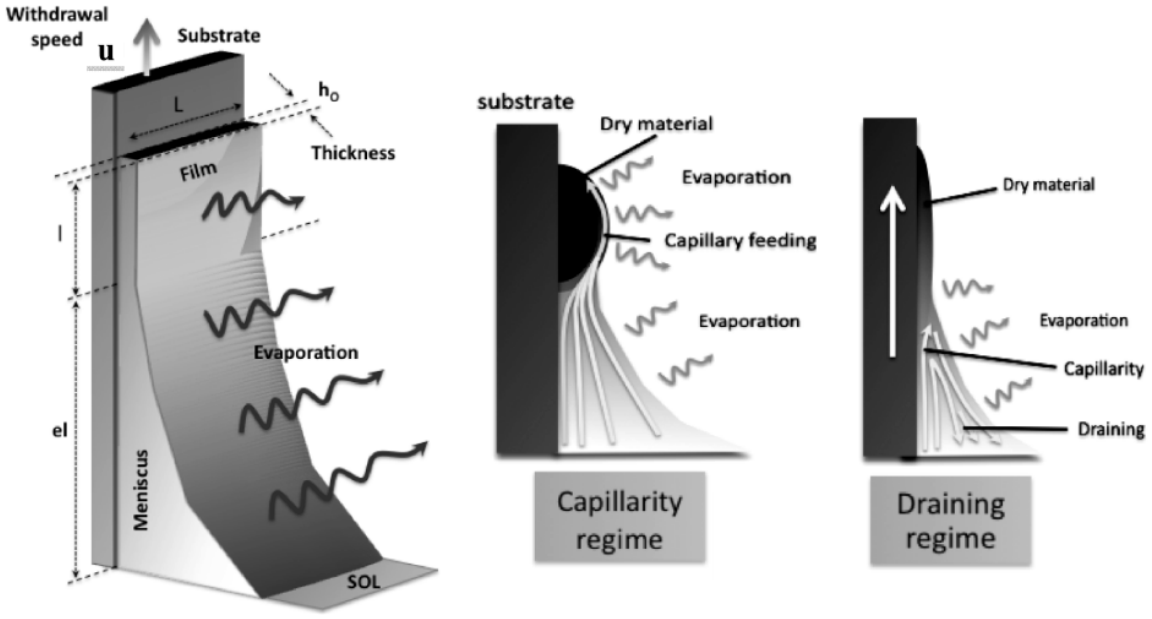

Figure 6.10. Schemes of dip-coating method and both capillarity and draining regimes involved at low and fast withdrawal speeds, respectively. Images are from reference [43].

We made dried chromonic films from dilute PDI solutions on glass substrates by the dip-coating method, as shown in Figure 6.11. The glass substrate (18mm x18mm, cover glass from VWR®) was dipped into the PDI solution first and then was withdrawn from it at a constant speed controlled by the computer under the atmospheric condition. Figure 6.12 shows the contact angle produced by PDI solutions, 7wt% and 17wt%, on the glass substrates, with contact angles ~66.6º and ~75.5º, respectively. Solutions at lower concentration spread more uniformly on the glass surface; as we know, if it is a pure water drop, it spreads easily on the glass surface. In order to get a homogeneous film, the PDI solution has to be very dilute. When concentrated PDI solutions in the nematic N phase are used, the coated films are never homogeneous. In our experiments, the thinnest (close to monolayer) and homogeneous films are obtained by using 0.75wt% dilute PDI solution with withdrawing speed of 1.0 mm/min, that is, ~16.7 μm/sec. Atomic force microscopy (AFM) studies on the thin film were performed on a Veeco Dimension 3100 Scanning Probe Microscope in a tapping mode. Figure 6.13 shows the 3-D height images of the thin film made from 0.75wt% PDI solution with 1.0 mm/min withdrawing speed. It is widely accepted that the surfaces of the glass slide and the cover glass are rough and not good for measuring the thickness of thin film, while mica is the best choice, which will be described later in this chapter.

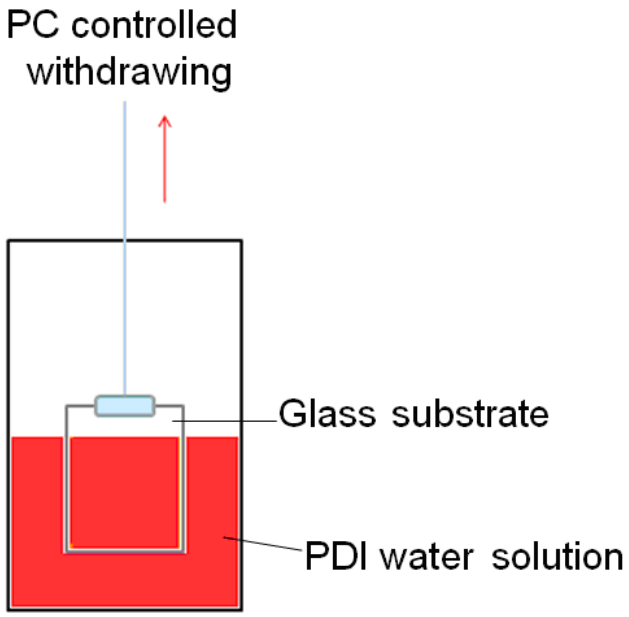

Figure 6.11. Scheme of the dip-coating experiment. Glass coverslip (18mm×18mm) is used and pinned vertically by a holder whose motion can be controlled by computer. It was done at Prof. Mostafa El-Sayed's lab.

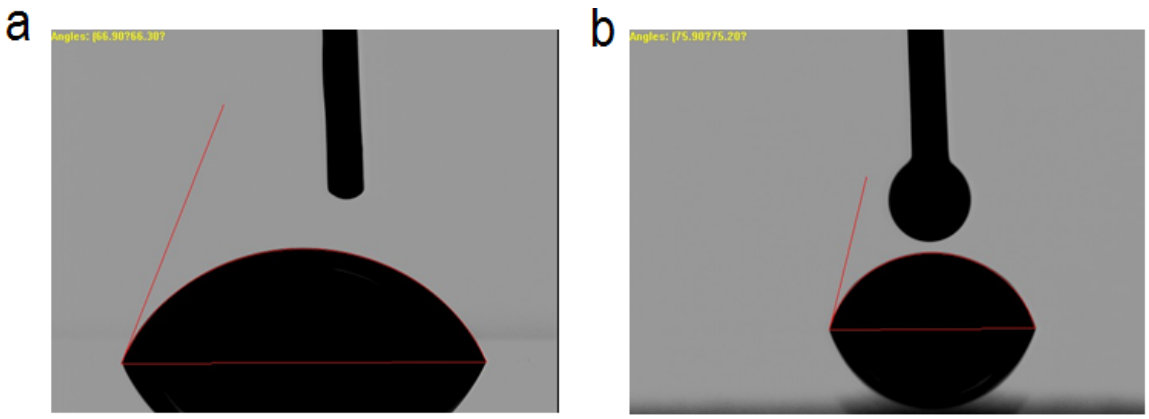

Figure 6.12. PDI drops on glass substrates. The drops do not spread but, instead, form at equilibrium spherical caps resting on the glass substrate with a contact angle. a. A 7wt% PDI aqueous solution drop on glass substrate. Contact angle: ~66.6°. b. A 17wt% PDI aqueous solution drop on glass substrate. Contact angle: ~75.5°.

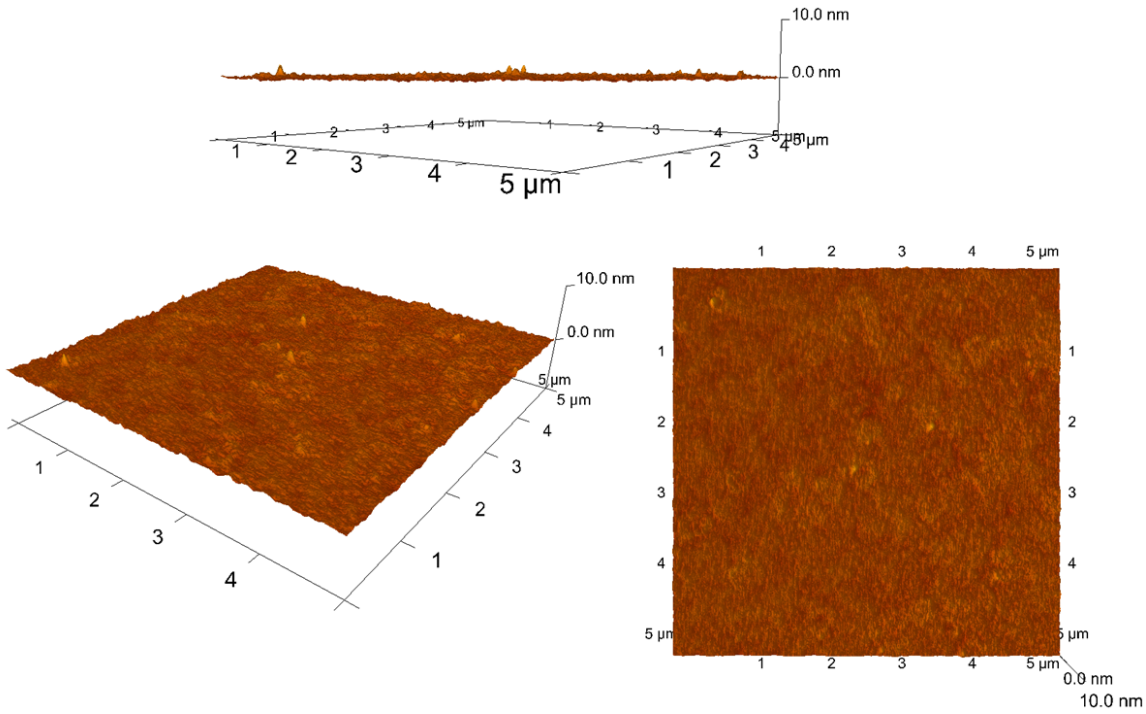

Figure 6.13. AFM images of a PDI thin film on the glass substrate.

6.4.2 Sensor applications

The conducting nature of thin PDI films makes it possible to measure the electric current or resistance. Figure 6.14 shows the experimental setup we used to measure this electronic property. We found that the resistance of the PDI thin film decreases remarkably after exposure to saturated vapors (at 25ºC) of H_2O and H_2O·HCl, respectively, as shown in Figures 6.15 and 6.16. "On" and "off" in the figures indicate the time the sample was exposed to the vapor and taken away from the vapor while the experiment was repeated. As soon as the film was exposed or "on", it responded immediately; while for recovering after leaving from the vapor, it took longer for the case of H_2O·HCl than that of H_2O. The sensitivity is also comparable to other thin film sensors [45-47]. We also tried to expose it to other volatile organic compounds. The

response to ethanol and methanol was very low; the response to pyridine was lower at each time repeated, so not reproducible.

Much work remains to be done. For example, studying the effect of vapor concentrations, and trying more other volatile organic compounds. Moreover, from point of view of device power consumption, one needs to find the maximum sensitivity to certain vapors as a function of temperature. However, at this point, what interests us most is the mechanism of sensing H_2O and $H_2O \cdot HCl$. Since the film is very thin (close to a monolayer), the trace amounts of H_2O may change the degree of freedom of PDI columns as well as the phase of the PDI layer, which may contribute to the change of conductivity. Another fact is that both H_2O and HCl change the chemical and electronic environment thus changing the conductivity. For pyridine, the reproducibility was not satisfactory. One of the possible reasons is that pyridine (C_5H_5N) with its lone pair electrons on N atom, may compete with PDI for H^+ and irreversibly change the original aggregation structure of PDI. Studies in the literature also show the addition of some salts can shift the isotropic-nematic phase boundary upward or downward by more than 10ºC, as rod-like aggregates probably transform a higher order aggregation into other structures [48, 49].

In addition to the above, it should be mentioned that the measurement of H_2O vapor is important in many applications ranging from predicting changes in the weather to ensuring heating and cooling comfort in our homes [50]. In manufacturing, H_2O vapor measurements help to control performance properties of engineered materials and optimize fuel efficiency in power generation [51]. Our studies reveal the possibility that PDI thin films will be one of the candidates in those applications.

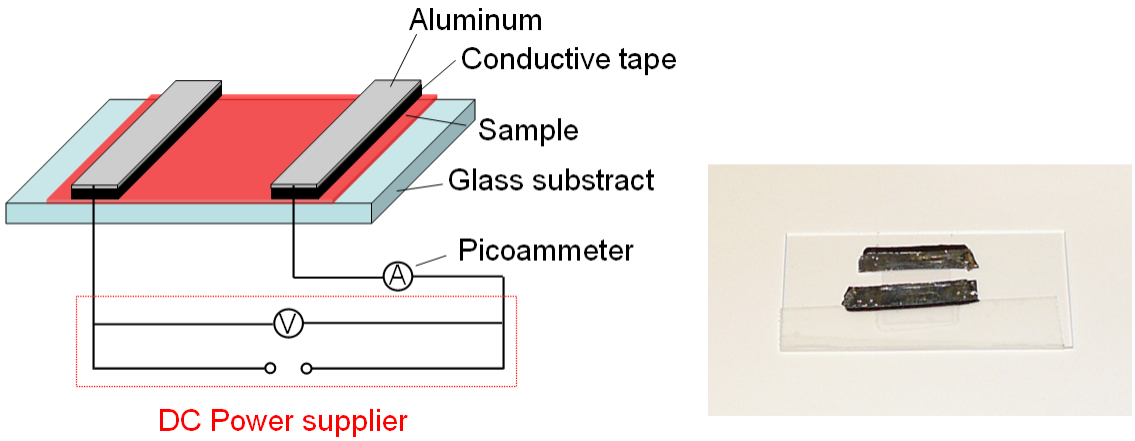

Figure 6.14. Electronic measurement of PDI film on glass substrate. The left one shows the scheme of setup. The right one shows the real images of sample with conductive tapes.

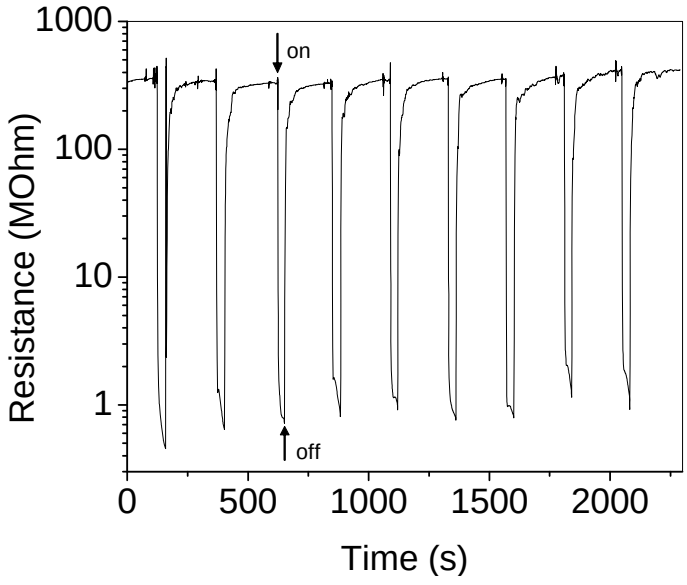

Figure 6.15. PDI thin film exposed to the H_2O vapor at 25ºC.

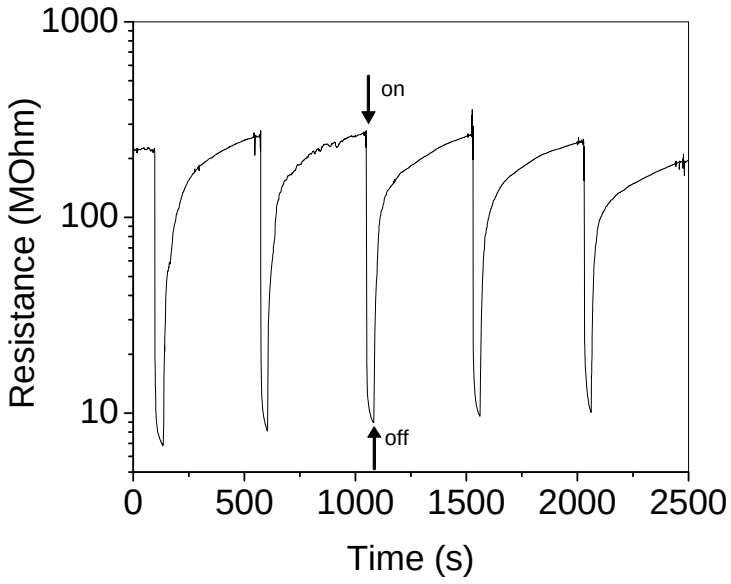

Figure 6.16. PDI thin film exposed to the $H_2O \cdot HCl$ vapor at 25ºC.

6.4.3 Dip-coating on mica substrates

Micas have atomically flat surfaces and are popular for AFM imaging. Micas are sheet silicates, consisting of two tetrahedral Al and Si sheets and an octahedral sheet in between [52-54]. There are two types of mica: muscovite ($K_2Al_4(Si_6Al_2O_{20})(OH)_4$, dioctahedral) and phlogopite ($KMg_3(Si_3AlO_{10})(OH)_2$, trioctahedral), as shown in Figure 6.17. Generally, one differs from the other by color. Muscovite is ruby, green or white; phlogopite is amber, yellow, or silver.

We used yellow phlogopite mica (25mm x 25mm) in our experiment. The PDI thin film was made on the freshly-cleaved mica surface by the same dip-coating method from 0.75wt% PDI solution with 1.0 mm/min withdrawing speed as used for the glass

substrates in 6.4.1. Figure 6.18 shows the AFM height image of the PDI thin film as well as the cross sectional analysis. Most of the mica surface in the image is covered by the PDI film except some cracks, where the surface of mica is exposed. The thickness of the film is about 1.5~2nm by comparing the height of the mica surface and the film surface in the cross sectional analysis along two green dashed lines. As the perylene core (PTCDA) has the dimension 14.2Å x 9.2Å in Figure 6.1, considering the length from the diethylethylenediamine (DEDA), we estimate the diameter of the columns of the PDI aggregates to be between 1.5nm and 2nm. Therefore, this PDI thin film is a monolayer film.

For the AFM morphology in Figure 6.18, there are some preferential orientations existing in the PDI monolayer film. A larger portion has orientation along the pink line direction; a smaller portion has orientation along the white line direction. Moreover, the angle between two directions is about 120º, reminiscent of the role of the mica surface and the lattice structure of phlogopite mica in Figure 6.17 c. This anisotropy may come from the existence of the epitaxial interaction between PDI molecules and the lattice of the phlogopite mica substrate. In the literature, there are similar reports. Ono et al studied the AFM morphology of mica in the air, as shown in Figure 6.19 a. Spots corresponded to alignment of holes left by the dissociating K+ ions on the freshly-cleaved surface of mica. Arrows show the periodic orientation of these holes. They found that J aggregates of pseudoisocyanine dye have anisotropic growth at a mica/solution interface, as shown in Figure 6.19 b [53, 54]. Others also reported the epitaxial growth of oligo-phenylenes, oligo-thiophenes and thiophene/phenylene co-oligomerssexithiophene on mica surfaces [52, 55, 56].

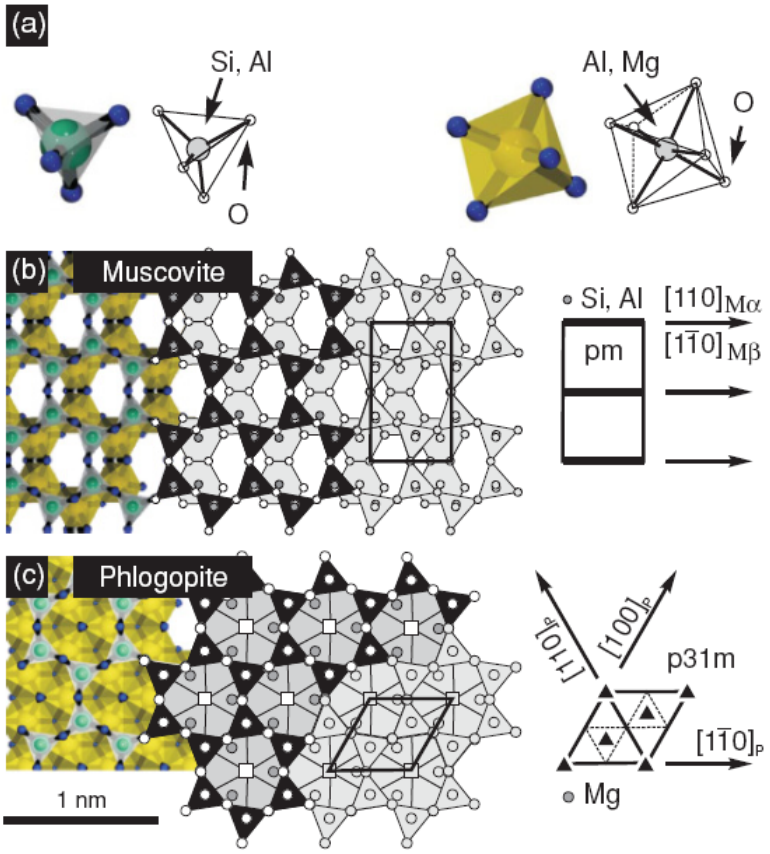

Figure 6.17. (a) Left: tetrahedral unit built up by $Si(Al)O_4$; right: octahedral unit built up by $Al(Mg)O_6$. (b) Top view onto a {001} surface of a dioctahedral phyllosilicate (muscovite). As indicated by the *pm* space group symbol beside, surface symmetry is characterized by parallel aligned mirror axes. (c) Comparable view onto the surface of a trioctahedral phyllosilicate (phlogopite) which can be characterized by three mirror axes as indicated by the *p31m* space group symbol. From reference [52].

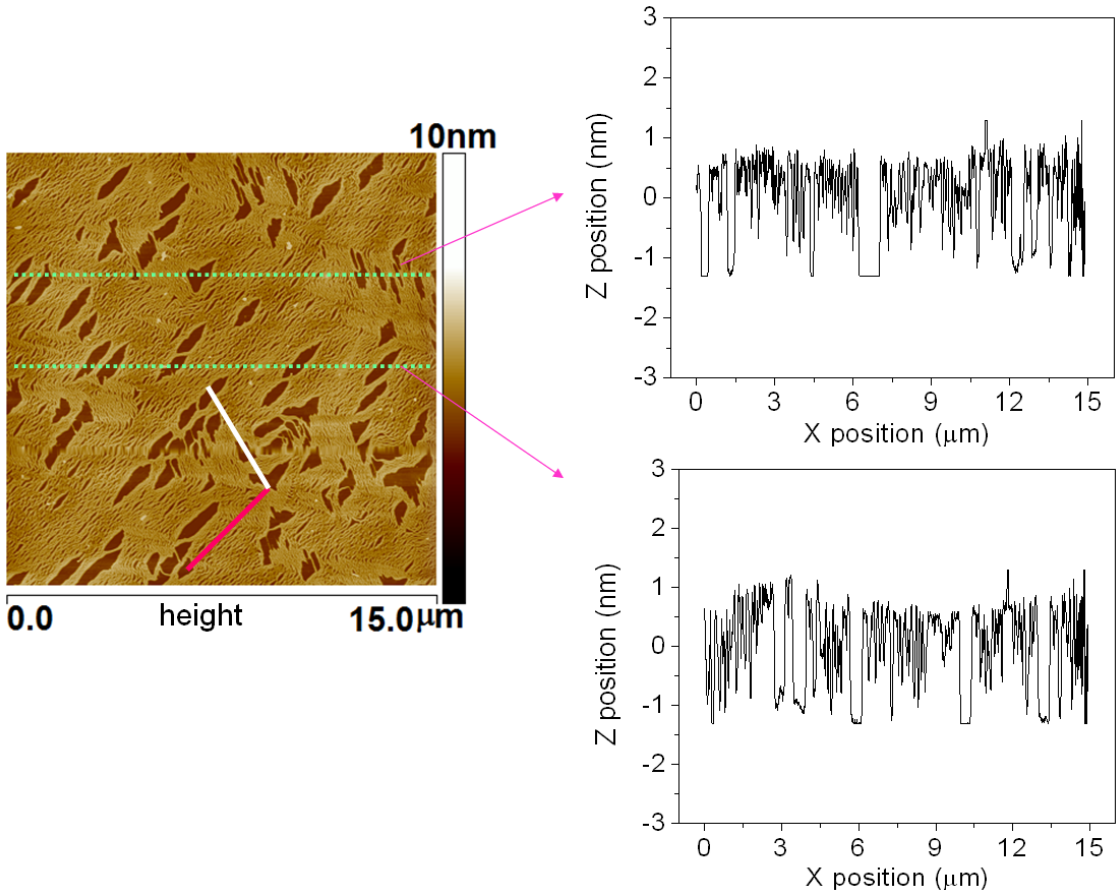

Figure 6.18. AFM height images of the PDI thin film on phlogopite mica and the cross sectional analysis along the green dashed lines.

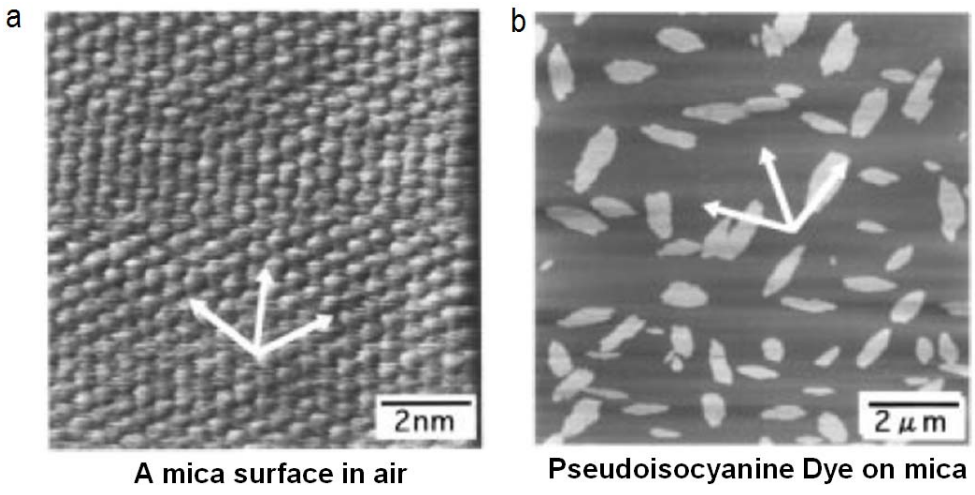

Figure 6.19. a. AFM image of a mica surface in air. b. AFM image of J aggregates of pseudoisocyanine dye on mica surface. Arrows show the periodic orientation of holes on mica surface and periodic orientation of aggregate islands. From reference [54].

6.4.4 Surface enhanced Raman scattering of PDI thin films

Since it was difficult for us to get characteristic Raman shifts of PDI thin films, gold nanoparticles were introduced into the system to enhance the Raman scattering intensity of PDI. Introduction to surface enhanced Raman scattering (SERS) [57-59] was also provided in Chapter 3. The gold nanoparticles (AuNPs) coated substrates (both glass and mica) were provided by Dr. Mahmoud A. Mahmoud from Prof. Mostafa El-Sayed's group at Georgia Tech. Their average size is about 75 nm and they absorb light around 810nm in the visible spectrum. The absorption band is broad enough to cover the wavelength of 785nm which is the Raman laser wavelength. The PDI thin film was coated onto AuNPs-coated substrates by the same dip-coating method from 0.75wt% PDI solution with 1.0 mm/min withdrawing speed as described in 6.4.1. During the coating, some AuNPs left the surface and fell into PDI solution, as there was a layer of AuNPs suspending on the surface of PDI solution after the experiment was done.

The AFM height image in Figure 6.20 shows the final morphology of the AuNPs/PDI film on mica. Not all area of the surface is covered by AuNPs; one AuNP (~75nm) or aggregation of two AuNPs (~150nm) are in the Z direction according to the cross sectional analysis along the blue lines. Absorption measurement confirmed that there were thin films coated on the substrates, as shown in the Figure 6.21. The peak around 500nm is from the absorption of PDI. For the absorption peak of AuNPs, as you may have noted, it shifts to ~900nm in the AuNPs/PDI film on glass from original 810nm in the pure AuNPs film. Although the one on mica doesn't show the absorption peak within 1000nm range, it also has the trend moving towards the longer wavelength. The observed red shift in the plasmon peak position is most likely from the significant change in the nature of the medium surrounding the particles. The dielectric properties of glass substrates and mica substrates are different; it probably also relates to charge transfer between the chemisorbed PDI and the AuNP surface [60].

For Raman scattering, AuNPs make the characteristic bands of PDI vibrations appear from the relatively strong and broad background, as shown in the Figure 6.22. Modes involving vibrations of the perylene ring are located between 1200 and 1700cm^{-1}. The first C-H bending starts at 1290cm^{-1}. Ring deformation modes are observed around 530cm^{-1}. Assignment of most bands is indicated in the Figure 6.22 according to literatures [61-64].

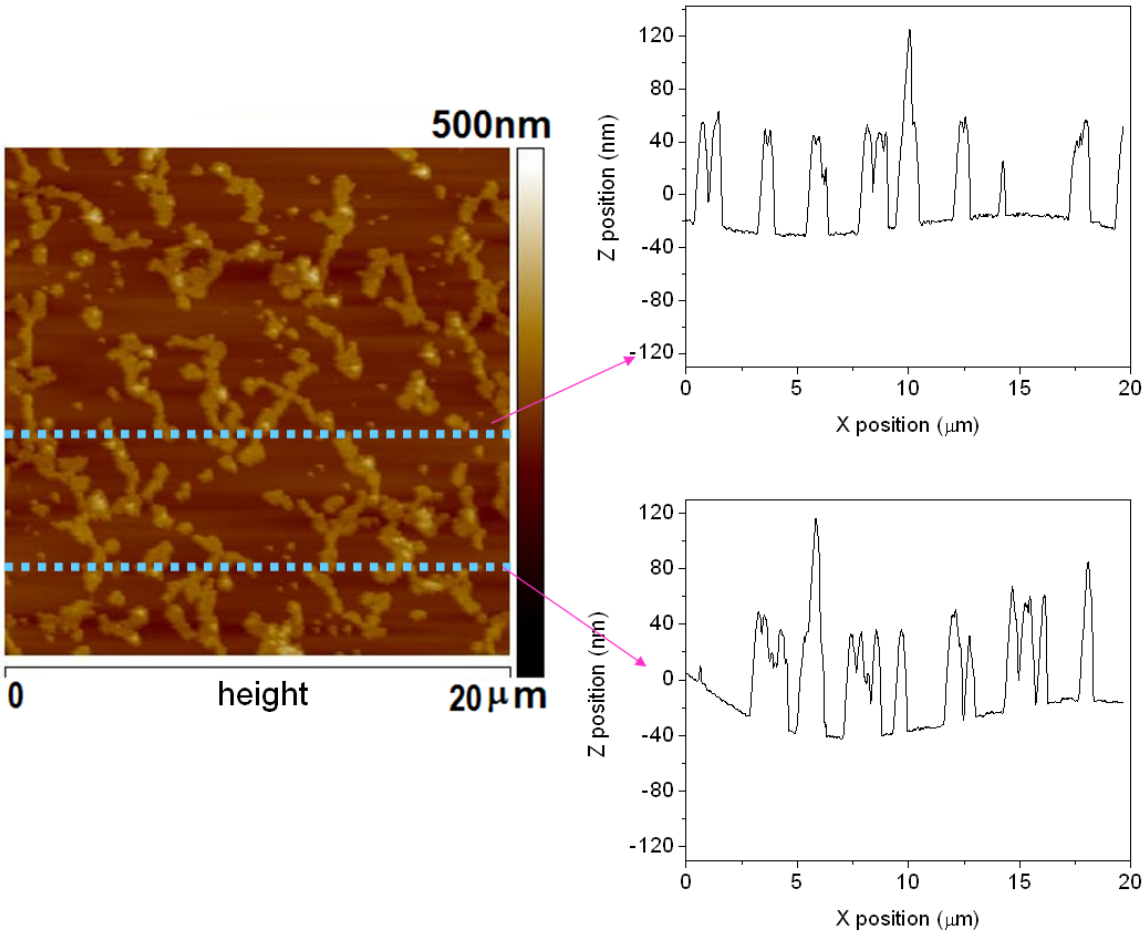

Figure 6.20. AFM height image of the AuNPs/PDI film on mica and the cross sectional analysis along the blue dashed lines.

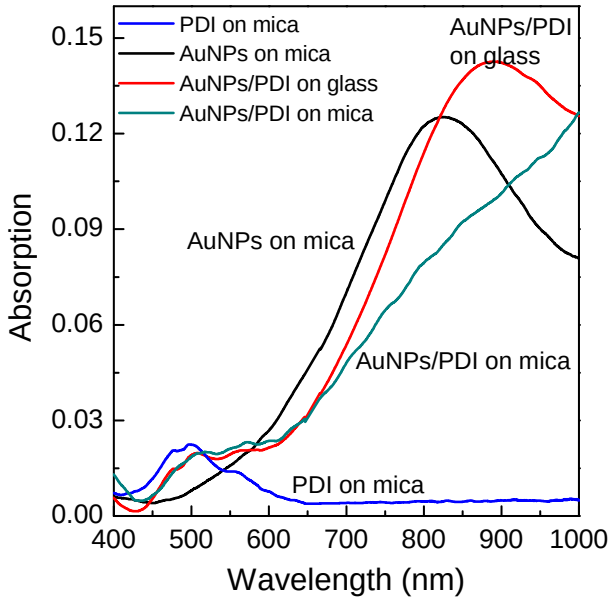

Figure 6.21. Absorption of PDI and AuNPs/PDI films on mica and glass substrates.

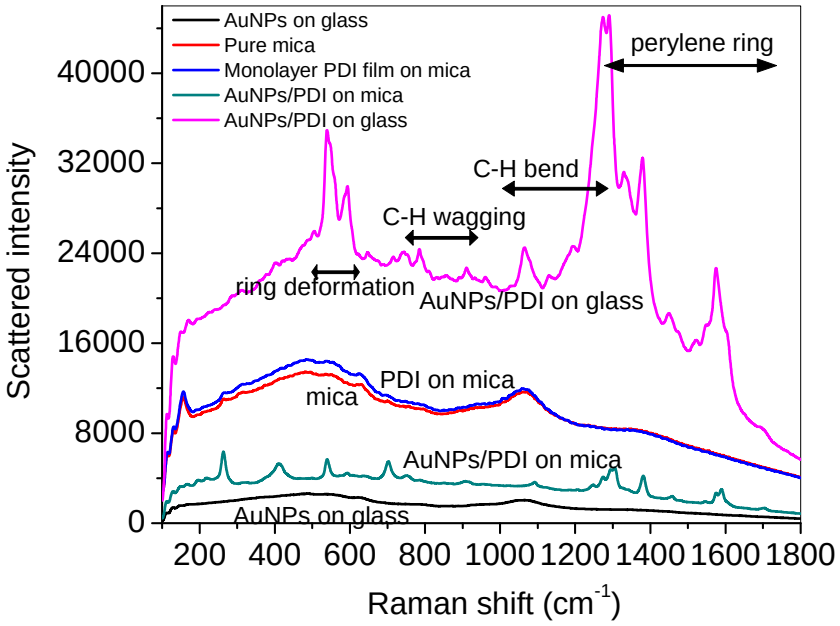

Figure 6.22. Raman scattering of PDI and AuNPs/PDI films on the mica and glass substrates. Raman laser wavelength is 785nm.

6.5 Oriented PDI films

By using a wirewound wet-film applicator rod with 0.003 inch wire size to rub the PDI solution with a relatively high concentration (in nematic N phase) on the glass substrate, as shown in Figure 6.23, we achieved an anisotropic solid film after drying in the air at room temperature. By rotating the polarizer, we measured the anisotropic absorbance of the film. Orientation dependent absorbance at peak position 500nm of the PDI film was plotted in the Figure 6.24, where it also shows anisotropic absorbance at 480nm of the oriented SSY film made using the same rubbing method as described in Chapter Two. Similar to SSY, the absorption dipole moment of PDI is also aligned along the long molecular axes within their molecular planes, therefore, low absorbance at 0º and high absorbance at 90º in Figure 6.24 also indicate that PDI molecules on the glass substrate are oriented with their long axes orthogonal to the rubbing direction, that is, the PDI columns are aligned along the rubbing direction. Considering the difference of the absorbance at the orthogonal directions of these two particular films, rubbed PDI film even has better anisotropy than the rubbed SSY film.

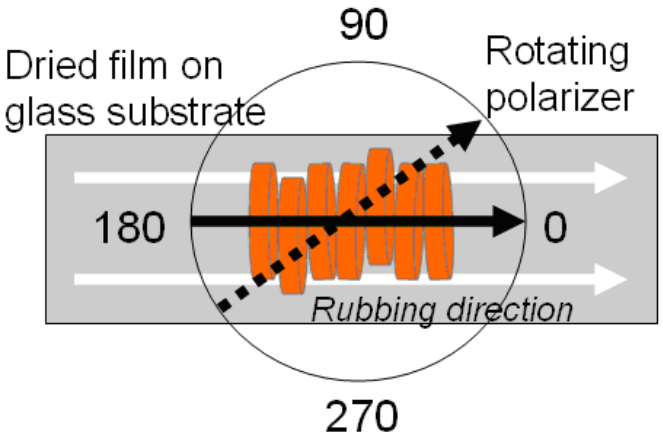

Figure 6.23. Anisotropic PDI film on the glass substrate after rubbing using a wirewound wet-film applicator rod. White arrows indicate the rubbing direction. Black solid and dashed arrows indicate the polarizer direction in the absorption measurement. More information about this rod, please see Chapter Two.

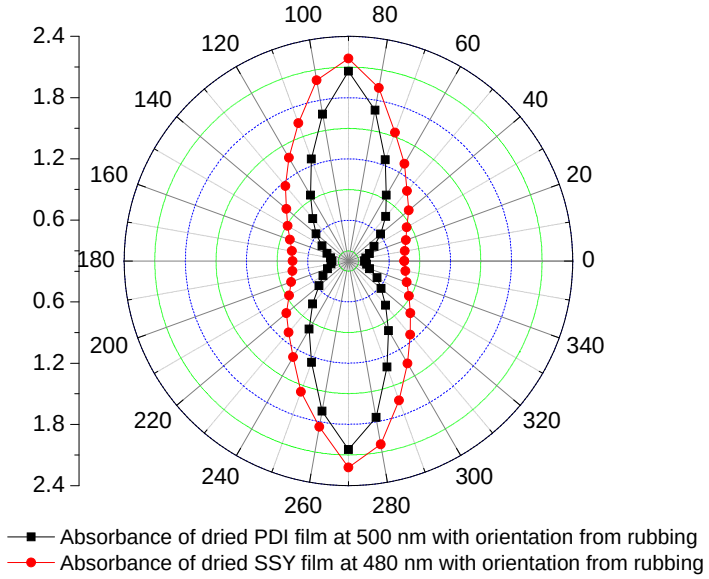

Figure 6.24. Anisotropic absorbance of PDI and SSY films.

In the literature, few studies have been done on electronic properties of chromonic liquid crystals or their dried films. π -Stacking leads to higher mobilities, although this statement is over simplified. Strong electronic coupling between molecules, which is associated with excellent overlap between the π -systems on adjacent molecules, is a necessary criterion for ensuring high mobilities. It is desirable if we can make all the chromonic stacking columns orient along one direction. A recent report on a chromonic dye Violet 20 [65] shows that the field-effect carrier mobility along the molecular aggregates is 0.03 $cm^2 V^{-1} s^{-1}$, however, the resulting mobility depend strongly on the details of sample fabrication, prehistory, and ambient conditions, and might differ by several orders of magnitude if measured for two devices constructed and handled in a similar way. They also pointed out that the residual water in the film can play a critical role in the mobility measurement. We also tried similar field effect experiments for PDI at Prof Elsa Reichmanis' lab at Georgia Tech. It turned out that the curve of source-drain current and gate voltage varied every time and results were not reproducible when using

the same sample and different samples. Probably more effort need to specially control the amount of residual water in the film.

Instead of focusing on field effect, we studied on the conductivity of the PDI film from the two-electrode gap type arrangement, as shown in Figure 6.14. Resistivity is always a strong function of depth, and it is often convenient to work with a parameter called the "sheet resistance". It can be calculated based on this equation [66]:

$$R_{sheet}=(V_{sheet}/I_{sheet})\cdot(W_{sheet}/L_{electrode}) \quad (6.1)$$

where V_{sheet} is the voltage applied on the sheet, I_{sheet} is the current flowing on the sheet, W_{sheet} is the width of sheet the electrode covers and $L_{electrode}$ is the distance between two electrodes. As shown in the Figure 6.25, the voltage applied on the PDI film has a linear relation with the current for both cases: current parallel and perpendicular to the rubbing direction, which is also the direction PDI columns pointing along. Sheet resistance parallel to PDI columns is about 42 MΩ while perpendicular to PDI columns is about 420 MΩ, so R_{sheet} perpendicular to PDI columns is about 10 times R_{sheet} along the PDI columns. It is more conductive along the PDI columns.

For the parallel case, by varying the distance between two electrodes from 1.25cm to 4.60cm, we got a series of current-voltage curves with linearity, as shown in the Figure 6.26. The calculated sheet resistance along the PDI columns fluctuates between 34 MΩ and 53 MΩ. It reveals that the rubbed PDI film is not perfectly uniform in the macroscopic scale. We also tried to explore the relation between the current and the distance between electrodes ($L_{electrode}$) when different voltages applied. The double logarithmic plot in Figure 6.27 shows the power law: $I_{sheet} \propto L_{electrode}^{\upsilon}$, υ is -0.16, -0.14 and -0.13 when voltage is 10, 20 and 30V, respectively. For materials like copper phthalocyanine (CuPc) thin films and para-sexiphenyl nano-needles, at low fields, the conduction is ohmic, with space-charge-limited conductivity (SCLC) becoming dominant

at high fields. Based on both theory and experiments, current I_{SCLC} is proportional to the power of -2 of the distance between two electrodes [67-69].

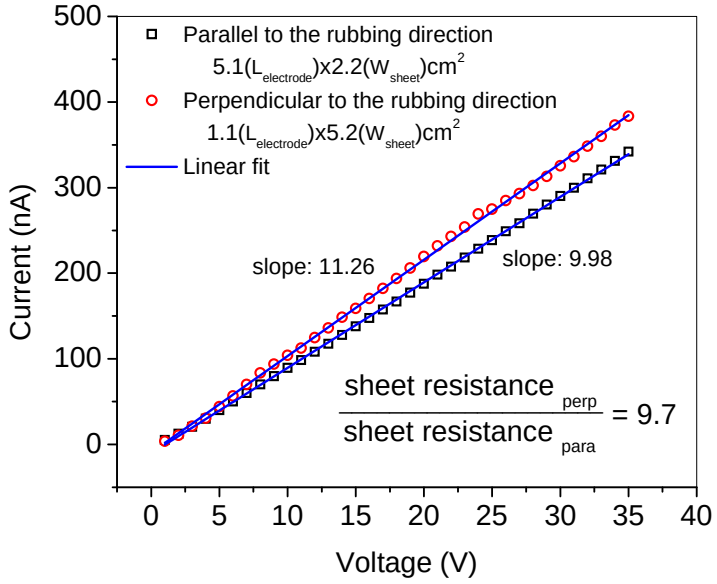

Figure 6.25. Plot of current - voltage at orthogonal directions.

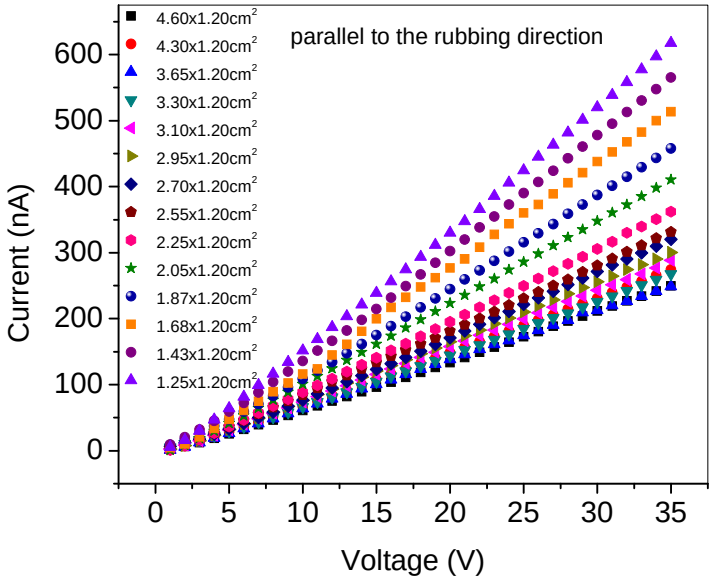

Figure 6.26. Plot of current- voltage for various distances between electrodes ($L_{electrode}$). Current direction is parallel to the rubbing direction.

Table 6.1. Sheet resistance along the columns in the PDI film with different distances between electodes.

$L_{electrode}$/cm	Slope (current/voltage)/(nA/V)	Sheet resistance /MOhm
4.60	7.41	35.2
4.30	8.10	34.5
3.65	7.41	44.4
3.30	7.83	46.4
3.10	8.42	46.0
2.95	8.90	45.7
2.70	9.47	46.9
2.55	9.73	48.4
2.25	10.74	49.7
2.05	12.23	47.9
1.87	13.53	47.4
1.68	15.54	46.0
1.43	16.71	50.2
1.25	18.21	52.7

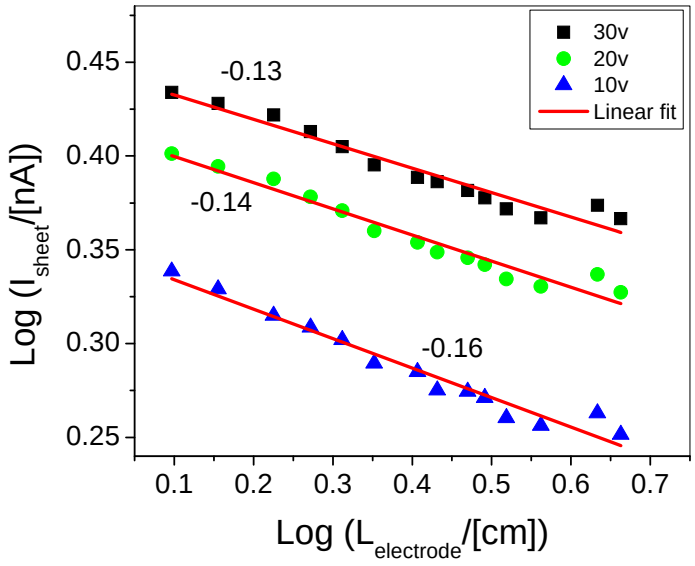

Figure 6.27. Logarithmic plot of current – distance between electrodes ($L_{electrode}$).

6.6 Conclusions

A perylene derivative, PDI, was synthesized and characterized by FTIR and NMR spectroscopies. The liquid crystalline behavior of PDI in water was studied. The phase diagram and optical textures under crossed POM were all presented. Since PDI chromonic liquid crystal is so difficult to align, we only got planar alignment with an area about 400μm x 300μm by using common rubbed polyimide surface. PDI Thin films were prepared by the dip-coating method. We found their application in sensing H_2O and $H_2O{\cdot}HCl$ vapors. The thickness of PDI thin film on the mica was characterized by AFM. The anisotropic morphology of the PDI thin film was probably caused by the lattice structure of the mica surface. Gold nanoparticles successfully enhanced the Raman scattering of the PDI monolayer and made the Raman study on the PDI monolayer possible. By rubbing the PDI solution in the nematic phase, an oriented solid film was

obtained after drying in the air. The absorbance measurement shows good anisotropy and PDI columns were aligned along the rubbing direction. The order and orientation of the solid film most likely were inherited from those of the nematic PDI solution under rubbing. Electronic measurement confirmed the anisotropy in the film again. The sheet resistance along the columns was about 10 times that perpendicular to the columns. The good conductivity along the columns comes from the overlap between the π systems. The sheet resistance also fluctuates to some extent by varying the distance between electrodes due to the inhomogeneous nature of the rubbed film. The power law between the current and the distance between electrodes was also explored and compared with another similar law of other materials.

6.7 References

[1] Schmidt-Mende, L., Fechtenkotter, A., Mullen, K., Moons, E., Friend, R. H., and MacKenzie, J. D. Self-organized discotic liquid crystals for high-efficiency organic photovoltaics. Science **2001**, 293(5532), 1119-1122.

[2] Zuilhof, H. T., Schaafsma, T. J., and Sudhoelter, E. J. R. Liquid crystalline perylene diimides: highly organized electron carriers. Proceedings of SPIE-The International Society for Optical Engineering **2001**, 4108 (Organic Photovoltaics), 31-40.

[3] Kojima, H., Ozawa, A., Takahashi, T., Nagaoka, M., Homma, T., Nagatomo, T., and Omoto, O. A structural study for highly efficient electroluminescence cells using perylene-doped organic materials. Journal of the Electrochemical Society **1997**, 144(10), 3628-3633.

[4] Langhals, H., Jona, W., Einsiedl, F., and Wohnlich, S. Self-dispersion: Spontaneous formation of colloidal dyes in water. Advanced Materials **1998**, 10(13), 1022-1024.

[5] Han, S. H., Lee, K. J., Lee, S. H., and Jang, J. N-type organic thin-film transistor using N, N'-dioctyl-3,4,9,10-perylene tetracarboxylic diimides grown by organic vapor deposition. Journal of Non-Crystalline Solids **2008**, 354(19-25), 2870-2874.

[6] del Cano, T., Parra, V., Rodriguez-Mendez, M. L., Aroca, R., and de Saja, J. A. Molecular stacking and emission properties in Langmuir-Blodgett films of two alkyl substituted perylene tetracarboxylic diimides. Organic Electronics **2004**, 5(1-3), 107-114.

[7] Kamm, V., Battagliarin, G., Howard, I. A., Pisula, W., Mavrinskiy, A., Li, C., Mullen, K., and Laquai, F. Polythiophene: perylene diimide solar cells - the impact of alkyl-substitution on the photovoltaic performance. Advanced Energy Materials **2011**, 1(2), 297-302.

[8] Zhou, E., Cong, J., Wei, Q., Tajima, K., Yang, C., and Hashimoto, K. All-polymer solar cells from perylene diimide based copolymers: material design and phase separation control. Angewandte Chemie, International Edition **2011**, 50(12), 2799-2803, S2799/1-S2799/16.

[9] Anthony, J. E., Facchetti, A., Heeney, M., Marder, S. R., and Zhan, X. n-Type organic semiconductors in organic electronics. Advanced Materials **2010**, 22(34), 3876-3892.

[10] Bao, Q., Goh, B. M., Yan, B., Yu, T., Shen, Z., and Loh, K. P. Polarized emission and optical waveguide in crystalline perylene diimide microwires. Advanced Materials **2010**, 22(33), 3661-3666.

[11] Schmitz-Hübsch, T., Sellam, F., Staub, R., Tö rker, M., Fritz, T., Kubel, Ch., Müllen, K., and Leo, K., Direct observation of organic–organic heteroepitaxy: perylenetetracarboxylic-dianhydride on hexa-peri-benzocoronene on highly ordered pyrolytic graphite. Surface Science **2000**, 445, 358–367.

[12] Huang, C., Barlow, S., and Marder, S. Perylene-3,4,9,10-tetracarboxylic acid diimides: Synthesis, physical properties, and use in organic electronics. Journal of Organic Chemistry **2011**, 76(8), 2386-2407.

[13] Huang, L., and Tam-Chang, S.-W. Ionic perylene-3, 4-dicarboximide as chromonic mesogens and the use of a fluorescence technique in determining phase-transition temperatures. Liquid Crystals **2010**, 37(5), 555-561.

[14] Tam-Chang, S.-W., Mahinay, D., and Huang, L. Multifunctional materials via molecular self-organization into liquid-crystalline phase. Advanced Materials Research **2008**, 47-50 (Pt. 1, Multi-Functional Materials and Structures), 165-168.

[15] Tam-Chang, S.-W., and Huang, L. Chromonic liquid crystals: properties and applications as functional materials. Chemical Communications **2008**, 17, 1957-1967.

[16] Tam-Chang, S.-W., Huang, L., Gyan, A., Seo, W., Mahinay, D., and Iverson, I. K. Designing chromonic mesogens for the fabrication of anisotropic optical materials. Proceedings of SPIE **2008**, 6911(Emerging Liquid Crystal Technologies III), 691107/1-691107/12.

[17] Tam-Chang, S.-W., Helbley, J., and Iverson, I. K. A study of the structural effects on the liquid-crystalline properties of ionic perylenebis(dicarboximide)s using UV-Vis spectroscopy, polarized light microscopy, and NMR spectroscopy. Langmuir **2008**, 24(5), 2133-2139.

[18] Huang, L., Tam-Chang, S.-W., Seo, W., and Rove, K. Microfabrication of anisotropic organic materials via self-organization of an ionic perylenemonoimide. Advanced Materials 2007, 19(23), 4149-4152.

[19] Huang, L., Catalano, Vincent J., and Tam-Chang, S.-W. Anisotropic fluorescent materials via self-organization of perylenedicarboximide. Chemical Communications **2007**, 20, 2016-2018.

[20] Tam-Chang, S.-W., Helbley, J., Carson, T. D., Seo, W., Iverson, I.K. Template-guided organization of chromonic liquid crystals into micropatterned anisotropic organic solids. Chemical Communications **2006**, (5), 503-505.

[21] Carson, T. D., Casey, S. M., Iverson, I. K., Seo, W., and Tam-Chang, S.-W. Materials and methods for the preparation of anisotropically-ordered solids using soluble orienting compounds. PCT Int. Appl. **2005**, WO 2005089094.

[22] Tam-Chang, S.-W., Seo, W., Rove, K., and Casey, S. M. Molecularly designed chromonic liquid crystals for the fabrication of broad spectrum polarizing materials. Chemistry of Materials **2004**, 16(10), 1832-1834.

[23] Tam-Chang, S.-W., Seo, W., and Iverson, I. K. Synthesis and studies of the properties of a liquid-crystalline quaterrylenebis(dicarboximide) by ^{1}H NMR and UV-vis spectroscopies. Journal of Organic Chemistry **2004**, 69(8), 2719-2726.

[24] Tam-Chang, S.-W., Iverson, I. K., and Helbley, J. Study of the chromonic liquid-crystalline phases of bis-(N, N-diethylaminoethyl) perylene-3,4,9,10-tetracarboxylic

diimide dihydrochloride by polarized optical microscopy and ^{2}H NMR spectroscopy. Langmuir **2004**, 202, 342-347.

[25] Carson, T. D., Seo, W., Tam-Chang, S.-W., and Casey, S. M. Novel polarized photoluminescent films derived from sequential self-organization, induced-orientation, and order-transfer processes. Chemistry of Materials **2003**, 15(12), 2292-2294.

[26] Tam-Chang, S.-W., Seo, W., Iverson, I.K., and Casey, S. M. Ionic quaterrylenebis (dicarboximide): A novel mesogen and long-wavelength polarizing material. Angewandte Chemie, International Edition **2003**, 42(8), 897-900.

[27] Iverson, I.K., Casey, S. M., Seo, W., Tam-Chang, S.-W., and Pindzola, B. A. Controlling molecular orientation in solid films via self-organization in the liquid-crystalline phase. Langmuir **2002**, 18(9), 3510-3516.

[28] Iverson, I.K., and Tam-Chang, S.-W. Cascade of molecular order by sequential self-organization, induced orientation, and order transfer processes. Journal of the American Chemical Society **1999**, 121(24), 5801-5802.

[29] Seo, W. W. The design and synthesis of chromonic mesogens for the generation of anisotropic materials via self - organization. Ph.D. thesis, University of Nevada, **2004**, 183 pp.

[30] Lee, M. H., Shin, S. H., Jung, G. U., and Bae, Y. J. Chiral lyotropic perylene chromonic liquid crystal compound, its preparation method, liquid crystal, and liquid crystal thin film. Repub. Korean Kongkae Taeho Kongbo **2009**, KR 2009128866.

[31] Naidu, J. J., Bae, Y. J., Jeong, K.-U., Shin, S., and Lee, M.-H. Color tuning of perylene based lyotropic chromonic liquid crystal. Bulletin of the Korean Chemical Society **2009**, 30(1), 224-226.

[32] Kang, S.-W., Joshi, L., Bae, Y.-J., Naidu, J. J., Jeong, K.-U., Lee, M.-H., and Kumar. S. Mesophases of chiral and achiral aggregates based on chromonic perylene mesogens, 22nd International Liquid Crystal Conference, Jeju Island, S. Korea, **2008**.

[33] Satas, D. (ed.) Coatings Technology Handbook **2000**, Marcel Dekker: New York, p. 679, 902 pp.

[34] Tracton, A. A. (ed.) Coatings Technology Handbook **2005**, Marcel Dekker: New York, p. 679, 936 pp.

[35] Ryntz. A., and Yaneff, P. V. (ed.) Coatings of Polymers and Plastics **2003**, Marcel Dekker: New York, p. 121, 416 pp.

[36] Satas, D. (ed.) Plastics Finishing and Decoration **1986**, Van Nostrand Reinhold: New York, p. 113, 528 pp.

[37] Park, J. O., Rey, A. D., and Srinivasarao, M. Non-classical scaling for forced wetting of a nematic fluid on a polymeric fiber. Soft Matter **2009**, 5(11), 2277-2280.

[38] Shim, E., Park, J. O., and Srinivasarao, M. Forced coating of polypropylene fibers with non-wetting fluids: The scaling of the film thickness. Modern Physics Letters B **2008**, 22(22), 2043-2053.

[39] Weatherspoon, M. R., Cai, Y., Crne, M., Srinivasarao, M., and Sandhage, K. H. 3D rutile titania-based structures with Morpho butterfly wing scale morphologies. Angewandte Chemie, International Edition **2008**, 47(41), 7921-7923.

[40] Mitzi, D. B., Kosbar, L. L., and Murray, C. E., et al. High-mobility ultrathin semiconducting films prepared by spin coating. Nature **2004**, 428, 299-303.

[41] Sakka, S., and Yoko, T. Sol gel-derived coating films and applications. Structure and Bonding **1992**, 77, 89-118.

[42] Landau, L., and Levich, B. Dragging of a liquid by a moving plate. Acta Physicochimica (USSR) **1942**, 17, 42–54.

[43] Faustini, M., Louis, B., Albouy, P. A., Kuemmel, M., Grosso, D. Preparation of sol-gel films by dip-coating in extreme conditions. Journal of Physical Chemistry C **2010**, 114(17), 7637-7645.

[44] Xue, L., Gao, X., Zhao, k., Liu, J., Yu, X., and Han, Y. The formation of different structures of poly(3-hexylthiophene) film on a patterned substrate by dip coating from aged solution. Nanotechnology **2010**, 21, 145303.

[45] Bruckman, M. A., Liu, J., Koley, G., Li, Y., Benicewicz, B., Niu, Z., and Wang, Q. Tobacco mosaic virus based thin film sensor for detection of volatile organic compounds. Journal of Materials Chemistry **2010**, 20(27), 5715-5719.

[46] Serra, A., Re, M., Palmisano, M., Vittori A. M., Filippo, E., Buccolieri, A., and Manno, D. Assembly of hybrid silver-titania thin films for gas sensors. Sensors and Actuators, B: Chemical **2010**, B145(2), 794-799.

[47] Liu, X., Zhang, D., Zhang, Y., and Dai, X. Preparation and characterization of p-type semiconducting tin oxide thin film gas sensors. Journal of Applied Physics **2010**, 107(6), 064309/1-064309/5.

[48] Kostko, A. F, Cipriano, B. H, Pinchuk, O. A, Ziserman, L., Anisimov, M. A, Danino, D., and Raghavan, S. R. Salt effects on the phase behavior, structure, and rheology of chromonic liquid crystals. Journal of Physical Chemistry B **2005**, 109(41), 19126-19133.

[49] Joshi, L., Kang, S.-W., Agra-Kooijman, D. M., and Kumar, S. Cocentration, temperature, and pH dependence of sunset-yellow aggregates in aqueous solutions: An x-ray investigation. Physical Review E: Statistical, Nonlinear, and Soft Matter Physics **2009**, 80, 041703/1-041703/8.

[50] Morosi, C., and Remich, N., "2000 annual industry outlook: 2000 a pretty good encore following a rousing 1999," Appliance Manufacturer **2000**, 54–66.

[51] Fenner, R., and Zdankiewicz, E. Micromachined water vapor sensors: A review of sensing technologies. IEEE Sensors Journal **2001**, 1(4), 309-317.

[52] Simbrunner, C., Hernandez-Sosa, G., Oehzelt, M., Djuric, T., Salzmann, I., Brinkmann, M., Schwabegger, G., Watzinger, I., Sitter, H., and Resel, R. Epitaxial growth of sexithiophene on mica surfaces. Physical Review B: Condensed Matter and Materials Physics **2011**, 83(11), 115443/1-115443/8.

[53] Ono, S. S., Yamamoto, S., Yao, H., Matsuoka, O., and Kitamura, N. Morphological control of the supramolecular pseudoisocyanine J-aggregates by the functions of a mica/solution interface. Applied Surface Science **2001**, 177(3), 189-196.

[54] Ono, S. S., Yao, H., Matsuoka, O., Kawabata, R., Kitamura, N., and Yamamoto, S. Anisotropic growth of J aggregates of pseudoisocyanine dye at a mica/solution

interface revealed by AFM and polarization absorption measurements. Journal of Physical Chemistry B **1999**, 103(33), 6909-6912.

[55] Balzer, F. Growth of oriented organic nanoaggregates via molecular beam deposition. Springer Series in Materials Science **2008**, 101(Organic Nanostructures for Next Generation Devices), 31-65.

[56] Simbrunner, C., Nabok, D., Hernandez-Sosa, G., Oehzelt, M., Djuric, T., Resel, R., Romaner, L., Puschnig, P., Ambrosch-Draxl, C., and Salzmann, I. et al. Epitaxy of rodlike organic molecules on sheet silicates - A growth model based on experiments and simulations. Journal of the American Chemical Society **2011**, 133(9), 3056-3062.

[57] Alessio, P., Constantino, C. J. L., Aroca, R. F., and Oliveira, O. N., Jr. Surface-enhanced Raman scattering: metal nanostructures coated with Langmuir-Blodgett films. Journal of the Chilean Chemical Society **2010**, 55(4), 469-478.

[58] Fan, M. Andrade, G. F. S., and Brolo, A. G. A review on the fabrication of substrates for surface enhanced Raman spectroscopy and their applications in analytical chemistry. Analytica Chimica Acta **2011**, 693(1-2), 7-25.

[59] Aroca, R. F., Constantino, C. J. L., and Duff, J., Surface-enhanced Raman scattering and imaging of Langmuir-Blodgett monolayers of bis(phenethylimido)perylene on silver island films. Applied Spectroscopy **2000**, 54(8), 1120.

[60] Albrecht, M. G., and Creighton, J. A. Anomalously intense Raman spectra of pyridine at a silver electrode. Journal of the American Chemical Society **1977**, 99(15), 5215-17.

[61] Aroca, P., Jr., Aroca, R., Kovacs, G. J., and Loutfy, R. O. Vibrational characterization of Langmuir-Blodgett monolayers and evaporated films of a bisphenylene-substituted perylene-3,4,9,10-tetracarboxylic acid derivative. Langmuir **1990**, 6(6), 1050-1054.

[62] Zhanpeisov, N. U., Nishio, S., and Fukumura, H. Density functional theory study of vibrational properties of the 3,4,9,10-perylene tetracarboxylic dianhydride (PTCDA) molecule: IR, Raman, and UV-vis spectra. International Journal of Quantum Chemistry **2005**, 105(4), 368-375.

[63] Lin-Vien, D., Colthup, N. B., Fateley, W. G., and Grassetti, J. G. The Handbook of Infrared and Raman Characteristics Frequencies of Organic Molecules. **1991**, Academic: San Diego, 503 pp.

[64] Wagner, V., Muck, T., Geurts, J., Schneider, M., and Umbach, E. Raman analysis of first monolayers of PTCDA on Ag (111). Applied Surface Science **2003**, 212-213, 520-524.

[65] Nazarenko, V. G., Boiko, O. P., Anisimov, M. I., Kadashchuk, A. K., Nastishin, Yu. A., Golovin, A. B., and Lavrentovich, O. D. Lyotropic chromonic liquid crystal semiconductors for water-solution processable organic electronics. Applied Physics Letters **2010**, 97(26), 263305/1-263305/3.

[66] Boussey-Said, J. Sheet and spreading resistance analysis of ion implanted and annealed semiconductors. Semiconductors and Semimetals **1997**, 45, 129-163.

[67] Geurst, J. A. Theory of space-charge-limited currents in thin semiconductor layers. Physica Status Solidi **1966**, 15(1), 107-18.

[68] Singh, Th. B., Hernandez-Sosa, G., Neugebauer, H., Andreev, A., Sitter, H., and Sariciftci, N. S. Electrical transport properties of hot wall epitaxially grown para-sexiphenyl nano-needles. Physica Status Solidi B: Basic Solid State Physics **2006**, 243(13), 3329-3332.

[69] Gould, R. D. The effects of oxygen doping and annealing on the surface and bulk electrical conductivity in planar copper phthalocyanine thin films for gas-sensing applications.Thin Solid Films **1998**, 317, 432–435

CHAPTER 7

TACTOIDS AND CHROMONIC DISPERSION IN POLYMERS

7.1 Introduction to tactoids

In the early literature, tactoid formation was reported from concentrated colloidal solutions of the dyestuff such as benzopurpurin, inorganic particles such as vanadium pentoxide (V_2O_5), tungstic acid (WO_3), aluminum oxyhydroxide, iron oxide and iron oxyhydroxide, etc [1-8]. Watson et al did comparative electron and light microscopic investigations of tactoid structures in V_2O_5 solutions [6], as shown in Figure 7.1 a-c. They also described the formation of tactoid-like aggregates of nematic phase (or single crystals of unusual shape) for WO_3 (Figure 7.1 d) [7]: "The first particles of well defined shape to form from an aqueous solution of tungstic acid are exceedingly thin, electron-optically, highly transparent platelets of surprisingly uniform elliptical shape which always seem to have a remarkably uniform initial size (major axis) of 0.2-0.3 micron. Immediately after formation, these 'nuclei' grow rapidly in length and width, with continuous perfection of their elliptical shape." Later, tactoids were also observed in the study of biological systems, such as collagen fibril, hemoglobin, tobacco mosaic virus (TMV), tropomyosin, F-actin, etc [9-14]. Clay tactoids, made of stacks of parallel clay platelets, were also reported [15-18]. In recent years, studies on tactoids formed in carbon nanotube aqueous solution [19] and in some chromonic liquid crystals (DSCG, Violet 20) were also reported [20-22].

Tactoids are formed as the nuclei of the new phase in the biphasic region of lyotropic liquid crystals containing highly anisometric colloidal particles. Basically, there are two types of tactoids, positive tactoids and negative tactoids. As shown in Figure 7.2, positive tactoids refers to the non spherical nematic droplets in the isotropic phase;

negative tactoids mean the non spherical isotropic droplets in the nematic phase. Those non spherical tactoids were described as “bipolar”, “elliptical”, “elongated”, “prolate-shaped”, or “spindle-shaped”. Defect points, located at the tactoid vertexes, are called “boojum” [23].

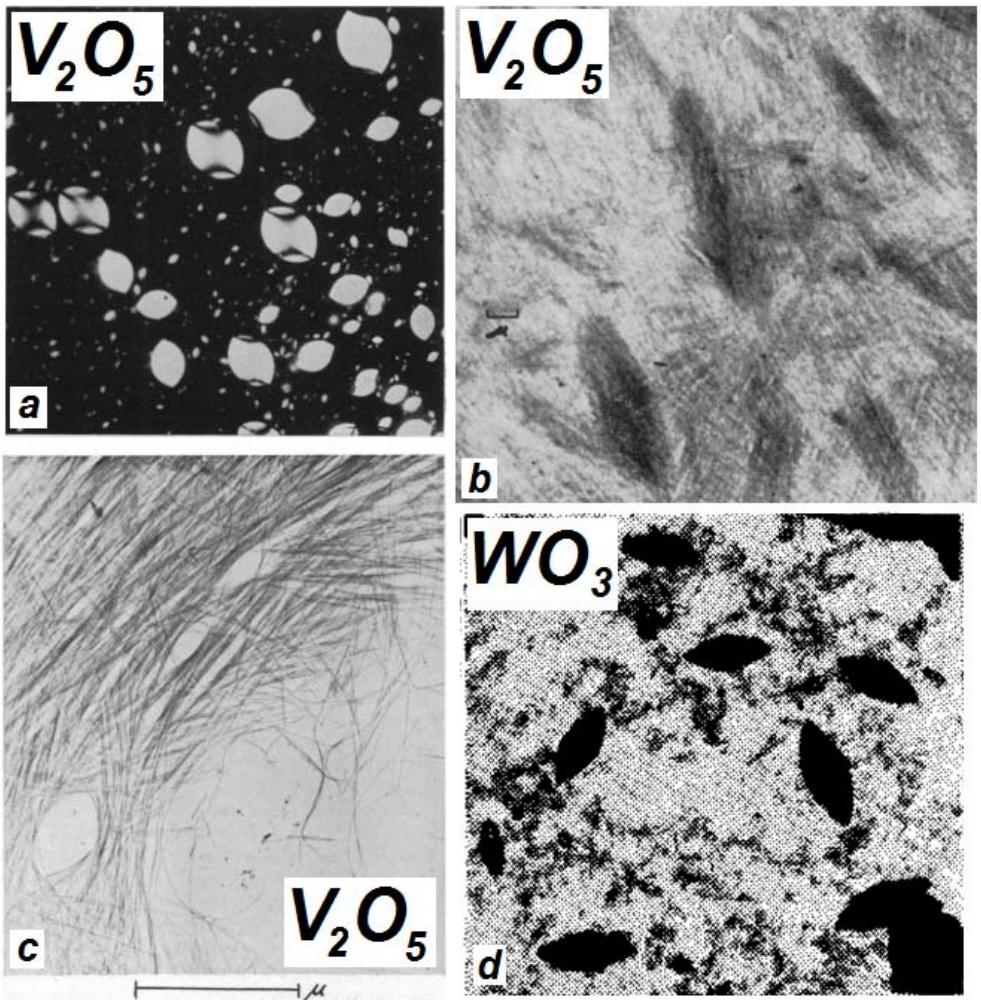

Figure 7.1. a. Photomicrograph between crossed nicols of V_2O_5 tactoids, x100 [6]. b. Electron micrograph of a 24-hour specimen of V_2O_5 showing positive tactoids, x5000[6]. c. Electron micrograph of a 72-hour specimen of V_2O_5 showing negative tactoids, x28000 [6]. d. Electron micrographs of WO_3, x1167, to show the particle shape [7].

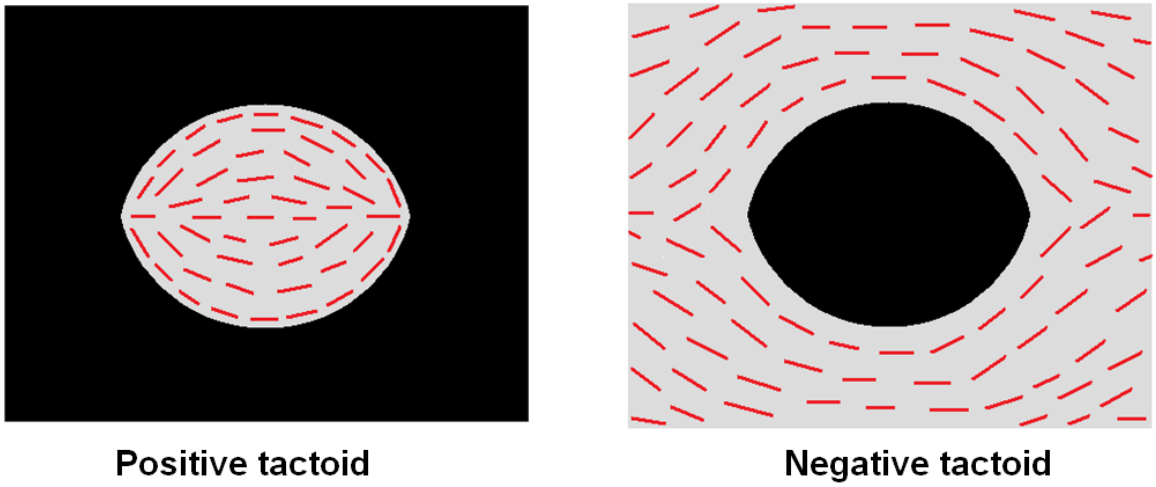

Figure 7.2. Schematic diagram of positive and negative tactoids.

There is also tactoidal shell defect, or called "nematic-nematic tactoids" (nematic droplets in a nematic medium), occurring in lyotropic liquid crystals under magnetic field [24-26]. According to Filas [24], tactoidal shell defects can be produced in magnetically oriented samples of poly(γ-benzyl-D-glutamate) liquid crystals: "Their shape is reminiscent of liquid crystalline droplets or tactoids found in various biphasic colloidal systems and solutions of plant viruses. In contrast to tactoids, however, tactoidal shell defects form a boundary surface which separates two regions of identical structure of the same phase. They are metastable in nature and may persist for many days as long as the bulk of the sample remains oriented by the field." Srinivasarao [25] observed elliptical defects formed in another lyotropic polymer liquid crystal: poly(1,4-phenylene-2,6-benzobisthiazole) (PBT) in methane sulfonic acid subjected to a magnetic field, as shown in Figure 7.3 a-d. The orientations of the directors inside and outside the defect were different. The ratio of the major to the minor axis of such defects was found to be about 2.3 to 2.4. Van den Pol et al [26] discovered (parallel) nematic–(perpendicular) nematic phase separation induced by applying an external magnetic field to a nematic liquid crystal of boardlike colloidal goethite and studied "nematic–nematic tactoids": nematic

droplets sedimenting within a nematic medium with mutually perpendicular orientations, as shown in Figure 7.3 e and f.

Both experimental and theoretical studies have been carried out about the shape and the director-field configuration of tactoids resulted from the competition between the anisotropic surface tension and the elastic property of the liquid crystalline phase [27-29]. Studies also show that large-sized tactoids were shown to be prolate because of the competition between the elastic energy of the nematic phase of the tactoid and the surface energy; small-sized tactoids were prolate because of the competition of the surface energy with the anchoring energy between the director and the boundary of the tactoid [30]. Some theoretical results agree with available experimental data that the aspect ratio of tactoids has size dependence [31, 32]; the director field crosses over smoothly from a homogeneous to a bipolar configuration with increasing droplet size, while the two point defects move from infinity towards the poles on the surface of the droplet [31]. Some Monte Carlo simulations indicate that the aspect ratio of the droplet doesn't change, albeit over a small range of droplet sizes [33]. Shape and director field deformation of tactoids of plate-like colloids in a magnetic field was also studied [34, 35]. A simulation on kinetics of the I-N phase transition of a system of colloidal hard rods shows spinodal decomposition as well as nucleation and growth depending on the supersaturation and finds ellipsoidal nematic clusters with an aspect ratio of about 1.7 as well as order parameter decaying slowly from the center to the surface of the clusters [36].

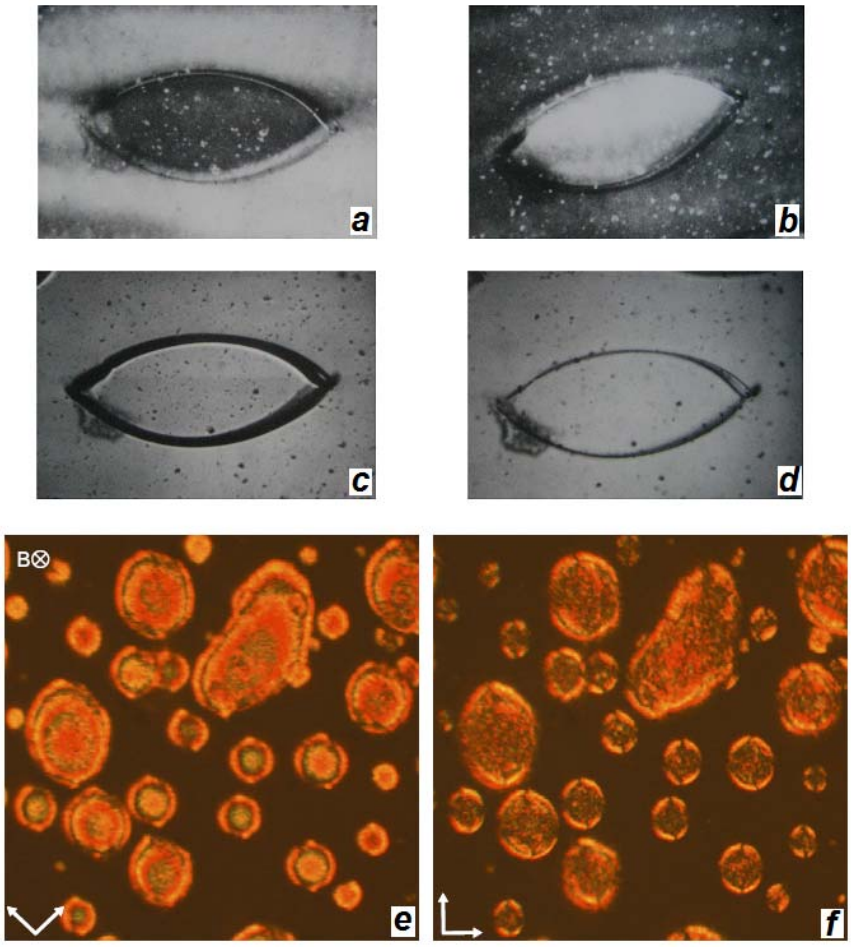

Figure 7.3. Images a, b, c and d: PBT (4.51wt% in methane sulfonic acid) subjected to a magnetic field [25]. a. Under polarized light, no analyzer. b. Under crossed polarizers. c. Polarizer along director. d. Polarizer was normal to director. e and f. Droplets of perpendicular nematic phase in the parallel nematic phase, with different orientations of polarizers [26]. The width of the images is 0.45mm. B is the magnetic field. White arrows indicate the polarizer and analyzer.

7.2 Chromonic tactoids

7.2.1 Tactoids as the "compass" of the director field

Not so many studies have been done on tactoids from chromonic liquid crystals. Our interests in tactoids increase continuously with more phenomena we observed in experiments, like their orientation, fluctuation, growth and pattern under confinement.

First, we discuss their orientation. As temperature increases, tactoids formed as the nuclei of the new isotropic phase in N-I coexistent sample. The orientation of tactoids indicates the director field around them. As shown in Figure 7.4, tactoids in the planar aligned nematic region all oriented along the director direction (green line), while tactoids in the unaligned nematic region oriented more randomly. Tactoids act as the "compass" of the director field of the surrounding medium.

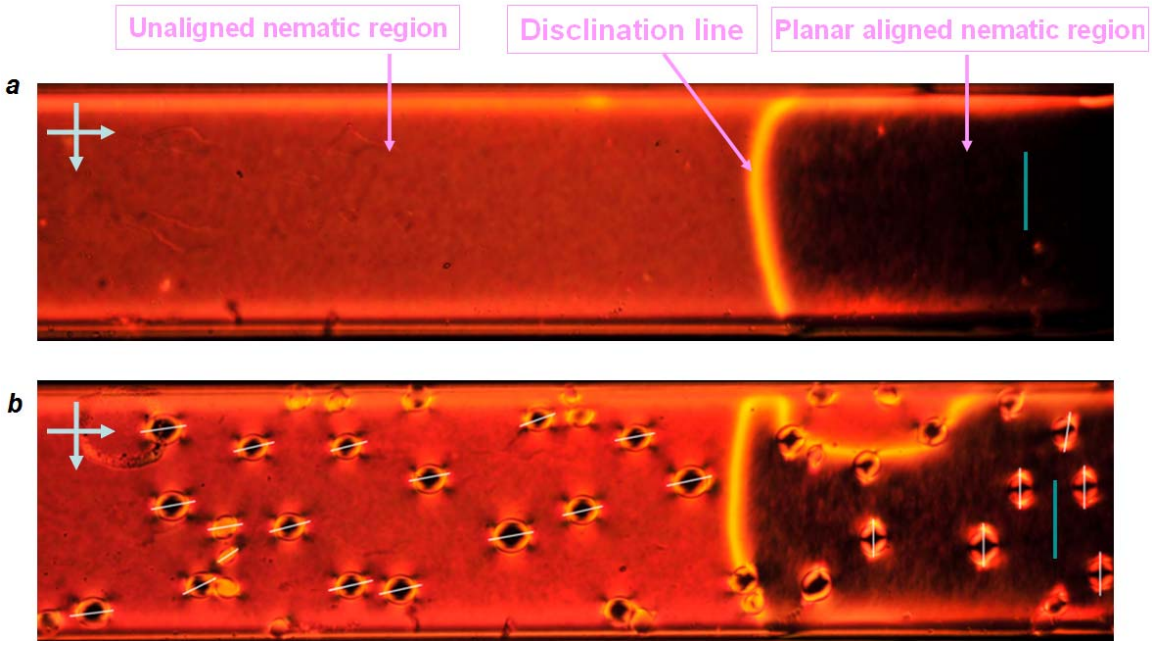

Figure 7.4. Tactoids as "compass" of the director field. a. 1.0M SSY nematic N sample with unaligned and planar aligned regions in a flat capillary (0.2mm/0.02mm/5cm) under crossed polarization. b. As temperature increases, tactoids formed. Green lines indicate the director direction of the planar aligned regions. White lines indicate the long axis (the orientation) of the tactoids. This is the top view of the capillary showing the width of capillary 0.2mm.

7.2.2 Fluctuation and growth of SSY tactoids

When we maintained the biphasic sample of 1.0M SSY in flat capillary on the top of hotstage which was at 40.7 ºC, the size of the tactoids fluctuated while the temperature of the sample vibrated due to the environmental reasons, such as small temperature variation due to air conditioning. As shown in the Figure 7.5, tactoid #3 & #1 were close to other tactoids, so the fluctuation and orientation were influenced; tactoid #2 & #4 were more independent, so their fluctuation steps were exactly synchronous. The fluctuation of tactoids contains information of SSY chromonic, such as the viscosity at this temperature, because fluctuation creates a shape distortion and it should be the sum of a Frank elastic part and a dissipative part which is related to viscosity. Models of the tactoid fluctuation will be our future work.

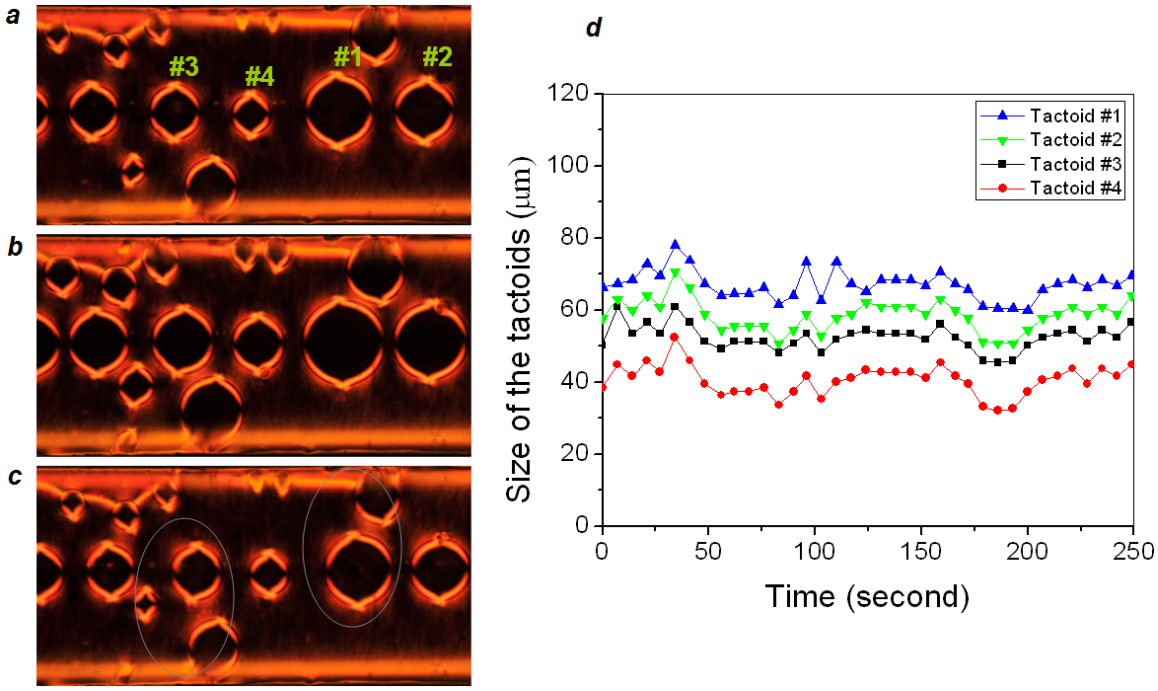

Figure 7.5. Fluctuation of tactoids at 40.7 ºC. a-c. POM images of biphasic 1.0M SSY sample in a flat capillary (0.2mm/0.02mm/5cm) under crossed polarization at different times. This is the top view of the capillary showing the width of capillary 0.2mm. d. Size fluctuation of tactoids as a function of time due to environmental reasons.

Figure 7.6 shows the growth of the tactoids while heating 1.0M SSY chromonics from nematic phase at room temperature to isotropic phase at rate of 0.1ºC/min. As the heating rate was slow, biphasic region/tactoids started to occur earlier (~33º) than that (~38.8º) indicated in the phase diagram in Chapter Two where the heating rate was 0.4ºC/min. As different tactoids nucleated and formed at different time, there was always size-distribution in the snapshot of the system. The tactoid grew until it met another tactoid and coalesced.

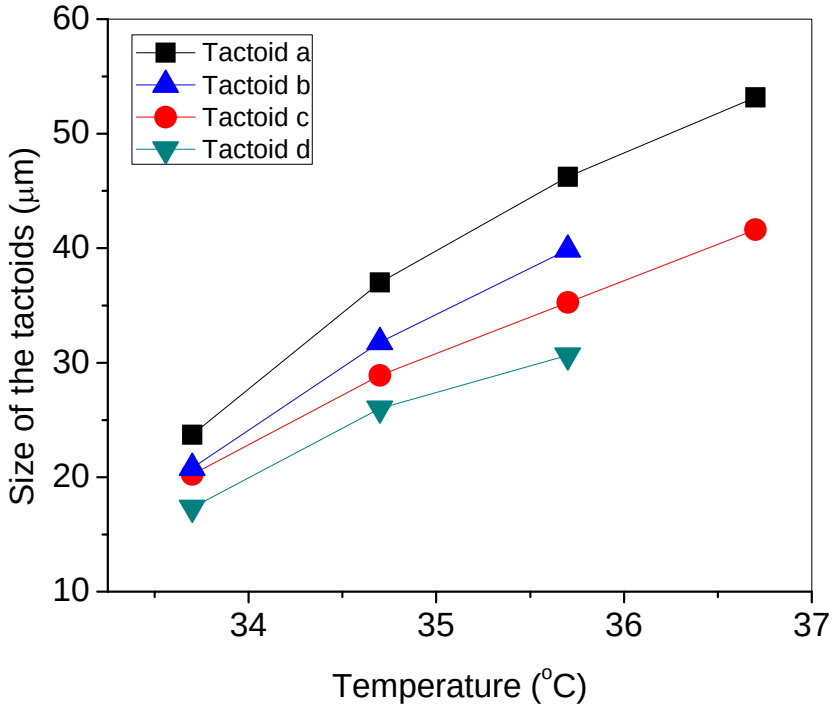

Figure 7.6. The size of tactoids as a function of temperature.

7.2.3 Interaction between disclination lines and SSY tactoids

A negative tactoid linked by disclination lines was observed when the 1.0M SSY sample in a flat capillary was cooling from N-I coexistent region to nematic N phase, as shown in Figure 7.7. Here, we saw the case when disclination lines met with point defects, "boojum", at the surface of the tactoid, as well as the case when the disclination lines (one end stuck at the glass-nematic interface) met with the surface of the tactoid. Compared to the other prolate shape of other tactoids or the bipolar shape of the individual SSY tactoids, the shape was very elliptical and could be fitted with the equation $\frac{X^2}{39.8^2}+\frac{Y^2}{35.6^2}=1$ perfectly, taking the one at the relative time of 0s as shown in the Figure 7.8. It seems that the shape of the left half of the tactoid was not affected by the attachment of disclination lines at the surface comparing to the right half of the tactoid without attachment of disclination lines. The force from the disclination line must be negligible compared to that of the tactoid surface. In the Chapter Five, we observed the splitting process of the disclination line; here we observed the growth process of the disclination line when the tactoid was shrinking as the sample was cooling.

After 58s, the tactoid totally disappeared and disclination lines met with each other at one point, where the energy was high and thus pinch-off the disclination lines happened. After pinch-off, disclination lines relaxed as we observed in Chapter Five.

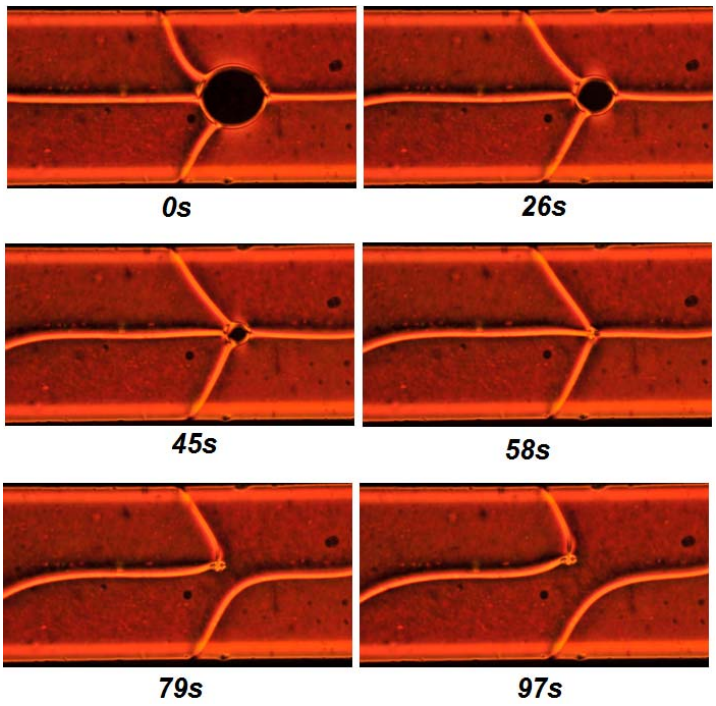

Figure 7.7. Tactoids linked with disclination lines at different relative times. 1.0M SSY sample in a flat capillary (0.2mm/0.02mm/5cm) under crossed polarization was cooling from N-I coexistent region to nematic N phase.

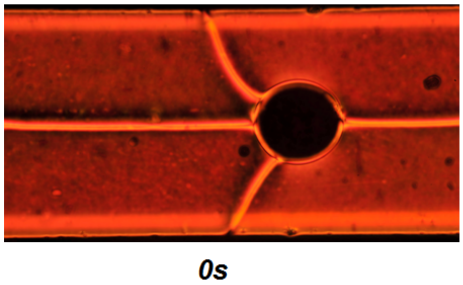

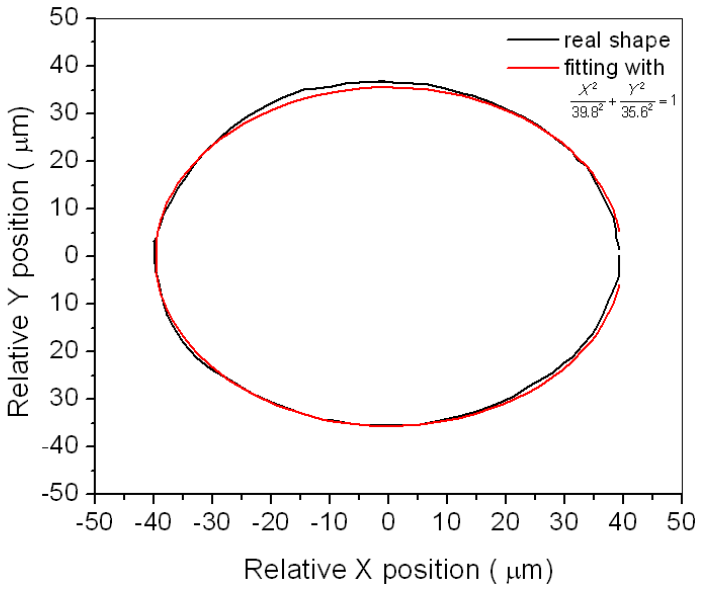

Figure 7.8. Fitting of the tactoid shape at the relative time 0s.

7.2.4 The shape of DSCG tactoids

Based on the research from Lavrentovich's group on tactoids of DSCG (structure and phase diagram of DSCG were shown in the Chapter One) [20-22], the birefringence of DSCG is about -0.02, the DSCG molecule planes are perpendicular to the director, tactoids were formed with or without additives, twisted tactoids in a wedge cell were created by the balance between the geometrical anchoring imposed by the surface tilt and the physical anchoring at the bottom substrate while fluorescent confocal microscopy reveals that the chiral N tactoids are located at the boundaries of cells, thus the chiral symmetry was broken by spatial confinement. In our research, we prepared the DSCG tactoids and studied the elastic property of DSCG chromonics based on Kaznacheev's model [28].

"Positive" DSCG tactoids, more like "nematic-nematic tactoids", look different from SSY tactoids which are usually positive. After studying numbers of tactoids, we found that the aspect ratio of them had a distribution and the major short axes could be different even when the major long axes were the same. The average aspect ratio of "positive" tactoids was about 1.35 as shown in Figure 7.9, while for negative DSCG tactoids, the average aspect ratio of them was about 1.16, as shown in Figure 7.10. Figure 7.11 shows the rotation of "positive" DSCG tactoids under crossed polarization. Both the tactoid and surrounding medium had orientation dependent birefringent color.

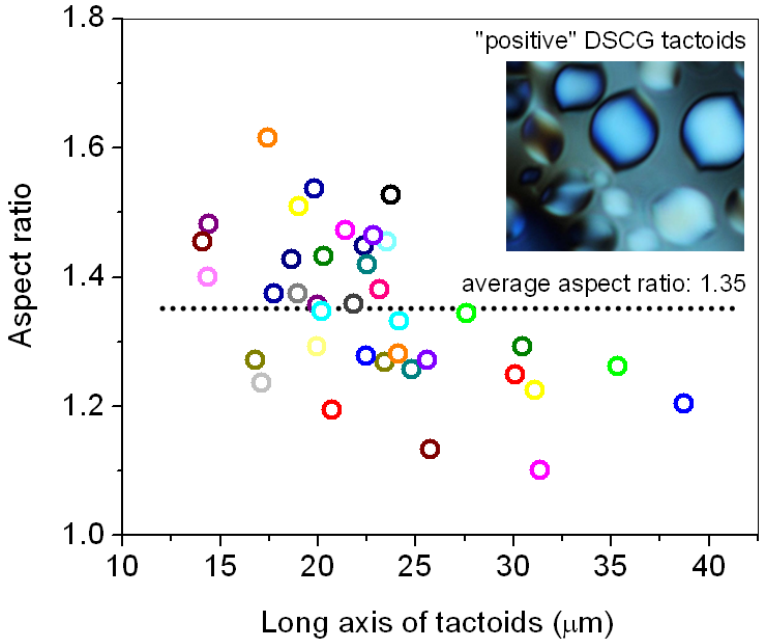

Figure 7.9. Aspect ratios of "positve" DSCG tactoids. The color of each circle was randomly chosen for each tactoid. The dashed line indicates the average value of aspect ratio.

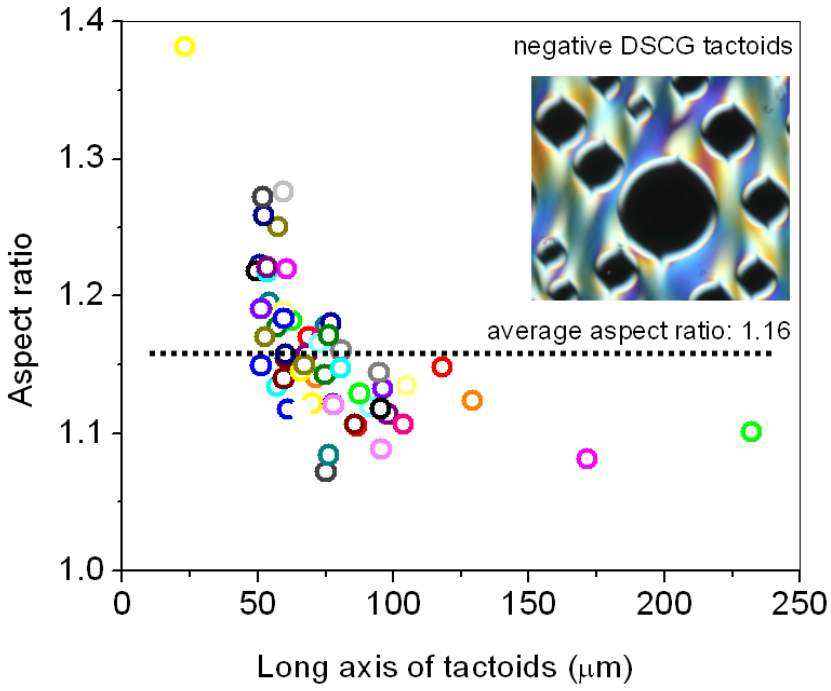

Figure 7.10. Aspect ratios of negative DSCG tactoids. The color of each circle was randomly chosen for each tactoid. The dashed line indicates the average value of aspect ratio.

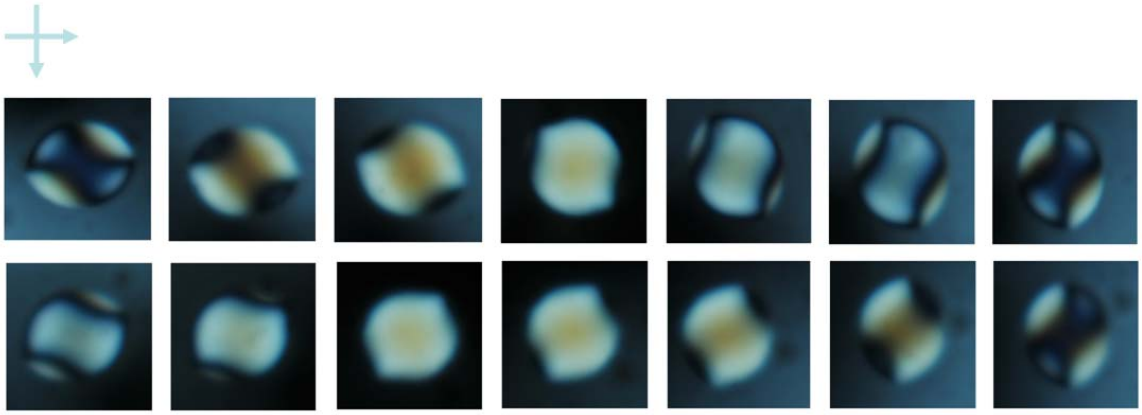

Figure 7.11. Rotation of DSCG tactoids (12wt%, biphasic) in a flat capillary (1.0mm/0.1mm/5cm) under crossed polarizers, long axis of the tactoid is 25 μm. Sample thickness is 100 μm.

According to Kaznacheev's model [28], the tactoid free energy is made up of the elastic energy of nematic phase and surface energy; the shape of a tactoid is defined by two parameters, R_t and Θ, as shown in Figure 7.12a. The tactoid boundary is the surface of revolution of a circular arc of radius R_t about the z axis:

$$R_t = \frac{K_i}{\sigma} f_i(\Theta) \tag{7.1}$$

where K_i is the elastic constant, σ is the surface energy, and $f_i(\Theta)$ is a function of angle Θ:

$$f_1(\Theta) = \frac{\Theta \sin\Theta - 2\Theta^2 \cos\Theta + \sin^2\Theta \cos\Theta}{\cos\Theta[\Theta(\Theta + \sin\Theta\cos\Theta) - 2\sin^2\Theta]} \tag{7.2}$$

$$f_3(\Theta) = \frac{(\Theta^2 - \sin^2\Theta)[\Theta(1+2\cos^2\Theta) - 3\sin\Theta\cos\Theta]}{4\sin\Theta\cos\Theta[\Theta(\Theta + \sin\Theta\cos\Theta) - 2\sin^2\Theta]} \tag{7.3}$$

Therefore, the ratio of bend and splay elastic constants, K_{33}/K_{11}, equally K_3/K_1, can be obtained by knowing the angle Θ with certain R_t of the tactoid.

In our experiment, we obtained data of DSCG tactoids (12wt %) of radius R_t as a function of angle Θ, as shown in Figure 7.13. By applying the Kaznachev's model, we obtained $K_{33}/K_{11} \approx 4.0$ for average at room temperature. In the literature, dynamic light scattering measurement of DSCG of 14 wt% in the nematic N phase was performed, and elastic constants were obtained: $K_{33}/K_{11} \approx 2.1$, $K_{11} \approx 12.5$ pN, $K_{22} \approx 0.67$ pN, $K_{33} \approx 25$ pN at room temperature [37]. So our $K_{33}/K_{11} \approx 4.0$ is on the same order of magnitude with $K_{33}/K_{11} \approx 2.1$ from dynamic light scattering measurement.

Based on equation (7.1) and experimental data, we also calculated the ratio $K_{11}/\sigma \approx 0.9$ μm. Assuming $K_{11} \approx 10$pN, we obtained $\sigma \approx 11 \times 10^{-6}$ N/m ≈ 0.011erg/cm^2 for DSCG chromonics. Therefore, the surface tension for DSCG chromonics is really small compared to a typical thermotropic liquid crystal which is usually about 10erg/cm^2 [38]. It also explains that no prolate shape (usually spherical shape, instead) of droplets is observed in thermotropic liquid crystals due to the large surface tension.

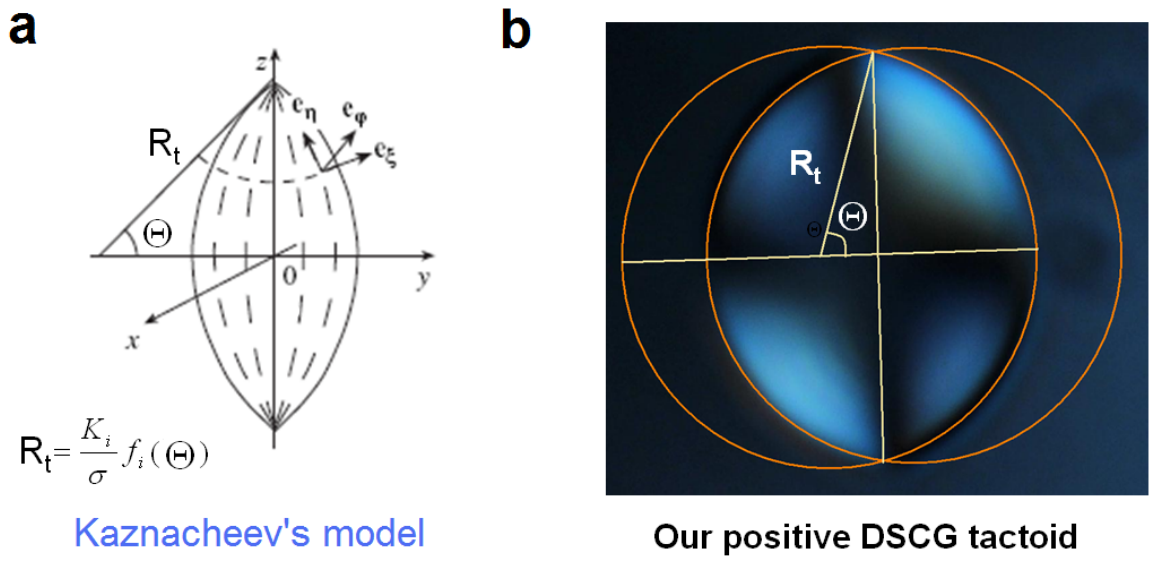

Figure 7.12. Shape analysis of tactoids. a. Kaznacheev's model, the tactoid boundary is the surface of revolution of a circular arc of radius R_t about the z axis. b. Our DSCG tactoid.

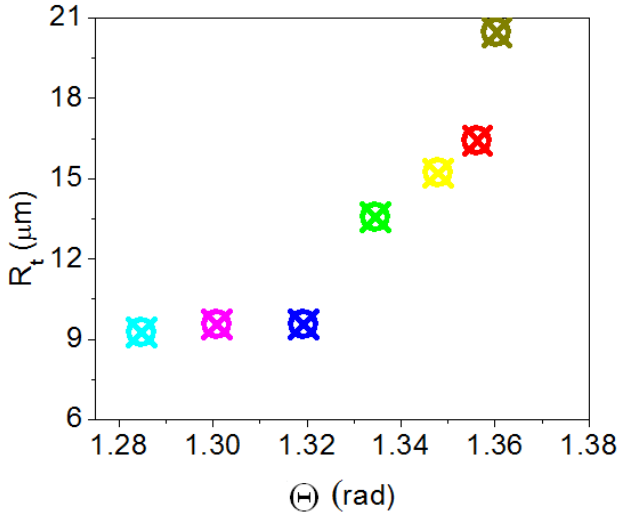

Figure 7.13. Measured data of DSCG tactoids of radius R_t as a function of angle Θ.

7.3 Biphasic chromonics under capillary confinement

By filling the 12wt% biphasic DSCG chromonics into the capillaries with different geometries, a lot of interesting patterns were observed, as shown in Figure 7.14. Due to the confinement effect of circular capillary, the shape of the I-N interface was deformed, as shown in the Figure 7.14a and its enlarged image in Figure 7.15. However, the curvature of the interface is constant with $R_{curvature}$ ~140μm. From Figure 7.14 b, c, e, and f, the isotropic droplets were all aligned along the long axis of the capillary. The distance between two isotropic droplets is governed by their interaction energy. Figure 7.14d shows a big isotropic region confined in the capillary.

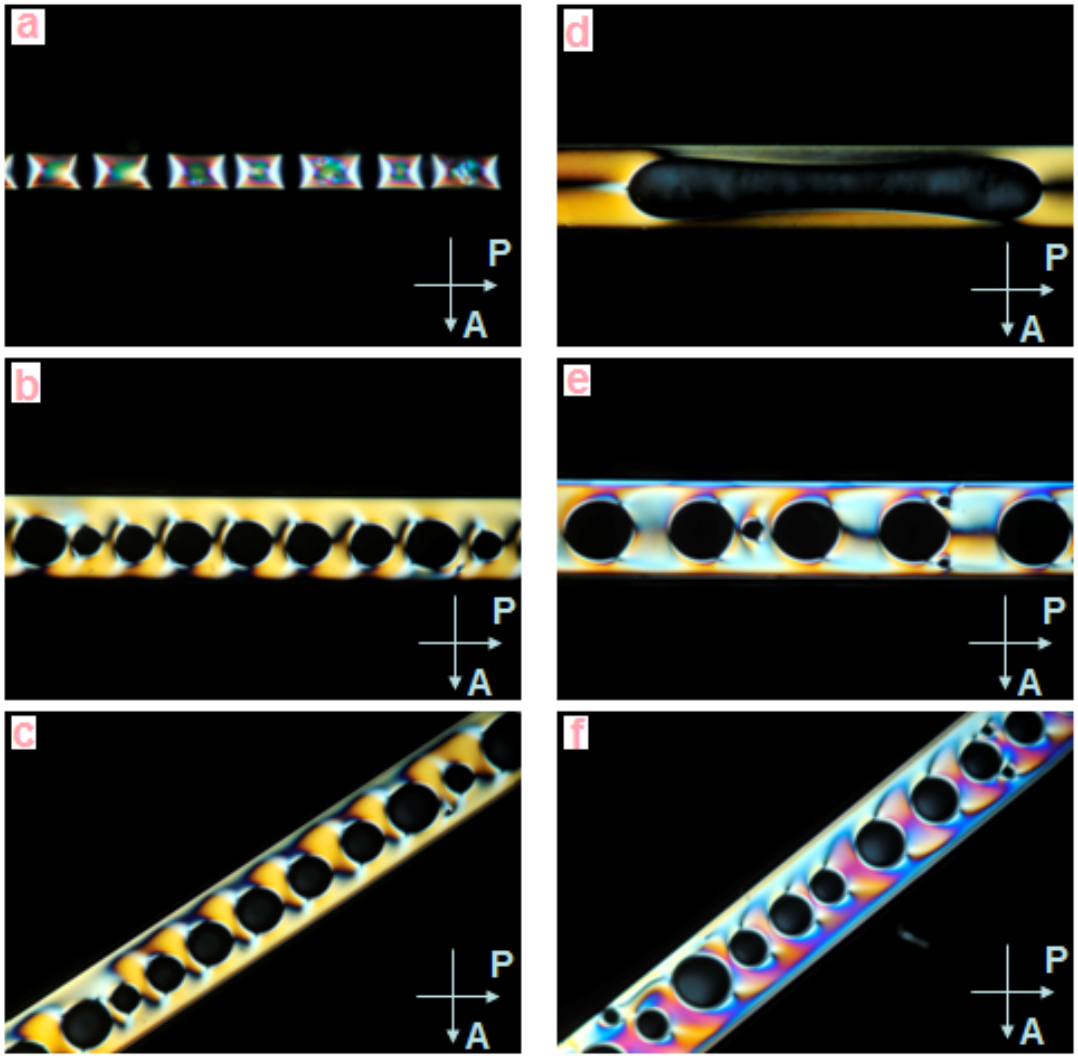

Figure 7.14. DSCG chromonics (12wt%, biphasic) under confinement of capillaries with various geometries. a. A circular capillary with radius 70μm. b c and d. Flat capillaries (0.02mm/ 0.2mm/5cm) with width 0.2mm. e and f. Flat capillaries (0.03mm/0.3mm/5cm) with width 0.3mm. Magnification is 5x.

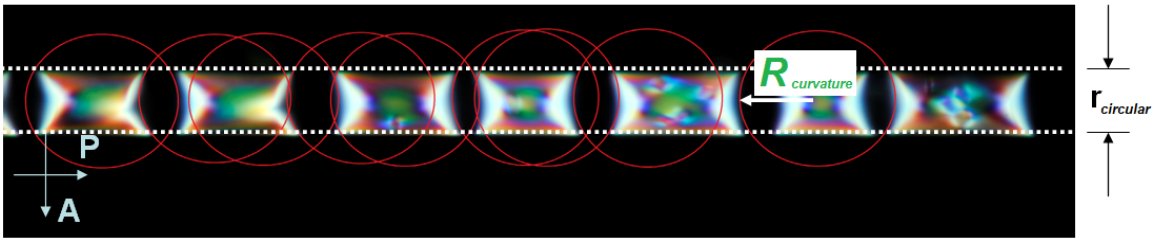

Figure 7.15. Enlarged image of 7.14a. Radius ($r_{circular}$) circular capillary is 70μm. $R_{curvature}$ is about 140μm.

7.4 Polymer dispersed chromonic liquid crystals

Polymer dispersed thermotropic liquid crystal materials are well studied mainly because of their electro-optical properties and their potential application in displays [39-43]. Research on polymer dispersed lyotropic chromonic liquid crystals (PDLCLCs) has just been started in recent years [21, 22, 44]. Fundamental understanding on the interaction between polymers and chromonic liquid crystals in aqueous solution as well as application of PDLCLCs need to be explored. In this Chapter, we study the anchoring effect of polymers on the director configuration of chromonic liquid crystal droplets.

Three water soluble macromolecules were used to mix with SSY and DSCG chromonics at different ratios. Figure 7.16 shows the name, molecular weight and molecular structures of three macromolecules: polyvinylpyrrolidone (PVP), polyvinyl alcohol (PVA) and bovine serum albumin (BSA).

As we know, the SSY aqueous solution only starts to form chromonic liquid crystalline phase from about 0.9M. But water soluble polymer PVP acting as an osmotic compression agent can condense the SSY aqueous solution and chromonic nematic droplets form with initial concentration as low as 0.7M. As shown in the Table 7.1, SSY aqueous solution of low concentrations with PVP becomes biphasic and forms PDLCLCs. POM images in Figure 7.17 shows the bipolar droplets, so PVP induced planar alignment for the droplets. Figure 7.18 shows the periodic intensity change in the center when the sample was rotated, because the stacking columns in the central area were oriented more or less parallel to bipolar axis for the bipolar configuration. From Figure 7.17b, it could be seen the isotropic area surrounding the droplet was sunset yellow which was the color of SSY. As the PVP solution is transparent, so the isotropic area consisted of a mixture of SSY, PVP and water. Since the droplet size was larger than

the glass cell thickness, droplets were squeezed in two ways both shown in Figure 7.17c: one still had the bipolar shape, the other, also seen in Figure 7.17d, was disk-like.

More experiments were conducted on other mixture systems: SSY/PVA, SSY/BSA, DSCG/BSA, DSCG/PVP, DSCG/PVA, as shown in Figure 7.19. Both planar alignment of spherical bipolar (SSY/PVP and SSY/BSA) and ellipsoidal bipolar droplets (SSY/PVA and DSCG/BSA), and homeotropic alignment of radial droplets (DSCG/PVP and DSCG/PVA) were created. Figure 7.20 shows the schemes of different director configurations of macromolecule dispersed chromonics in aqueous solutions. Table 7.2 summarizes the different director configurations of PDLCLCs. The same macromolecule has different anchoring effect on the different chromonics. It tells us that the property of different chromonic liquid crystals varies and individual study is needed for each system. The same chromonic liquid crystal has different droplet shapes and director configurations in presence of different macromolecules. It tells us that droplets can be tuned by macromolecular additives.

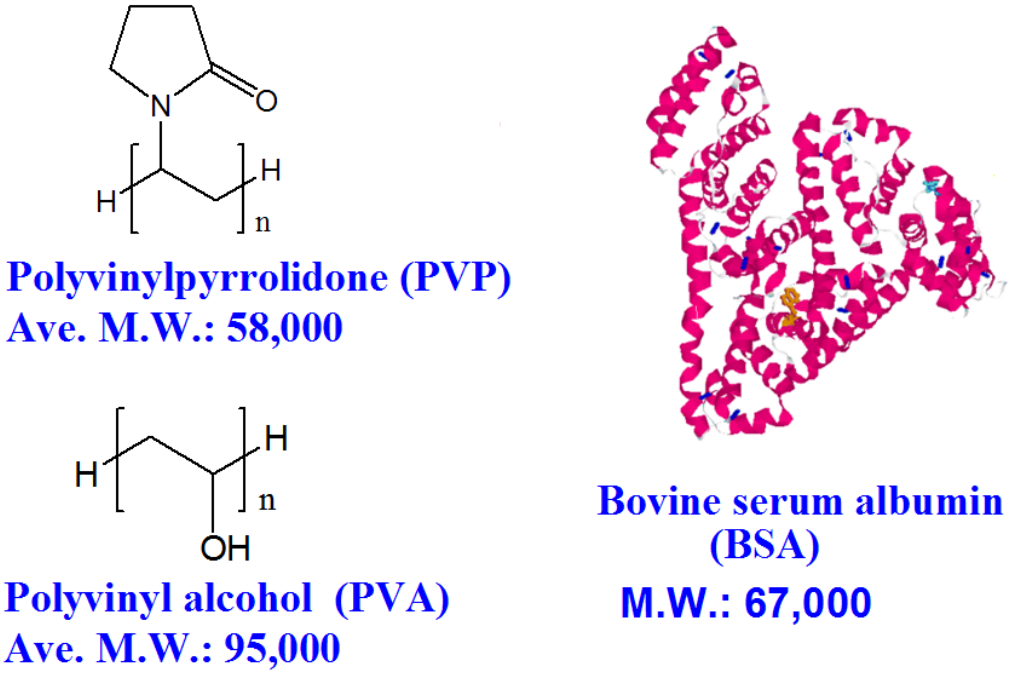

Figure 7.16. Molecular structures of macromolecules used to disperse chromonic liquid crystals.

Table 7.1. Mixtures of PVP and different SSY aqueous solutions with different weight ratios (biphasic: SSY N phase and (SSY+PVP) isotropic phase coexist).

SSY/PVP (wt)	1:0.125	1:0.25	1:0.5	1:1	1:2	1:2.5	1:3
0.6M SSY	isotropic	isotropic	isotropic	isotropic	isotropic	isotropic	isotropic
0.7M SSY	isotropic	biphasic	biphasic	biphasic	biphasic		
0.8M SSY	biphasic	biphasic	biphasic				
1.0M SSY	biphasic	biphasic	biphasic				

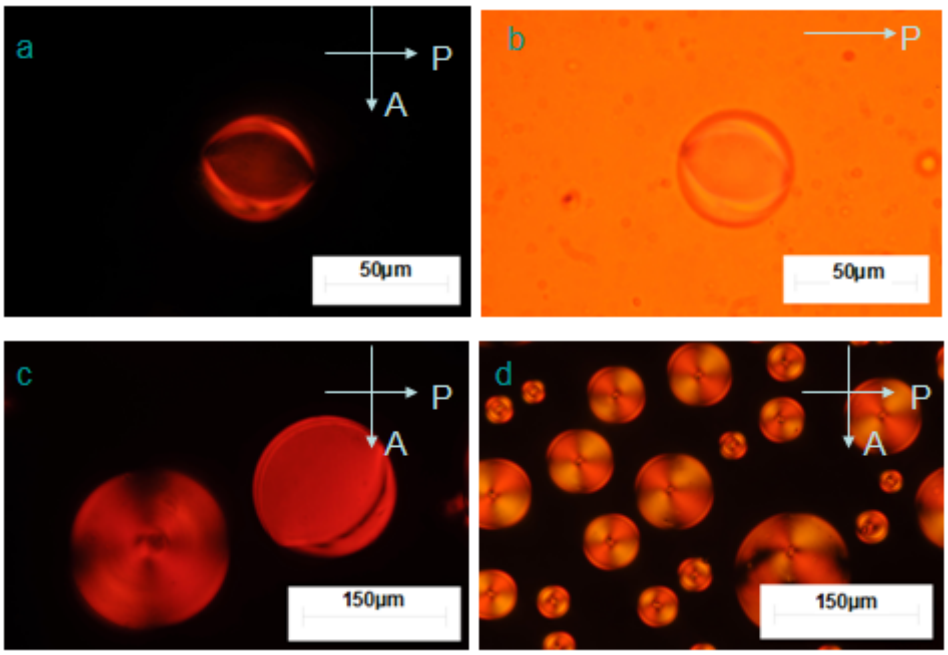

Figure 7.17. POM images of bipolar droplets from the mixture of SSY and PVP in aqueous solutions in the glass cells with thickness 10μm. Images a, c and d are under crossed polarizers; image b was taken without analyzer corresponding to a. Sample a b and c: 0.8 M SSY, SSY: PVP=1:0.5 (wt%); sample d: 0.7M SSY, SSY: PVP=1:2 (wt%).

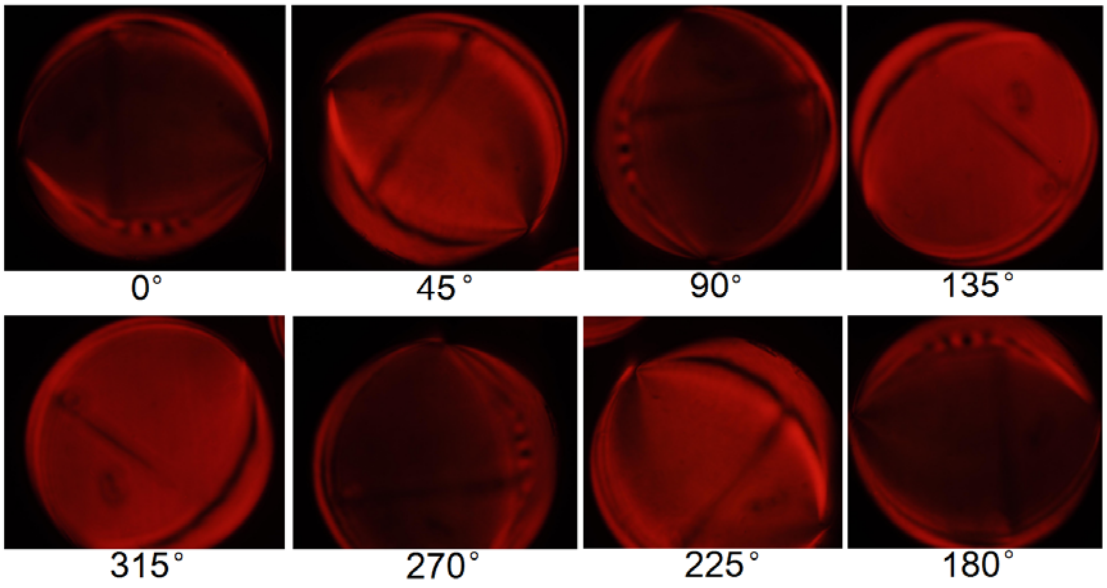

Figure 7.18. POM images of the SSY/PVP bipolar droplet rotating under the crossed polarizers. The distance between two poles is about 163μm.

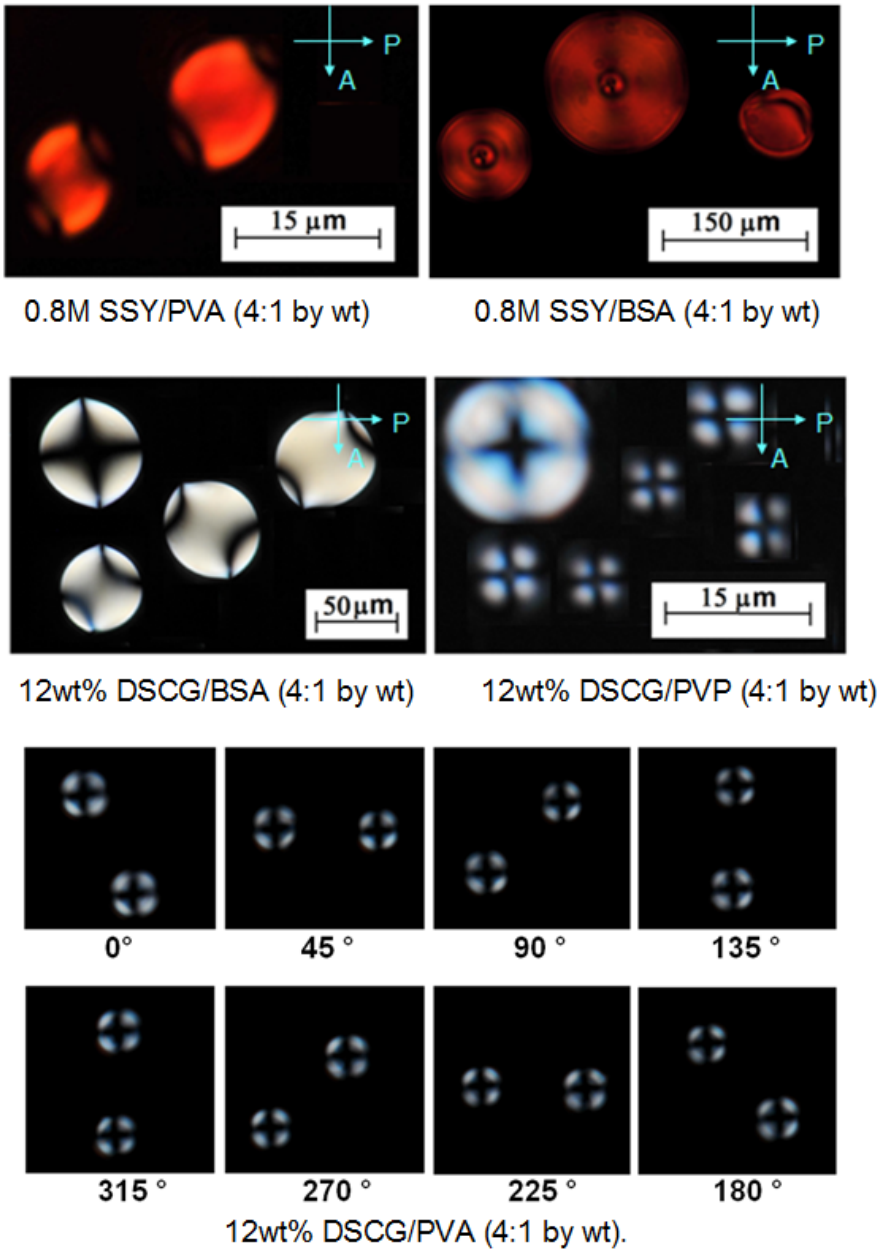

Figure 7.19. POM images of droplets from the mixture of macromolecule dispersed chromonics in aqueous solutions in the glass cells with thickness 15µm under the crossed polarizers. The bottom eight images are radial droplets of DSCG/PVA rotating under the crossed polarizers. The droplets are about 163µm.

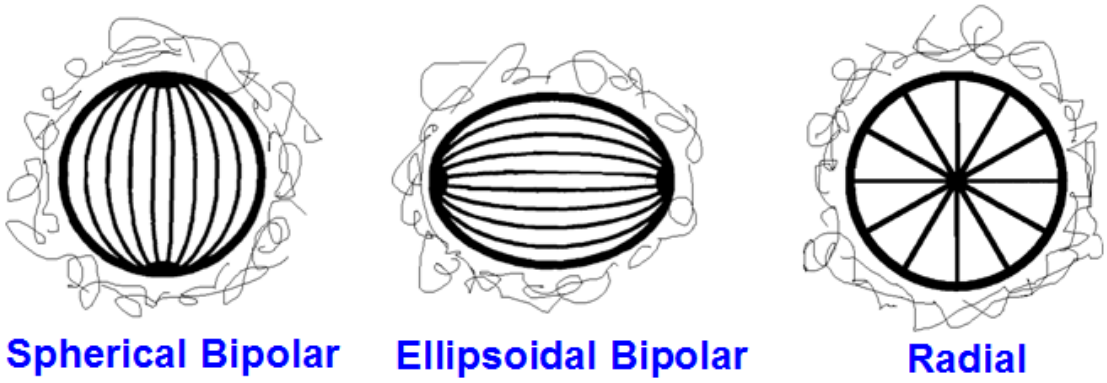

Figure 7.20. Schemes of different director configurations of macromolecule dispersed chromonics in aqueous solutions. The local symmetry axis is parallel to the lines.

Table 7.2. Summary of different director configurations of macromolecule dispersed chromonics in aqueous solutions.

	PVP	PVA	BSA
SSY	Planar (bipolar)	Planar (bipolar)	Planar (bipolar)
DSCG	Homeotropic (radial)	Homeotropic (radial)	Planar (bipolar)

7.5 Conclusions

SSY tactoids were prepared in the biphasic region of SSY chromonics. Negative tactoids acting as the "compass" of the surrounding nematic medium was described. It also provides a way to identify the director field of nematic chromonics: just by simply heating the nematic sample into N-I coexistent region and waiting to see the orientation of the tactoids. Fluctuation of tactoids was also observed. Growth of tactoids under slow heating was also studied. A tactoid linked by disclination lines was also observed. Its shape was perfectly elliptical. While the tactoid was shrinking as temperature decreased, the growth of disclination lines was observed. DSCG tactoids were also prepared and the

aspect ratios of both “positive” and negative tactoids were calculated. The ratio of bend and splay elastic constants were generated based on the shape and Kaznacheev's theoretical model. Pattern information was also obtained for biphasic DSGC under circular or flat capillary confinement, where Physics governed interesting phenomena. Polymer dispersed lyotropic chromonic liquid crystals were also fabricated by using three water soluble macromolecules PVP, PVA and BSA. Both planar alignment of spherical bipolar (SSY/PVP and SSY/BSA) and ellipsoidal bipolar droplets (SSY/PVA and DSCG/BSA), and homeotropic alignment of radial droplets (DSCG/PVP and DSCG/PVA) were created.

For future work on these chromonic droplets, tactoids or polymer dispersed droplets, we recommend more study of the statics (shape) and dynamics (fluctuation, growth) of tactoids to obtain information on the bulk properties, such as elastic constants and viscosity. We also recommend measuring the response of polymer dispersed droplets to the external electric and magnetic fields and exploring their possible device applications. As lyotropic systems are always biologically important, it will be good to study tactoids and spindles formed in mitosis together. These spindles made of microtubules and motor proteins are double refracting and also look like tactoids [45-50]. However, there is no well-established framework for predicting the behaviors of such nonequilibrium systems [51-54]. Probably, tactoids may work as a simplified model for these spindles in some manner.

7.6 References

[1] Zocher, H., and Jacobsohn, K. Taktosols. Kolloidchemische Beihefte **1929**, 28, 167-206.

[2] Freundlich, H., Enslin, O., and Sollner, K. The formation of tachoids in mixtures of two sols and their biological significance. Protoplasma **1933**, 17, 489-498.

[3] Coper, K., and Freundlich, H. The formation of tactoids in iron oxide sols. Transactions of the Faraday Society **1937**, 33, 348-350.

[4] Freundlich, H. Colloidal structures in biology. Journal of Physical Chemistry **1937**, 41, 1151-1161.

[5] Langmuir, I. The role of attractive and repulsive forces in the formation of tactoids, thixotropic gels, protein crystals and coacervates. Journal of Chemical Physics **1938**, 6, 873-896.

[6] Watson, J. H. L., Heller, W., and Wojtowicz, W. Comparative electron and light microscopic investigations of tactoid structures in V_2O_5 sols. Science **1949**, 109(2829), 274.

[7] Mackay, A. L. The micromorphology of β-FeOOH. Journal of the Physical Society of Japan **1962**, 17(Suppl. B-II), 317-319.

[8] Reed, R., Wood, M. J., and Keech, M. K. Helical nature of the collagen fibril. Nature **1956**, 177, 697-699.

[9] Moon, J. H. Tactoid formation in deer hemoglobin. American Journal of Physiology **1960**, 199, 190-192.

[10] Bernal, J. D., and Fankuchen, I. X-ray and crystallographic studies of plant virus preparations. I. Introduction and preparation of specimens. II. Modes of aggregation of the virus particles. Journal of General Physiology **1941**, 25, 111-20,120-146.

[11] Dudman, W. F. Precipitation of tobacco mosaic virus by macromolecules, a method for estimating molecular volumes. Nature **1966**, 211(5053), 1049-50, 1067.

[12] Murayama, M. Molecular aspects of tactoid formation in man and animals. Annals of the New York Academy of Sciences **1974**, 241(Hemoglobins: Comp. Mol. Biol. Models Study Dis.), 623-637.

[13] Hurwitz, F. I., and Walton, A. G. Structural analysis of tropomyosin tactoids. Biochemical and Biophysical Research Communications **1976**, 68(3), 1027-1033.

[14] Oakes, P. W., Viamontes, J., and Tang, J. X. Growth of tactoidal droplets during the first-order isotropic to nematic phase transition of F-actin. Physical Review E: Statistical, Nonlinear, and Soft Matter Physics **2007**, 75(6-1), 061902/1-061902/11.

[15] Shainberg, I., and Kaiserman, A. Kinetics of the formation and breakdown of calcium-montmorillonite tactoids. Soil Science Society of America Proceedings **1969**, 33(4), 547-551.

[16] Shomer, I., and Mingelgrin, U. A direct procedure for determining the number of plates in tactoids of smectites: the NA/CA-montmorillonite case. Clays and Clay Minerals **1978**, 26(2), 135-138.

[17] Kleijn, W. B., and Oster, J. D. A model of clay swelling and tactoid formation. Clays and Clay Minerals **1982**, 30(5), 383-390.

[18] Lahav, N., and Baenin, A. Tactoid rearrangement and the optical density of montmorillonite suspensions during sodium-calcium exchange reaction. Journal of Colloid and Interface Science **1968**, 26(2), 238-240.

[19] Puech, N., Grelet, E., Poulin, P., Blanc, C., and van der Schoot, P. Nematic droplets in aqueous dispersions of carbon nanotubes. Physical Review E: Statistical, Nonlinear, and Soft Matter Physics **2010**, 82(2-1), 020702/1-020702/4.

[20] Nastishin,Yu. A., Liu, H., Schneider, T., Nazarenko, V., Vasyuta, R., Shiyanovskii, S. V. and Lavrentovich, O. D. Optical characterization of the nematic lyotropic chromonic liquid crystals: Light absorption, birefringence, and scalar order parameter. Physical Review E **2005**, 72, 041711.

[21] Tortora, L. , Park, H.-S., Kang, S.-W., Savaryn, V., Hong, S.-H., Kaznatcheev, K., Finotello, D., Sprunt, S., Kumar, S., and Lavrentovich, O. D. Self-assembly, condensation, and order in aqueous lyotropic chromonic liquid crystals crowded with additives. Soft Matter **2010**, 6 (17), 4157-4167.

[22] Tortora, L., and Lavrentovich, O. D. Chiral symmetry breaking by spatial confinement in tactoidal droplets of lyotropic chromonic liquid crystals. Proceedings of the National Academy of Sciences of the United States of America **2011**, 108 (13), 5163-5168.

[23] Merimin N. D. E Pluribus Boojum: the physicist as neologist. Physics Today, **1981**, 34(4), 46.

[24] Filas, R. W. Tactoidal shell defects in poly(γ-benzyl-D-glutamate) liquid crystals. Journal de Physique (Paris) **1978**, 39(1), 49-56.

[25] Srinivasarao, M. Rheo-optical studies on a polymer liquid crystal under the influence of flow or magnetic fields. Ph.D. Thesis, Carnegie Mellon University, **1990**, 217 pp.

[26] van den Pol, E., Verhoeff, A. A., Lupascu, A, Diaconeasa, M. A., Davidson, P., Dozov, I., Kuipers, B. W. M., Thies-Weesie, D. M. E., and Vroege, G. J. Magnetic-field-induced nematic-nematic phase separation and droplet formation in colloidal goethite. Journal of Physics. Condensed matter: an Institute of Physics journal **2011**, 23(19), 194108.

[27] Trukhina, Yu., Jungblut, S., van der Schoot, P., and Schilling, T. Osmotic compression of droplets of hard rods: A computer simulation study. Journal of Chemical Physics **2009**, 130(16), 164513/1-164513/7.

[28] Kaznacheev, A. V., Bogdanov, M. M., and Taraskin, S. A. The nature of prolate shape of tactoids in lyotropic inorganic liquid crystals. Journal of Experimental and Theoretical Physics **2002**, 95(1), 57-63.

[29] Verhoeff, A. A., Bakelaar, I. A., Otten, R. H. J., van der Schoot, P., and Lekkerkerker, H. N. W. Tactoids of plate-like particles: size, shape, and director field. Langmuir **2011**, 27(1), 116-125.

[30] Kaznacheev, A. V., Bogdanov, M. M., and Sonin, A. S. The influence of anchoring energy on the prolate shape of tactoids in lyotropic inorganic liquid crystals. Journal of Experimental and Theoretical Physics **2003**, 97(6), 1159-1167.

[31] Prinsen, P., Van der Schoot, P. Continuous director-field transformation of nematic tactoids. European Physical Journal E: Soft Matter **2004**, 13(1), 35-41.

[32] Prinsen, P., and van der Schoot, P. Shape and director-field transformation of tactoids. Physical Review E: Statistical, Nonlinear, and Soft Matter Physics **2003**, 68(2-1), 021701/1-021701/11.

[33] Bates, M. A. Computer simulation studies of nematic liquid crystal tactoids. Chemical Physics Letters **2002**, 368(1, 2), 87-93.

[34] Verhoeff, A. A., Otten, R. H. J., van der Schoot, Paul, Lekkerkerker, and Henk N. W. Shape and director field deformation of tactoids of plate-like colloids in a magnetic field. Journal of Physical Chemistry B **2009**, 113(12), 3704-3708.

[35] Verhoeff, A. A., Otten, R. H. J., van der Schoot, Paul, and Lekkerkerker, H. N. W. Magnetic field effects on tactoids of plate-like colloids. Journal of Chemical Physics **2011**, 134(4), 044904/1-044904/14.

[36] Cuetos, A., and Dijkstra, M. Kinetic pathways for the isotropic-nematic phase transition in a system of colloidal hard rods: A simulation study. Physical Review Letters **2007**, 98(9), 095701/1-095701/4.

[37] Nastishin, Y., Neupane, K., Baldwin, A. R., Lavrentovich, O. D., and Sprunt, S. Elasticity and viscosity of a lyotropic chromonic nematic studied with dynamic light scattering. arXiv.org, e-Print Archive, Condensed Matter **2008**, 1-4, arXiv: 0807.2669v1.

[38] Blinov, L. M., Kats, E. I., and Sonin, A. A. Surface physics of thermotropic liquid crystals. Uspekhi Fizicheskikh Nauk **1987**, 152(3), 449-77.

[39] Drzaic, P. S. Liquid Crystal Dispersions. **1995**, World Scientific: Singapore, 429 pp.

[40] Zhou, J. Study of anchoring behavior of nematic fluids at the interface of polymer-dispersed liquid crystals. Ph.D. thesis, Georgia Institute of Technolog, **2003**, 184 pp.

[41] Bunning, T. J., Natarajan, L. V., Tondiglia, V. P., and Sutherland, R. L. Holographic polymer-dispersed liquid crystals (H-PDLCs). Annual Review of Materials Science **2000**, 30, 83-115.

[42] Doane, J. W., Golemme, A., West, J. L., Whitehead, J. B., Jr., and Wu, B. G. Polymer dispersed liquid crystals for display application. Molecular Crystals and Liquid Crystals **1988**, 165, 511-32.

[43] Crawford, G. P., and Doane, J. W. Polymer dispersed liquid crystals. Condensed Matter News **1992**, 1(6), 5-11.

[44] Simon, K. A., Sejwal, P., Gerecht, R. B., and Luk, Y.-Y. Water-in-water emulsions stabilized by non-amphiphilic interactions: polymer-dispersed lyotropic liquid crystals. Langmuir **2007**, 23(3), 1453-1458.

[45] Aman, R. R., and Parks, J. E. Effects of cooling and rewarming on the meiotic spindle and chromosomes of in vitro-matured bovine Oocytes. Biology of Reproduction **1994**, 50, 103-110.

[46] Liu, L., Trimarchi, J. R., Oldenbourg, R., and Keefe, D. L. Increased birefringence in the meiotic spindle provides a new marker for the onset of activation in living Oocytes. Biology of Reproduction **2000**, 63, 251–258.

[47] Wang, W.-H., and Keefe, D. L. Spindle observation in living mammalian oocytes with the polarization microscope and its practical use. Cloning and Stem Cells **2002**, 4(3), 269.

[48] Wang, W.-H., and Keefe, D. L. Prediction of chromosome misalignment among in vitro matured human oocytes by spindle imaging with the PolScope. Fertility and Sterility **2002**, 78(5), 1077.

[49] Moon, J.-H., Hyun, C.-S., Lee, S.-W., Son, W.-Y., Yoon, S.-H., and Lim, J.-H. Visualization of the metaphase II meiotic spindle in living human oocytes using the Polscope enables the prediction of embryonic developmental competence after ICSI. Human Reproduction **2003**, 18(4), 817.

[50] Sun, X.-F., Zhang, W.-H., Chen, X.-J., Xiao, G.-H., Mai, W.-Y., and Wang, W.-H. Spindle dynamics in living mouse oocytes during meiotic maturation, ageing, cooling and overheating: a study by polarized light microscopy. Zygote **2004**, 12, 241-249.

[51] Brugues, J., Needleman, D. J., and Chien, L.-C. Nonequilibrium fluctuations in metaphase spindles: polarized light microscopy, image registration, and correlation functions. Proceedings of SPIE **2010**, 7618(Emerging Liquid Crystal Technologies V), 76180L/1-76180L/10.

[52] Gatlin, J., C., Matov, A., Groen, A. C., Needleman, D. J., Maresca, T. J., Danuser G., Mitchison, T. J., and Salmon, E. D. Spindle fusion requires dynein-mediated sliding of oppositely oriented microtubules. Current Biology: CB **2009**, 19(4), 287-96.

[53] Needleman, D. J. Cellular allometry: the spindle in development and inheritance. Current Biology: CB **2009**, 19(18), R846-7.

[54] Needleman, D. J., and Farhadifar, R. Mitosis: taking the measure of spindle length. Current Biology: CB **2010**, 20(8), R359-60.